

Development of Precipitation-Strengthened Aluminum Alloys and Manufacturing Processes
for Next Generation Automotive Powertrains

by

Joshua Stroh

B.A.Sc, University of British Columbia, 2018

A DISSERTATION SUBMITTED IN PARTIAL FULFILLMENT
OF THE REQUIREMENTS FOR THE DEGREE OF
DOCTOR OF PHILOSOPHY

in

The College of Graduate Studies
(Mechanical Engineering)

THE UNIVERSITY OF BRITISH COLUMBIA
(Okanagan)

April 2021

© Joshua Stroh 2021

The following individuals certify that they have read, and recommend to the College of Graduate Studies for acceptance, a thesis/dissertation entitled:

Development of Precipitation-Strengthened Aluminum Alloys and Manufacturing Processes for Next Generation Automotive Powertrains

submitted by Joshua Stroh in partial fulfillment of the requirements of

the degree of Doctor of Philosophy in Mechanical Engineering.

Dr. Dimitry Sediako, Faculty of Applied Science

Supervisor

Dr. Lukas Bichler, Faculty of Applied Science

Supervisory Committee Member

Dr. Jian Liu, Mechanical Engineering, Faculty of Applied Science

Supervisory Committee Member

Dr. Mahmudur Fatmi, Civil Engineering, Faculty of Applied Science

University Examiner

Dr. Mihriban Pekguleyuz, Faculty of Materials Engineering

External Examiner

Abstract

The cumulative global emissions produced by the automotive industry over the last decade have put significant strain on the environment. Consequently, automotive engineers and manufacturers have made tremendous efforts toward increasing the efficiencies of automobiles. Several methods exist for improving efficiencies, but this is typically accomplished by either weight reduction, through use of lightweight materials, or increasing the internal operating pressure and, therefore, the temperature of the combustion engine. Unfortunately, the currently-used lightweight alloys have a high tendency to weaken with increasing temperatures, limiting the alloys' practical use to applications that operate under 200-250 °C (i.e., the current operating temperature of engines). Consequently, this prevents the transportation industry from increasing the efficiencies of engines and reducing greenhouse gas (GHG) emissions. Thus, it is necessary to investigate new methods of improving the elevated temperature strength and thermal stability of lightweight alloys. Preliminary research on the effects of rare earth element (RE) additions, such as cerium or lanthanum, to aluminum (Al) alloys, has shown tremendous progress toward improving the elevated temperature performance of the alloys. REs are considered a byproduct when mining for more valuable minerals such as scandium or yttrium. Fortunately, contrary to their name, REs are widely abundant, economical feasible, and produce thermally stable compounds in Al alloys. However, due to the lack of published literature on the high temperature properties of Al-RE alloys, a commercially viable option is still unavailable.

This research aims to develop a new Al-RE alloy, focused on improving the performance at engine operating conditions. The findings from this research suggest that a 3.5 wt.% RE addition to an A356 alloy can improve the alloy's strength by 130-175% at 250-300 °C. Further, as compared to one of the most used alloys for engine block production, T7 A319, the new A356RE alloy demonstrated improved strength (i.e., 65-118% higher YS) and creep resistance at 250 and 300 °C. This increase in elevated temperature properties may provide the transportation industry with a potential replacement alloy capable of withstanding the increase in thermo-mechanical loading that is necessary for improving vehicle efficiency and, thereby, improving the sustainability of the global environment.

Lay Summary

Over the past several decades, the transportation industry has invested a considerable amount of time and resources on reducing their environmental impacts. Focused on improving the efficiency of automobiles, automotive manufacturers have been developing new materials for lightening and strengthening many components of their vehicles. A large focus has been placed on the vehicle's engine since it provides the greatest potential for weight reduction and its efficiency can be improved. However, to improve the efficiency, the pressure and temperature must increase. Unfortunately, current lightweight materials begin to weaken at elevated temperatures.

Thus, this dissertation focused on improving the high temperature performance of aluminum alloys through the addition of inexpensive rare earth elements. The newly developed alloy boasts superior performance at engine operating conditions, as compared to the currently used engine block alloys. These improvements will help the automotive industry increase their operating efficiencies and provide a greener means of transportation.

Preface

This dissertation presents the original research work conducted by the author. Several parts of the current research were developed in collaboration with individuals from Canadian and International research facilities. These individuals include Dr. Dimitry Sediako from the Faculty of Applied Science at the University of British Columbia Okanagan (Canada); Dr. Glenn Byczynski and Dr. Anthony Lombardi from Nemak (Canada); Dr. David Weiss from Eck Industries Inc. (USA); Dr. Anna Paradowska and Dr. Mark Reid from the Australian Nuclear Science and Technology Organization (Australia); and several student members from the High Performance Powertrain Materials Laboratory at the University of British Columbia Okanagan (Canada).

Chapter 3 of this dissertations includes versions of:

- **J. Stroh**, A. Piche, D. Sediako, A. Lombardi, G. Byczynski, “The Effects of Solidification Cooling Rates on the Mechanical Properties of an A319 Inline-6 Engine Block,” The Minerals, Metals & Materials Society (TMS). Aluminum Alloys, Processing and Characterization, Light Metals, 2019, pp. 505-512.
- **J. Stroh**, D. Sediako, G. Byczynski, A. Lombardi, A. Paradowska, “Stress Characterization of Bore-Chilled Sand-Cast Aluminum Engine Blocks in As-Cast and T7 Condition with application of Neutron Diffraction,” Aluminum Alloys, Processing and Characterization, Light Metals, 2020, pp. 153-157, invited.
- **J. Stroh**, D. Sediako, A. Lombardi, G. Byczynski, M. Reid, A. Paradowska, “Residual Stress Evolution of Sand-Cast Aluminum Engine Blocks Manufactured with Pressed-In Iron Liners,” Materials Processing Technology, submitted (December 2020).

I conducted the experimental work included in the aforementioned papers and prepared the original draft of the research articles. A. Piche participated in experimental work and contributed to the manuscript. D. Sediako secured funding and participated in experimental work, discussed results, provided equipment for experiments, provided guidance, and reviewed and edited all manuscripts. G. Byczynski and A. Lombardi provided sample material, participated in experimental work and data processing, discussed the results, and reviewed and edited the manuscripts. A. Paradowska and M. Reid contributed to securing beam time, conducted experimental work, and reviewed and edited the manuscripts.

- D. Sediako, **J. Stroh**, S. Kianfar, “Residual Stress in Automotive Powertrains: Methods and Analyses,” Materials Research Forum, Scientific. Net, 2021.

I participated in experimental setup and data analysis and drafted the original manuscript. D. Sediako provided experimental guidance, discussed results, and reviewed and edited the manuscript. S. Kianfar conducted finite element analysis, processed data, and reviewed and edited the manuscript.

Chapter 4 of this dissertation includes components from:

- **J. Stroh**, T. Davis, Alexandra McDougall, D. Sediako, “In-situ Study of Solidification Kinetics of Al-Cu and Al-Ce Alloys with Application of Neutron Diffraction,” The Minerals, Metals & Materials Society (TMS), Cast Shop Technology: Fundamentals of Aluminum Alloy Solidification, Light Metals 2018, pp. 1059-1065, 2018, Invited.
- **J. Stroh**, D. Sediako, “Microstructure and In-Situ Solidification Analysis of Al-Ce-Mg Alloy,” Physics in Canada, vol. 74, no. 1–2, pp. 41–44, 2018, Invited.
- **J. Stroh**, D. Sediako, D. Weiss, “Development of Cerium-Reinforced Specialty Aluminum Alloy with Application of X-ray and Neutron Diffraction,” International Journal of Metal Casting, vol. 15, issue 1, 2021.
- **J. Stroh**, D. Sediako, D. Weiss, V. Peterson, “In-Situ Neutron Diffraction Solidification Analyses of Rare Earth-Reinforced Hypoeutectic and Hypereutectic Aluminum-Silicon Alloys,” Aluminum Alloys, Processing and Characterization, Light Metals 2020, pp. 174-178, 2020.

I contributed to the bulk of the experimental work conducted in the research articles above. In addition, I wrote all original drafts of the manuscripts. D. Sediako secured funding, provided equipment for experiments, participated in experimental work, discussed results, provided guidance, and reviewed and edited all manuscripts. D. Weiss provided sample material, participated in discussion of the results and reviewed and edited the manuscripts. V. Peterson participated in setup of the neutron diffraction experiment and contributed to writing and editing the manuscript. T. Davis and A. McDougall participated in experimental setup and data analyses.

Chapter 5 of this dissertation includes components from:

- **J. Stroh**, D. Sediako, D. Weiss, “The Effect of Rare Earth Mischmetal on the High Temperature Tensile Properties of an A356 Aluminum Alloy”, *Aluminum Alloys, Processing and Characterization, Light Metals 2021*, pp. 184-191, 2021.

I contributed to the bulk of the experimental work conducted in the research articles above. In addition, I wrote all original drafts of the manuscripts. D. Sediako secured funding, provided equipment for experiments, participated in experimental work, discussed results, provided guidance, and reviewed and edited all manuscripts. D. Weiss provided sample material, participated in discussion of the results, and reviewed and edited the manuscripts. V. Peterson participated in setup of the neutron diffraction experiment and contributed to writing and editing the manuscript. T. Davis and A. McDougall participated in experimental setup and data analyses.

- E. Aghaie, **J. Stroh**, D. Sediako, A. Rashidi, A. S. Milani, “Improving the Mechanical Properties of the B319 Aluminum Alloy by Addition of Cerium,” *Material Science & Engineering A*, 2020.

I participated in experimental setup and data analyses and contributed to the original draft of the manuscript. In addition, I reviewed and edited the final draft of the manuscript. E. Aghaie conducted the bulk of the experimental work, wrote the original draft of the research article, and conducted the majority of the data analyses. D. Sediako secured funding, participated in experimental work, provided equipment for experiments, discussed results, provided guidance, and reviewed and edited the manuscript. A. Rashidi conducted a portion of the experimental work, and edited and reviewed the final manuscript. A. Milani provided access to his advanced electron microscope and contributed to reviewing and editing the final manuscript.

The following copyrighted materials were used in this dissertation:

1. Figure 1.1-1. CAFE standards and achieved fuel economy [4]
2. Figure 2.1-1. Simulated temperature distribution in inline diesel powered engine, note that cylinder bridge temperatures reach 250-300 °C (adapted from [26], [27])
3. Figure 2.2-1. Contribution from fatigue/creep damage with relation to cycles and temperature [43]
4. Figure 2.2-3. Influence of stress on steady-state creep rate, adapted from [51], [52]

5. Figure 2.2-4. Minimum creep rate at 300°C vs. stress for dispersion-strengthened Al-Si-Mg-Cu-Ni alloy (Adapted from [27]). Note high apparent stress exponents n_a and presence of threshold stress σ_{th}
6. Figure 2.2-5. (a) Plot of $\dot{\epsilon}_s^{1/n}$ vs. stress using $n = 4.4$ for dislocation creep region (region (II) in Figure 2.2-4) and (b) double-logarithmic plot of minimum creep rate vs. effective stress ($\sigma - \sigma_{th}$) [27]
7. Figure 2.2-6. Deformation mechanism map for pure Al, original [64], *adapted from* [65]
8. Figure 2.2-7. Microstructure of Al-7Si-Mg alloy in a) as-cast condition and b) T6 heat-treated condition. Note the spheroidization of eutectic silicon particles after heat treatment [78]
9. Figure 2.2-8. (a) Needle-like β -Al₅FeSi and (b) Chinese script α -Al₁₅(Fe,Mn)₃Si₂ [100]
10. Figure 2.3-1. The as-alloyed cost of Al-Ce material with respect to the cost of current powertrain alloys, price for Ce was USD 4/lb in 2017 (*adapted from D. Weiss* [115])
11. Figure 3.1-1. Schematic of NemaK-Cosworth mould design used to cast the engine blocks (*Adapted from Byczynski and MacKay* [183])
12. Figure 3.3-2. Schematic view of the dendritic structure and SDAS in Al-Si alloy [186]
13. Figure 3.4-1. Planes of atoms' interaction with incident beam of particles used to describe Bragg's law by path length difference method [196]

Table of Contents

Abstract.....	iii
Lay Summary.....	iv
Preface.....	v
Table of Contents.....	ix
List of Tables.....	xii
List of Figures.....	xiii
List of Abbreviations.....	xix
List of Symbols.....	xx
List of Elements.....	xxi
List of Units.....	xxii
Acknowledgements.....	xxiii
Chapter 1 Introduction.....	1
1.1 Scope of Research.....	4
1.2 Structure of Dissertation.....	4
Chapter 2: Literature Review.....	7
2.1 Powertrain Applications.....	7
2.1.1 Powertrain Components and Operation.....	7
2.1.2 Manufacturing Processes and Problems.....	11
2.2 Powertrain Alloys.....	15
2.2.1 Required Fitness-for-Service Properties.....	16
2.2.1.1 Thermo-Mechanical Fatigue.....	16
2.2.1.2 Creep Resistance.....	17
2.2.1.3 Thermal Stability.....	26
2.2.1.4 Summary of Required Properties for Powertrain Alloys.....	28
2.2.2 Current Commercial Powertrain Alloy Systems.....	28
2.3 Aluminum-Rare Earth Alloy System.....	37
2.3.1 Economics.....	37
2.3.2 Microstructure and Mechanical Properties of the Al-RE system.....	39
2.4 Chapter Summary.....	50
Chapter 3: Characterization of Residual Stress in I6 Diesel Engine Block and Evaluation of Fitness-for-Service of A319 Alloy.....	51

3.1	Manufacturing Process.....	54
3.2	Thermodynamics of A319 Alloy (ThermoCalc™).....	56
3.3	Metallography	59
3.3.1	As-Cast (TSR) Microstructure	60
3.3.2	T4/T7 Heat Treated Microstructure	66
3.3.3	Summary of Microstructural Analysis.....	69
3.4	Residual Stress/Strain Characterization	71
3.4.1	Residual Strain/Stress in Bore-Chilled Engine Block	77
3.4.1.1	Residual Strain in the TSR + Chills Engine Block.....	77
3.4.1.2	Residual Strain in the TSR Engine Block with Chills Removed	79
3.4.1.3	Residual Strain in T4 and T7 Treated Engine Blocks	80
3.4.1.4	Residual Strain in the T7 Treated Engine Block with Pressed-in Liners	82
3.4.1.5	Residual Stress Evolution.....	83
3.5	Fitness-For-Service Evaluation of A319 Alloy	87
3.5.1	Tensile: A319 Alloy from I6 Engine Block.....	87
3.5.2	Creep: A319 Alloy from I6 Engine Block.....	93
3.6	Chapter Summary	100
Chapter 4: Development of Next Generation Powertrain Alloys		105
4.1	Thermodynamics (ThermoCalc™).....	107
4.1.1	Thermodynamics Al-6%Ce and Al-16%Ce.....	109
4.1.2	Thermodynamics Al-8%Ce-10%Mg	112
4.1.3	Thermodynamics of A356 and A356RE.....	118
4.1.4	Thermodynamics A390 and A390RE.....	127
4.2	Metallography of Al-RE Alloys.....	134
4.2.1	Binary Al-6%Ce and Al-16%Ce alloys	134
4.2.2	Al-8%Ce-10%Mg	139
4.2.3	T6 A356 and A356RE (as-cast + T6)	143
4.2.4	A390RE.....	149
4.3	Solidification Analyses Using In-Situ Neutron Diffraction.....	152
4.3.1	Neutron Diffraction of Al-6%Ce and Al-16%Ce	154
4.3.2	Neutron Diffraction Al-8%Ce-10%Mg Alloy	157
4.3.3	Neutron Diffraction of A356RE	162

4.3.4	Neutron Diffraction of A390RE	169
4.4	Chapter Summary	171
Chapter 5:	Fitness-For-Service Properties of Al-RE Alloys.....	175
5.1	Tensile: Al-8%Ce-10%Mg	176
5.2	Tensile: T6 A356 and A356RE (As-Cast and T6).....	177
5.3	Creep: Al-8%Ce-10%Mg.....	181
5.4	Creep: T6 A356 and A356re (As-Cast and T6).....	182
5.5	Modified A356RE (A356RE-A and A356RE-B).....	188
5.5.1	Thermodynamic Simulations	190
5.5.2	Microstructure of A356RE-A and A356RE-B	194
5.5.3	Tensile: A356RE-A and A356RE-B.....	198
5.5.4	Creep: A356RE-A and A356RE-B.....	199
5.6	Chapter Summary	208
Chapter 6:	Conclusions	213
6.1	Contributions of Research.....	216
Chapter 7:	Future Recommendations.....	220
References	221

List of Tables

Table 2.1-1. Residual stress evolution in cast engine blocks produced with cast-in Fe liners (units in MPa).....	15
Table 2.2-1. Temperature effect on yield strength (in MPa) of current powertrain alloys (A319 alloy, not conditioned), approximate values extracted from [106].....	35
Table 2.3-1. List of published mechanical properties for Ce-containing Al casting alloys.....	49
Table 3.1-1. Composition of aluminum A319 alloy used for production of the cast engine blocks	55
Table 3.2-1. Mass fraction of phases in A319 alloy	58
Table 3.3-1. Summary of average SDAS and cooling rate for cylinder wall	61
Table 3.3-2. Approximate composition of phases throughout TSR engine block (obtained with EDS).....	66
Table 3.3-3. Summary of phases in I6 engine block (values shown as at.%).....	70
Table 3.5-1. Room temperature tensile test results of TSR A319 alloy (taken from cylinder bridge of I6 engine block).....	88
Table 3.5-2. Tensile test results of conditioned (200 hours) T7 A319 alloy	93
Table 3.5-3. Steady-state creep rate for T7 A319 extracted from cylinder bridge of I6 engine block (units: 10^{-8} /s)	99
Table 3.6-1. Residual stress evolution in sand-cast Al (A319) engine blocks (units in MPa) ...	102
Table 3.6-1. Alloy composition in wt.%	106
Table 4.1-1. List of phases shown in ThermoCalc simulations.....	108
Table 4.1-2. Mass fraction of phases in Al-6%Ce alloy	111
Table 4.1-3. Mass fraction of phases in Al-16%Ce alloy	112
Table 4.1-4. Mass fraction of phases in Al-8%Ce-10%Mg alloy.....	116
Table 4.1-5. Mass fraction of phases in A356 alloy	121
Table 4.1-6. Mass fraction of phases in A356RE alloy	125
Table 4.1-7. Mass fraction of phases in A390 alloy	128
Table 4.1-8. Mass fraction of phases in A390RE	132
Table 4.2-1. Composition of intermetallics in Al-6%Ce alloy	136
Table 4.2-2. Composition of intermetallics in Al-8%Ce-10%Mg	141
Table 4.2-3. EDS elemental analysis of phases present in A356 and A356RE alloys (at.%)	148
Table 4.2-4. EDS elemental analysis of phases present in A390RE alloy (at.%).....	152
Table 4.3-1. Comparison of results from Reitveld refinement and ThermoCalc	166
Table 5.4-1. Steady-state creep rates for T6 A356 alloy (units: 10^{-8} /s).....	184
Table 5.5-1. Composition of cleaned and modified A356RE alloys	190
Table 5.5-2. Mass fraction of phases in A356RE-B	192
Table 5.5-3. Composition of phases in A356RE-A (at.%)	195
Table 5.5-4. Composition of phases in A356RE-B (at.% \pm standard deviation).....	197
Table 5.5-5. Steady-state creep rates for A356RE-A and A356RE-B at 250 °C (units: 10^{-8} /s).	204
Table 5.5-6. Steady-state creep rates for A356RE-B 300 °C (units: 10^{-8} /s).....	207
Table 5.6-1. Summary of mechanical properties at 250 and 300 °C	211

List of Figures

Figure 1.1-1. CAFE standards and achieved fuel economy [4].....	2
Figure 2.1-1. Simulated temperature distribution in inline diesel powered engine, note that cylinder bridge temperatures reach 250-300 °C (adapted from [26], [27])	8
Figure 2.1-2. Simplified model of spark ignition engine cycle (based on Otto cycle)	9
Figure 2.1-3. Simplified model of compression ignition engine cycle (based on diesel cycle)	9
Figure 2.1-4. Simplified relationship of alloy strength and temperature	10
Figure 2.1-5. Representation of sand cast, closed deck engine block.....	13
Figure 2.2-1. Contribution from fatigue/creep damage with relation to cycles and temperature [43].....	17
Figure 2.2-2. Stages of creep	18
Figure 2.2-3. Influence of stress on steady-state creep rate, adapted from [51], [52]	21
Figure 2.2-4. Minimum creep rate at 300°C vs. stress for dispersion-strengthened Al-Si-Mg-Cu-Ni alloy (Adapted from [27]). Note high apparent stress exponents n_a and presence of threshold stress σ_{th}	23
Figure 2.2-5. (a) Plot of $\epsilon\dot{\sigma}^{1/n}$ vs. stress using $n = 4.4$ for dislocation creep region (region (II) in Figure 2.2-4) and (b) double-logarithmic plot of minimum creep rate vs. effective stress ($\sigma - \sigma_{th}$) [27].....	24
Figure 2.2-6. Deformation mechanism map for pure Al, original [64], <i>adapted from</i> [65]	26
Figure 2.2-7. Microstructure of Al-7Si-Mg alloy in a) as-cast condition and b) T6 heat-treated condition. Note the spheroidization of eutectic silicon particles after heat treatment [78]	32
Figure 2.2-8. (a) Needle-like β -Al ₅ FeSi and (b) Chinese script α -Al ₁₅ (Fe,Mn) ₃ Si ₂ [100]	33
Figure 2.2-9. Temperature effects on yield strength of A319 alloy (approximate values extracted from [106]).....	35
Figure 2.2-10. Effect of conditioning process on strength of alloy	36
Figure 2.3-1. The as-alloyed cost of Al-Ce material with respect to the cost of current powertrain alloys, price for Ce was USD 4/lb in 2017 (<i>adapted from</i> D. Weiss [115])	38
Figure 2.3-2. Calculated Al-Ce binary phase diagram (ThermoCalc™).....	40
Figure 2.3-3. Effect of Mg on strength of Al-Ce alloys (data extracted from [115])	42
Figure 2.3-4. SEM micrographs of Al-12%Ce-4%Si-0.4%Mg alloy (adapted from [122])	43
Figure 3.1-1. Schematic of NemaK-Cosworth mould design used to cast the engine blocks (<i>Adapted from</i> Byczynski and MacKay [183])	54
Figure 3.2-1. Mass fraction of phases in A319 alloy A) full solidification process, B) solidification process, emphasizing minority phases (equilibrium solidification)	57
Figure 3.2-2. Mass fraction of phases in A319 alloy A) full solidification process, B) solidification process, emphasizing minority phases (non-equilibrium solidification)	59
Figure 3.3-1. Location of metallurgical samples	60
Figure 3.3-2. Schematic view of the dendritic structure and SDAS in Al-Si alloy [186]	60
Figure 3.3-3. SEM micrographs of various locations in the TSR Al engine block at 1000x, A) Top, B) Upper Middle, C) Lower Middle, D) Bottom, E) Starter Case, F) Starter Case. Note: Micrographs were selected to display all phases and may not represent the general microstructure at each location	62

Figure 3.3-4. Optical micrographs of A319 alloy taken from the top of the cylinder bridge of the TSR I6 engine block, left) 100x, right) 500x.....	63
Figure 3.3-5. Optical micrographs of A319 alloy taken from the top of the cylinder bridge of T4 I6 engine block, left) 100x, right) 500x	67
Figure 3.3-6. SEM micrograph of T4 A319 alloy (Top of I6 Block)	68
Figure 3.3-7. Optical micrographs of T7 A319 alloy taken from the top of the cylinder bridge of I6 engine block, left) 100x, right) 500x	69
Figure 3.3-8. SEM micrograph of T7 A319 alloy (Top of I6 Block)	69
Figure 3.4-1. Planes of atoms' interaction with incident beam of particles used to describe Bragg's law by path length difference method [196]	72
Figure 3.4-2. Measurement of stress-free ($d_{hkl,0}$) matchstick samples	73
Figure 3.4-3. The component of strain, ϵ , parallel to the bisector of the incident and diffracted neutron beams	74
Figure 3.4-4. Orientation of casting for the axial, hoop, and radial components of strain	74
Figure 3.4-5. Radial measurement of strain in I6 engine block showing all three orientations of measurements.....	75
Figure 3.4-6. Engine block samples used for the completion of this study	76
Figure 3.4-7. Location of scan lines.....	76
Figure 3.4-8. Removal of iron from neutron beam path for the TSR +Chills engine block.....	77
Figure 3.4-9. Residual strain profiles for TSR + Chills engine block; left) edge bridge, right) middle bridge	77
Figure 3.4-10. Graphical representation of compression forming in radial orientation	78
Figure 3.4-11. Residual strain profiles for TSR engine block; left) edge bridge, right) middle bridge	80
Figure 3.4-12. Residual strain profiles for T4 engine block; left) edge bridge, right) middle bridge	81
Figure 3.4-13. Residual strain profiles for T7 engine block; left) edge bridge, right) middle bridge	82
Figure 3.4-14. Residual strain profiles for T7LM engine block; left) edge bridge, right) middle bridge	83
Figure 3.4-15. Residual stress profiles for TSR + Chills engine block	84
Figure 3.4-16. Residual stress profiles for TSR engine block	84
Figure 3.4-17. Residual stress profiles for T4 engine block; left) edge bridge, right) middle bridge	85
Figure 3.4-18. Residual stress profiles for T7 engine block; left) edge bridge, right) middle bridge	86
Figure 3.4-19. Residual stress profiles for production ready T7LM engine block; left) edge bridge, right) middle bridge	86
Figure 3.5-1. Tensile test setup including MTS extensometer	87
Figure 3.5-2. Stress - strain curve for cylinder web of as-cast engine block (after TSR).....	88
Figure 3.5-3. Experimental setup for elevated temperature tensile tests	90
Figure 3.5-4. 250 °C tensile tests for T7 A319 alloy, extracted from cylinder bridge of an I6 engine block	92

Figure 3.5-5. Elevated temperature tensile tests for T7 A319 alloy, extracted from cylinder bridge of an I6 engine block	93
Figure 3.5-6. Staircase creep results of T7 A319 alloy (taken from cylinder bridge of engine block). Sample was conditioned at 250 °C for 200 hours prior to initiating test.....	94
Figure 3.5-7. Minimum creep rate as a function of applied stress for the T7 A319 alloy at 250 °C. Note apparent stress exponent n_a and threshold stress σ_{th}	95
Figure 3.5-8. A plot of $\epsilon\dot{s}^{1/n}$ vs. σ for the T7 A319 alloy at 250 °C.....	96
Figure 3.5-9. Staircase creep results of T7 A319 alloy (taken from cylinder bridge of engine block) Note: Sample was conditioned at 300 °C for 200 hours prior to initiating test.....	97
Figure 3.5-10. A plot of $\epsilon\dot{s}^{1/n}$ vs. σ for the T7 A319 alloy at 300 °C.....	98
Figure 3.5-11. Minimum creep rate as a function of applied stress for the T7 A319 alloy at 300 °C. Note apparent stress exponent n_a and threshold stress σ_{th}	99
Figure 3.5-12. Minimum creep rate plotted against the reciprocal of the absolute temperature. Note apparent activation energies, Q_a	100
Figure 4.1-1. Binary Al-Ce phase diagrams calculated using ThermoCalc™ software.....	110
Figure 4.1-2. Mass fraction of phases in Al-6%Ce alloy, A) Equilibrium, B) Non-equilibrium Scheil solidification	111
Figure 4.1-3. Mass fraction of phases in Al-16%Ce alloy, A) Equilibrium, B) Non-equilibrium Scheil solidification	112
Figure 4.1-4. Ternary phase diagram of Al-8%Ce-10%Mg alloy at 25 °C.....	113
Figure 4.1-5. Mass fraction of phases in Al-8%Ce-10%Mg alloy A) full solidification process, B) progression of minority phase solidification (equilibrium solidification).....	114
Figure 4.1-6. Mass fraction of phases in Al-8%Ce-10%Mg alloy A) full solidification process, B) progression of minority phase solidification (non-equilibrium Scheil solidification).....	117
Figure 4.1-7. Mass fraction of phases in A356 alloy A) full solidification process, B) progression of minority phase solidification (equilibrium solidification).....	120
Figure 4.1-8. Mass fraction of phases in A356 alloy A) full solidification process, B) progression of minority phase solidification (non-equilibrium Scheil solidification)	122
Figure 4.1-9. Mass fraction of phases in A356RE alloy A) full solidification process, B) progression of minority phase solidification (equilibrium solidification).....	124
Figure 4.1-10. Mass fraction of phases in A356RE alloy A) full solidification process, B) progression of minority phase solidification (non-equilibrium Scheil solidification).....	126
Figure 4.1-11. Mass fraction of phases in A390 alloy (equilibrium solidification)	127
Figure 4.1-12. Mass fraction of phases in the A390 alloy A) full solidification process, B) progression of minority phase solidification (non-equilibrium Scheil solidification).....	129
Figure 4.1-13. Mass fraction of phases in A390RE alloy A) full solidification process, B) progression of minority phase solidification (equilibrium solidification)	131
Figure 4.1-14 Mass fraction of phases in A390RE alloy A) full solidification process, B) progression of minority phase solidification (non-equilibrium Scheil solidification).....	133
Figure 4.2-1. SEM micrograph of Al-6%Ce alloy, left) 500x, right) 5000x	135
Figure 4.2-2. SEM micrograph of oxide in Al-6%Ce alloy, 500x.....	136
Figure 4.2-3. SEM micrograph of Al-16%Ce, left) 500x, right) 2000x. Note microcracking in the primary $Al_{11}Ce_3$ crystals	137

Figure 4.2-4. FWHM peak broadening for $Al_{11}Ce_3$ intermetallic in Al-6%Ce and Al-16%Ce alloy.....	138
Figure 4.2-5. XRD diffraction pattern for the A) Al-6%Ce and B) Al-16%Ce alloy.....	139
Figure 4.2-6. SEM micrograph of the Al-8%Ce-10%Mg alloy, 500x.....	140
Figure 4.2-7. Non-homogenous structure of the β -AlMg phase in Al-8%Ce-10%Mg alloy	141
Figure 4.2-8. XRD diffraction pattern for the Al-8%Ce-10%Mg alloy	142
Figure 4.2-9. X-ray micro computed tomography machine (X-Ray Micro-CT, Zeiss/Xradia X-400) [21].....	142
Figure 4.2-10. XMCT results for $Al_{11}Ce_3$ intermetallics in Al-8%Ce-10%Mg alloy	143
Figure 4.2-11. SEM micrograph of the T6 A356 alloy, left) 500x and right) 1000x	144
Figure 4.2-12. Microstructure of the as-cast A356RE alloy, left) 500x and right) 1000x.....	145
Figure 4.2-13. Optical micrograph of as-cast A356RE alloy	145
Figure 4.2-14. Microstructure of the T6 A356RE alloy, left) 500x and right) 1000x	147
Figure 4.2-15. SEM micrographs A356RE alloy: left) as-cast, right) T6 heat-treated.....	147
Figure 4.2-16. XMCT results of AlSiRE phase in T6 A356RE alloy	149
Figure 4.2-17. Optical micrograph of A390RE alloy	150
Figure 4.2-18. SEM micrograph of A390RE alloy.....	151
Figure 4.3-1. Sample setup used in ND solidification experiment	153
Figure 4.3-2. Full neutron diffraction pattern of A) Al-6%Ce and B) Al-16%Ce alloys prior to solidification experiment	155
Figure 4.3-3. Temperature-dependent neutron powder diffraction data of the Al-6%Ce alloy showing the Al (111) reflection (left) and the corresponding solid fraction (right). Data are shown as points with the solid and dashed line guiding the eye.....	156
Figure 4.3-4. Temperature-dependent neutron powder diffraction data of the Al-6%Ce alloy showing the $Al_{11}Ce_3$ (112) reflection (left) and the corresponding solid fraction (right). Data are shown as points with the solid and dashed line guiding the eye.....	156
Figure 4.3-5. Temperature-dependent neutron powder diffraction data of the Al-16%Ce alloy showing the Al (111) reflection (left) and the corresponding solid fraction (right). Data are shown as points with the solid and dashed line guiding the eye.....	157
Figure 4.3-6. Temperature-dependent neutron powder diffraction data of the Al-16%Ce alloy showing the $Al_{11}Ce_3$ (112) reflection (left) and the corresponding solid fraction (right). Data are shown as points with the solid and dashed line guiding the eye.....	157
Figure 4.3-7. Full neutron diffraction pattern for the Al-8%Ce-10%Mg alloy prior to solidification	158
Figure 4.3-8. Temperature-dependent neutron powder diffraction data of the Al-8%Ce-10%Mg alloy showing the Al (111) reflection (left) and the corresponding solid fraction (right). Data are shown as points with the solid and dashed line guiding the eye.....	159
Figure 4.3-9. Progression of Al (111) reflection towards higher angles at lower temperatures in Al-8%Ce-10%Mg alloy (left) and calculated mass percent of dissolved Mg in Al as a function of temperature (right)	160
Figure 4.3-10. Transformation of $Al_{11}Ce_3$ into Al_8CeMn_4 for Al-8%Ce-10%Mg alloy (data from ThermoCalc simulation)	160

Figure 4.3-11. Temperature-dependent neutron powder diffraction data of the Al-8%Ce-10%Mg alloy showing the Al ₁₁ Ce ₃ (112) reflection.....	161
Figure 4.3-12. Temperature-dependent neutron powder diffraction data of the Al-8%Ce-10%Mg alloy showing the Al ₁₁ Ce ₃ (150) reflection (left) and the corresponding solid fraction (right). Data are shown as points with the solid and dashed line guiding the eye	161
Figure 4.3-13. Full neutron diffraction pattern for A) A356RE and B) T6 A356RE alloys prior to solidification experiment	164
Figure 4.3-14. Rietveld refinement of T6 A356RE alloy using GSASII.....	165
Figure 4.3-15. Temperature-dependent neutron powder diffraction data of the A356RE alloy showing the Al (111) reflection (left) and the corresponding solid fraction (right). Data are shown as points with the solid and dashed line guiding the eye.....	166
Figure 4.3-16. Temperature-dependent neutron powder diffraction data of the A356RE alloy showing the Si (111) reflection (left) and the corresponding solid fraction (right). Data are shown as points with the solid and dashed line guiding the eye	167
Figure 4.3-17. Calculated mass fraction as a function of temperature for left) Al (111) and right) Si (111) reflection in A356RE alloy	167
Figure 4.3-18. Dissolution of Mg ₂ Si phase during heating of the A356RE alloy	168
Figure 4.3-19. Progression of peak intensities for Al ₂₀ Ti ₂ RE and AlSiRE phases during solidification of A356RE alloy	169
Figure 4.3-20. Full neutron diffraction pattern for the A390RE alloy prior to solidification experiment.....	170
Figure 4.3-21. Temperature-dependent neutron powder diffraction data of the A390RE alloy showing the Al (111) reflection (left) and the corresponding solid fraction (right). Data are shown as points with the solid and dashed line guiding the eye.....	171
Figure 4.3-22. Temperature-dependent neutron powder diffraction data of the A390RE alloy showing the Si (111) reflection (left) and the corresponding solid fraction (right). Data are shown as points with the solid and dashed line guiding the eye	171
Figure 5.1-1. Tensile test results for Al-8%Ce-10%Mg alloy at left) 250 °C and right) 300 °C (Conditioned for 200 hours).....	177
Figure 5.2-1. Room-temperature tensile test results for T6 A356 alloy	178
Figure 5.2-2. Tensile test results for T6 A356 alloy at left) 250 °C and right) 300 °C (conditioned for 200 hours).....	179
Figure 5.2-3. Tensile test results for as-cast A356RE alloy at left) 250 °C and right) 300 °C (conditioned for 200 hours)	179
Figure 5.2-4. Room-temperature tensile test results for T6 A356+3.5% alloy	180
Figure 5.2-5. Tensile test results for T6 A356RE alloy at left) 250 °C and right) 300 °C (conditioned for 200 hours)	181
Figure 5.2-6. SEM micrographs of T6 A356RE alloy throughout the conditioning process	181
Figure 5.3-1. Creep test results for Al-8%Ce-10%Mg alloy at left) 250 °C and right) 300 °C (conditioned for 200 hours)	182
Figure 5.4-1. Creep test results for T6 A356 alloy at left) 250 °C and right) 300 °C (conditioned for 200 hours).....	183

Figure 5.4-2. Creep test results for T6 A356 alloy at left) 250 °C and right) 300 °C (conditioned for 200 hours).....	183
Figure 5.4-3. A plot of $\epsilon s^{1/n}$ vs σ for the T6 A356 alloy at 250 °C.....	185
Figure 5.4-4. Minimum creep rates as a function of applied stress for T6 A356 alloy. Note apparent stress exponent n_a and threshold stress σ_{th}	185
Figure 5.4-5. Creep test results for as-cast A356RE alloy at left) 250 °C and right) 300 °C (conditioned for 200 hours)	187
Figure 5.4-6. Creep test results for T6 A356RE alloy at left) 250 °C and right) 300 °C (conditioned for 200 hours)	187
Figure 5.4-7. RE cluster in A356RE alloys	188
Figure 5.5-1. Mass fraction of phases in the A356RE-B alloy A) full solidification process, B) progression of minority phase solidification (equilibrium solidification).....	191
Figure 5.5-2. Mass fraction of phases in the A356RE-B alloy A) full solidification process, B) progression of minority phase solidification (non-equilibrium solidification).....	193
Figure 5.5-3. Optical micrograph of A356RE-A	194
Figure 5.5-4. SEM micrograph of A356RE-A left) 500x, right) 1000x	195
Figure 5.5-5. Optical micrograph of A356RE-B (low Mg, high Mn)	196
Figure 5.5-6. SEM micrograph of A356RE-B left) 500x, right) 1000x (low Mg, high Mn)	197
Figure 5.5-7. Tensile test results of A356RE-A at 250 °C (conditioned for 200 hours at 250 °C)	198
Figure 5.5-8. Tensile test results of A356RE-B left) 250 °C, right) 300 °C (low Mg, high Mn) (conditioned for 200 hours at test temperature).....	199
Figure 5.5-9. Staircase creep results of A356RE-A at 250 °C (conditioned for 200 hours at 250 °C).....	200
Figure 5.5-10. Minimum creep rate as a function of applied stress for A356RE-A at 250 °C. Note apparent stress exponent n_a and threshold stress σ_{th}	201
Figure 5.5-11. Staircase creep results of A356RE-B at 250 °C (low Mg, high Mn) (conditioned for 200 hours at 250 °C)	202
Figure 5.5-12. Minimum creep rate as a function of applied stress for A356RE-B at 250 °C. Note apparent stress exponent n_a and threshold stress σ_{th}	203
Figure 5.5-13. A plot of $\epsilon s^{1/n}$ vs. σ for the A356RE-B alloy at 250 °C	204
Figure 5.5-14. Staircase creep results of A356RE-B (low Mg, high Mn) (conditioned for 200 hours at 300 °C)	205
Figure 5.5-15. A plot of $\epsilon s^{1/n}$ vs. σ for the A356RE-B alloy at 300 °C	206
Figure 5.5-16. Minimum creep rate as a function of applied stress for A356RE-B at 300 °C. Note apparent stress exponent n_a and threshold stress σ_{th}	207
Figure 5.5-17. Minimum creep rates plotted against the reciprocal of the absolute test temperature for the A356RE-B alloy (note apparent activation energies, Q_a)	208
Figure 5.6-1. Summary of Tensile Test Results at left) 250 and right) 300 °C	210
Figure 5.6-2. Summary of staircase creep results at left) 250 °C and right) 300 °C	212

List of Abbreviations

ASTM	American Society for Testing and Materials
CAFE	Corporate Average Fuel Economy
CALPHAD	Calculation of Phase Diagram Modelling
CR	Cooling Rate
DSC	Differential Scanning Calorimetry
EDS	Energy Dispersive X-ray Spectroscopy
FCC	Face-Centered-Cubic
FE	Finite Element
FEG-SEM	Field Emission Gun Scanning Electron Microscope
FFS	Fitness-for-Service
FWHM	Full-Width-Half-Max
HPDC	High Pressure Die Cast
ICSD	Inorganic Crystal Structure Database
ICE	Internal Combustion Engine
ND	Neutron Diffraction
OSM	Optical Stereoscopic Microscope
PID	Proportional-Integral-Derivative
RE	Rare Earth
RPM	Revolution Per Minute
SDAS	Secondary Dendrite Arm Spacing
SEM	Scanning Electron Microscope
TSR	Thermal Sand Reclamation
UTS	Ultimate Tensile Strength
XRD	X-ray Diffraction
XMCT	X-ray Micro-Computed Tomography
YS	Yield Strength

List of Symbols

α	Coefficient of Thermal Expansion
b	Burger's Vector
d_{hkl}	Interplanar Spacing of Specimen
d_{0hkl}	Interplanar Spacing of Stress-Free Specimen
ε	Strain
ε_r	Radial Strain
ε_a	Axial Strain
ε_h	Hoop Strain
σ_r	Radial Stress
σ_a	Axial Stress
σ_h	Hoop Stress
θ	Angle of Diffraction
λ	Wavelength
L	Interparticle Spacing
ΔL	Change in Length
n_a	Apparent Stress Exponent
n	Stress Exponent
P	Pressure
Q_a	Apparent Activation Energy
Q	Activation Energy for Creep
R	Universal Gas Constant
$\dot{\varepsilon}_s$	Steady-state Creep Rate
E	Modulus of Elasticity
G	Shear Modulus
V	Volume
γ	Interfacial Energy

List of Elements

Al	Aluminum
C	Carbon
Ce	Cerium
Cu	Copper
Cr	Chromium
Er	Erbium
Fe	Iron
La	Lanthanum
Mg	Magnesium
Mn	Manganese
Mo	Molybdenum
Nd	Neodymium
Ni	Nickel
O	Oxygen
Pb	Lead
Pr	Praseodymium
Sc	Scandium
Si	Silicon
Sr	Strontium
Ti	Titanium
V	Vanadium
Y	Yttrium
Zn	Zinc
Zr	Zirconium

List of Units

mm	Millimetre
°C	Degree Celsius
K	Kelvin
kg	Kilogram
kJ	Kilojoule
min	Minute
MPa	Mega Pascal
GPa	Giga Pascal
ppm	Parts Per Million
rpm	Revolutions Per Minute
s	Second
t	Time
T	Temperature

Acknowledgements

There are several individuals who have had a huge impact on the successful completion of my dissertation and who deserve a great deal of credit. First, I would like to thank my graduate studies' supervisor and professional and life mentor, Dr. Dimitry Sediako, for his guidance and support over the past several years. I was fortunate to have met Dr. Sediako during my undergraduate degree and he has helped me grow as a professional engineer and has given me an appreciation for engineering science. Under Dr. Sediako's supervision, I have learnt a lot about proper engineering etiquette, the importance of creating and maintaining good professional relationships with my peers, and how to enjoy and appreciate the work I've chosen to do. I am forever grateful for the years that I have spent working alongside Dr. Sediako.

This dissertation would not have been possible without the technical, financial and professional support from our industry collaborators. I would like to thank the Research & Development (R&D) leaders at Nematik, Dr. Glenn Byczynski and Dr. Anthony Lombardi, who have provided professional expertise and the engine blocks used in this study, as well as technical guidance during the experiments. In addition, I would like to thank Dr. David Weiss from Eck industries for sharing with me his broad knowledge and years of R&D experience with developing the rare earth reinforced aluminum alloys.

A large portion of this research would not have been possible without the support from our collaborators at several nuclear facilities. I would like to thank Dr. Anna Paradowska for her critical involvement at the Australian Nuclear Science and Technology Organization. Not only did Anna help conduct our experiments, but her never-ending excitement about the work inspired my own passion for engineering. I would also like to thank Dr. Ron Rogge and Chad Boyer from the Canadian Nuclear Laboratories and Drs. Chris Fancher and Jeff Bunn from the Oak Ridge National Laboratory.

The support and constructive input of my committee members, Dr. Lukas Bichler and Dr. Jian Liu, has helped develop my research and dissertation into the format it is today. Thank you.

Further, I would like to thank all members of our research team at the High Performance Powertrain Materials Laboratory for your support along my graduate studies journey. It has been

great working with all of you and I look forward to a long-term personal and professional relationship with each of you.

I would not have made it this far without the continuous support from my amazing father, mother, sister, and loving girlfriend. I love you all and appreciate all that you have done for me and continue to do. Thank you.

Chapter 1 Introduction

Automotive vehicle sales have grown by approximately 20% over the last two decades [1] to support the rapid development of import/export industries as well as transportation (both for goods and pedestrians). Not only has the number of vehicles increased, but the average time a person spends driving has increased by approximately 20 minutes per day (from 2014 to 2019). The greater number of automobiles and longer driving times has significantly increased the world's CO₂ emissions. For example, a recent report published by the United States Environmental Protection Agency (EPA) [2] has indicated that, from 1990 to 2006, the greenhouse gas (GHG) emissions from the transportation industry have increased by 25% (~1500 to 2000 million metric tons). It should be noted that, from 2006 to 2017, the GHG emissions have reduced by approximately 12% (i.e., from 2000 to 1750 million metric tons). The reason for the recent decrease in emissions can be strongly correlated to government legislation, enacted in 2012 ("Phase 2"), which mandates that the corporate average fuel economy (CAFE) of the automotive industry must be 54.5 MPG by the year 2025. As a reference, the CAFE in 2017 was approximately 29.8 MPG [3]. It is worthwhile mentioning that due to the slow progress made by 2020, the USA issued the Executive Order 13990, "Protecting Public Health and the Environment and Restoring Science to Tackle the Climate Crisis," to review and revise the current GHG and CAFE standards [4]. As a result, a new Safer, Affordable, Fuel-Efficient (SAFE) Vehicles rule was introduced. Part of the new SAFE rule includes a projected 1.5%/year increase in the average fuel economy of vehicles between 2021 and 2026. This is markedly lower than the original 5%/year following the original "Phase 2" 2012 regulations. Figure 1.1-1 shows the projected efficiency targets following the new SAFE rule as compared to the original Phase 2 standard. Even though the new SAFE rule lowers the required average fuel economy of vehicles, the transportation industry is still under immense pressure and must continue to investigate new methods for improving the operating efficiency of the vehicle's power source (i.e., internal combustion engine) while also reducing the vehicle's weight.

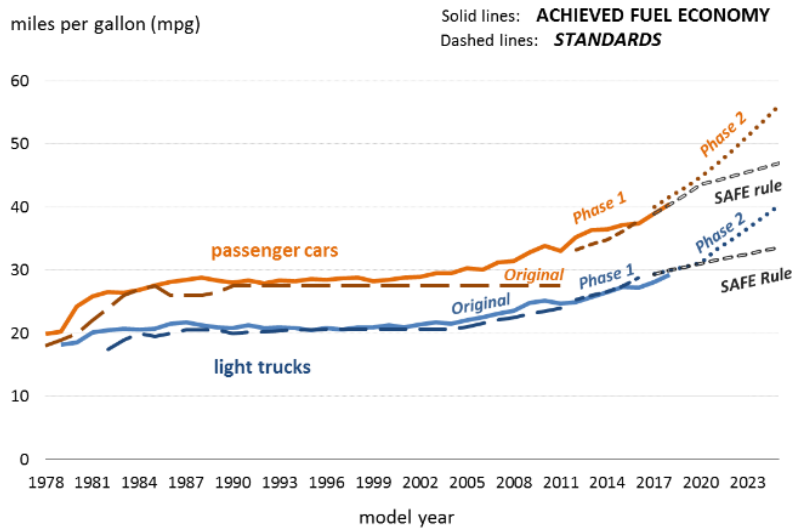


Figure 1.1-1. CAFE standards and achieved fuel economy [4]

In an effort to improve vehicle fuel efficiency, the use of aluminum (Al) alloys in automotive and marine powertrain components such as engine blocks, cylinder heads and transmission gearcases has continued to increase over the last two decades. Al alloys are lightweight and they have good casting characteristics, high thermal conductivity, and adequate mechanical properties, making them an excellent choice for powertrain applications [5], [6]. However, there are two primary issues that manufacturers are currently facing: the generation of residual stresses during manufacturing and processing of cast components, and the insufficient strength and wear-resistance of aluminum alloys at elevated temperature.

Two of the root causes for residual stress development include thermal gradients produced during casting and coefficient of thermal expansion (CTE) mismatches between dissimilar materials [7]. Thermal gradients may be caused by variations in wall thicknesses within a component or during application of external cooling such as in the quenching portion of the heat treatment process. The faster-cooling thin sections of a component contract much quicker than the surrounding thicker sections, resulting in localized stretching/compressing of the material. A common case in which a CTE mismatch can be observed is in Al engine blocks which typically require protective iron (Fe) cylinder liners to resist the wear caused by the reciprocating piston during operation. During the manufacturing process, molten Al is typically poured around these Fe liners (i.e., cast-in Fe liners) and due to the CTE mismatch between the Fe liners and the Al engine block, high tensile residual stresses have been observed to accumulate along the cylinder bores during casting and post-heat

treatment cooling. The magnitude of residual stress from the thermal gradients and/or CTE mismatch can exceed the yield strength of the currently used materials, leading to permanent dimensional distortion and/or cracking in the component during in-service operation [8]. Although distortion does not cause complete engine failure, sufficient distortion can cause “blow by” which effectively lowers the pressure inside the combustion chamber and greatly reduces the operating efficiency of the engine.

To date, aluminum-silicon (Al-Si)-based alloys with magnesium (Mg) and/or copper (Cu) additions have dominated the market for powertrain applications due to their low density ($\sim 2.67\text{-}2.79\text{ g/cm}^3$), high strength, and great castability. One of the reasons for their respectable mechanical properties lies in the formation of strengthening phases such as eutectic Si, $\text{Al}_5\text{Cu}_2\text{Mg}_8\text{Si}_6$, Al_2Cu , and Mg_2Si . However, the transportation industry is currently facing a few major barriers with using conventional Al-Si-Cu-Mg alloys. First, the demand for improved fuel economy mandates that the weight of powertrain components must be reduced while congruently increasing the operating conditions (i.e. forces, pressures, and temperatures). The weight may be reduced by minimizing the component’s wall thickness; however, without improving the material’s mechanical properties, the increased load per unit area (i.e., stress) can quickly surpass the strength of the thin-walled sections and can result in complete component failure. To add to this, the strength-contributing intermetallics present in Al-Si-Cu-Mg alloys, specifically $\text{Al}_5\text{Cu}_2\text{Mg}_8\text{Si}_6$, Al_2Cu , and Mg_2Si , usually coarsen or even dissolve at temperatures exceeding $\sim 170\text{-}250\text{ }^\circ\text{C}$ [9], [10], thereby eliminating the original strengthening effect from the phases. With current engines operating above $200\text{ }^\circ\text{C}$, the current powertrain alloys are already being pushed to their physical limit [11], [12]. Moreover, the accumulation of residual stress during the manufacturing process suppresses the useable strength of the Al alloys, and in many cases, the combined operational and residual stresses approach or exceed the alloy’s yield strength. Because of this, manufacturers have been forced to invest time and resources in developing new techniques aimed at reducing the magnitude of residual stress in cast components, in improving the microstructure and mechanical properties of the currently available alloys, and in searching for a replacement alloy that may be suitable for the increased operating conditions of next generation powertrain components.

A potential solution to the poor thermal stability of Al-Si/Mg/Cu alloys is the introduction of rare earth (RE) elements such as cerium (Ce) and/or lanthanum (La). The effects that RE additions have on Al alloys has been studied for over a century [13]–[19]; however, the early studies were restricted by the rapidly-soaring price of RE elements. It was not until the turn of the 20th century, when the price for many REs dropped below \$10/kg, that manufacturers were able to revisit the effects of RE elements on conventional materials. The development of specific RE-bearing intermetallics has been shown to improve the mechanical properties and thermal stability of the alloy system. Recent studies have shown that Ce additions to Al-Mg/Si alloys can increase the elevated temperature strength of the system through precipitation of temperature-resistant $\text{Al}_{11}\text{Ce}_3$ and Al_4CeSi_6 phases [20], [21]. However, there is an incomplete understanding of the full effect that RE additions have on the microstructure as well as on the fitness-for-service properties (i.e., tensile strength, fatigue strength and creep resistance at both ambient and elevated temperatures) of powertrain alloys. Before the Al-RE system can be effectively utilized in the highly demanding environment of powertrain applications such as engine blocks, cylinder heads and turbochargers, it is first necessary to achieve a better understanding of how the REs can be used to modify the microstructures and improve the fitness-for-service properties of various Al-based alloys.

1.1 Scope of Research

This dissertation characterizes the effects that current day manufacturing innovations (integrated bore chills, replacement of cast-in iron liners with pressed-in liners) have on the microstructure, mechanical properties, and the evolution of residual stress in cast Al engine blocks. This research provides a good indication of the baseline material properties required for the next generation of powertrain alloys. Further, this dissertation progresses the understanding of the effects that RE additions have on Al alloys with a primary focus on developing a new cost-effective Al alloy with improved temperature resistance. This will provide the transportation industry with a replacement alloy capable of withstanding the increase in thermal and/or mechanical loading that is necessary to meet the strict governmental regulation for improved vehicle efficiency.

1.2 Structure of Dissertation

This dissertation has been structured as followed:

Chapter 2: Literature Review This chapter provides a review of relevant literature relating to the evolution of powertrain components, the currently used powertrain alloys, and the tailoring of the mechanical properties of the alloys. Concluding the chapter is a detailed discussion of the economics and the effects that REs have on the microstructure and mechanical properties of Al alloys.

Chapter 3: Characterization of Residual Stress in I6 Diesel Engine Block and Evaluation of Fitness-for-Service of A319 This chapter characterizes the evolution of residual stress along each stage of the manufacturing process of a sand-cast aluminum engine block. Further, the microstructure and evolution of phases in the A319 alloy are described. Lastly, the fitness-for-service feasibility of the A319 alloy is evaluated at current engine operating temperatures (i.e., 250 °C) and at next-generation engine temperatures (300 °C).

Chapter 4: Development of Next-Generation Powertrain Alloys This chapter characterizes the effects that RE additions have on the microstructure and evolution of phases during solidification of Al alloys. Thorough thermodynamic simulations using ThermoCalc™ are conducted to determine the evolution of phases following equilibrium and non-equilibrium solidification. Further, comprehensive electron microscopy and x-ray spectroscopy analyses are performed to identify the morphology and composition of the phases. Finally, *in-situ* solidification studies are performed using neutron diffraction to determine the actual solidification kinetics of the RE-modified alloys.

Chapter 5: Fitness-for-Service Assessment of Al-RE Alloys This chapter evaluates the fitness-for-service performance of the Al-RE alloys discussed in Chapter 4. Specifically, the alloys are subjected to elevated temperature (250 and 300 °C) tensile and creep tests. The minimum applied load during the creep tests is similar to the peak operating pressure inside internal combustion engines (i.e., 22 MPa). This chapter concludes by comparing the fitness-for-service performance of the newly developed RE-modified A356 alloy and the T7 A319 alloy used in engine block production to determine the feasibility of the Al-RE system for current and next-generation powertrains.

Chapter 6: Conclusions This chapter provides a detail summary of the conclusions drawn from chapters 3 to 5.

Chapter 7: Recommendations For Future Work This chapter outlines the recommendations for further validating the RE alloys. Moreover, a discussion around methods for further improving the fitness-for-service properties will be briefly discussed.

Chapter 2: Literature Review

This chapter begins with an introduction to the components and operating conditions of internal combustion engines (ICE), focused on the largest sub-component, the engine block. This introduction is followed by a description of one of the most common casting processes for engine block production and the corresponding issues that manufacturers are currently facing. The following sub-section focuses on characterizing the advantages and disadvantages of the two most common powertrain alloy systems, specifically the 2xx series (i.e. Al-Cu based) and 3xx series (i.e., Al-Si) with respect to the alloys' fitness-for-service properties and manufacturability/castability. Next, a detailed discussion of creep theory and thermal stability is provided. The chapter concludes with a comprehensive review of the currently available literature on the effects that RE elements have on the microstructure, mechanical properties, and castability of Al alloys.

2.1 Powertrain Applications

This section describes the current operating conditions inside engine blocks as well the mechanical properties that are most desirable for the alloys used for this elevated temperature application.

2.1.1 Powertrain Components and Operation

To achieve the impressive performance and efficiency of modern ICEs, engineers utilize sophisticated electronics, advanced materials, and creative designs for each of the components used in the complex engines. However, at the root of every engine lies several key components that all work synchronously to provide an efficient combustion of an air-fuel mixture inside the combustion chamber of the engine block.

Depending on the type of ICE, whether it is compression ignition (CI) (i.e., powered by diesel fuel) or spark ignition (SI) (i.e., powered by gasoline or propane), the ignition of the air-fuel mixture occurs in one of two ways. For modern CI engines, the air enters the combustion chamber and is compressed by the piston. Following this, fuel (diesel) is injected at extremely high pressures, resulting in the atomization of the diesel. The high pressure inside the combustion chamber results in the self-ignition of the air-fuel mixture. For inline and V engine block configurations, the combustion process can result in peak cylinder pressures of 17 (170 bar, 2465 PSI) and 15 MPa (150 bar, 2175 PSI), respectively [22]. The peak firing pressure has also been

reported to be as high as 20 MPa (200 bar, 2901 PSI) in some European diesel applications [23]. SI engines operate in a similar manner; however, rather than compressing the air-fuel mixture to its self-igniting pressure/temperature, the air-fuel mixture is ignited by the ignition system (i.e., spark plug). As a result, the cylinder pressures in SI engines are typically much lower as compared to CI engines (i.e., ~10 MPa). In either case, once ignited, the hot air-fuel mixture attempts to quickly expand; however, since the exhaust valves remain closed, this leads to a large pressure increase inside the combustion chamber. Following the ideal gas law (n and R are the number of moles and ideal gas constant, respectively), shown in Equation 1 [24], the increase in pressure (P) results in a proportional increase in the temperature (T) until the volume (V) is increased.

$$PV = nRT \quad (1)$$

Since the peak cylinder pressures in diesel CI engines are considerably greater than for gasoline SI engines, the operating temperatures of diesel engines are also much higher. For example, in current gasoline-powered engines, the typical operating temperature is approximately 200 to 225 °C and upwards of 250-300 °C for race engines as well as some diesel engines (see Figure 2.1-1) [25], [26].

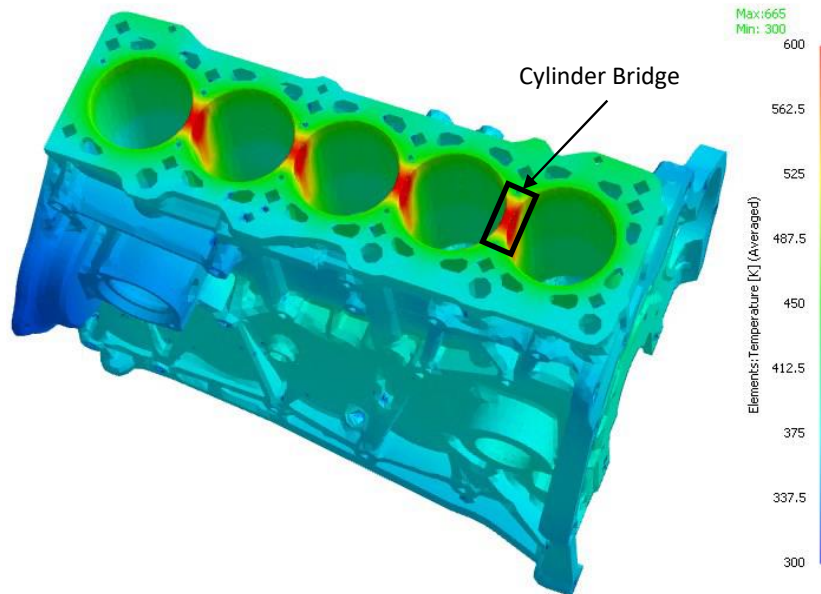


Figure 2.1-1. Simulated temperature distribution in inline diesel powered engine, note that cylinder bridge temperatures reach 250-300 °C (adapted from [26], [27])

A simplified thermodynamic model of the SI and CI cycle is shown graphically in Figure 2.1-2 and Figure 2.1-3. The figures on the left represent the relationship between pressure and volume

and the figures on the right represent the temperature-enthalpy relationship. In either case, the efficiency of the system is a direct function of the work extracted during the combustion process (W_{net}) and the energy input (Q_{in}). Thus, in simple terms, if we can increase the engine's W_{net} , the efficiency of the system will increase.

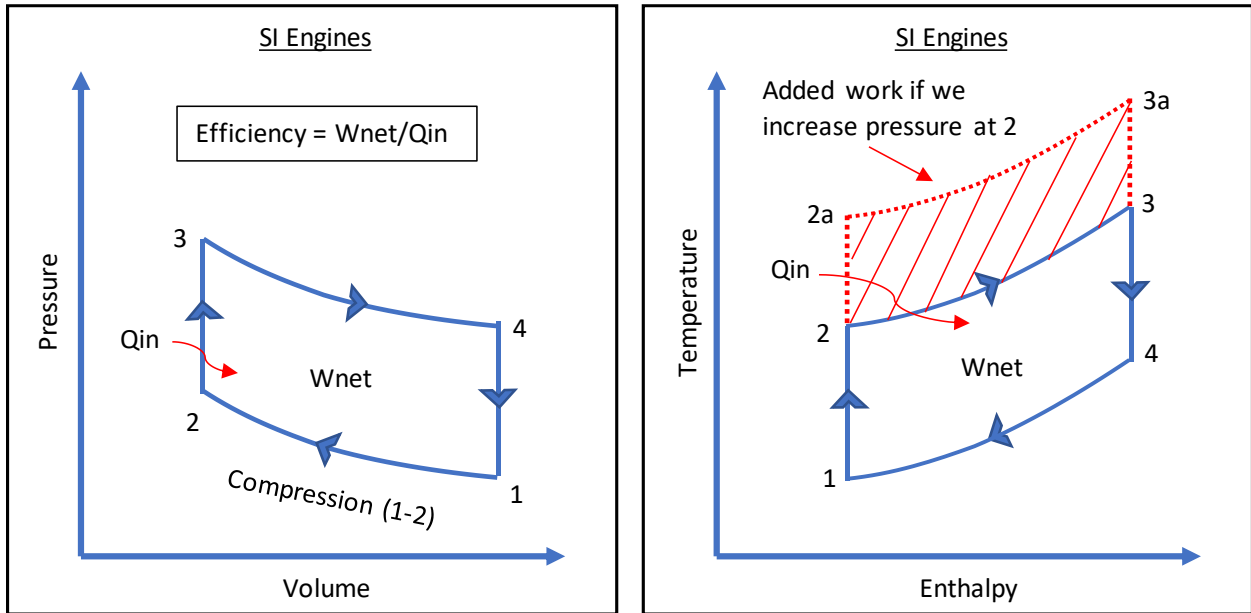


Figure 2.1-2. Simplified model of spark ignition engine cycle (based on Otto cycle)

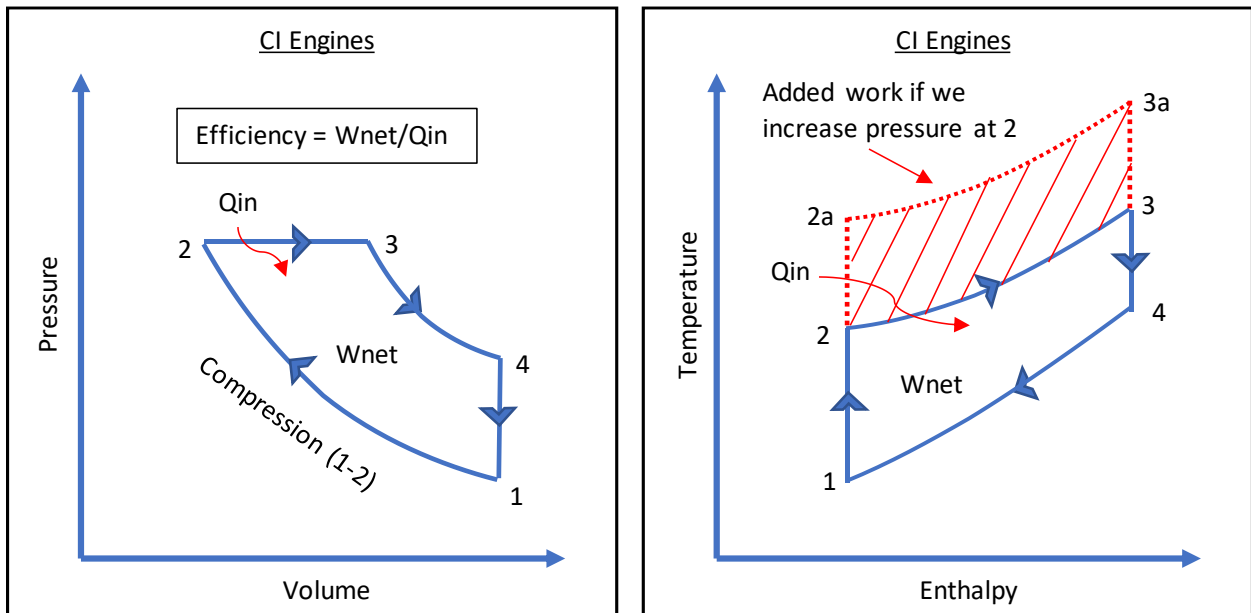


Figure 2.1-3. Simplified model of compression ignition engine cycle (based on diesel cycle)

One of the most common ways to increase the W_{net} of the Si and CI cycle is to elevate the pressure of the system at points 1 or 2. This can be achieved through introduction of a turbo charger, tuning

the engine control unit (ECU), or by changing the engine's compression ratio (ratio between max volume and minimum volume). The requirement for higher cylinder pressures in diesel engines is one of the reasons for the larger compression ratios (8:1-12:1 for gasoline vs 14:1-23:1 for diesel engines). As a result, greater efficiencies are generally obtained from diesel-fueled engines (~30-35% for gasoline vs. 40-42% for diesel). The higher potential for elevated efficiencies is one of the reasons for the recent increasing popularity of diesel-powered vehicles in North America.

No matter what method(s) is used to increase the pressure of the system, the increase in pressure will cause the temperature to rise proportionally (see equation 1). Although the increased pressure adds additional stress on the surrounding components, it is the rise in temperature that causes the greatest issues. In simple terms, as the temperature of the system is increased, the strength of the conventional powertrain alloys decreases, particularly when exposed for extended durations (see Figure 2.1-4).

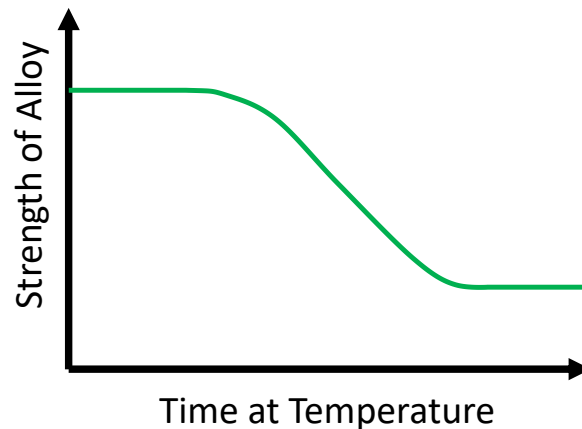


Figure 2.1-4. Simplified relationship of alloy strength and temperature

Consequently, the alloys used for the manufacturing of powertrain components must have adequate material and mechanical property retention at elevated temperatures, and the alloys must maintain their integrity throughout the entirety of the engine's operating life (see section 2.2.1 for a detailed description of the properties). The currently-used powertrain alloys (see section 2.2) meet today's requirements for engine block production; however, the increase in demand for higher cylinder pressures and operating temperatures is quickly pushing the current alloys past their useable limit. To add to this, manufacturers frequently face issues that minimize the material's useable strength and/or impair the integrity of the component.

2.1.2 Manufacturing Processes and Problems

This section describes the basic workings of two of the most frequently-used manufacturing processes for engine block production. The section concludes by describing two issues that manufacturers are currently facing, including microstructural defects and the development of residual stress. Both issues can lead to premature failure of the components, which may result in inefficient operation and costly recalls for the manufacturers.

For applications where high volume and fast production rates are critical, high-pressure die casting (HPDC) is one of the most used casting processes. In general, the HPDC process consists of forcing molten metal into a metal die cavity by means of an external pressure. After the metal solidifies, the die is opened, and the casting is ejected. Due to the relatively-high applied pressure (~10-175 MPa), the casting has a near net finish which reduces the amount of post-process machining. Moreover, the applied pressure allows manufacturers to produce castings with relatively thin wall sections (i.e. <4 mm) which can result in the production of lightweight components. For HPDC aluminum, a steel mold is commonly used to generate greater cooling rates as compared to other casting methods such as sand casting.

Although the production rates of HPDC are quite rapid, there are a few issues that manufacturers must deal with. First, the variation in wall thickness between thick and thin sections of an HPDC component is generally accompanied by large thermal gradients; and consequently, the development of residual stress (discussed in more detail in the following sections) [28]. In addition, the high velocity (~20-80 m/s [29]) of molten metal into the die cavity can result in turbulent flow which entraps unwanted gas, leading to relatively high volume fractions of porosity. The irregular geometry of porosity induces localized stress concentrations and can significantly impair a material's mechanical properties [30], [31]. Moreover, during solution heat treatment, the high magnitude of entrapped gas frequently releases and causes blisters to form on the surface of the HPDC component, leading to another reduction of mechanical properties and, usually, additional post processing. Lastly, the design complexity for HPDC is more restricted as compared to sand casting, due to the use of a permanent mold which must be opened after the casting has solidified. Thus, for components with greater geometrical complexity, an alternative casting process must be used.

Sand casting is a manufacturing process that utilizes a single-use sand mold to produce geometrically complex castings. A chemical binding agent and fine-particle sand are used as the material for the sand mold. The external and internal geometries of the sand molds and cores are typically created by compacting the sand around solid models or by 3D printing each layer of the mold. Sand cores allow for the integration of internal structures, such as certain cooling channels, which cannot be obtained with the conventional HPDC process. One of the major advancements of engine block production, was the development of “closed deck” engine blocks (see Figure 2.1-5) which can tolerate significantly greater loading as compared to the original “open deck” configuration. The “deck” of an engine block refers to the top surface which mates to the cylinder head. During the combustion process, the expanding gas applies a force onto the cylinder walls in all directions. If the pressure or temperature rises too high, the cylinder walls can deform or crack and lead to inefficient combustion and/or failure of the engine. Typically, the cylinder wall material between two adjacent cylinders (i.e., the cylinder bridge, see Figure 2.1-1 and Figure 2.1-5) is usually the location most prone to cracking since it experiences the greatest magnitude of thermo-mechanical loading. This is because the cylinder pressure and magnitude of heat flux reaches a maximum shortly after the piston passes top dead center (i.e., when the piston is near the top of its upward motion) [32], [33]. Thus, partial or complete reinforcement of the top portion of the cylinder walls (i.e., closing the deck) not only greatly reduces the engine block’s susceptibility to premature failure but has also allowed the automotive industry to increase cylinder pressures and has ultimately lead to improved operating efficiency. Although sand casting can improve design complexity, sand cast components typically experience slower cooling rates as compared to HPDC components, leading to larger grain sizes and, therefore, reduced mechanical properties.

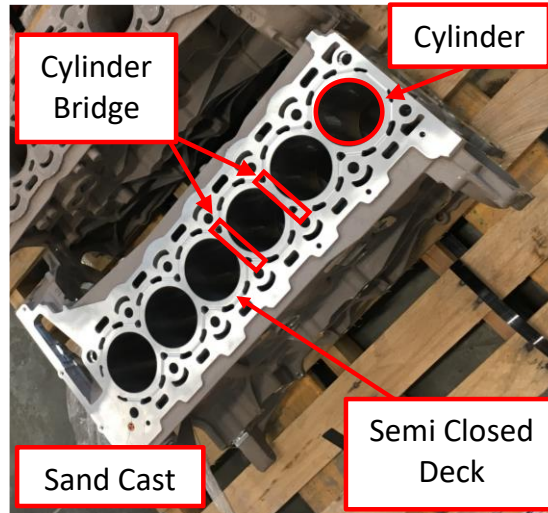


Figure 2.1-5. Representation of sand cast, closed deck engine block

Although HPDC and sand casting are suitable for many applications, both techniques suffer from the generation of residual stress during casting. Residual stress is a type of stress that exists on an elastic body without the presence of a thermal gradient and/or an externally applied load [34]. Two of the root causes for the development of residual stress are: i) large thermal gradients during casting/solidification (caused by non-homogenous cooling) and ii) CTE mismatches between dissimilar material compositions (i.e., Fe adjacent to Al). During cooling or quenching, the material will solidify and cool from the surfaces of the volume towards the interior of the volume. Consequently, the sections with the smallest wall thickness will contract much earlier in the cooling process as compared to the thicker sections. If a thin-walled section is located adjacent to a much thicker section, then towards the very end of the solidification process (i.e., when the thin section has completely solidified and the amount of solid in the thick section is approaching 100%), the thick section will contract after the thin section and will pull or push the thin section into tension or compression. To add to this, if a portion of the molten metal comes into contact with another material with different thermophysical properties (i.e., coefficient of thermal expansion, heat capacity, thermal conductivity), the dissimilar contraction rates and heat dissipation of the two materials can lead to the generation of additional residual stress. This occurs in conventional Al engine blocks which require protective gray Fe cylinder liners to resist the wear caused by the reciprocating piston rings. These Fe liners are typically inserted into the mold (sand or permanent) and fixed in place prior to pouring the molten Al. Due to the CTE mismatch between the gray Fe liners ($\sim 10 \times 10^{-6} \text{ }^\circ\text{C}^{-1}$) and the molten Al alloy used for the engine block ($\sim 23 \times 10^{-6} \text{ }^\circ\text{C}^{-1}$), the rate

of contraction of Al is more than twice that of the Fe liners. Since the Al has bonded to the rough surface of the fixed Fe liners, the Al, which wants to contract, is held in place by the Fe liners which leads to a “stretching” of the Al. This “stretching” of the Al is one of the major factors contributing to the development of high tensile residual stresses in Al engine blocks.

For example, approximately 170-200 MPa of tensile residual stress was observed in the Al cylinder bridges of an as-cast V6 Al SI engine block produced with cast-in Fe liners [35], [36]. This magnitude of residual stress accounts for more than 80% of the alloy’s available strength at room temperature. Once the engine block is subjected to in-service operating conditions (i.e., 3.5-10 MPa and 150-250 °C), the engine block may endure permanent dimensional distortion or cracking. This distortion can increase carbon emissions, reduced engine efficiency, and/or lead to complete engine breakdown. Fortunately, this unwanted residual stress can be reduced by post-processing techniques such as solution heat treatment (SHT) and artificial aging [37]–[39]. Solution heat treatment of A319 (AlSiCuMg alloy) Al engine blocks with cast-in Fe liners has been carried out to analyze the relief of the residual axial strain via neutron diffraction [36]. It was observed that soaking the engine block at 470-500 °C for 8 hours led to an ~50% reduction of the tensile residual stress present in the cylinder bridges. Furthermore, after applying a commercial T4 heat treatment, the stress in certain locations of the cylinder bridge were observed to be in compression rather than in tension. This transition from tension to compression is particularly beneficial, and though it may still contribute to possible engine block distortion, it should not cause cracking. Lombardi et al. [40] also observed that the magnitude of residual stress in the cylinder bridges of a sand cast V6 Al (A319 alloy) engine block was reduced considerably after a T7 heat treatment. It was noted that the T4 portion of the T7 treatment caused a near complete relief of residual stress at the bottom of the cylinder, whereas, the top and middle regions experienced only a partial relief. This was presumed to be attributed to non-uniform cooling throughout the cylinder bores following solution treatment. It was also found that the over aging (T7) treatment caused a redistribution of the tensile residual stress from the top of the cylinder to the bottom. Consequently, upon completion of the full T7 treatment, the residual stress was reduced by ~90 % at the top and 10% at the bottom of the cylinder as compared to the pre-heat-treated state (i.e., after thermal sand reclamation process). The two described engine blocks were successfully introduced into the automotive market and contributed to improving the efficiency of automobiles. However, although a considerable amount of residual stress was alleviated after heat treatment, a great deal of stress still remained in the

engine block due to the use of cast-in Fe liners (see Table 2.1.2-1). Moreover, the non-homogenous cooling of the cylinder bridge during solidification resulted in inconsistent microstructures and the variance of mechanical properties from the top to bottom of the cylinder bridge.

Table 2.1-1. Residual stress evolution in cast engine blocks produced with cast-in Fe liners (units in MPa)

Location along cylinder bridge of engine block		Stress in sand-cast V6 with cast-in Fe liners [36], [40] (MPa)		
		TSR ^a	T4	T7
Top	Radial	-65	25	17
	Axial	63	55	9
	Hoop	158	120	21
Upper middle	Radial	38	-75	55
	Axial	160	45	101
	Hoop	225	100	103
Lower middle	Radial	55	-80	41
	Axial	160	35	102
	Hoop	202	-10	149
Bottom	Radial	-95	-125	49
	Axial	15	5	106
	Hoop	88	-30	157

^a Average between TSR A (470 °C) and TSR B (500 °C)

Thus, to develop the next generation of cast powertrain components, it is necessary to modify the currently-used manufacturing methods to focus on reducing the initial development of residual stress and then introduce new alloys with improved elevated temperature mechanical properties.

2.2 Powertrain Alloys

This section begins by describing some of the most desirable material and mechanical properties of powertrain alloys, specifically, fatigue strength, creep resistance, and thermal stability. In the subsequent section, the Al-Cu and Al-Si alloy systems are described, with emphasis on their castability, mechanical properties and ability for property improvements.

2.2.1 Required Fitness-for-Service Properties

As described in section 2.1.1, the efficiency of internal combustion engines relies on high cylinder pressures and, therefore, operating temperatures inside the combustion chambers. Due to frequent heat cycling (engine startup → normal operating temperature → engine cool down), the cylinder bridge material in engine blocks experiences a great deal of cyclic thermo-mechanical loading which can lead to rapid failure of the component if the material has insufficient material and mechanical properties. This section describes the alloy properties that are most critical in powertrain components that are exposed to high thermo-mechanical stresses.

2.2.1.1 Thermo-Mechanical Fatigue

Fatigue exists when cyclic stresses or deformations occur in a component due to a repeated applied stress and/or change in temperature. In many powertrain applications, there may exist a combination of traditional mechanical fatigue (high cycle fatigue) as well as temperature-driven fatigue (i.e. thermal fatigue), both of which may result in the development and propagation of cracks [41]. The combination of the two types of fatigue is commonly described as thermo-mechanical fatigue (TMF).

For applications such as engine blocks, mechanical fatigue develops due to the cyclic loading that occurs during power production/transmission. Mechanical fatigue occurs in the cylinder bridges of ICEs from the alternating pressure inside the combustion chamber which may shift from atmospheric pressure (~0.1 MPa) to upwards of 20 MPa 500-8000 times per minute (depending on engine configuration).

Thermal fatigue is complex; however, it is caused by thermal gradients that develop during an engine's heat cycle. The damage caused by thermal fatigue is typically worse than the damage caused by mechanical fatigue, and thus, it is the rate-controlling fatigue mechanism that determines the lifetime of the component [42]. For "water" cooled engines, thermal fatigue is present throughout several locations in the engine block; however, it is more severe in locations adjacent to cooling channels, such as the cylinder wall/bridge material. During initial engine startup, the temperature of the cylinder wall surface quickly rises while the interior, near the cooling channels, remains relatively low. The rising temperature should naturally lead to a volumetric expansion of the material; however, the rigidity of the "cold" bulk restricts this expansion, leading to localized

tensile and compressive stresses. Not only does this lead to damage caused by thermal fatigue, the stresses that are present at elevated temperatures lead to another failure mechanism known as creep.

According to Wong et al. [43], the amount of damage caused by fatigue or creep is related to the frequency of the cycles as well as the temperature of the environment. The longer the cycle and higher the temperature, the greater the damage caused by creep (see Figure 2.2-1). Thus, it can be deduced that the long heat cycle and elevated temperatures of engine blocks lead to greater failures caused by creep. Consequently, more emphasis should be placed on developing alloys with improved creep resistance.

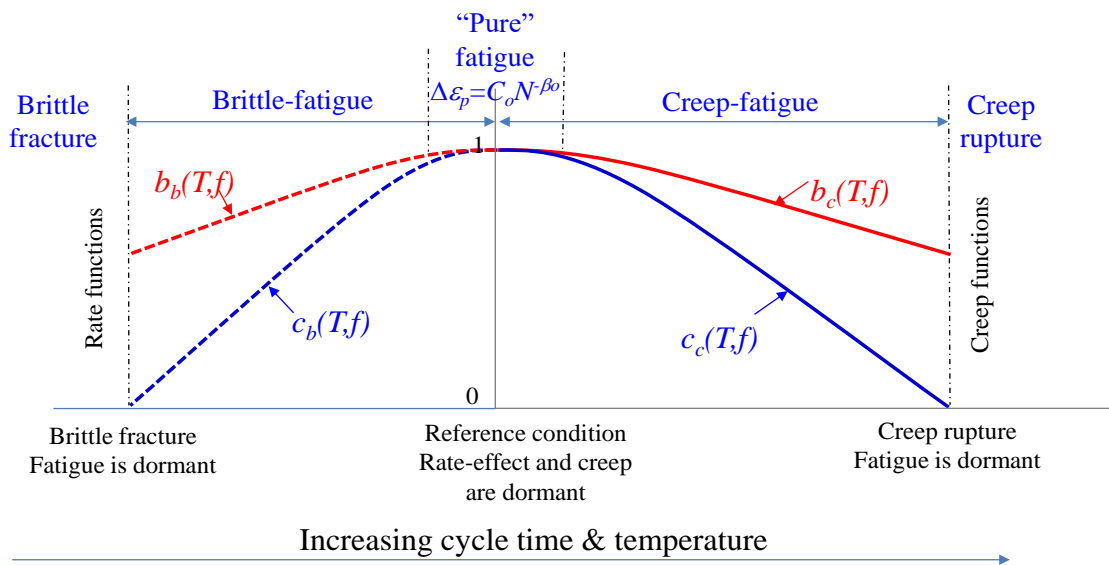


Figure 2.2-1. Contribution from fatigue/creep damage with relation to cycles and temperature [43]

2.2.1.2 Creep Resistance

Creep is characterized as the time-dependent, slow deformation of material under continuous elevated temperature and stress conditions, and can result in the failure of a component below the material's yield strength. For many alloys, the basic mechanism of creep deformation is the movement of dislocations that induces slip in crystal grains. For Al and Al alloys, slip occurs preferentially on the {111}, {100} and {211} planes.

Creep can occur at all stress and temperature magnitudes but is of greater concern when the temperature reaches $0.4-0.5T_{\text{melt}}$ [44]. For Al-based alloys, this situation corresponds to

temperatures above 200 °C. The creep strain ϵ is measured as a function of time t under a tensile or compressive load σ at a given temperature T . Figure 2.2-2 graphically displays the three stages of creep where I (primary creep) is after instantaneous deformation, II (secondary creep) is the steady-state region and, III (tertiary) is the rapidly increasing creep up to fracture.

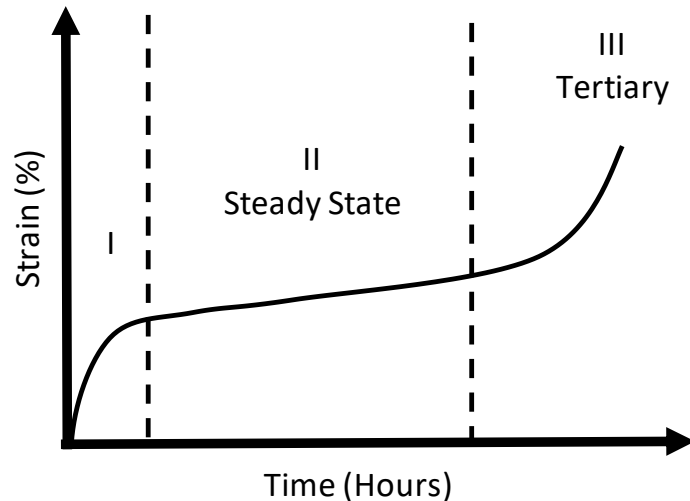


Figure 2.2-2. Stages of creep

During the first stage of creep (i.e., primary creep), the initial loading causes an instantaneous increase in the strain that is followed by a decrease in the creep rate. The creep rate decreases by consequence of strain hardening. During primary creep, the lattice may bend near the grain boundaries which can result in a cluster of dislocations of one sign, and since dislocation climb is facilitated by the elevated temperature, the dislocations can arrange themselves into a low-angle grain boundary [45]. This sub-grain network is an effective barrier against dislocation motion and contributes to hardening of the material. The formation of sub-grain structures occurs more readily in materials with high stacking fault energies, such as FCC aluminum.

In the second stage of creep, known as steady-state creep, the creep rate is nearly constant due to a balance between thermal recovery by annihilation and rearrangement of dislocations and strain hardening [46]. The nature of work-hardening in creep is the same as in plastic deformation. When an external load is applied to an alloy, the number of dislocations increases. This leads to the formation of a three-dimensional network of tangled dislocations which act as a barrier against dislocation motion. However, when the energy (i.e., temperature) of the system is increased,

vacancies in the crystals can diffuse more readily toward a dislocation, resulting in dislocation movement to an adjacent slip plane (i.e., dislocation climb). Originally pinned by other dislocation, defects or obstacles (i.e., intermetallics), the climbing of dislocations to adjacent slip planes allows for facilitated dislocation movement and, thus, further deformation (i.e., thermally activated recovery or “softening” of the material). The rate at which vacancies diffuse to the location of a dislocation is largely dependent on the temperature of the system [47]. In general, the higher the temperature, the faster the rate of vacancy diffusion.

The steady-state creep rate $\dot{\epsilon}_s$ is an important parameter that is often included in the design requirements for powertrain components. At moderate temperatures (0.4 to 0.5 T_{melt}), the steady-state creep rate is generally governed by a power-law (PL) relation and is calculated using Equation 2, where A is a material constant, σ is the applied stress, n_a is the apparent stress exponent, Q_a is the apparent activation energy for steady-state creep, R is the universal gas constant, and T is the absolute temperature [48], [49]. The apparent stress exponent n_a and activation energy Q_a provide an indication of which creep mechanisms are predominant.

$$\dot{\epsilon}_s = A\sigma^{n_a} \exp\left(-\frac{Q_a}{RT}\right) \quad (2)$$

Q_a and n_a are calculated with Equation 3 and 4 and are obtained by performing creep tests at different temperatures and stresses.

$$Q_a = -R \left[\ln\left(\frac{\dot{\epsilon}_1}{\dot{\epsilon}_2}\right) / \left(\frac{1}{T_1} - \frac{1}{T_2}\right) \right] \text{ at constant } \sigma \quad (3)$$

$$n_a = [\ln(\dot{\epsilon}_1 - \dot{\epsilon}_2) - \ln(\sigma_1 - \sigma_2)] \text{ at constant } T \quad (4)$$

In the last stage, tertiary creep, the creep rate begins to accelerate quickly until the component fractures. Tertiary creep mainly occurs in constant-load creep tests at high stresses and temperatures and when there is an effective reduction in the cross-sectional area either by formation of internal voids or necking. Metallurgical changes (coarsening of precipitates, recrystallization or diffusion changes in the phases) can sometimes be observed in the tertiary stage of creep [48].

Since stress and temperature are held constant during a creep test, the variation in creep strain throughout the test is a direct result of internal structure changes within the material. For example, slip, sub-grain formation, and grain-boundary sliding are some of the structural changes that occur

during a high-temperature creep test. At elevated temperatures, the grains in polycrystalline materials can slide more readily relative to each other. This phenomenon occurs via a shear process which is oriented along the direction of the grain boundary. The strain from grain-boundary sliding represents approximately 50% of the total strain that occurs in a creep test (depending on material and testing conditions). For grain boundary deformation to occur without producing cracks at the grain boundaries, folds and grain boundary migration allow for continuity of strain along the grain boundary. Grain-boundary migration occurs when the grain boundary moves normal to itself which can relieve strain concentration. Frequently, wavy grain boundaries are observed after high-temperature creep which is a result of inhomogeneous grain-boundary deformation and grain-boundary migration [48].

The primary mechanisms for creep deformation can broadly be separated into i) dislocation glide, ii) dislocation creep, and iii) diffusion creep [45]. Dislocation glide involves the movement of dislocations along slip planes and the overcoming of barriers by thermal activation (occurs at high stress, $\sigma/G > 10^{-2}$). The impediment of dislocation motion by precipitates, solute atoms and other dislocations establishes the creep rate caused by dislocation glide. Dislocation creep involves the diffusion of vacancies or interstitials which assists the dislocations to overcome obstacles (i.e., intermetallics, other dislocations, etc.) This typically occurs at moderate stress, $10^{-4} < \sigma/G < 10^{-2}$. The first models of dislocation creep were developed by J. Weertman who claimed that dislocation climb plays a major role [50]. At elevated temperatures, if an obstacle prevents the continuous gliding of a dislocation, a small amount of thermally-assisted climb may allow the dislocation to surpass the obstacle and allow it to glide to the next barrier. Dislocation climb has little effect on the strain but largely controls the velocity of the dislocations. Dislocation climb requires the diffusion of vacancies or interstitials and, therefore, the rate-controlling mechanism is atomic diffusion. For intermediate stress magnitudes at elevated temperatures (i.e., powertrain applications that operate above 0.4 to $0.5T_m$ and $\sim 10^{-4} < \sigma/G < 10^{-2}$), the steady-state creep rate, as described by the power-law relation in Equation 2, is predominantly governed by dislocation creep. Figure 2.2-3 shows the steady-state creep rate, normalized with the diffusion coefficient plotted against the stress (σ), and normalized against shear modulus (G). The power-law governed creep occupies the central region of the normalized stress.

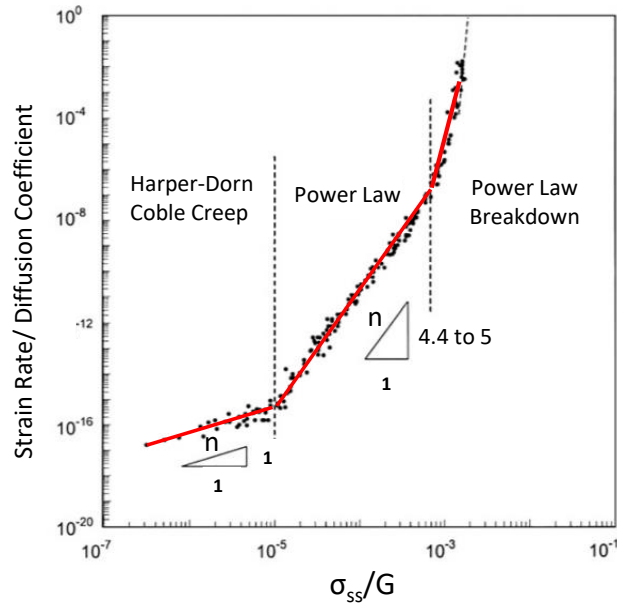


Figure 2.2-3. Influence of stress on steady-state creep rate, adapted from [51], [52]

At low stresses ($\sigma/G = 5 \cdot 10^{-6}$), a linear dependence on stress ($n = 1$ in Equation 2) is observed. This region is governed by Harper-Dorn creep [53]. This region is presumed to be ruled by climb-controlled creep, where the dislocation density remains unchanged with varying stress [45].

At temperatures less than $0.6 T_{\text{melt}}$, and depending on the strain rate, the activation energy Q_a may decrease well below the activation energy for self diffusion Q_{sd} . This situation generally occurs at the power-law to power-law breakdown transition when $n = \sim 5-6$ [54]. It has been postulated that the rate-controlling mechanism may be controlled by dislocation climb assisted by short-circuit diffusion of vacancies via the high density of dislocations attributed to the increased stress at 0.3 to $0.6 T/T_{\text{melt}}$. However, there is little published confirmation and, thus, the mechanism for creep in the PLB region is still not completely understood.

Diffusional creep involves the flow of vacancies and interstitials through a crystal under the influence of an applied stress (occurs at $\sigma/G < 10^{-4}$). Diffusional creep includes Nabarro-Herring (Equation 5, where d is the diameter of the grain) and Coble creep (use Equation 6 when lower temperature grain-boundary diffusion is predominant, where D_{gb} is the grain-boundary diffusion coefficient). Diffusion creep becomes the controlling mechanism at high temperatures and relatively low stresses. For these conditions, Nabarro and Herring proposed that the creep process was controlled by stress-directed atomic diffusion. Stress changes the chemical potential of atoms on the surface of grains in polycrystalline materials in such a way that there is a flow of vacancies

from grain boundaries that are experiencing tensile stress toward those under compressive stress. Congruently, there is a corresponding flow of atoms in the opposite direction; leading to the elongation of the grain [48].

$$\dot{\epsilon}_{Nabarron-Herring} = \frac{14\sigma b^3 Dv}{kTd^2} \quad (5)$$

$$\dot{\epsilon}_{Coble} = \frac{50\sigma b^4 Dgb}{kTd^3} \quad (6)$$

Although the applied stress and temperature affect which creep mechanism is controlling the strain rate, in reality there are multiple mechanisms that all contribute to the total strain. Thus, to understand how a component may perform in its intended environment, it is important to understand the basics of each of the mechanisms that contribute to creep deformation.

For current powertrain applications such as cylinder heads and engine blocks, the applied stress and temperature range is expected to lead to deformation behavior (i.e., steady-state creep rate) following the conventional phenomenological power-law relation (i.e., Equation 2) for steady-state creep. In general, engineers and manufacturers are most interested in the material's steady-state creep rate since this is a direct measure of how the material/component will perform during elongated exposure to an elevated temperature and applied load. However, comparing the stress exponent and activation energies may provide additional information on how the microstructure and/or composition of the alloy affects the steady-state creep rate. In general, a material with a lower value of n_a and a greater value of Q_a will have a slower steady-state creep rate.

It should be mentioned that the creep theory listed above has been derived from experiments performed on pure metals or solid-solution materials, and it is generally accepted that multicomponent alloys, particularly alloys with high concentrations of intermetallics and dispersoids, can and will perform much differently,. For example, values for n_a and Q_a were observed to reach upwards of 40 and 570 kJmol⁻¹, respectively, for a dispersion-strengthened Al-Si-Mg-Cu-Ni alloy (see Figure 2.2-4) [55].

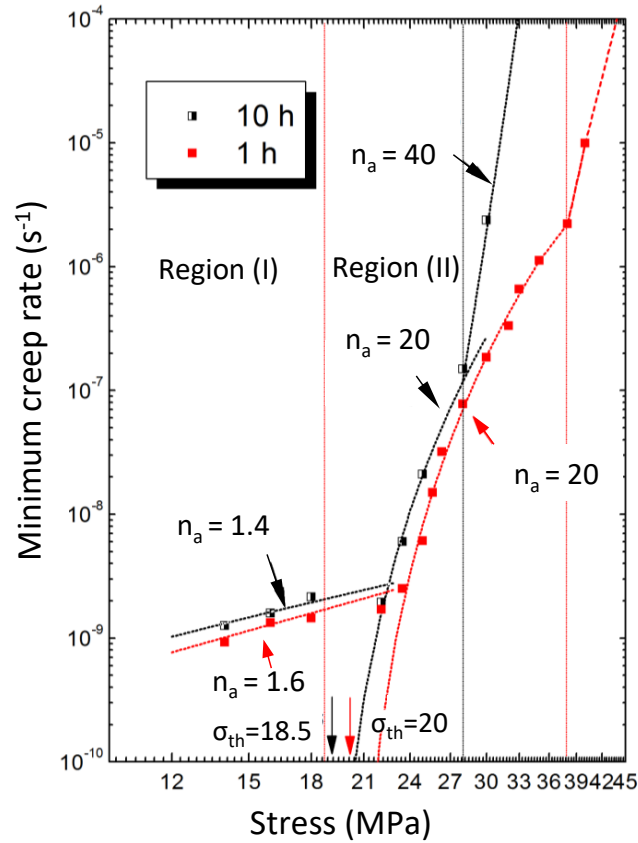


Figure 2.2-4. Minimum creep rate at 300°C vs. stress for dispersion-strengthened Al-Si-Mg-Cu-Ni alloy (Adapted from [27]). Note high apparent stress exponents n_a and presence of threshold stress σ_{th}

Such high values cannot be easily translated to realistic creep mechanisms. As a result, for dispersion-strengthened alloys, a threshold stress σ_{th} is introduced to account for the inexplicably-high (with regards to the thermally-activated dislocation mechanisms) and varying apparent n_a and Q_a values (see Equation 7, where G is the shear modulus). The threshold stress is estimated by plotting $\dot{\epsilon}_s^{1/n}$ vs. σ on a double-linear scale and extrapolating to $\dot{\epsilon}_s = 0$ (see Figure 2.2-5A) for the region corresponding to apparent stress exponent values greater than $\sim 4.4-5$ (i.e., region (II) in Figure 2.2-4) [55]. When plotting $\dot{\epsilon}_s^{1/n}$ vs. σ , a stress exponent value of $n = 4.4$ to 5, or 7 can be used, which represents dislocation creep and lattice diffusion-controlled creep with a constant subgrain structure, respectively [56]–[58]. The results can be verified by plotting the $\dot{\epsilon}_s$ vs. the effective stress ($\sigma - \sigma_{th}$) on a double-logarithmic scale and determining the goodness of fit (i.e., value of R^2 , see Figure 2.2-5B).

$$\dot{\epsilon}_s = A' \left(\frac{\sigma - \sigma_{th}}{G} \right)^n \exp \left(- \frac{Q}{RT} \right) \quad (7)$$

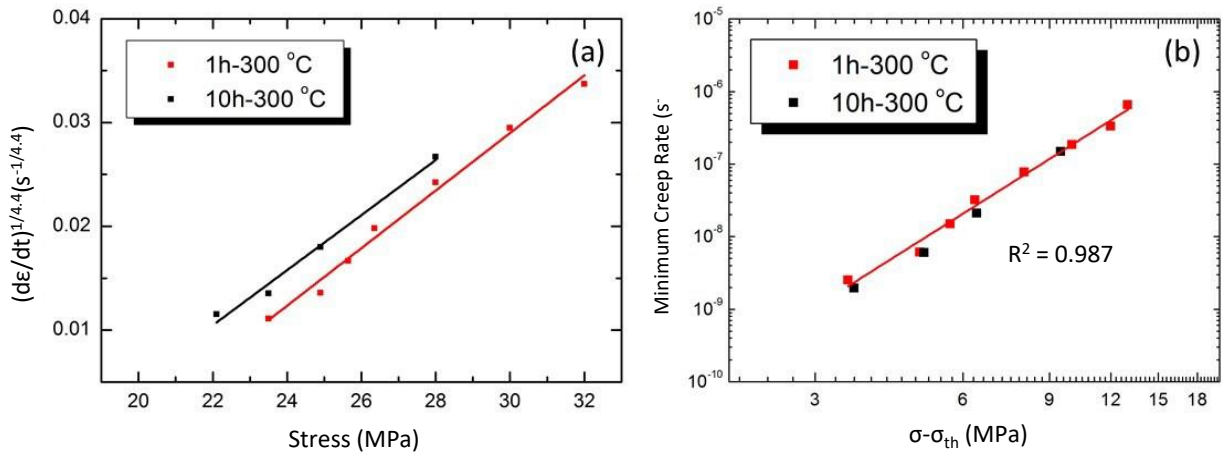


Figure 2.2-5. (a) Plot of $\dot{\epsilon}_s^{1/n}$ vs. stress using $n = 4.4$ for dislocation creep region (region II) in Figure 2.2-4) and (b) double-logarithmic plot of minimum creep rate vs. effective stress ($\sigma - \sigma_{th}$) [27]

The presence of a threshold stress is not unanimously accepted within the scientific and materials engineering community, and the exact mechanisms are not completely understood. However, it has been postulated that for non-shearable precipitates, a threshold stress may develop due to the interaction of dislocations with precipitates during dislocation climb/bypass or the Orowan bowing mechanism [59]. Krug et al. [60] suggests that the elastic interactions of dislocations with precipitates facilitates the dislocation climb process; however, the dislocations are pinned on the departure side which results in the development of a threshold stress. It is believed that dislocation creep is not significant below the threshold stress.

A creep test consists of applying a constant load to a creep sample, whose geometry follows the recommendations listed in ASTM standard E8M [61], while measuring the total plastic and elastic strain. The testing principles outline in ASTM E139-70 [62] should be followed. Typically, the magnitude of the applied load corresponds to a stress value below the material's yield strength. Similar to a tensile test, the most common method of measuring the strain is via extensometers.

At the upper end of the temperature range for engine blocks (i.e., 300 °C), the bulk of the material attempts to expand but its natural expansion is restricted by the surrounding material and preload from the fasteners. This restriction has been reported to result in the development of compressive stress on the magnitude of 20-30 MPa [42]. Once the engine block begins to cool, the restriction to contraction now shifts parts of the engine block into tension. However, since the temperature is

now much lower than the peak operating temperature and thus considerably less than $0.4T_m$, creep plays only a minor role and tensile properties now become critical [63]. Because creep is dependent on the temperature at which the material is exposed to, creep tests should be performed at different temperatures and loads to evaluate the suitability of the alloy for different applications. For current combusting engines, the temperature and stress conditions of creep tests should be $\sim 200\text{-}250\text{ }^\circ\text{C}$ and $10\text{-}20\text{ MPa}$ for gasoline engines, and up to $300\text{ }^\circ\text{C}$ and $20\text{-}30\text{ MPa}$ for diesel applications [42], [63].

Due to the complex nature of creep in multicomponent alloys (i.e., powertrain alloys), the rate-controlling creep mechanisms are also commonly described with reference to the deformation mechanism map (see Figure 2.2-6) of the element of highest concentration, (i.e., aluminum for Al-based alloys or magnesium for Mg-based alloys) [64]–[67]. The two vertical dashed lines shown in Figure 2.2-6 represent the homologous temperature (T/T_m) for the operating conditions of current engine blocks (i.e. 250 and $300\text{ }^\circ\text{C}$).

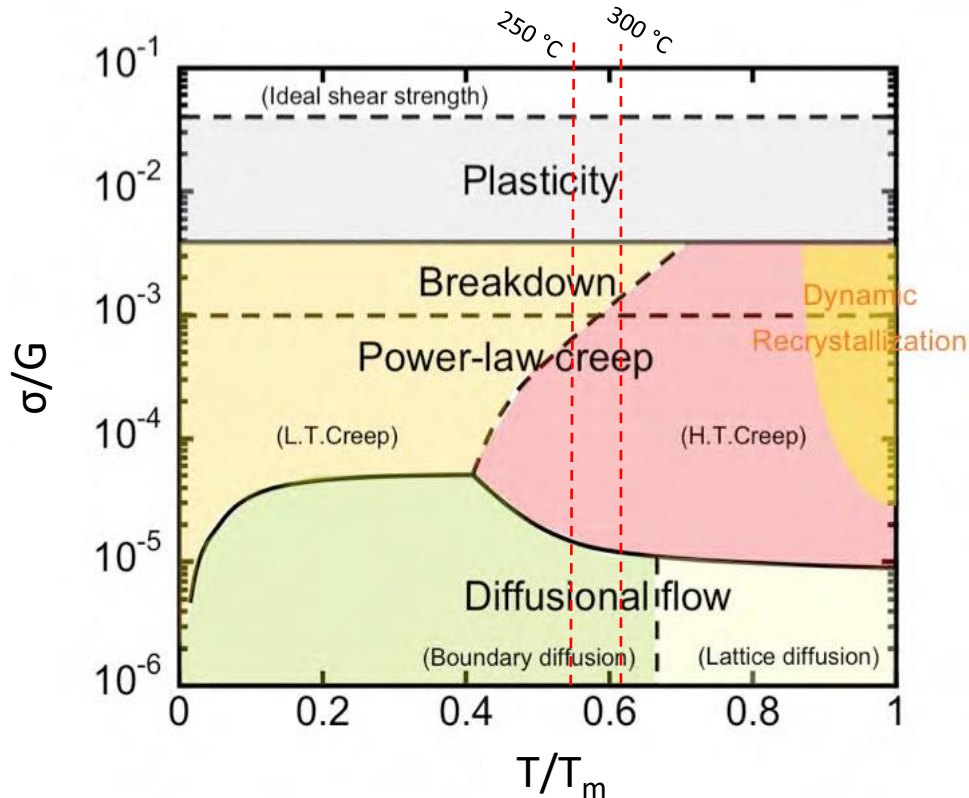


Figure 2.2-6. Deformation mechanism map for pure Al, original [64], *adapted from* [65]

Depending on the material's temperature-dependent shear modulus, G , and the applied stress, σ , the steady-state creep rate may be described by any of the creep mechanisms shown in Figure 2.2-6. For Al powertrain alloys tested between $\sim 250\text{--}300\text{ }^{\circ}\text{C}$, the rate-controlling creep mechanisms are diffusional creep (low stresses), high temperature creep and power-law-governed dislocation climb (moderate stress), power-law-breakdown dislocation creep (moderate to high stress) and, eventually, dislocation glide and plasticity (high stress).

2.2.1.3 Thermal Stability

The creep resistance, fatigue strength and tensile strength of Al alloys are directly affected by the microstructure of the alloys; specifically, the grain size, presence of primary and secondary phases and the size, morphology, and coherency of these phases. For example, the yield strength of an alloy is commonly approximated by the grain size of the primary phase via the Hall-Petch equation that is shown below (Equation 8), where σ_y is the yield strength, σ_0 is the stress associated to the resistance of lattice dislocation motion, k_y is a strengthening coefficient, and d is the grain diameter.

$$\sigma_y = \sigma_o + \frac{k_y}{\sqrt{d}} \quad (8)$$

In addition to grain size, the mechanical properties of complex alloys rely on several additional attributes, including solid solution strengthening and dispersion strengthening. Solid solution strengthening involves the dissolution of solute elements into the matrix, thereby creating strain fields which improve the resistance to dislocation motion. Dispersion strengthening is related to the interactions between precipitates and dislocations, and its effect on the materials yield strength is associated with the Orowan mechanism, as described in Equation 9 where M is the Taylor factor, G and ν are the shear modulus and Poisson's ratio of the matrix, b is the magnitude of the burgers vector, L is the interparticle spacing, D is the diameter of the precipitate, [68]. As described by Equation 9, the strength of an alloy is related to the size (D) and spacing (L) of the precipitates.

$$\sigma_{Orowan} = M \frac{0.4Gb}{\pi L \sqrt{1-\nu}} \ln \left(\frac{\pi D}{2b} \right) \quad (9)$$

Regardless of the size, morphology, and interparticle spacing between precipitates, the strength associated with their presence must be maintained at elevated temperatures. When the temperature increases, many intermetallics can coarsen and lose their functionality, thereby eliminating some, if not all, of their contribution to the material's strength. The Ostwald ripening rate constant K provides an indication of how well a precipitate may resist coarsening (see Equation 10) [69], [70]. D is the diffusion coefficient of the rate-controlling solute, γ is the interfacial energy between the precipitate and the matrix, C_α is the solubility of the solute element in the Al matrix, and C_β is the solute concentration in the precipitate. A smaller K results in a greater coarsening resistance, and thus, would indicate that the precipitate has improved thermal stability.

$$K \propto \frac{D\gamma}{(C_\beta - C_\alpha)^2} \quad (10)$$

The greatest coarsening resistance is obtained when the coherency of the precipitate with the matrix is high (ideally, the precipitate has a similar crystal structure as the matrix), the diffusivity of solute elements and the solid solubility of solute in the matrix are low, and the concentration of solute in the precipitate is high.

In addition to calculating the Ostwald ripening rate constant, there are a few other ways to estimate the thermal stability of phases. These include optical microscopy, X-ray diffraction (XRD), and neutron diffraction (ND). Each of these methods have their own unique advantages and

disadvantages. For instance, an optical analysis may be performed on an alloy prior to and after subjecting it to service operating temperatures. By comparing the two microstructures, the dissolution of phases and/or morphology changes may be observed. This technique is the least expensive; however, the results will likely provide only a portion of the entire story. It is possible that the intermetallic may dissolve at higher temperatures but once the sample is brought back to room temperature, the phase could re-appear in the microstructure, resulting in false claims that the intermetallic is stable through the entire temperature range. This ambiguity suggests that the more commonly used diffraction techniques may be preferable. XRD and ND are advantageous over optical analyses because they can enable phase characterization in real-time as the temperature is increased.

2.2.1.4 Summary of Required Properties for Powertrain Alloys

The difficulty associated with alloy design for powertrain applications, specifically engine blocks and cylinder heads, lies in obtaining the optimum combination of material and mechanical properties. Moreover, the inherent difficulties of measuring the actual in-service stress experienced by critical locations in these components adds a layer of ambiguity. Regardless, to obtain the greatest performance from powertrain alloys, the alloys should have an optimum ratio of the following properties:

- Creep resistance up to ~250-300 °C: To minimize creep deformation and maintain geometric stability.
- Strength at room temperature to 300 °C: To elastically accommodate stress when ductility is low.
- Ductility: To provide manufacturers with a safety factor by minimizing crack formation through elastically dissipating stress.
- Thermal stability/coarsening resistance: To retain mechanical properties at elevated temperatures.

2.2.2 Current Commercial Powertrain Alloy Systems

Currently, 2xx (Al-Cu based: A/B206) or 3xx (Al-Si based: A319, A356, A380, and A390) series cast Al alloys are two of the most commonly used alloys in the automotive, aerospace and marine industries. Al-Cu alloys are commonly found in many automotive, aerospace and defense

components where greater strength to weight ratios are required [71], [72], such as truck and aircraft wheels, vehicle suspension components, aircraft fuselage and wing skins. However, many factors affect the mechanical properties of 2xx alloys, including, but not limited to, the amount of Cu and other alloying elements in the alloy, the type of heat treatment, and the alloy modifications such as additions of strontium (Sr) or nano-particles. High Cu content (~9-11 wt. % Cu) Al-Cu alloys are typically used in aerospace and automobile engines due to their higher temperature-strength and wear resistance, whereas lower Cu content alloys (4-6 wt. % Cu) are more commonly used in structural components since they have a greater combined UTS and ductility. To further improve certain mechanical properties and to improve the heat treatability, a combination of Si, Ni, and/or Mg are added to the Al-Cu alloys. Some of these alloying elements are added to intentionally form more favourable precipitates with impurity elements like Fe.

One of the most widely used Al-Cu-based alloy is A/B206 (4.2-5.0 wt.% Cu) due to its high strength produced by precipitation hardening, good low-cycle fatigue, and great ductility. The high solubility of Cu in the Al matrix (~5.6 wt.% at the solidus temperature of ~546 °C) allows for a substantial magnitude of solid solution strengthening when applying a conventional solutionizing and quenching heat treatment. In addition, the precipitation of specific Al-Cu intermetallics such as Al_2Cu , $\text{Al}_3(\text{CuNi})$ and $\text{A}_7\text{Cu}_4\text{Ni}$ can further improve the alloy's strength and thermal stability. The mechanical properties of the 206 alloy can vary significantly and depend not only on good casting practices but also on the applied temper and amount of Fe [73]. For instance, the T4 temper (natural aging after solutionizing) has been recognized as giving the greatest quality for the 206 alloy and is likely attributed to the high maximum solubility of Cu in Al [71] and the lower sensitivity to Fe contamination as compared to other tempers such as T7. G. Sigworth and J. Major suggested that this alloy has a high sensitivity to solidification cooling rates and to Fe content in the T7 temper, and that the T6 temper should not be considered since it does not promote stress corrosion cracking in the alloy [74].

A study performed by H. Kamga et al. [71] evaluated the effects of the T4 and T7 heat treatment on various cast and wrought Al-Cu alloys, including the B206 alloy. For all of the alloys they investigated, both the YS and UTS were significantly improved after applying the T4 and T7 heat treatments. For example, the YS and UTS of the as-fabricated (F temper) B206 alloy increased

from ~170 MPa and ~240 MPa, respectively, to ~270 MPa and ~435 MPa after the T4 heat treatment, and to ~390 MPa and ~455 MPa after the T7 heat treatment.

Although the T7 heat treatment consistently produces higher YS and UTS values for the alloys in the study, the benefit of the T4 temper was clearly observed when the material's elongation was evaluated, for example, the elongation of the as-cast B206 alloy increased from approximately 4% to 15% after applying the T4 temper. Conversely, minimal change was observed after the T7 temper. It should be noted that in industry, most powertrain applications only require a minimum of 1% elongation. The results from this study also indicate that the elongation in certain alloys may be negatively affected by the T7 temper. The authors indicate that this negative effect may be attributed to sensitivity of the T7 treatment to Fe content, resulting in a larger network of β -Al₇FeCu₂ platelets which act as crack initiation sites.

The most detrimental issue associated with Al-Cu casting alloys is that the high Cu content (up to approximately 5 wt.% of Cu) in the 2xx series alloys promotes the precipitation of Cu-bearing intermetallics late during the solidification process which, if not properly addressed, can hinder the metal feeding process during casting and decrease the castability and mechanical properties of the alloy [75]. In addition, the long solidification range of Al-Cu alloys promotes a phenomenon known as hot tearing which is considered one of the most serious defects in castings [76]. D. Eskin et al. reviewed the theories of hot tearing (stress-based, strain-based and strain-rate-based), and indicated that sufficient feeding of the forming solid phase (i.e., primary Al for Al-Cu alloys) with the liquid metal is essential for the continuity of the solid phase, thus playing a crucial role in suppressing the hot tearing phenomena [77]. Fortunately, grain refinement and mold temperature control can reduce hot tearing susceptibility in Al-Cu castings. Several options are available for grain refinement, including but not limited to faster cooling rates or the addition of nano-particle inoculants or Sr [76]. However, regardless of the additional alloy modification, the hot-tearing tendency of Al-Cu alloys remains far worse than Al-Si alloys. Thus, although the strength of Al-Cu-based alloys is typically greater than the strength of Al-Si alloys, the poor castability (caused by shrinkage, hot tearing, and poor melt fluidity) minimizes or restricts the practical use of Al-Cu alloys for complex castings such as engine blocks and cylinder heads.

Thus, the Al-Si system (i.e., 3xx series) is more widely used for powertrain components such as engine heads, engine blocks, pistons, and gearcases [8], [78], [79]. In addition to improved

castability, Al-Si alloys have a lower coefficient of thermal expansion, excellent fluidity during casting, good abrasion resistance, and a sufficient strength to weight ratio. The highly ordered structure of Si requires a large amount of entropy to shift from a solid to liquid state and, thus, a high amount of energy is required to melt Si. Consequently, during melting and subsequent heating of Al-Si alloys, the energy is stored and then released during solidification. This release of energy during solidification improves the interdendritic metal feeding, alloy fluidity and, ultimately, the alloy's castability [80].

3xx series Al alloys are present with a hypoeutectic (i.e., below eutectic Si composition or 12.6 wt. % Si) or hypereutectic (i.e. above 12.6 wt. % Si) composition. Hypoeutectic Al-Si alloys, such as A319, A356, and A380, have improved wear resistance as compared to the 2xx series alloys, greater castability, and have sufficiently high fracture toughness and thermal conductivity. The advantage of hypereutectic Al-Si alloys, such as A390, is the higher dimensional stability associated with the improved modulus of elasticity (approximately 15-20% stiffer than hypoeutectic alloys and 25% stiffer than pure Al [75]), and the lower coefficient of thermal expansion (approximately 20% lower than hypoeutectic alloys [75], [81], [82]). Dimensional stability is crucial for components which rely on tight tolerances. However, the large size and brittleness of the primary Si crystals in hypereutectic alloys can increase the alloys' susceptibility to cracking under load. Moreover, similar to the Al-Cu alloys, the large primary Si crystals in hypereutectic Al-Si alloys can block interdendritic feeding during the solidification process and can lead to higher magnitudes of porosity as compared to hypoeutectic Al-Si alloys. As a result, hypoeutectic alloys are generally preferred for production of complex castings like engine blocks.

The mechanical properties of hypoeutectic Al-Si alloys, like many other alloy systems, can be improved in several ways, including but not limited to: i) grain refinement (primary Al or eutectic Si), ii) precipitation of strengthening/hardening intermetallics by alloying and/or heat treatment, and iii) chemical modification of harmful intermetallics.

Elements such as phosphorus (P), Sr, sodium (Na) and barium (Ba) may be added to refine the alloy's microstructure by suppressing the growth of specific phases or altering the structure of the phase into a more coherent morphology. Sr is the most common modifier because it is less reactive as compared to the other elements [83]. For example, the addition of Sr to Al-Si alloys has been shown to refine the eutectic Si particles from coarse flakes to a more fine and fibrous structure

which improves the alloy's strength [84], [85], [78], [86]. In addition to chemical refinement, the solutionizing stage of a T6 heat treatment has been shown to fragment and spheroidize (see Figure 2.2-7) the Si particles in 0.5-4 hrs, depending on the state of the Al-Si alloy (i.e., modified or not) and the solutionizing temperature [78], [86], [87]. The semi-spherical shape of the modified Si particles reduces stress concentrations and improves the alloy's YS and UTS [88]. A study performed by R. Chen et al. investigated the effects of quenching as well as a T6 heat treatment on the mechanical properties an Al-7Si-Mg cast alloy [86]. They observed that a 2-hour solution treatment at 535 °C, followed by quenching, improved the YS, UTS, and elongation as compared to the as-cast state. These improvements are likely associated with the homogenization of the solute atoms, an alteration to the eutectic Si morphology, and the dissolution of weakening intermetallics. After artificial aging and after completing the T6 temper, a significant increase in both the YS and UTS was observed; however, a reduction in the elongation was also noted. The increase in strength was likely attributed to the precipitation of nano-sized phases, and the decrease in elongation may be associated to further spheroidization of eutectic Si [88].

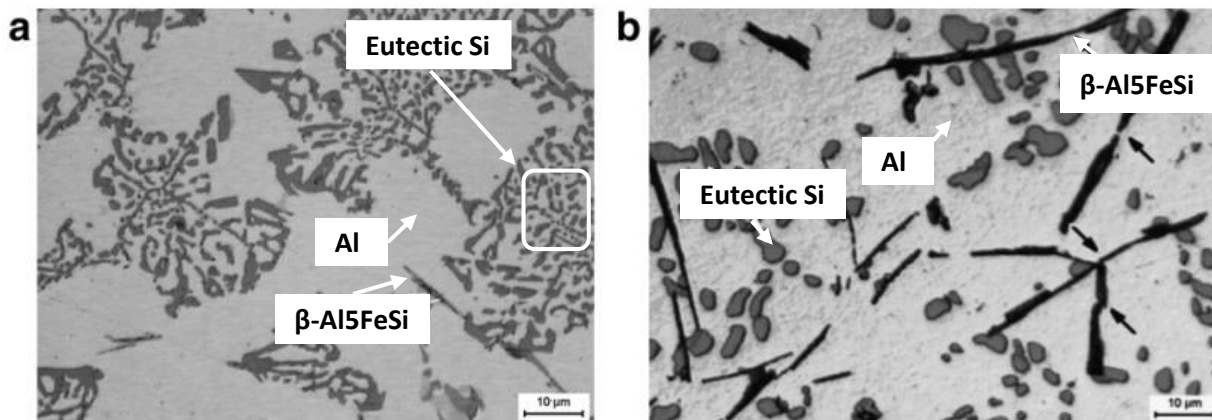


Figure 2.2-7. Microstructure of Al-7Si-Mg alloy in a) as-cast condition and b) T6 heat-treated condition. Note the spheroidization of eutectic silicon particles after heat treatment [78]

Typically, several additional elements such as Cu, Fe, Mg, Ni, molybdenum (Mo), vanadium (V), titanium (Ti), and zirconium (Zr) are present in Al-Si alloys; some are purposely added to increase the strength and/or hardness of the material and some are only present as impurities. There are several reasons why the solute element additions and formation of intermetallics improve the mechanical properties of the Al-Si alloys; however, the most effective benefits occur when the precipitate is fine and uniformly distributed throughout the microstructure, the solute element has

a low diffusivity and solubility with the aluminum matrix, and the precipitate has a low lattice mismatch with the matrix [89]. Some of the intermetallics that enhance the mechanical properties of Al-Si alloys include: Mg_2Si , $Al_5Cu_2Mg_8Si_6$, $\delta-Al_3(CuNi)$ [90], $(AlSi)_x(ZrVTi)$, and $Al_{22}(Fe_{6-8}Mo)Si_4$ [91]. Magnesium silicide, Mg_2Si , is one of the most common precipitation hardeners in hypoeutectic Al-Si alloys. During solution heat treatment (SHT) of Al-Si alloys containing Mg, the Mg forms a supersaturated solid solution with Si. Following SHT, quenching results in the precipitation of Mg_xSi_y particles [80]. Then, natural or artificial aging around 165-200 °C [92] will transform the Mg_xSi_y particles into Mg_2Si . The high hardness ($4.5 \times 10^9 \text{ Nm}^{-2}$), low coefficient of thermal expansion ($7.5 \times 10^{-6} \text{ }^\circ\text{C}^{-1}$), low density (1.99 kgm^{-3}), and high modulus of elasticity (120 GPa) of Mg_2Si [93], [94], are some of the reasons which make the Mg_2Si phase highly desirable for certain powertrain alloys. However, the poor thermal stability of Mg_2Si results in coarsening and dissolution of the precipitate at 170 °C [95], thereby eliminating a portion, if not all, of the original strengthening effects caused by the presence of the Mg_2Si intermetallic. It has been reported that the YS of hypoeutectic Al-Si alloys increases linearly with Mg concentrations up to about 0.4 to 0.6 wt.% (due to the precipitation of Mg_2Si); however, this magnitude of Mg content can result in the formation of a harmful Fe-bearing phase, specifically $\pi-Al_9FeSi_3Mg_5$ [96]–[99].

The natural presence of impurity elements, such as Fe, in Al-Si alloys poses a number of problems for the material's performance. The plate-like and needle-like morphology (see Figure 2.2-8) of specific Fe-bearing intermetallics (i.e., $\beta-Al_5FeSi$ (also reported as $Al_{4.5}FeSi$ or $Al_9Fe_2Si_2$) and $\pi-Al_9FeSi_3Mg_5$ (also reported as $Al_8FeSi_3Mg_6$) induces stress concentrations which can hinder the alloy's mechanical properties.

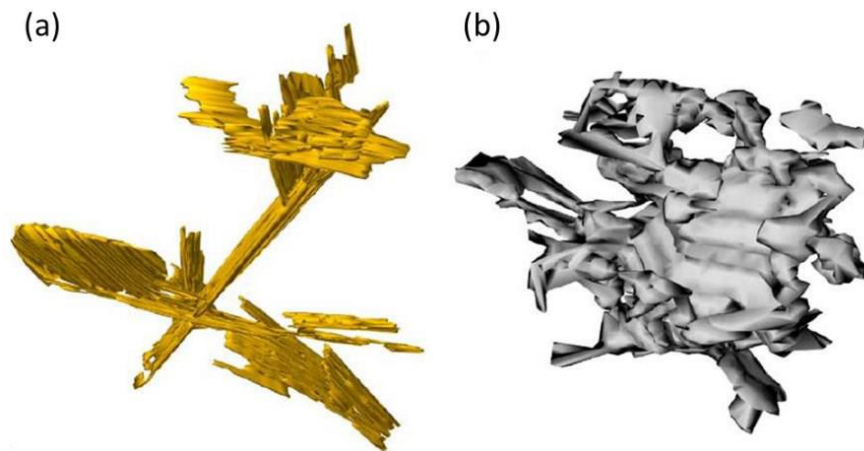


Figure 2.2-8. (a) Needle-like $\beta-Al_5FeSi$ and (b) Chinese script $\alpha-Al_{15}(Fe,Mn)_3Si_2$ [100]

Moreover, the high brittleness of β -Al₅FeSi and π -Al₉FeSi₃Mg₅ can result in particle cracking once subjected to an external load, thereby lowering the material's toughness. In addition, due to the low diffusivity of Fe in Al, the formation of π -Al₉FeMg₃Si₅ may occur at the expense of the Mg₂Si precipitate [86], [97]–[99], thereby eliminating the benefits of Mg₂Si. Thus, Fe concentrations should be kept at a minimum. However, this poses difficulties for manufacturers that utilize recycled alloys such as A319 and A390, which can have up to approximately 1 wt.% Fe [101]. The modification of Fe intermetallics is not easily attainable through application of heat treatments or modification of the solidification cooling rates. Q. Wang and C. Davidson report that during solution heat treatment at 540 °C, the π -Al₉FeMg₃Si₅ phase decomposes and releases Mg into solution; however, this occurs at a very slow rate and is, thus, not economically feasible for mass production [99]. Fortunately, manganese (Mn) may be used to chemically transform the harmful β -Al₅FeSi and π -Al₉FeMg₃Si₅ intermetallics to the more morphologically-favorable α -Al₁₅(Fe,Mn)₃Si₂ [101]–[103]. Further, the transformation of π -Al₉FeMg₃Si₅ to α -Al₁₅(Fe,Mn)₃Si₂ may restore some of the availability of Mg to form Mg₂Si, solution strengthening the Al matrix, and/or reduce the negative effects associated with the brittle β -Al₅FeSi and π -Al₉FeMg₃Si₅ crystals. According to Zahedi et al. [104], the transformation from β -Al₅FeSi to α -Al₁₅(Fe,Mn)₃Si₂ increases the alloy's tensile strength and elongation due to its improved morphology (Chinese script vs needle-like, see Figure 2.2-8) and its stronger bonding with the α -Al matrix. A better matrix-precipitate coherency reduces the susceptibility of crack formation at the particle-matrix interface and shifts the crack initiation from the Fe phase to the eutectic Si particles [104], [105]. It has been reported that a Mn:Fe ratio as low as 0.6:1 should sufficiently transform the β -Al₅FeSi into α -Al₁₅(Fe,Mn)₃Si₂. Further addition of Mn has a negligible effect on the alloy's mechanical properties [80], [104].

As the internal pressure and operating temperature of engine blocks continues to increase, the thermo-mechanically induced stress is approaching the temperature-sensitive yield strength of the currently used Al alloys. For example, Table 2.1-1 shows how the yield strength of a common powertrain alloy, A319, quickly diminishes as the temperature exceeds the current operational temperature for engine blocks (i.e., ~200-250 °C). This means that if the operating temperature of the earlier described V6 engine block with cast-in Fe liners was increased to 270 °C, the Al bridge would likely not be able to withstand the tensile residual stress that developed during the casting process.

Table 2.2-1. Temperature effect on yield strength (in MPa) of current powertrain alloys (A319 alloy, not conditioned), approximate values extracted from [106]

	F	T4	T7
25 °C	152	242	278
150 °C	155	190	250
180 °C	148	200	240
240 °C	145	190	190
270 °C	99	155	155
320 °C	75	76	99
370 °C	40	42	45
400 °C	25	25	25

F: as-fabricated

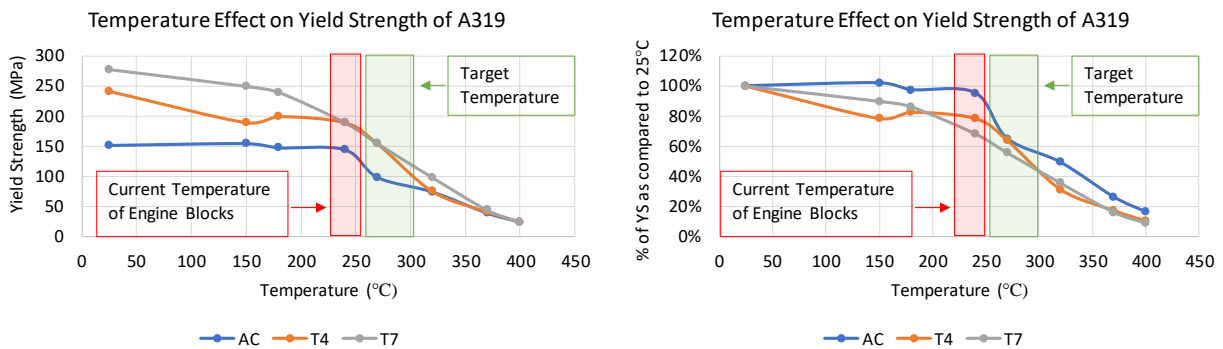


Figure 2.2-9. Temperature effects on yield strength of A319 alloy (approximate values extracted from [106])

It should be noted that the values shown in Table 2.1-1 represent the non-conditioned YS of the alloy, and thus, it is likely that the actual YS would be much lower than what is shown. For example, Jin et al. [107] reported that the yield strength, at 300 °C, of a T6 heat-treated A319 alloy was reduced by ~20-50% (depending on alloy modification) after conditioning the alloy at the testing temperature for 100 hours prior to initiating the elevated temperature tensile test. Subjecting the alloy to the testing temperature for 100-200 hours (i.e., conditioning) prior to initiating the tensile testing, allows for microstructural stabilization and provides a more realistic representation of the actual in-service performance of the alloy. A simplified representation of the effects of the conditioning process is shown in Figure 2.2-10. After a ~100-200-hour exposure to a constant

temperature, the strength of the alloy generally reaches a minimum, after which, no significant reductions are observed.

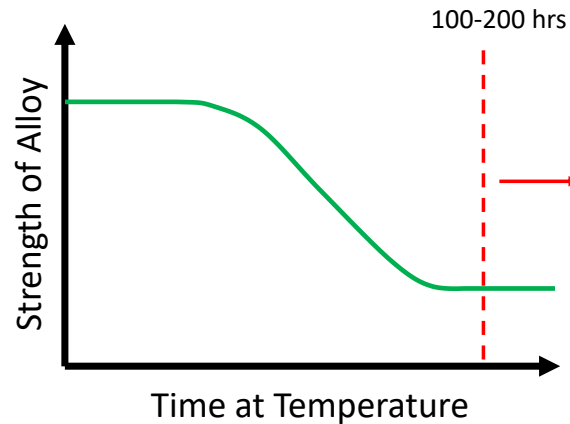


Figure 2.2-10. Effect of conditioning process on strength of alloy

In addition to the A319 alloy, comparing the results in [108], [109] suggests that the YS and UTS of a non-modified T6 A356 alloy decreases by approximately 25% (reaching ~170-180 MPa) when the temperature is increased to 235 °C. It should be noted that the alloys described [108] were only conditioned for 15 minutes prior to initiating the tensile tests. The reduction would likely be much greater if conditioned for an appropriate time (i.e., 100 to 200 hours).

The minimal published data on the conditioned elevated-temperature fitness-for-service (FFS) properties of the currently used hypoeutectic Al-Si alloys are inadequate for powertrain applications and the lack of data creates an unknown variable amongst the engineering and scientific community. Without well documented FFS properties of the currently used powertrain alloys, it is nearly impossible to understand how different heat treatments, alloy modification, and manufacturing processes will affect the alloy's performance. Without this understanding, the transportation industry will make slow progress toward improving the efficiency of its vehicles. Thus, it is necessary to determine the elevated temperature strength and creep resistance of the currently used powertrain alloys in the conditioned state. The performance of conventional powertrain alloys at elevated temperatures can then be used as a baseline for developing new powertrain alloys with improved temperature resistance.

2.3 Aluminum-Rare Earth Alloy System

A regained interest in the effects of having RE elements as alloying elements in Al alloys has led to the production of materials that boast superior high temperature strength and creep resistance as compared to more conventional Al alloys. This section begins by describing the economic feasibility of alloying Al alloys with RE elements. The following section describes the published microstructure and mechanical properties of the currently studied Al-RE alloys.

2.3.1 Economics

In 2018, it was estimated that USD 160 million worth of RE compounds and metals were imported by the United States, an increase from \$137 million in 2017. The world's total production of REs was estimated at 170,000 metric tons in 2018, up from 132,000 in 2017. The use of REs is primarily divided into catalysts (60%), ceramics and glass (15%), metallurgical applications (10%), polishing (10%), and other areas (5%). The total crustal abundance of REs is approximately 169 ppm, with Ce and La being the most prevalent (63 ppm and 31 ppm, respectively). This is more than the average crustal concentrations of Cu (28 ppm). Of all the REs consumed by the metallurgical sector, Ce represents the vast majority (5980 tonnes or 52.3 % CeO₂ in 2008) [110].

Rare earth additions to Al alloys have been a topic of interest amongst scientist and engineers since the beginning of the 20th century [13], [15], [111]–[113]. In the early years of RE research, the high cost associated with mining, processing, and refining prevented the REs from fully entering the industrial alloy and manufacturing market. However, with technological advancements as well as an increased demand for more expensive RE elements, such as Sc, Y, and terbium (Tb), the cost for Ce and La dramatically decreased (i.e., ~USD 2/kg of Ce oxide in 2019 [110]). The high availability and low cost of Ce and La during the last decade has allowed metallurgical engineers and scientist to revisit the effects of RE additions. A unique advantage of Ce and La is that the elements are often discarded during the refining of more valuable rare earths. Both the price and the supply-to-demand ratio differentiate Ce and La from other rare earths, supporting the elements' suitability as alloying agents. For example, according to the U.S. Geological Survey from 2018, the price for cerium oxide and lanthanum oxide (99.5% purity) was ~USD 2/kg as compared to ~USD 461/kg for Tb (99.5% purity) and ~USD 3500/kg for Sc (99.5% purity) [110].

Ce is found in a number of minerals (allanite, monazite, bastnasite, cerite and samarskite); however, monazite and bastnasite are currently the two most important sources of Ce. The extraction and purification process can be lengthy and typically includes mineral beneficiation, leaching, fractional crystallization, ion exchange, solvent extraction, precipitation from solution, and reduction to metals [114]. In 2017, taking into consideration the costs associated with post-processing of Ce oxide, the industrial cost for Ce metal was reported to be approximately USD 8-9/kg (USD 4-5/lb) [115]. Figure 2.3-1 displays the costs of Al-Ce alloys with respect to the price of Ce. Included in the chart are the prices of several common powertrain alloys, specifically A206, A319, and A356. At the time of the publication (2017), the price of Ce was ~USD 4/lb, suggesting that even at 12 wt.% Ce, the Al-12%Ce alloys remain as economically feasible as A319 and A356, and are, in fact, less expensive than Al-Cu alloys (A206, A224, and A201). Even with the relatively high processing costs of pure Ce metal, the use of Ce as an alloying element to Al alloys will remain economically feasible until the price of Ce increases above ~USD 20/kg (USD 10/lb) (see Figure 2.3-1). Fortunately, with the growing demand for more expensive RE elements, the price for Ce and La has declined year after year for the past five years.

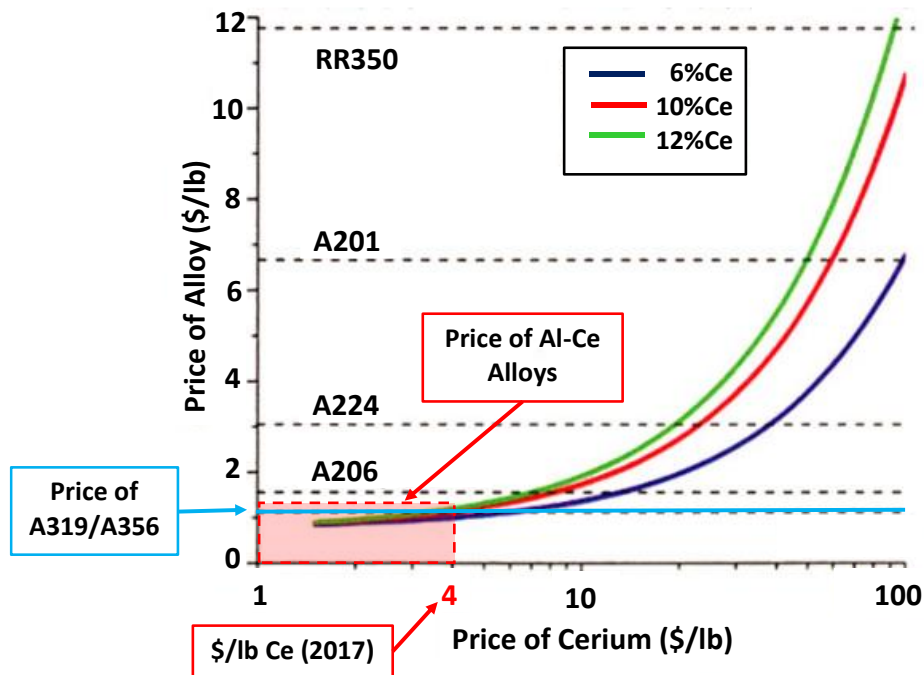


Figure 2.3-1. The as-alloyed cost of Al-Ce material with respect to the cost of current powertrain alloys, price for Ce was USD 4/lb in 2017 (adapted from D. Weiss [115])

Obtaining pure Ce metal is time and resource intensive; however, Ce is more readily available in a RE alloy called mischmetal (typically Ce- and La-dominant, with smaller concentrations of Nd and Pr). Z. Sims et al. [116] evaluated the efficacy of replacing Ce metal with RE mischmetal by comparing the mechanical properties, phase constituency, and thermal stability of Al alloyed with either 12wt.% Ce or 12 wt.% RE mischmetal. It was reported that the use of RE mischmetal led to a slight undercooling of the alloy, causing the formation a few primary $\text{Al}_{11}\text{Ce}_3$ crystals. The presence of the primary crystals led to a slight reduction in the alloy's ductility and UTS but a moderate increase in the YS. Despite the small differences between the two alloys, the use of RE mischmetal over Ce metal is a viable option that would diversify supply chains and reduce costs for aluminum alloy producers [115].

2.3.2 Microstructure and Mechanical Properties of the Al-RE system

The near-zero solubility of REs in Al (i.e., ~0.00012 to 0.005 wt.% Ce in Al at the eutectic temperature) as well as their low diffusion coefficients, results in the formation of several thermally stable eutectics in Al systems. In the low to moderate RE concentration (i.e. ~0-14 wt.% RE) of the binary Al-RE system, Al forms a very fine (i.e., as small as ~100 nm wide) eutectic lamellar structure with $\text{Al}_{11}\text{RE}_3$ [9]. However, when the concentration of REs exceeds the eutectic composition (~14 wt.% Ce in Al), large blocky primary $\text{Al}_{11}\text{Ce}_3$ crystals form [20]. Based on differential scanning calorimetry (DSC) measurements and crystallographic data, the proper stoichiometry of the $\text{Al}_{11}\text{Ce}_3$ compound is Al_4Ce ; however, researchers have favored $\text{Al}_{11}\text{Ce}_3$. Thus, this phase has been and may be written in either form [117]–[120]. $\beta\text{-Al}_{11}\text{Ce}_3$ (orthorhombic structure) has been observed to exist only at high temperatures [121], whereas $\alpha\text{-Al}_{11}\text{Ce}_3$ (tetragonal structure) is typically seen accompanied by $\alpha\text{-Al}$ below the eutectic temperature (see Figure 2.3-2).

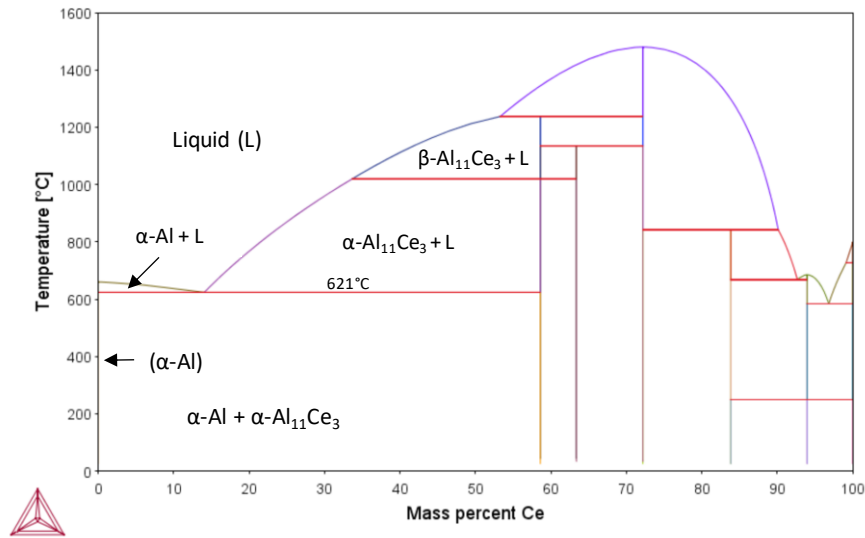


Figure 2.3-2. Calculated Al-Ce binary phase diagram (ThermoCalc™)

D. Weiss and Z. Sims et al. studied the effects that a 6 to 16 wt.% addition of Ce addition has on the YS and UTS of pure Al (i.e. YS of 34 MPa and UTS of 90 MPa) at room temperature [20], [122]. The results from the studies suggests that a 6 wt.% Ce addition had little effect on the YS and only slight UTS improvements were observed (i.e. YS of 30 MPa and UTS of 103 MPa). However, a near, but lower, eutectic wt.% addition (i.e. 12 wt.% Ce) increased the YS and UTS to ~57 and ~161 MPa, respectively. Further addition of Ce (i.e. 16 wt.% Ce) led to the formation of relatively large and block primary $\text{Al}_{11}\text{Ce}_3$ crystals which resulted in a slight decrease in the UTS to 144 MPa. The work also studied the effectiveness of a commercial T6 heat treatment. In general, the results indicate that the alloy's strength decreases after the T6 temper. For example, the UTS of the Al-12%Ce and Al-16%Ce alloy decreased by 31 and 26 MPa, respectively, after the T6 treatment. The strength of the lower Ce alloys were less affected by the T6 heat treatment. The T6 heat treatment of the hypoeutectic 6 and 12 wt.% Ce alloys resulted in a substantial increase in the elongation, reaching 33.5 and 26.5%, respectively. Although the T6 temper slightly increased the elongation of the hypereutectic Al-16%Ce alloy, the brittle and hard primary $\text{Al}_{11}\text{Ce}_3$ crystals restricted the elongation to only 3.5%. The results from this work indicate that a Ce content near the eutectic composition would result in the greatest ratio of strength and elongation. Moreover, due to the high melt fluidity and near-isothermal solidification, the Al-12%Ce alloy exhibited exceptional castability and hot tearing resistance. In fact, the castability of the Al-12%Ce alloy met or exceeded the castability of commercial Al-Si casting alloys [5]. The authors attribute the

exothermic reaction of Al-Ce intermetallics as one of the major factors contributing to the impressive castability.

Since Mg is typically used as a strengthening addition to conventional Al alloys, a 0.4 wt.% addition of Mg was introduced to the Al-12%Ce alloy [20], [122]. The Mg addition did not impair the alloy's castability and through forming a solid solution with the Al matrix and precipitation of an Al_3Mg_2 compound, the alloy's as-cast YS (i.e., increased from 57 to 79 MPa) and UTS (i.e., increased from 161 to 200 MPa) increased considerably. The authors postulated that the Mg addition may have suppressed the undercooling characteristics during solidification which forced a small amount of primary $\text{Al}_{11}\text{Ce}_3$ crystals to form. Solidification of primary crystals was observed in the DSC curve just before the beginning of eutectic solidification. The small Mg addition seems to have improved the alloy's heat treatability. Instead of the strength decreasing after a T6 heat treatment, as in the case of the Mg-free Al-12%Ce alloy, the T6 temper increased the room temperature UTS of the Al-12%Ce-0.4%Mg alloy from 200 MPa to 224 MPa. However, the authors state that due to small variations between test bars, the alloy's heat treatability is inconclusive.

In another study [115], the effects of elevated Mg additions (4-10 wt.%) were also investigated. It was observed that a 10 wt.% addition of Mg to an Al-8%Ce alloy (i.e. Al-8%Ce-10%Mg) resulted in the best room temperature YS (i.e., reaching 186 MPa) and UTS (i.e., reaching 227 MPa), as compared to Al-8%Ce-4%Mg and Al-8%Ce-7%Mg alloys. In fact, it was observed that the room temperature YS of Al-Ce alloys improves linearly with increasing Mg concentration, up to 10 wt.% (see Figure 2.3-3). It should be noted that Mg concentrations above 10 wt.% were not studied due to the expected formation of brittle primary $\text{Al}_{11}\text{Ce}_3$ crystals and excessive increase in the alloy's solidification range.

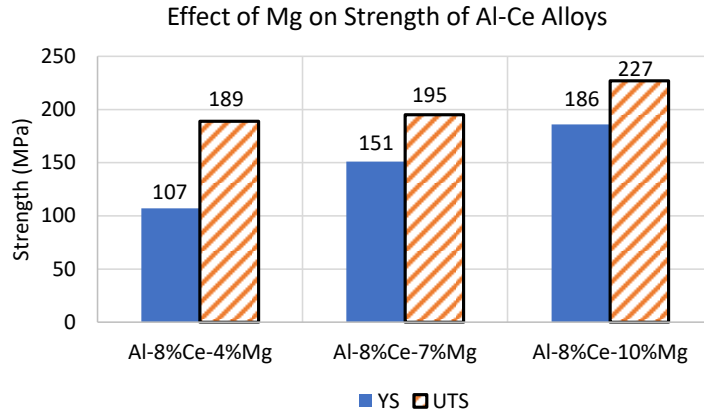


Figure 2.3-3. Effect of Mg on strength of Al-Ce alloys (data extracted from [115])

Although the room temperature properties of the Al-8%Ce-10%Mg alloy are slightly worse than the T6 Al-12%Ce-4%Si-0.4%Mg alloy, when the Al-8%Ce-10%Mg alloy was subjected to an elevated temperature tensile test at 260 °C, the alloy retained ~60-70% of its YS and UTS, reaching 130 and 137 MPa, respectively. Moreover, the Al-8%Ce-10%Mg did not require a costly heat treatment to achieve its impressive strength. It should be noted that none of the alloys were conditioned prior to the elevated temperature tensile tests, and thus, it is not known how the alloy will perform after an extended exposure at the elevated temperature. The authors report that the elevated Mg concentrations resulted in the formation of an AlMgCe or MgCe phase; however, they were still investigating the actual stoichiometry of the phase. Combined with the solid solution-strengthening effect of Mg in the Al matrix, the improved strength was attributed to the high density of AlMgCe/MgCe and Al-Mg precipitates as well as metastable Al-Mg clusters. Within the Al-Ce-Mg system, two ternary compounds (i.e., Al₄CeMg₄ and Al₂₁CeMg₈) have been reported [123]; however, the existence of two phases was not confirmed by the aforementioned work nor by subsequent studies [124]–[128]. Another ternary compound was identified in [127] as Al₂Mg_{0.8}Ce_{0.2} with the congruent melting point of 635 °C (reported as Al₁₃CeMg₆ in [124]); however, this phase was not observed in the microstructure of the Al-8%Ce-10%Mg alloy.

To improve the heat treatability of the Al-Ce-Mg system, Si was added to the Al-12%Ce-0.4%Mg alloy [122]. The addition of Si in Al alloys has two primary benefits: i) improving the castability and ii) when combined with Mg, the precipitation of hardening intermetallics such as Mg₂Si. Thus, a 4 wt.% addition of Si was introduced to an Al-12%Ce-0.4%Mg alloy. The as-cast microstructure of the Al-12%Ce-4%Si-0.4%Mg alloy comprises of FCC-Al, eutectic and primary Al₁₁Ce₃ and a

small volume fraction of an AlSiMg phase. In the as-cast condition, the Si addition had a negative effect on both the alloy's room-temperature UTS (i.e., decreased from 200 to 141 MPa) and YS (i.e., decreased from 79 to 75 MPa). However, after the T6 heat treatment, a new phase with a tetragonal structure was observed in the microstructure. The authors have labelled the new ternary phase as AlCeSi and suggest that during heat treatment, the ternary phase consumes the growth of eutectic and transforms the primary $\text{Al}_{11}\text{Ce}_3$ crystals into AlCeSi [122].

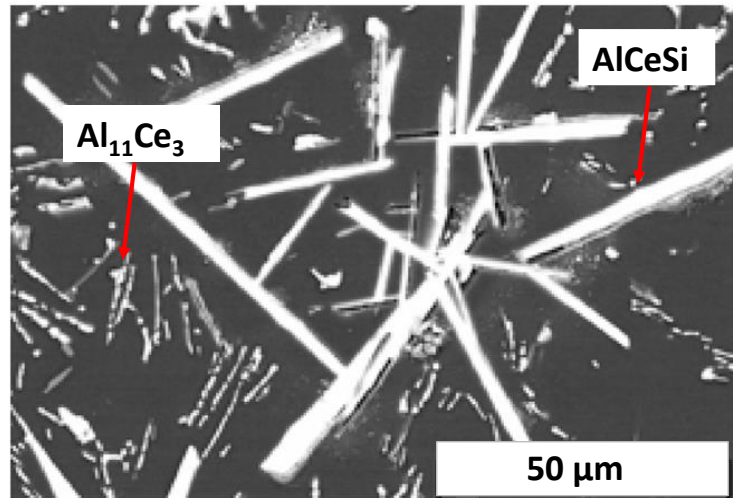


Figure 2.3-4. SEM micrographs of Al-12%Ce-4%Si-0.4%Mg alloy (adapted from [122])

In a following study, Z. Sims et al. [9] report that the AlCeSi phase is, in fact, the τ_1 phase with a stoichiometry of $\text{Ce}(\text{Si}_{1-x}\text{Al}_x)_2$, where $x = 0.1-0.9$. In the Al-Ce-Si system, two ternary phases, $\text{Ce}(\text{Si}_{1-x}\text{Al}_x)_2$ (τ_1) and AlCeSi_2 (τ_2), have been confirmed [9]. In addition, an Al_2CeSi_2 (τ_4) phase was also sporadically observed but is, apparently, metastable. The computed results in [129] were reviewed in [130], where five ternary compounds, namely $\text{Ce}(\text{Al}_x\text{Si}_{1-x})_2$, $\text{CeAl}_x\text{Si}_{2-x}$, CeAlSi_2 , $\text{Ce}_3\text{Al}_4\text{Si}_6$ and CeAl_2Si_2 , were all confirmed. The precipitation of the τ_1 phase, led to a significant improvement in the alloy's UTS (i.e., increasing from 141 MPa to 252 MPa) and YS (i.e., increasing from 75 to 128 MPa), as compared to the as-cast condition. At 200 °C, both the Al-12%Ce-0.4%Mg and Al-12%Ce-4%Si-0.4%Mg alloys retained a considerable amount of their tensile strength (i.e., both reaching 117 MPa), and, in fact, the YS of both alloys increased. The authors attribute the high degree of strength retention to the presence of the thermally stable τ_1 phase. Similar to $\text{Al}_{11}\text{Ce}_3$, the low solubility of Ce in Al and Si [131], the strong bonding of vacancies to Ce [132], the low enthalpy of formation (i.e., -67 kJ mol^{-1}), and the semi-coherent bonding with the Al matrix all contribute to the high thermal stability of the τ_1 phase [9]. In another

study, a relatively small amount of Ce (i.e., ~0.5 to 3.0 wt. %) was added to an Al alloy containing a higher concentration of Mg and Si (i.e., ~Al-12.5%Si-4%Mg) [133]. Even with the small amount of Ce, the addition led to the formation of the $\text{Al}_{11}\text{Ce}_3$ constituent in the Al matrix. It was observed that the microhardness of the as-cast alloy increased linearly with higher Ce contents, reaching a maximum of approximately 52 HV. The increase in hardness was attributed to the precipitation of the hard $\text{Al}_{11}\text{Ce}_3$ intermetallics. Moreover, clustering of Si and precipitation of fine $\text{Al}_{11}\text{Ce}_3$ phase during heat treatment at 200 °C led to a slight increase in microhardness, suggesting that the alloy has some response to age hardening. The results from these studies indicate that Si, in the presence of Mg in Al-Ce alloys, can improve the heat treatability of the Al-Ce system while also further improving the castability.

In an attempt to improve the mechanical properties of the existing commercial powertrain alloys (i.e., A319, A356, A380, and A390), researchers have investigated the microstructural refinement capabilities of low RE additions (i.e., ~0.1-2 wt.%). The common features of microstructure refinement includes grain-size reductions of α -Al grain, primary Si in hypereutectic Al-Si alloys, eutectics, as well as morphological changes to the intermetallics [134]. Similar to the effect of adding Sr to Al-Si alloys, an addition of more than 1.5 wt.% of La was reported to modify the morphology of the Al-Si eutectic structure in an A356 (~Al-7%Si-0.35%Mg) alloy [135]. In contrast, the addition of 0-1.5 wt.% of Ce to the A356 alloy resulted in an enlargement of the Si particles. The study also noted that Ce and La have an affinity to react with Sr, resulting in a notable decrease in the effectiveness of Sr. The authors postulated that although a 1.5 wt.% or greater addition of La to the A356 will result in Si refinement, the elevated concentration of La will lead to the precipitation of insoluble intermetallics which may be harmful to the alloy's performance. This claim, however, was not supported by any mechanical testing, and the benefits associated with the high thermal stability of the insoluble intermetallics was not discussed.

In another study, it was found that a 3 wt.% addition of La to an A390 (~Al-17.5%Si-4.8%Cu) alloy had little effect on the Si phases [136]. It is difficult to say if this observation contradicts the previous study or if the elevated concentration of Si in the A390 alloy is playing a role. Unlike the previous study, a 0.3 wt.% La and Ce addition to a hypereutectic Al-18%Si-4%Cu-0.5%Mg alloy was reported as a successful Si refiner [137]. The RE addition led to a reduction of the size of primary Si from 61 to 28 μm and modified its morphology from coarse blocks and irregular

polygons to fine flakes. As a result, the UTS increased by 9% and the elongation increased by 97%. Conversely, E. Elgallad et al. performed a comprehensive microstructural analysis to characterize the effects of 1 wt.% additions of La and Ce to a hypoeutectic Al-Si (A356, ~Al-7%Si-0.35%Mg) and an eutectic Al-Si (A413, ~Al-12%Si) alloy [138]. The primary observations from the study were that neither La nor Ce had a positive effect in refining eutectic Si, but instead, coarsened the Si particles. Furthermore, similar to [135], both Ce and La poisoned the Si-refining effects of Sr, particularly in the case of La. Ce and/or La additions to the A413 alloy resulted in a significant suppression of the eutectic temperature, leading to a 20 °C increase in the solidification range of the primary α -Al. Consequently, the solidification range of the A413 alloy was significantly increased, rendering it susceptible to porosity formation [139]. M. Mahmoud also indicated that increasing La and Ce content up to approximately 1.5 wt.% in an A356 alloy led to a substantial increase in shrinkage porosity [140].

For an Al-17%Si alloy containing ~1.6%Cu and 0.3%Mg, the optimum microstructure refinement occurred with a 1 wt.% Ce addition [141]. The Ce addition led to a simultaneous refinement of both the primary and the eutectic silicon particles and, consequently, increased the room temperature tensile strength from 170 to 195 MPa, as compared to the Ce-free Al-17%Si alloy. Further addition of Ce to 1.5 wt.% reduced the tensile strength from 195 to 186 MPa. Although the tensile strength of the alloy containing 1.5 wt.% Ce is still higher than the Ce-free alloy, the decreasing trend suggests that a Cu:Ce ratio between 1.5:1 and 2.0:1 may result in the optimal improvement. This claim is partially supported by the results presented in [142] which studied the effects of small Ce additions (i.e., 0.1 to 1.0 wt.%) to ~Al-12%Si-2%Cu-1%Fe-0.2%Mg alloys. The study reports that the higher the Ce concentration, up to 1 wt.%, the greater the refinement of Si. 1 wt.% of Ce results in a Cu:Ce ratio of approximately 2:1. However, similar to the observations in [143], the presence of Ce led to the formation of plate/needle-like intermetallic compounds which interrupted the full modification of Si.

The effectiveness of Ce refinement was examined for another hypereutectic Al-Si alloy (i.e., Al-20%Si) [144]. It was observed that varying additions of Ce (0.3, 0.5, 0.8 and 1.0 wt.%) led to a significant refinement of primary Si crystals. The shape of primary Si changed from a coarse polygonal morphology to a fine blocky shape with smooth edges. Smooth edges, as opposed to sharp corners or interfaces, minimizes the stress-concentrating effect of the particles which

favorably affects the mechanical properties. In addition, it was observed that the coarse plate-like/needle-like eutectic Si particles were also refined and their shape transformed to a more fibrous structure with discrete particles. As a result of the refinement, the UTS and elongation increased by 68.2 and 53.1%, respectively. For the same Al-20%Si alloy, higher Ce additions (i.e., 0.46 to 2.24 wt.%) led to the formation of fine cells that consisted of eutectic Si particles with Al_3Ce and $\text{CeAl}_{1.2}\text{Si}_{0.8}$ intermetallics within the Al matrix. This fine-celled structure resulted in an increase in the alloy's microhardness [145]. The results from this study contradict the previously mentioned observations [136] on the effects of Ce addition to hypereutectic Al-Si alloys. However, the Al-20%Si alloy contained only trace amounts of Cu as compared to the A390 alloy. This observation further supports the earlier claim that suggested that the ability for Ce to improve the mechanical properties of Al-Si alloys largely depends on the ratio of Cu to Ce.

In commercial Al alloys, varying amounts of unwanted impurity elements like Fe are typically present due to the use of recycled alloys. These impurities cause the formation of needle-like Fe-rich phases in hypoeutectic Al-Si alloys which have a negative impact on the mechanical properties of the alloy. For example, the needle-like $\beta\text{-Al}_5\text{FeSi}$ phase provides potential sites for crack initiation and, therefore, has a deleterious effect on elongation and tensile properties [146], [147]. There are currently a few well-known methods for modifying the Fe-bearing phases and for reducing their negative impacts (see sub section 2.2.2); however, manufacturers are constantly searching for alternative and potentially more effective solutions. Minor additions of Ce (0.1 to 0.9%) to an A380 cast alloy (Al-7.5%Si-3.5%Cu-3%Zn) were observed to effectively modify the eutectic Si. It was reported that a Ce concentration of 0.1-0.5% resulted in the greatest refinement and that further addition does not lead to additional improvements. These results contradict the observations reported in [135], [136], [148]. The discrepancy between the studies is not completely understood; however, may be associated with the difference in the casting process as well as the alloy composition. For example, the modified A356 alloy in [135] had a Cu and Zn concentration of less than 0.20 wt.% and 0.1 wt.%, respectively and was cast into a graphite mold preheated to 600 °C. Conversely, the modified A380 alloy contained a much higher Cu and Zn concentration (i.e., 3.5 and 3 wt.%, respectively) and was squeeze-cast in a mold preheated to 250 °C using an applied pressure of 100 MPa. It is unclear how the differences are affecting the Si refinement; however, it is likely that they are all contributing in some manner. In addition to Si modification, [134] reported that the Ce addition reduced the length of the needle-like $\beta\text{-Al}_5\text{FeSi}$ phases from 51

to 21 μm and modified the aspect ratio from 8.7 to 2.2. Moreover, the volume fraction $\beta\text{-Al}_5\text{FeSi}$ decreased from 3.85% to a minimum of 3.17% after a 0.7wt.% Ce addition. Although a 0.7wt.% Ce addition led to the largest reduction of the harmful $\beta\text{-Al}_5\text{FeSi}$ phase, the alloys containing more than 0.3wt.% of Ce suffered from the precipitation of another needle-like intermetallic, $\text{Al}_8\text{Cu}_4\text{Ce}$, which functioned as a crack initiator and reduced the elongation of the tested alloys. The results from this study suggest that there are optimum ratios of Cu:Ce and Fe:Ce. There is a balance between having enough Ce to refine the $\beta\text{-Al}_5\text{FeSi}$ phase, while also having a proper Cu:Ce ratio to avoid precipitation of harmful AlCuCe compounds. Another study [149] reported that a 0.25 wt.% Ce addition to an Al-4.6%Cu-0.4%Ag-1.3%Li-0.4%Mg-0.13%Zr alloy improved the recrystallization inhibition, and attributed that improvement to the large number of small $\text{Al}_8\text{Cu}_4\text{Ce}$ precipitates which formed along the grain boundaries. The relatively exotic alloying elements in this alloy may have prevented the growth of the needle-like $\text{Al}_8\text{Cu}_4\text{Ce}$ phase, suggesting that it is the size and morphology of $\text{Al}_8\text{Cu}_4\text{Ce}$ phase [134] that weakened the alloy, rather than the strength of the intermetallic, itself. As a result of the fine distribution of $\text{Al}_8\text{Cu}_4\text{Ce}$ precipitates, the fracture toughness was improved by more than 50%.

Kores et al. [143] studied the effects of a 1.035wt.% Ce addition to a near-eutectic composition Al-12%Si alloy. The study reported that a 1.035 wt.% Ce addition resulted in the transformation of the $\alpha\text{-Al}_{15}(\text{Fe},\text{Mn})_3\text{Si}_2$ phase from a Chinese script morphology into the more harmful needle-like $\beta\text{-Al}_5\text{FeSi}$ phase. The results from their DTA analysis revealed that the 1.035 wt.% Ce addition also led to the formation of the AlCeSi phase which masked the peak in the cooling curve that correlated to the $\beta\text{-Al}_5\text{FeSi}$ phase. Because of this, the authors suggest that AlCeSi and $\beta\text{-Al}_5\text{FeSi}$ phases solidify together at the end of solidification.

In an attempt to develop Al alloys with improved casting properties, such as hot tearing and fluidity, as compared to 2xx series commercial casting alloys such as A206, the Al-Cu-Ce system was investigated. An alloy's ease of forming a quality casting (i.e., castability), is directly influenced by melt fluidity, solidification shrinkage, reactivity between die and melt material, and alloy mechanical properties along with solidus and liquidus temperatures. Ce has been shown to reduce alloy sticking to a die [5], increase fluidity, and substantially reduce hot-tear sensitivity [150]. Ce is also sometimes used as a desludging agent to reduce the contents of gases and some impurities [151]. Three Al-Ce-Cu compositions have been of particular interest: (i) 20 wt.% Cu

(up to 12.5 wt.% Ce), (ii) 14 wt.% Cu (up to 10 wt.% Cu) and (iii) at a ratio Cu/Ce = 2:1 (up to 10 wt.% Ce and 20 wt.% Cu) [152], [153]. Hypoeutectic Al-Cu-Ce alloys with concentrations near the quasi-binary section Al–Al₈Cu₄Ce (i.e., Cu:Ce of 2:1), will have a microstructure of composite materials and a narrow solidification range, resulting in greatly improved casting properties as compared to conventional Al-Cu alloys [153]. However, due to the low Cu content in the hypoeutectic Al-Cu-Ce system, the effectiveness of heat treatments is unimpressive. Combined with the additional casting difficulties associated with the alloy's Cu concentration, the Al-Si-RE system shows much greater potential for production of complex castings that operate at elevated temperatures.

The role of REs in Al alloys, in terms of thermal stability, is sometimes compared with other elements such as Ti, V, Zr [154]–[156], Cr [157], [158], Mn, Mo [159] or Sc [160]. The high-temperature properties of Al alloys with transient metals or Sc, generally relies on the formation of coherent precipitates. However, the coherency of these precipitates is greatly reduced with increasing temperatures, which for Al₃Sc is about 300 °C [161]. An example of thermal stability of Al alloys with RE additions is described in [162], [163], where microhardness levels were maintained at 400 °C in Erbium (Er)-containing alloys. In addition, no phase structure transition of the Al₁₁Ce₃ phase occurred up to temperatures reaching 400 °C [164]. Although the Ce bearing intermetallics in Al-Ce alloys remain stable at temperatures close to the solidus, the large size and morphology of the precipitates currently do not provide strengthening levels comparable to typical Sc-containing alloys. Therefore, to optimize the Al-Ce system and obtain the greatest level of mechanical properties, additional research is needed to investigate ways to refine the size and morphology of the relatively large but very thermally stable Al-Ce intermetallics.

To date, the room temperature mechanical properties of Al-Ce casting alloys have been relatively well documented (see Table 2.3-1). The results suggest the following:

- 1) The Ce content should be kept below the eutectic composition
- 2) The addition of Mg to Al-Ce alloys greatly improves the strength at the expense of ductility
- 3) The addition of Si to Al-Ce-Mg alloys lowers the as-cast strength and ductility but improves the heat treatability of the alloy, leading to greater strengths in the heat-treated condition

- 4) The strength and elongation of an Al-20%Si alloy improves somewhat linearly with Ce content up to 1 wt.%
- 5) In the case of commercial alloys A356 and A413, a 1 wt.% Ce addition slightly reduces the room temperature strength and ductility
- 6) The room temperature and elevated temperature (250 °C) YS, UTS and elongation of a commercial B319 alloy improves with a 0.1 wt.% Ce addition

Table 2.3-1. List of published mechanical properties for Ce-containing Al casting alloys

Alloy (wt.%)	As-Cast			T6 Heat Treated			Ref.
	UTS (Mpa)	YS (MPa)	Elong. (%)	UTS (Mpa)	YS (MPa)	Elong. (%)	
Al-6Ce	103	30	25	103	33	33.5	[165]
Al-12Ce	163	58	13.5	132	48	26.5	[165]
Al-16Ce	144	68	2.5	118	78	3.5	[165]
Al-8Ce-4Mg	189	107	3.0	-	-	-	[165]
Al-8Ce-10Mg	227	186	1.0	-	-	-	[165]
Al-12Ce-0.4Mg	200	78	6.0	224	62	8.5	[122]
Al-12Ce-4Si-0.4Mg	141	75	2.0	252	128	8.5	[122]
Al-20Si-1Ce	154 ^a	-	7.5 ^a	-	-	-	[144]
Al-20Si	91 ^a	-	4.6 ^a	-	-	-	
A356-1Ce	185 ^a	105 ^a	3.8 ^a	265 ^a	240 ^a	1.0 ^a	[166]
A356	210 ^a	124 ^a	3.9 ^a	310 ^a	260 ^a	2.0 ^a	
A413-1Ce	220 ^a	128 ^a	2.3 ^a	265 ^a	180 ^a	2.1 ^a	[166]
A413	224	130 ^a	3.0 ^a	280 ^a	160 ^a	3.2 ^a	
B319-0.1Ce	234	165	1.25	-	-	-	[167]
B319-0.1Ce	149*	125*	5.9*	-	-	-	[167]

*At 250 °C, not conditioned

^a values are approximated from chart in referenced article

The somewhat contradicting effects of REs on the microstructure and mechanical properties of Ce-containing Al alloys currently presented in literature requires that a more comprehensive analysis is performed. In addition, in F. Czerwinski's recent comprehensive literature review of

the Al-Ce system [151], he states that “very little high temperature properties are available” for Al-Ce based alloys. Therefore, before Al-RE based alloys can be appropriately proposed as a potential replacement alloy for the next generation of powertrain components, it is required that the elevated-temperature fitness-for-service properties are determined, specifically in the conditioned state (described in section 2.2.1). A better understanding of the effects that varying RE content and additions of Mg/Si/Cu have on the microstructure and mechanical properties of Al and Al-RE based alloys, may allow manufacturers to produce the next generation of lightweight, temperature-resistant alloys, thereby enabling higher pressures and temperatures in internal combustion engines and enhancing the powertrain efficiency in the transportation industry.

2.4 Chapter Summary

This chapter described the working principles of combustion engines, issues that manufacturers are currently facing, the strengths and weaknesses of current powertrain alloys, and the economics and benefits associated with alloying Al alloys with RE elements. The subsequent chapters aim to answer the following gaps/questions in literature:

- 1) How can manufacturers further reduce the accumulation of residual stress in complex castings such as engine blocks?
- 2) Can the currently used Al powertrain alloys withstand the necessary increase in pressure and temperature required to improve the operating efficiency of internal combustion engines?
- 3) What effects do REs have on the elevated-temperature tensile and creep performance of Al alloys, particularly those containing Si, Mg and/or Cu?
- 4) Can RE-modified Al alloys be used for current and/or next generation powertrains that operate at 250 to 300 °C?

Chapter 3: Characterization of Residual Stress in I6 Diesel Engine Block and Evaluation of Fitness-for-Service of A319 Alloy

In the early development of combustion engines, cast iron alloys were the most frequently used materials due to their high-temperature strength, good castability, and their responsiveness to commercial heat treatments. However, the relatively high density of iron (Fe, density: 7.87 g/cm³) resulted in excessively heavy engines that prevented manufacturers from meeting strict government-mandated efficiency regulations (USA: increase 1.5%/year in vehicle fuel economy from 2021 to 2026, Canada: reduce GHG by 5%/year between 2022-2025, Europe: reduce GHG from 96 to 59 gCO₂/km by 2030). Thus, it was necessary for manufacturers to start developing and utilizing lighter materials such as aluminum (Al, density: 2.70 g/cm³) and/or magnesium (Mg, density: 1.74 g/cm³)-based alloys. Shifting toward using low-density materials for powertrain applications, such as engine blocks, can remove substantial mass from the system and can greatly improve the efficiency of the vehicle. A Massachusetts Institute of Technology study found that approximately 35% of the weight from automobiles can be removed without sacrificing any safety or performance [168]. This magnitude of mass removal could result in an efficiency increase by nearly 20%.

During the early implementation of lightweight materials, both Mg- and Al-based alloys were used for engine block production. Initially, the high tendency for Mg-based alloys to creep during elevated temperature loading (i.e., at ~125-150 °C [169]), resulted in inferior performance as compared to their stronger Al-based competitors. The poor elevated temperature properties of the conventional Mg-based alloys, such as AZ91D (~8.5 wt.% Al + 0.6 wt.% Zn + 0.25 wt.% Mn + Bal. Mg) and AM60B (~5.7 wt.% Al + 0.02 wt.% Zn + 0.25 wt.% Mn + Bal. Mg), is associated with the lack of thermal stability of their primary strengthening intermetallic, Mg₁₇Al₁₂/Al₁₄₀Mg₈₉ (~100 to 125 °C [9], [169]–[171]). These precipitates have a low melting point, are thermally unstable, and can accelerate grain boundary diffusion and microstructural instability near the grain boundaries [172], [173], preventing their use in modern engines which operate at temperatures far exceeding their current practical limit.

To improve the elevated temperature performance of Mg-based alloys, specifically targeting better creep resistance, rare earth elements [44] and Sr [174], [175] additions have given some of the best results. Specifically, AE44 (Mg-4Al-4Ce) and AJ62 (Mg-6Al-2Sr) raised the temperature at which

the alloy was able to perform adequately (i.e., 175-200 °C). The AE44 alloy was used in the General Motors corvette engine cradle and AJ62 was used in the BMW hybrid engine block. Both alloys showed improved creep resistance but M. Pekguleryuz [44] reports that the performance is still limited in AE44 due to the decomposition of the primary strengthening intermetallic, $Al_{11}Ce_3$, into the less desirable $Mg_{17}Al_{12}$. Although the creep resistance has improved to the point where Mg-based alloys may be used for certain powertrain applications, M. Pekguleryuz and M. Celikin indicate that the engine cradle has much lower performance requirements than engine blocks, and that the BMW hybrid engine block was designed with Al inserts which act as the primary load bearing component. Hence, a commercially available monolithic engine block has yet to be developed [46]. Since the operating temperatures of engine blocks is currently above 200 °C, Al-based alloys have taken over the market for engine block production.

Al alloys containing Si, Mg and/or Cu form several intermetallics with greatly improved thermal stability. For example, nearly all of the retained phase fraction of Al_2Cu and Al-Si eutectic is present at ~225 and 250 °C, respectively [9]. Moreover, it has been reported that the small addition of Ni can further improve the high-temperature properties of the alloy through formation of γ - Al_7Cu_4Ni or δ - Al_3CuNi intermetallics [176], [177]. Combined with great castability, a high strength to weight ratio, and a relatively low cost, it's no wonder why Al alloys are currently so widely used in many highly demanding powertrain applications, such as engine blocks, pistons and cylinder heads [178]–[181]. However, as time persists, Al alloys will continue to battle the rapidly increasing loads and temperatures that the automotive, marine, and aerospace industries are demanding (see chapter 2). Without continuous research on improving the mechanical properties and manufacturing techniques, the performance of the currently used Al alloys will soon reach their physical limit (i.e., temperature-sensitive strength and stability).

Leading manufacturers such as Nemak have begun introducing new methods for increasing the solidification cooling rates, minimizing gas entrapment during casting, and refining the microstructure of powertrain alloys, all focused on reducing the formation of residual stress and improving the mechanical properties of the alloy [35], [40], [180], [182]. Particular attention has been placed on the areas subjected to the highest magnitudes of thermo-mechanical loading, which are, therefore, the locations most prone to failure. These areas are primarily seen in cylinder bridges and crankcase girdles in engine blocks.

During in-service operation of engines, the combined contribution of thermo-mechanical stress (i.e., stress caused by the combustion process and rotating assembly) and the residual stress that accumulated during casting (see chapter 2), greatly suppresses the amount of useable strength of the alloy. In some cases, these combined stresses approach or surpass the alloy's room temperature yield strength. To add to this, the elevated and cyclic operating temperature of engines induces metallurgical changes and thermomechanical creep and fatigue which causes the material to weaken over time and may even lead to distortion and/or cracking of the components. Ultimately, this damage can lead to a reduction in the engine's performance and efficiency. To combat this, manufacturers have two options for maintaining/improving the performance and efficiency of engines: reducing the magnitude of residual stress, and/or improving the mechanical properties of the alloy.

This chapter aims to characterize, for the first time, the effects that the integration of Fe bore chills during casting, the incorporation of an inter-bridge cooling channel, and the replacement of the cast-in Fe liners with pressed-in Fe liners have on the microstructure, mechanical properties, and evolution of residual stress in the cylinder bridge of sand-cast Al engine blocks.

This chapter describes the analyses that were performed on five sand-cast Al diesel engine blocks in the as-cast (TSR), T4, and T7 conditions. Diesel engine blocks were selected for this study due to their higher potential for greater efficiencies as compared to gasoline-fueled engines (see section 2.1.1). The experiments executed in this chapter can broadly be separated into the following sections:

1. Phase Analysis and Metallography
 - a. Thermodynamic Simulation (equilibrium and non-equilibrium solidification)
 - b. Optical Microscopy
 - c. Scanning Electron Microscopy/Energy Dispersive X-ray Spectroscopy
 - d. X-ray Diffraction
2. Residual Stress Characterization
3. Fitness-for-Service Analysis
 - a. Tensile Test (room temperature, 250 °C and 300 °C)
 - b. Staircase Creep Test (250 °C and 300 °C)

The FFS results from this chapter are used to determine the baseline mechanical properties required by the alloys described in the alloy development chapter (i.e., Chapter 4 and 5).

3.1 Manufacturing Process

The diesel engine blocks examined in this research were produced at the NemaK Windsor Aluminum Plant in Windsor, Canada. The blocks were cast using a precision sand casting technique that is based on the Cosworth process. This casting process ensures quiescent mould metal filling, thereby improving component structural integrity by reducing the entrained oxide biofilms as well as oxide-induced shrinkage porosity in the castings. A schematic of the NemaK-Cosworth core package, with an illustration of the “rollover” process, is shown in Figure 3.1-1.

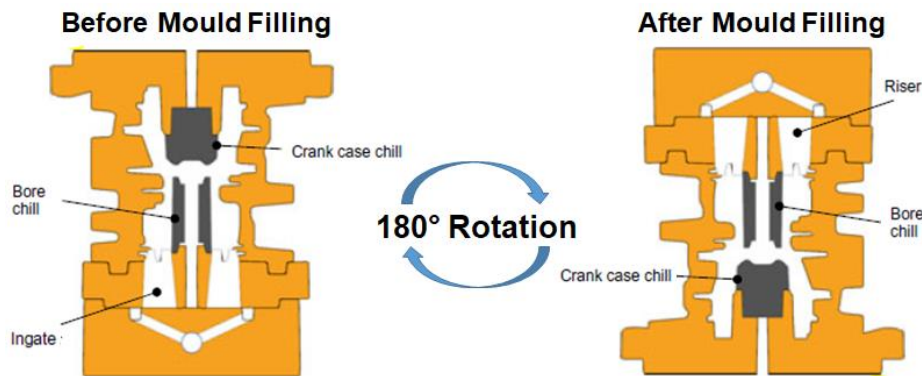


Figure 3.1-1. Schematic of NemaK-Cosworth mould design used to cast the engine blocks
(Adapted from Byczynski and MacKay [183])

The modified NemaK-Cosworth casting process, which is detailed by Byczynski and MacKay [183], utilizes a mechanical pump to enable complete uphill filling, eliminating the need for a pouring basin and downsprue, and ensuring precise control of the mould filling profile to mitigate the formation of casting defects. After completely filling the sand mould, the package is rotated 180° (“rollover”), while remaining pressurized by the pump to ensure effective feeding of shrinkage from the risers (which acted as the in-gates prior to the rollover). These steps are a crucial component in minimizing the volume fraction of porosity in the castings. In addition, the most recent NemaK-Cosworth process utilizes stainless iron-based chills inserted into the cylinder bores and the crankcase (bulkhead) to accelerate the cooling rates in the regions adjacent to the chills. The primary goal of the chills is to increase the local strength in these critical locations and reduce the shrinkage porosity defects in the thicker sections of the castings. To facilitate the removal of the chills, the cylinder walls were tapered which resulted in a gradual increase in the

thickness of the cylinder bridge from the top (12 mm thick) to the bottom (19 mm thick). In addition to facilitating the chill extraction, the thinner wall section at the top of the cylinder bridge is expected to result in a faster solidification rate at the top, and therefore, smaller grain sizes and improved mechanical properties at this critical location.

Preliminary tensile tests of the material near the head bolt columns (location adjacent to the cylinder bridge) suggests that the introduction of bore chills in the I6 block greatly improves the material's strength, as compared to the engine's predecessor. It was observed that the strength of the material at head bolt columns reached approximately 271 MPa [183] in a T7 heat-treated state. Comparing the strength of the chilled block (I6 engine) to the strength (i.e., 183 MPa [183]) of its predecessor (V6 engine), it is evident that the chills are strongly contributing to the alloy's strength. It should be noted that both the I6 and the V6 engine blocks were produced using the same A319 type alloy.

The I6 engine blocks described in this chapter were sand-cast using an A319 aluminum alloy with an approximate composition as indicated in Table 3.1-1. Following casting, the engine blocks were subjected to a thermal sand reclamation (TSR) treatment at 485 °C for approximately 5 hours (although the casting will only be at this temperature for ~1.5 hours during TSR) to ensure that the casting was effectively removed from the sand mould. The castings were then de-gated, followed by the mechanical removal of the bore and crankcase chills. The heat-treated blocks in this study underwent a solution heat treatment at 485 °C for 6 hours followed by a forced air quench (T4 condition) and artificial aging at 210 °C for 5.5 hours (T7 condition). The T7 temper was selected to improve the dimensional stability of the engine blocks during service operation.

Table 3.1-1. Composition of aluminum A319 alloy used for production of the cast engine blocks

Alloy	Si	Fe	Cu	Mn	Mg	Sn	Ti	Ni	Cr	Sr	Al
A319	8.5	0.59	2.76	0.44	0.33	0.08	0.13	0.07	0.04	0.01	Bal.
		max									

The high-performance I6 engine is expected to experience average peak operating temperatures in the range of ~190-225 °C, depending on location. In the TSR and T4 condition, this temperature would artificially age the A319 alloy quite rapidly and, while the property changes are not necessarily problematic, the dimensional growth is an issue for bearing clearances and bore distortion. Thus, to minimize issues related to dimensional stability, a T7 heat treatment was

applied. Following the T7 treatment, select blocks were machined to a production-ready state. The cylinder bore regions were then heated to approximately 150 °C and the gray Fe liners were press-fit into the cylinder bores.

The multistep production process of the diesel engine blocks was specifically designed with the target goal of refining the microstructure, homogenizing the mechanical properties, and reducing the magnitude of residual stress. Thus, the following questions must be answered:

1. What effect does the rapid cooling from the integrated bore chills have on the microstructure and mechanical properties of the cylinder bridge?
2. How do the bore chills affect the magnitude of residual stress in the engine block, as compared to engine blocks with cast-in liners, and does the stress change after removal of the chills?
3. Does the rapid quenching alter the magnitude of residual stress in the engine block?
4. How does the machining process and cylinder liner insertion affect the residual stress?

3.2 Thermodynamics of A319 Alloy (ThermoCalc™)

The following section utilizes a commercially available thermodynamic simulation software, ThermoCalc™, to determine the liquidus and solidus temperatures as well as the evolution of phases during equilibrium and non-equilibrium solidification (i.e., Scheil solidification). Utilizing the CALPHAD (CALculation of PHase Diagrams) method, ThermoCalc™ processes all available information (experimental and theoretical) on phase equilibria and thermochemical properties of an alloy system. A mathematical model, containing adjustable variables, is used to describe the thermodynamic properties of each of the phases. This is achieved by assessing the chemical and physical properties (i.e., Gibbs free energy, crystallography, type of bonding, order-disorder transitions, magnetic properties, etc.) of the system in the thermodynamic model. ThermoCalc's TCAL 7 database was used for this portion of the study.

The composition listed in Table 3.1-1 was entered into ThermoCalc's thermodynamic simulation software. The following analysis emphasizes the phases present at room temperature as well as any phase transformations that occur near the operating temperatures of engines (250-300 °C).

Figure 3.2-1 represents the equilibrium solidification of the A319 alloy. The results suggest, at room temperature, the microstructure of the alloy should consist of FCC-Al, eutectic Si, Al₂Cu,

$\text{Al}_9\text{Fe}_2\text{Si}_2$, $\text{Al}_5\text{Cu}_2\text{Mg}_8\text{Si}_6$, $\text{Al}_{15}(\text{Fe},\text{Mn})_3\text{Si}_2$, $\text{Al}_{31}\text{Mn}_6\text{Ni}_2$, Al_3Ti , $\text{Al}_{13}\text{Cr}_4\text{Si}_4$, and Mg_2Si . The phases are listed in order from highest to lowest concentration and the corresponding mass fractions are listed in Table 3.2-1. The Si, Al_2Cu , $\text{Al}_5\text{Cu}_2\text{Mg}_8\text{Si}_6$, and Mg_2Si phases are generally known to improve the mechanical properties of Al alloys at both room temperature and elevated temperatures. Under certain conditions and heat treatments, several of these phases may undergo metastable changes. However, the tracing of these changes falls outside the scope of the dissertation.

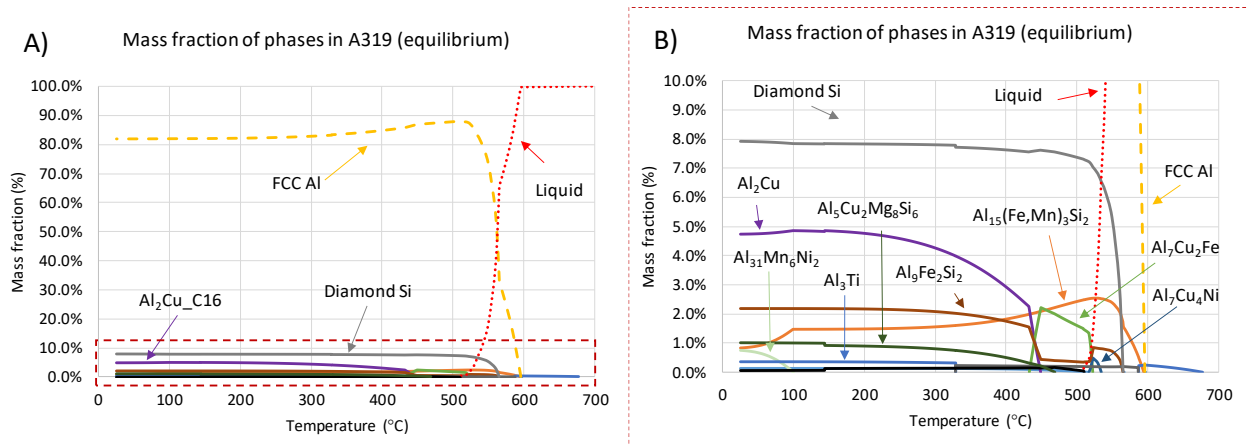


Figure 3.2-1. Mass fraction of phases in A319 alloy A) full solidification process, B) solidification process, emphasizing minority phases (equilibrium solidification)

Following equilibrium solidification, ThermoCalc suggests that the liquidus and solidus temperatures are 677 and 509 °C, respectively. However, above 600 °C, the mass fraction of solid phase is less than 0.5%, and is attributed to the initial formation of Al_3Ti . More important, is the solidification range of the primary phase, FCC Al. The nucleation and solidus temperature of Al were determined to be 596 and 509 °C, resulting in a solidification range of 87 °C. This relatively long solidification range could result in the formation of porosity [139]. The geometry of porosity is inconsistent; the pores contain many sharp edges where stress can concentrate and, consequently, lead to impaired mechanical properties.

It is not always accurate to compare the evolution of phases during solidification and cooling to the phase kinetics during heating; however, this method does provide some indication of what may be occurring to the phases as the temperature is increased.

Table 3.2-1. Mass fraction of phases in A319 alloy

Phase	Mass Fraction (%)	
	Equilibrium (25 °C)	Scheil (504 °C)
FCC Al	Bal.	Bal.
Diamond Si	7.92	6.81
Al ₂ Cu	4.73	2.73
Al ₉ Fe ₂ Si ₂	2.19	0.97
Al ₅ Cu ₂ Mg ₈ Si ₆	1.00	0.53
Al ₁₅ (Fe,Mn) ₃ Si ₂	0.83	2.34
Al ₃₁ Mn ₆ Ni ₂	0.74	-
Al ₃ Ti	0.35	0.24
Al ₁₃ Cr ₄ Si ₄	0.13	-
Mg ₂ Si	0.06	-
Al ₇ Cu ₂ Fe (metastable 523 to 420 °C)	0 (2.22)	0.02
Al ₇ Cu ₄ Ni (metastable 535 to 517 °C)	0 (0.49)	0.43
AlSi ₃ Ti ₂ (metastable 587 to 329 °C)	0 (0.24)	-

The non-equilibrium solidification chart of the A319 alloy is shown below in Figure 3.2-2, and the corresponding mass fractions of each phase at the solidus temperature are shown above in Table 3.2-1. No major differences were observed for the liquidus, solidus or solidification range of FCC Al and Si. However, due to the assumptions associated with the Scheil model, a higher mass fraction of the Al₇Cu₄Ni phase was observed at the end of solidification. This phase is known to have one of the best thermal stabilities of AlCuNi intermetallics, falling just behind Al₃CuNi [176]. The Scheil model also indicates that the mass fraction of Al₁₅(Fe,Mn)₃Si₂ should greatly increase while the more harmful Al₉Fe₂Si₂ (more commonly described as Al₅FeSi) should decrease. The Chinese script or polygonal morphology of the Al₁₅(Fe,Mn)₃Si₂ phase is known to lower the energy

at the matrix-precipitate interface as well as reducing stress concentrations, as compared to the high-aspect ratio needle-like morphology of $\text{Al}_9\text{Fe}_2\text{Si}_2$. As a result, this transformation commonly leads to improved mechanical properties.

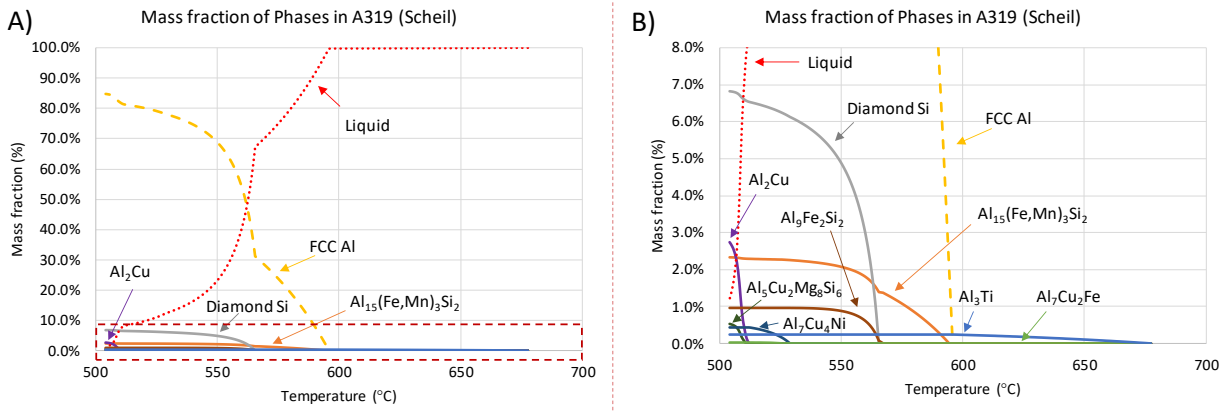


Figure 3.2-2. Mass fraction of phases in A319 alloy A) full solidification process, B) solidification process, emphasizing minority phases (non-equilibrium solidification)

3.3 Metallography

This section provides a microstructural analysis of various locations of interest in the I6 engine blocks. To evaluate the effects of the tapered cylinder wall (12 mm at the top and 19 mm at the bottom), four samples were extracted from the Top (~6 mm below head deck), Upper Middle (~50 mm from head deck), Lower Middle (~100 mm from head deck) and the Bottom (~150 mm from head deck) sections of the cylinder bridge. To determine the effects that the chills have on the alloy's microstructure, an additional sample was taken from a non-chilled location (i.e., the starter bracket). Following the principles outlined in the ASTM standard E3 – 11 [184], each sample was mounted in fast-curing acrylic resin, sequentially ground with silicon-carbide paper (from 120 to 600 grit), and then polished with colloidal diamond suspension (from 9 μm to 1 μm). To further reveal the microstructure, each sample was electro-etched at 30 V in Barkers etchant (2.5 ml of fluoroboric acid in 200 ml of distilled water) for 15-20 seconds.

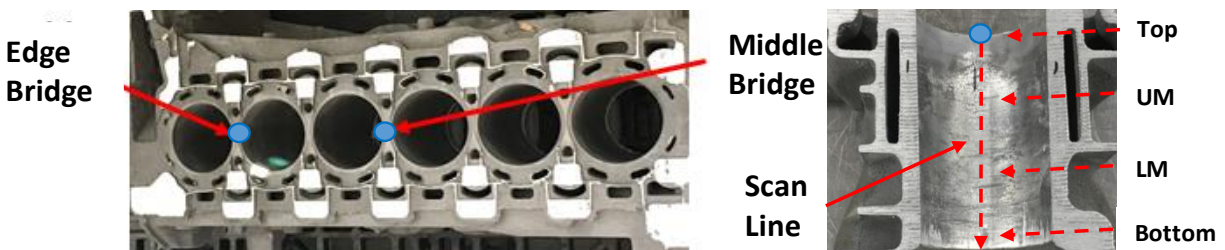


Figure 3.3-1. Location of metallurgical samples

The size of the primary phase dendrites are quantified by their secondary dendrite arm spacing (SDAS) [185]. The schematic view of the SDAS is shown in Figure 3.3-2. A Zeiss optical stereoscopic microscope (OSM) was used to measure the grain size and SDAS with a microscope accuracy of $\pm 0.1 \mu\text{m}$. The SDAS was measured to determine the cooling rate at each location during the casting process. The cooling rate (CR) can be calculated using Equation 11, given as [185]:

$$SDAS = 36.1(CR)^{-0.34} \quad (11)$$

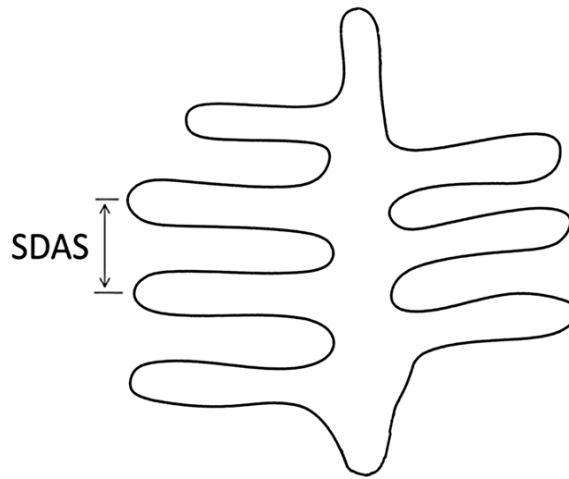


Figure 3.3-2. Schematic view of the dendritic structure and SDAS in Al-Si alloy [186]

An OSM and field emission gun-scanning electron microscope (FEG-SEM, Tescan Mira3 XMU) operating at an accelerating voltage of 20 kV were used to characterize the microstructure. Oxford Instruments Aztec data acquisition and processing software with an 80 mm² Oxford EDS detector were utilized to determine the composition analysis of the various phases. The morphology and EDS spectra for each phase were compared to literature and the inorganic crystal structure database (ICSD) [187] to determine the approximate stoichiometry of each phase.

3.3.1 As-Cast (TSR) Microstructure

The measured SDAS and calculated cooling rates for the as-cast (TSR) engine block are presented below in Table 3.3-1. Although there was significant variation in the wall thickness from the top of the cylinder bridge to the bottom (12 mm vs 19 mm, respectively), there was a relatively small change in the SDAS. This finding indicates that Nematik's modified casting method and unique use

of chills is an effective manufacturing process for producing a relatively uniform microstructure, likely leading to more consistent mechanical properties along the depth of the cylinder bridge.

Table 3.3-1. Summary of average SDAS and cooling rate for cylinder wall

Measurement	Top	Upper Middle	Lower Middle	Bottom	Starter Bracket*
SDAS ± ST. DEV (μm)	15.0 ± 1.4	18.1 ± 2.1	19.4 ± 2.2	21.4 ± 2.9	47.8 ± 5.8
Cooling Rate (°C/sec)	13.1 ± 3.1	7.6 ± 2.1	6.2 ± 1.7	4.6 ± 1.4	0.4 ± 0.1

*Note: the starter bracket is included for demonstration of the effects of the cooling rate and is not a critical location in the engine block

The lack of chilling applied to the starter bracket has clearly had a significant effect on the microstructure, leading to a SDAS that more than doubles all measurements taken from the cylinder bridge. It is expected that this large of a SDAS difference will result in a large reduction of the material's strength [188]. However, since the starter bracket is only exposed to ambient temperature loading (i.e., during engine start up), which is low in magnitude, the reduction of strength is not of concern.

SEM and EDXS analyses were performed on the as-cast samples to determine if any microstructural variations (i.e., size, shape and morphology of primary and secondary phases) are present throughout the engine block. Several SEM micrographs of the samples are shown below in Figure 3.3-3 A-F.

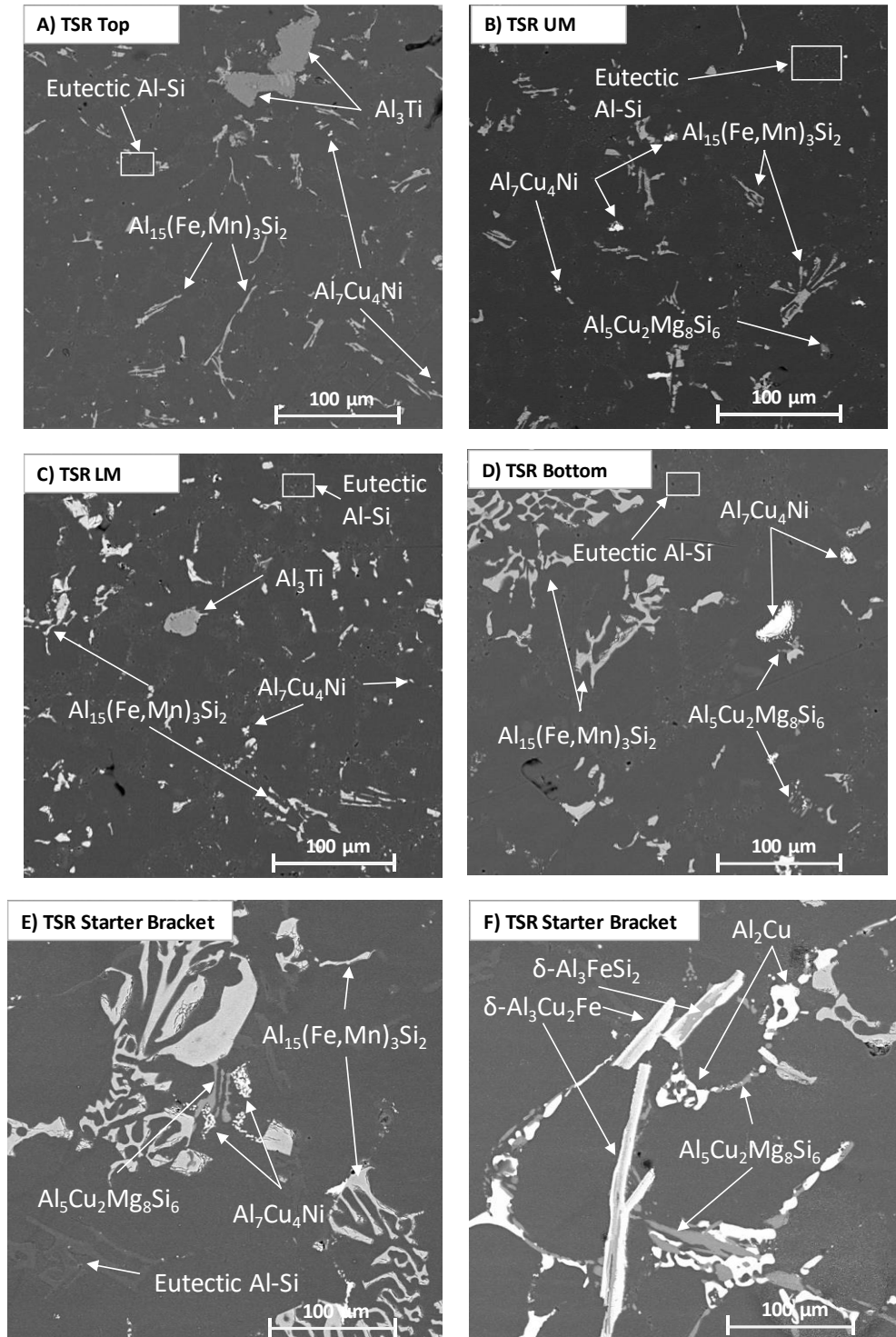


Figure 3.3-3. SEM micrographs of various locations in the TSR Al engine block at 1000x, A) Top, B) Upper Middle, C) Lower Middle, D) Bottom, E) Starter Case, F) Starter Case. Note: Micrographs were selected to display all phases and may not represent the general microstructure at each location

The results from the SEM/EDXS analyses at the top section of the cylinder wall revealed the presence of four phases surrounded by primary α -Al dendrites and semi-spherical eutectic Si particles. Due to the similar densities of Al and Si, there is minimal contrast between the two phases shown in the SEM micrographs (see Figure 3.3-3). Thus, to clearly differentiate the Al and Si phases, an optical micrograph is shown in Figure 3.3-4.

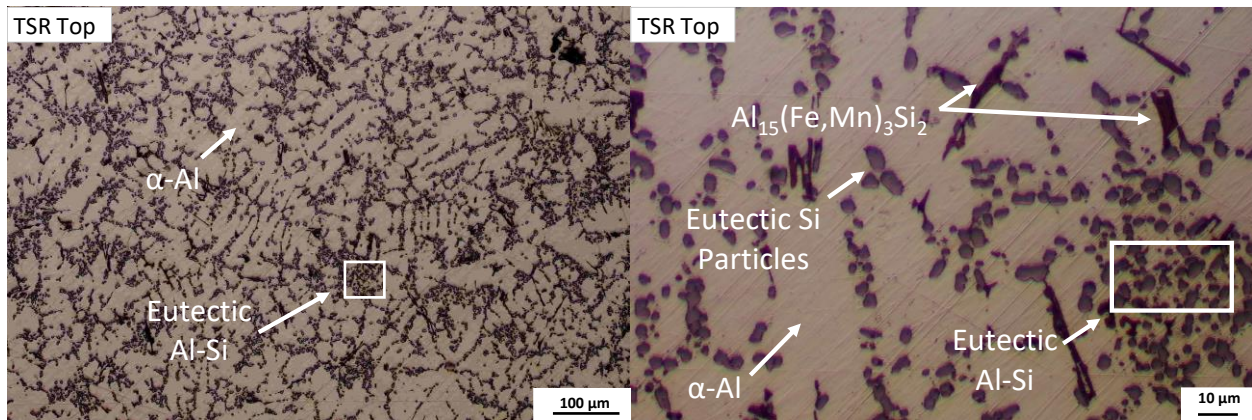


Figure 3.3-4. Optical micrographs of A319 alloy taken from the top of the cylinder bridge of the TSR I6 engine block, left) 100x, right) 500x

The semi-spherical morphology of the eutectic Si particles is generally observed after heat treatment of Al-Si alloys; however, it is likely that the relatively quick cooling rate has restricted the growth of the Si particles and minimized the presence of their less favorable plate-like and needle-like morphology [101], [189], [190]. The rectangular sharp-edged grey phases in Figure 3.3-3A were identified as α - $\text{Al}_{15}(\text{Fe},\text{Mn})_3\text{Si}_2$. It was observed that this phase was also present in a very low volume fraction in the more commonly reported Chinese script morphology. Similar to the eutectic Si particles, it is likely that the fast cooling rates have restricted the complete growth of the Chinese script. In addition, a small volume fraction globular phase was observed and identified as $\text{Al}_7\text{Cu}_4\text{Ni}/\text{Al}_3(\text{CuNi})$. As discussed in the Chapter 2, these AlCuNi phases are generally seen forming together; however, due to the high solubility of Cu in Al and Ni, it is difficult to differentiate between the two phases. Li et al. [176] suggests that the magnitude of Cu content in this alloy would preferentially form the γ - $\text{Al}_7\text{Cu}_4\text{Ni}$ phase; however, the composition of the phases is closer to that of $\text{Al}_3(\text{CuNi})$. Although $\text{Al}_3(\text{CuNi})$ provides the greatest mechanical property improvement, the $\text{Al}_7\text{Cu}_4\text{Ni}$ phase is not far behind and still exhibits much improved thermal stability as compared to the Ni-free Al_2Cu precipitate. The third phase observed in the Top section of the cylinder wall is a large grey, irregularly shaped phase which was identified as Al_3Ti .

This phase, which is likely only present due to the small addition of the Al-5Ti-1B grain refiner to the alloy, is relatively large but only present in a very small quantity (i.e. less than 0.2 vol.%).

The SEM/EDXS results for the Upper Middle section of the cylinder wall revealed a similar microstructure as compared to the Top section (see Figure 3.3-3B). A high volume fraction of primary α -Al dendrites and eutectic Si particles were found surrounding a moderate quantity of the $\text{Al}_{15}(\text{Fe},\text{Mn})_3\text{Si}_2$ phase and a small quantity of the $\text{Al}_7\text{Cu}_4\text{Ni}$ precipitate. It appears that the $\text{Al}_{15}(\text{Fe},\text{Mn})_3\text{Si}_2$ phase is present in similar quantities as compared to the Top section of the cylinder wall; however, a slight increase in the Chinese script morphology of this phase was observed. In addition, the $\text{Al}_7\text{Cu}_4\text{Ni}$ can be also seen in a slightly greater quantity and the composition now more closely matches that of $\text{Al}_7\text{Cu}_4\text{Ni}$ rather than $\text{Al}_3(\text{CuNi})$. A new irregularly-shaped grey phase was identified as $\text{Al}_5\text{Cu}_2\text{Mg}_8\text{Si}_6$ but is present in a very low volume fraction. Shaha et al. report that when Al alloys contain more than 0.5 wt.% of Cu and Mg, the commonly observed Mg_2Si phase will be transformed into the $\text{Al}_5\text{Cu}_2\text{Mg}_8\text{Si}_6$ intermetallic [191]. They indicate that the transformation of Mg_2Si to $\text{Al}_5\text{Cu}_2\text{Mg}_8\text{Si}_6$ improves the thermal stability of Al-Si-Mg alloys above 200 °C.

The analysis of the Lower Middle sample revealed a similar microstructure to the Top and Upper Middle sections of the cylinder wall (see Figure 3.3-3C). However, it appears that the shape of the α - $\text{Al}_{15}(\text{Fe},\text{Mn})_3\text{Si}_2$ phase has more predominantly formed into a Polyhedral and Chinese script morphology. This formation is believed to be attributed to the slightly slower cooling rate (6.2 vs. 13.1 and 7.6 °C/s) as compared to the cooling rate at the Top and Upper Middle section. A small volume fraction of the Al_3Ti phase that was observed in the Top section was also seen in the Lower Middle sample; however, the amount was insignificant. In addition, a slight increase in the size and quantity of the AlCuNi phase was seen throughout the sample. Similar to the Upper Middle section, the composition of this phase more closely matches the stoichiometry of $\text{Al}_7\text{Cu}_4\text{Ni}$.

The microstructure at the bottom of the cylinder bridge was observed to have no new phases as compared to the other three cylinder sections (see Figure 3.3-3D). However, it appears that the $\text{Al}_{15}(\text{Fe},\text{Mn})_3\text{Si}_2$ phase has nearly completely formed in only the Chinese script morphology. The gradual morphology change of this phase from the top to the bottom of the cylinder suggests that the faster cooling rate at the top (~13 °C/s at the top vs. ~5 °C/s at the bottom) may have prevented the Chinese script morphology from being completely formed, while at lower cooling rates, the

additional solidification time enabled the complete formation of this morphology. It was also observed that the size of this phase has slightly increased as compared to all other cylinder wall sections. In addition, it appears that the γ -Al₇Cu₄Ni phase has also grown slightly in size. Similar to the Upper Middle and Lower Middle section, the composition of this phase correlates well with the Al₇Cu₄Ni phase. The shift in composition of the AlCuNi phase from Al₃CuNi to Al₇Cu₄Ni suggests that the faster cooling rate at the top restricts the amount of dissolved Cu whereas the slower cooling towards the bottom of the cylinder facilitates the dissolution of copper into the compound. A similarly small volume fraction of the Al₅Cu₂Mg₈Si₆ phase was also observed.

The effects of the chills are evident when the microstructure of the cylinder bridge is compared to the non-chilled starter bracket. First, in addition to the large increase in the SDAS, the size of the intermetallics has also grown substantially. For example, the largest α -Al₁₅(Fe,Mn)₃Si₂ crystal in the cylinder bridge is approximately 100 μ m (average is closer to 10-20 μ m), whereas the average grain size in the starter bracket is ~100 μ m with some grains reaching upwards of 600-800 μ m. As mentioned in Chapter 2, the size and spacing of the dominant phase and secondary intermetallics have a strong effect on the material's mechanical properties. Typically, the smaller the grain size and the more homogeneously dispersed the intermetallics, the greater the mechanical properties. Thus, the presence of such large phases will surely hinder the material's performance in the tensile test (described in section 3.5). Not only has the size of the α -Al₁₅(Fe,Mn)₃Si₂ precipitate increased, but the phase is present in only the Chinese script morphology (see Figure 3.3-3E). This finding supports the earlier claim that the cooling rate is influencing the morphology of this phase. In addition to the large increase in the size of the intermetallics, the morphology of the eutectic Si has changed from fine semi-spheres to elongated rods (see Figure 3.3-3E). As described in Chapter 2, the spheroidization of the eutectic Si particles greatly improves the mechanical properties of the alloys by decreasing the interfacial energy between the Al matrix and Si particles and by minimizing stress concentrations. The EDXS results also revealed the presence of a bright white irregularly-shaped phase throughout the starter bracket sample. This phase was identified as Al₂Cu and was typically seen forming in the grain boundaries of α -Al₁₅(Fe,Mn)₃Si₂ and α -Al. As mentioned in Chapter 2, the Al₂Cu phase does strengthen Al-Cu alloys; however, as compared to the Ni-containing Al-Cu precipitates, Al₂Cu has a much lower thermal stability. In addition, the growth of Al₂Cu suppresses the amount of Cu available for forming the Ni containing Al-Cu intermetallics, further weakening the mechanical properties of the material at elevated temperatures. A new long grey

needle-like phase was also observed (i.e., δ -Al₃FeSi₂) and it appears that this phase predominantly forms in between another needle-like phase, δ -Al₃Cu₂Fe (see Figure 3.3-3F). The large-size, needle-like morphology, and non-homogenous structure (i.e., presence of voids) of the δ -Al₃FeSi₂ and δ -Al₃Cu₂Fe phases all act as stress concentrators and are deleterious to the alloy's mechanical properties. Similar to the cylinder bridge samples, the Al₇Cu₄Ni and Al₅Cu₂Mg₈Si₆ phases were also observed. The EDS results for the approximate composition of each phase is presented below in Table 3.3-2.

Table 3.3-2. Approximate composition of phases throughout TSR engine block (obtained with EDS)

Phase	Al (at.%)	Si (at.%)	Fe (at.%)	Mn (at.%)	Cu (at.%)	Ti (at.%)	Ni (at.%)	Mg (at.%)
Al ₁₅ (Fe,Mn) ₃ Si ₂	69 - 77	8-15	4-9	4 - 7	1.5 - 4	-	-	-
Al ₅ Cu ₂ Mg ₈ Si ₆	22-27	30-31	-	-	8-9	-	-	34-38
Al ₇ Cu ₄ Ni	63-73	-	-	-	20-32	-	7-12	-
Al ₇ Cu ₂ Fe	67-70	-	8-10	-	16-21	-	-	-
Al ₃ FeSi ₂	62-66	18-22	11-12	-	-	-	-	-
Al ₂ Cu	66-69	-	-	-	30-32	-	-	-
Al ₃ Ti	67-75	-	-	-	-	24-26	-	-

3.3.2 T4/T7 Heat Treated Microstructure

Due to the high consistency of the microstructure from the top to the bottom of the TSR A319 alloy (see section 3.3.1), only the microstructure at the top of the cylinder bridge of the T4 and T7 engine blocks will be presented in this section.

A SEM micrograph of the T4 heat-treated A319 alloy is shown below in Figure 3.3-6. Similar to the TSR A319 alloy, the microstructure primarily consisted of primary α -Al, eutectic Al-Si, and Al₁₅(Fe,Mn)₃Si₂. In similarly low quantities, the γ -Al₇Cu₄Ni and λ -Al₅Cu₂Mg₈Si₆ phases were also observed. Typically, a solution heat treatment results in a supersaturated Al matrix; in this case, it would be Cu in Al. However, since the solutionizing temperature that was used for the T4 heat treatment is relatively low (i.e., 485 °C) [192] and, in fact, it is the same temperature that was used for the thermal sand reclamation process, the amount of copper dissolved in the matrix has remained unchanged (i.e., ~1.4-1.5 at.% Cu). The low solutionizing temperature was selected to

minimize the accumulation of residual stress in the engine block [193]. Moreover, the composition, size and morphology of the $\text{Al}_{15}(\text{Fe},\text{Mn})_3\text{Si}_2$, $\text{Al}_7\text{Cu}_4\text{Ni}$, and $\text{Al}_5\text{Cu}_2\text{Mg}_8\text{Si}_6$ intermetallics have also remained the same. The insignificant change in the microstructure between the TSR and T4 engine blocks is likely attributed to the fast cooling rates achieved during solidification, the use of steel bore chills, and the relatively low solutionizing temperature which causes a rather sluggish dissolution of the Al-Cu intermetallics, particularly the thermally stable $\gamma\text{-Al}_7\text{Cu}_4\text{Ni}$ compound. This claim is supported by the findings presented by A. Lombardi [194], who indicated that minimal changes occur in an A319 alloy until the solutionizing temperature is increased to 500 °C.

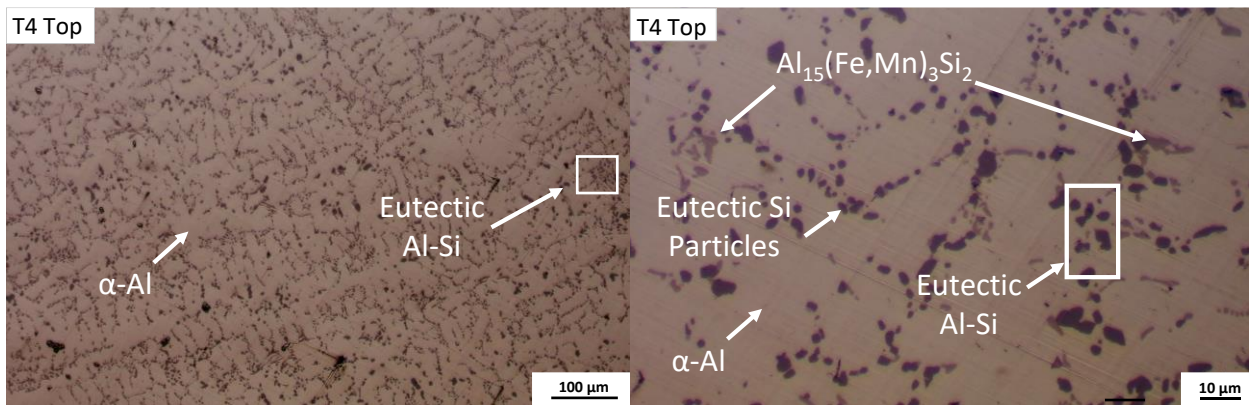


Figure 3.3-5. Optical micrographs of A319 alloy taken from the top of the cylinder bridge of T4 I6 engine block, left) 100x, right) 500x

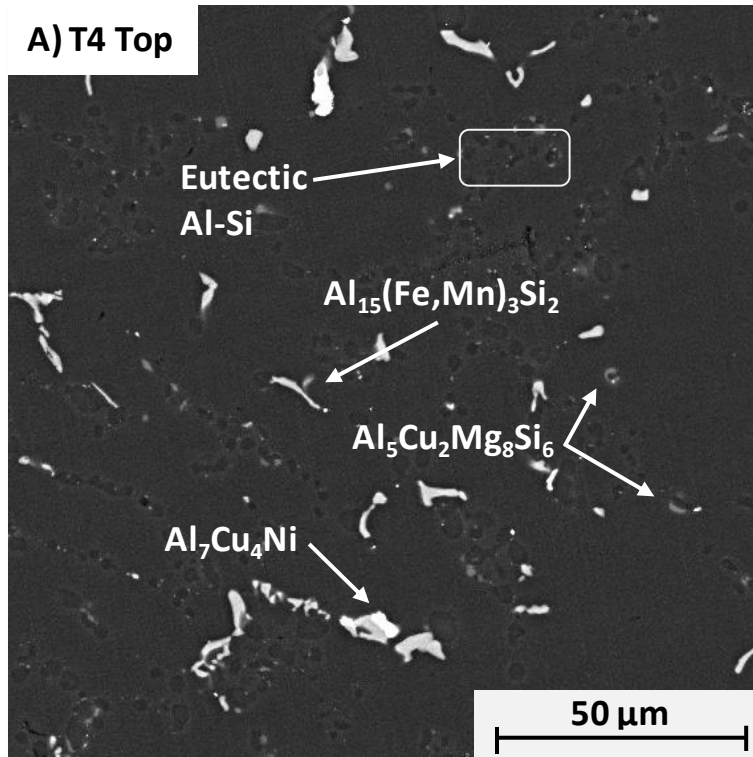


Figure 3.3-6. SEM micrograph of T4 A319 alloy (Top of I6 Block)

Figure 3.3-8 is a SEM micrograph of the T7 heat-treated A319 alloy, extracted from the top portion of the engine block's cylinder bridge. Due to the low solutionizing temperature, dissolution of the intermetallics was slow. Thus, the amount of solute (i.e., Mg and Cu) that is dissolved into the Al matrix was minimal. Consequently, this reduced the amount of available Mg and Cu for precipitation of hardening intermetallics such as γ -Al₇Cu₄Ni and λ -Al₅Cu₂Mg₈Si₆. This is one of the reasons why the artificial aging step of the T7 treatment did not lead to a noticeable increase in the volume fraction of the Cu-bearing intermetallics. However, Lee et al. indicate that aging can transform the λ phase into its metastable form, λ' , which is known to be one of the primary strengthening intermetallics in Al-Si-Cu-Mg alloys and can increase the alloy's hardness substantially [195]. One of the reasons for the increased hardness is due to the improved coherency with matrix of λ' as compared to the λ phase.

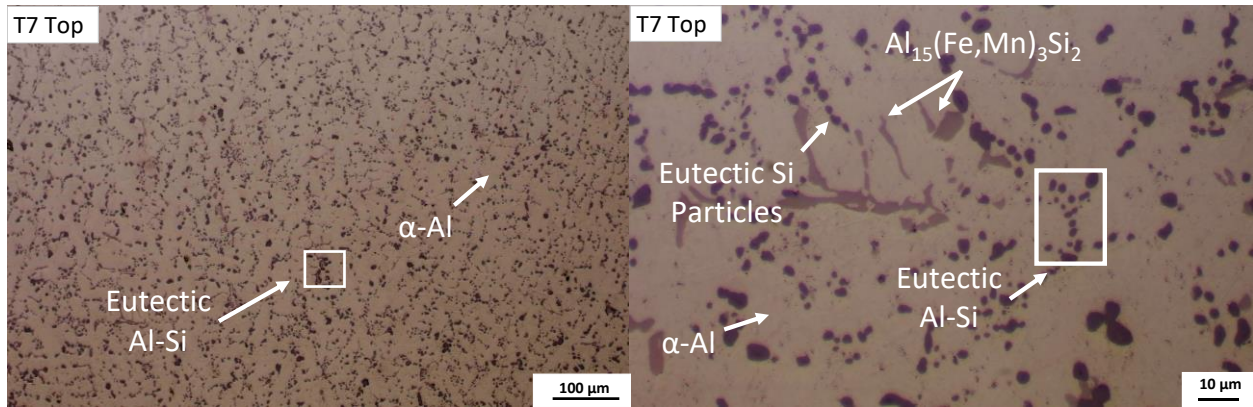


Figure 3.3-7. Optical micrographs of T7 A319 alloy taken from the top of the cylinder bridge of I6 engine block, left) 100x, right) 500x

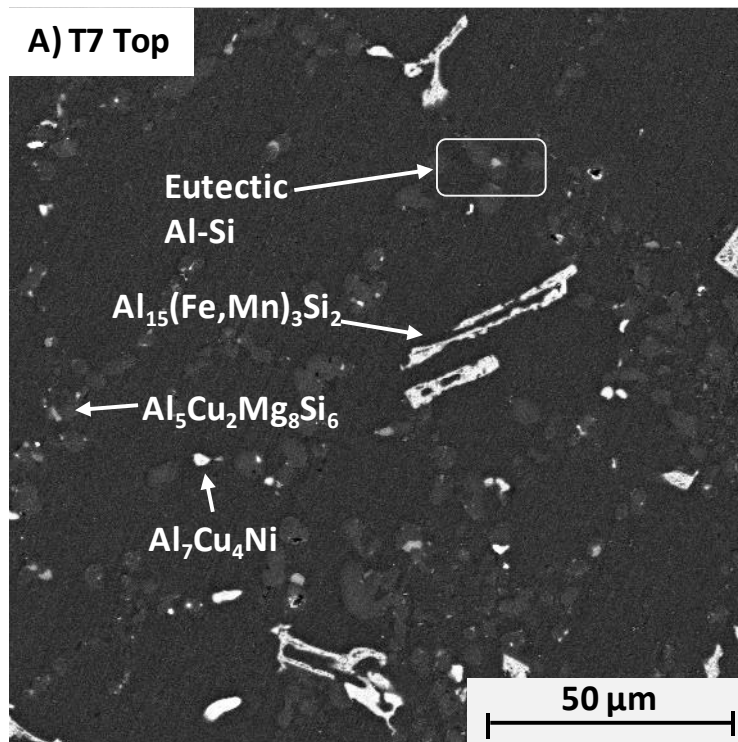


Figure 3.3-8. SEM micrograph of T7 A319 alloy (Top of I6 Block)

3.3.3 Summary of Microstructural Analysis

The microstructures of the A319 alloy following the TSR treatment, T4 and T7 heat treatments were analyzed using optical and scanning electron microscopy and energy-dispersive X-ray spectroscopy. The results reveal that the high solidification cooling rates, attributed to the integration of cylinder bore chills, led to a homogenous dispersion of fine intermetallics from the top to the bottom of the cylinder bridge. Moreover, the rapid chill effect led to semi-spherical Si

particles in all three conditions. Due to the fast solidification rates and low solutionizing temperature, the size, composition, and morphology of the intermetallics did not change significantly after the T4 and T7 heat treatment, as compared to the TSR condition (see Table 3.3-3).

Table 3.3-3. Summary of phases in I6 engine block (values shown as at.%)

	Phase	Shape	Al	Si	Fe	Mn	Cu	Ti	Mg	Ni	Other <1%
TSR Top	α -Al	Dendritic	Bal.	2.9± 0.2	1.5± 0.6	0.9± 0.4	1.5± 0.2	-	0.5± 0.5	-	Cr, Zn
	$\text{Al}_{15}(\text{Fe},\text{Mn})_3\text{Si}_2$	Blocky	Bal.	10.7± 2.3	7.2± 0.9	4.5± 0.7	2.8± 0.5	-	-	0.5± 0.2	Cr
	Al_3CuNi	Globular	Bal.	3.9± 1.8	0.8± 0.6	1.0± 1.0	13.8± 2.0	-	-	10.0± 1.9	Cr
	Al_3Ti	Irregular	Bal.	-	-	-	-	25.9± 0.1	-	-	-
TSR Bot	α -Al	Dendritic	Bal.	-	-	-	1.3± 0.2	-	-	1.0± 1.0	Zn
	$\text{Al}_{15}(\text{Fe},\text{Mn})_3\text{Si}_2$	Blocky + Chinese script	Bal.	12.4± 2.2	9.0± 0.8	6.4± 0.6	2.3± 0.5	-	-	0.4± 0.1	Cr
	$\text{Al}_7\text{Cu}_4\text{Ni}$	Globular	Bal.	0.96± 0.09	0.6± 0.5	0.8± 0.8	27.4± 1.6	-	-	8.4± 2.7	-
	$\text{Al}_5\text{Cu}_2\text{Mg}_8\text{Si}_6$	Irregular	Bal.	27.9± 3.1	-	-	7.6± 0.6	-	27.6± 3.1	0.3± 0.3	-
T4 Top	α -Al	Dendritic	Bal.	0.7± 0.1	-	0.1± 0.1	1.4± 0.0	0.1± 0	-	-	Zn, Ag
	$\text{Al}_{15}(\text{Fe},\text{Mn})_3\text{Si}_2$	Blocky	Bal.	-	-	-	-	-	-	-	-
	$\text{Al}_7\text{Cu}_4\text{Ni}/$ Al_3CuNi	Globular	Bal.	-	0.2± 0.2	-	21.0± 1.9	-	-	8.6± 0.3	-
	$\text{Al}_5\text{Cu}_2\text{Mg}_8\text{Si}_6$	Irregular	Bal.	27.1± 2.5	0.4± 0.4	0.7± 0.7	4.4± 1.1	0.1± 0.1	12.3± 5.1	0.1± 0.1	Cr

	Phase	Shape	Al	Si	Fe	Mn	Cu	Ti	Mg	Ni	Other <1%
T4 Bot	α -Al	Dendritic	Bal.								
	$\text{Al}_{15}(\text{Fe},\text{Mn})_3\text{Si}_2$	Blocky	Bal.								
	$\text{Al}_7\text{Cu}_4\text{Ni}/$ Al_3CuNi	Globular	Bal.								
	$\text{Al}_5\text{Cu}_2\text{Mg}_8\text{Si}_6$	Irregular	Bal.								
T7 Top	α -Al	Dendritic	Bal.	1.8 \pm 1.6	-	-	1.4 \pm 0.1	-	-	-	Zn
	$\text{Al}_{15}(\text{Fe},\text{Mn})_3\text{Si}_2$	Blocky	Bal.	11.1 \pm 2.6	6.1 \pm 1.4	4.4 \pm 1.0	3.2 \pm 0.8	-	-	0.5 \pm 0.2	Cr
	$\text{Al}_7\text{Cu}_4\text{Ni}/$ Al_3CuNi	Globular	Bal.	-	-	-	20.3 \pm 1.4	-	11.1 \pm 2.2	-	
	$\text{Al}_5\text{Cu}_2\text{Mg}_8\text{Si}_6$	Irregular	Bal.	40.5 \pm 5.5	-	-	4.9 \pm 1.2	-	16.8 \pm 5.8	-	
T7 Bot	α -Al	Dendritic	Bal.	0.8 \pm 0.8	-	-	1.4 \pm 0.1	-	-	-	Zn
	$\text{Al}_{15}(\text{Fe},\text{Mn})_3\text{Si}_2$	Blocky	Bal.	11.5 \pm 0.4	8.8 \pm 0.5	6.8 \pm 0.3	2.9 \pm 0.2	-	-	0.2 \pm 0.2	Zn, Cr, V
	$\text{Al}_7\text{Cu}_4\text{Ni}/$ Al_3CuNi	Globular	Bal.	0.7 \pm 1.2	0.2 \pm 0.2	0.1 \pm 0.2	19.8 \pm 4.5	-	0.6 \pm 1.4	7.1 \pm 1.6	
	$\text{Al}_5\text{Cu}_2\text{Mg}_8\text{Si}_6$	Irregular	Bal.								

The results presented in this chapter provide strong evidence of the effectiveness of the NemaK-Cosworth process as well as the use of cylinder bore chills at homogenizing the microstructure along the entire depth of the cylinder bridge. Although the microstructural refinement is expected to lead to consistent mechanical properties from the top to bottom of the cylinder bridge, the effects that the modified manufacturing process (i.e., casting process, use of press-fit liners as opposed to cast-in liners, and use of cylinder bore chills) has on the evolution of residual stress in the engine blocks is still unclear.

3.4 Residual Stress/Strain Characterization

Neutron diffraction is a non-destructive measurement tool for determining residual strains within a material. Neutrons are subatomic particles with no net electric charge, which allow for deep

penetration into metals (up to ~300 mm in Al). Nuclear reactors can provide a highly energized source of neutrons that can be collimated and directed toward the measurement location (i.e., gauge volume) within a specimen. The neutrons interact with the atoms arranged within the lattice crystal structure of a material and are diffracted, as illustrated in Figure 3.4-1.

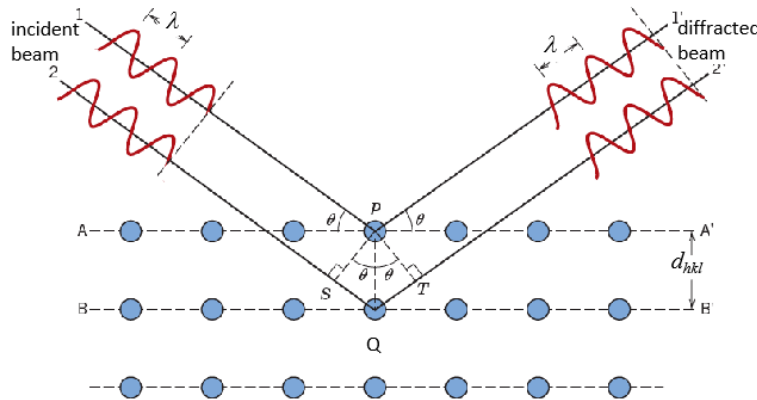


Figure 3.4-1. Planes of atoms' interaction with incident beam of particles used to describe Bragg's law by path length difference method [196]

For a Bragg's peak to be detected (constructive interference), the path length difference of two incident beams of neutrons must be an integer multiple of the wavelength, as described by Bragg's law given in Equation 12:

$$\lambda = 2d\sin\theta \quad (12)$$

where the scattering angle, 2θ , is the angle the neutrons are diffracted, λ , is wavelength of the incident neutron beam, and d , the spacing between the planes of adjacent atoms within the crystal structure of the material.

By measuring the stressed, (d_{hkl}) , and stress-free inter-planer spacing, $(d_{hkl,0})$, the lattice strain, ϵ_{hkl} , can be calculated, as described in Equation 13.

$$\epsilon_{hkl} = \frac{d_{hkl} - d_{hkl,0}}{d_{hkl,0}} \quad (13)$$

As can be seen from Equation 13, lattice strain is a dimensionless quantity. A negative strain corresponds to compression, while a positive strain represents tension. Although dimensionless, strain is often assigned units of microstrain, denoted by $\mu\epsilon$ and corresponds to strain* 10^{-6} . The acceptable uncertainty in engineering strain measurements by neutron diffraction is ~100 $\mu\epsilon$. The d_0 measurement is determined from a neutron scan of stress-free "matchstick" samples cut from

areas in such a way to relieve all of the residual stresses. The size of the stress-free matchstick samples are typically 2 x 2 x 20 mm (for stress free measurements in 2 directions) [8]; however, this is largely dependent on sample geometry and grain size. The premise of neutron diffraction is based on a high order of statistical accuracy, and thus, it is necessary to have a sufficiently large number of grains (on the order of 10000 grains) within the sample volume.

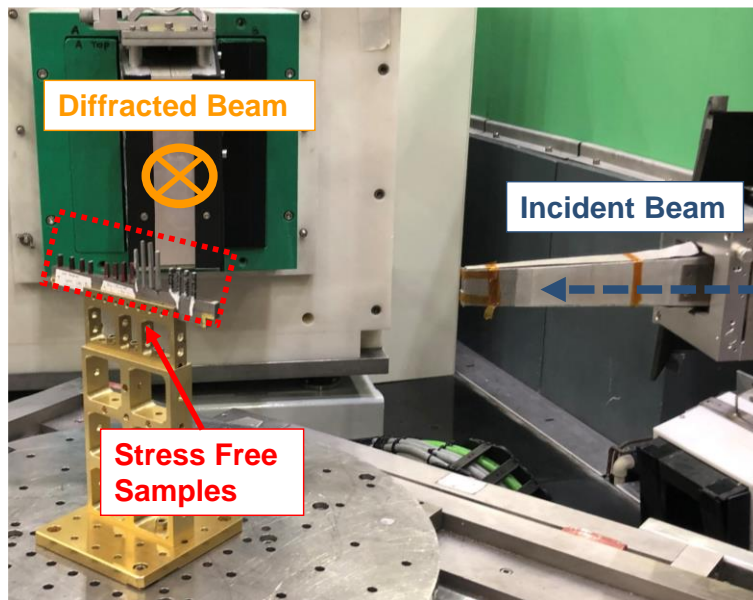


Figure 3.4-2. Measurement of stress-free ($d_{hkl,0}$) matchstick samples

The strain, as described by Equation 13, is measured in the specimen direction parallel to the bisector of the incident and diffracted neutron beams. This bisector is known as the scattering vector, Q , as shown in Figure 3.4-3.

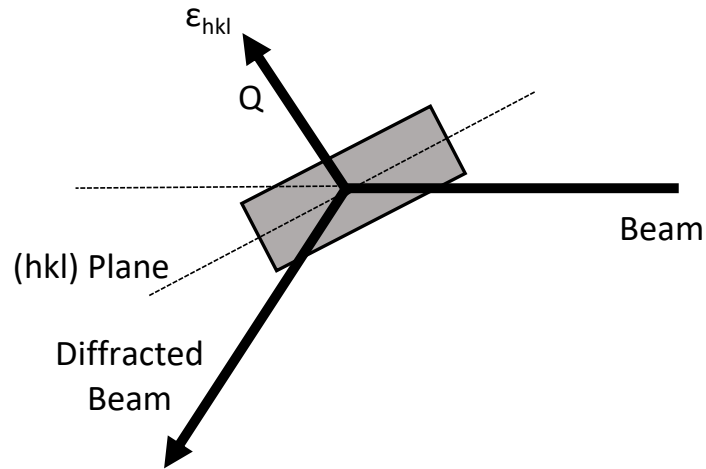


Figure 3.4-3. The component of strain, ϵ , parallel to the bisector of the incident and diffracted neutron beams

Therefore, only the grains whose (hkl) plane lies normal to the scattering vector will contribute to the diffraction signal. The strain calculated from a single diffraction measurement is a spatial sampling of only a subset of grains in the gauge volume whose (hkl) normal is parallel to the scattering vector [197]. Thus, by re-orienting the specimen, various components of strain can be determined (i.e., the radial (R), axial (A) and hoop (H) components for a cylindrically symmetric sample). Figure 3.4-4 and Figure 3.4-5 show the orientations that the engine blocks were placed in the neutron beam to obtain the axial, radial, and hoop components of strain in the cylinder bridge.

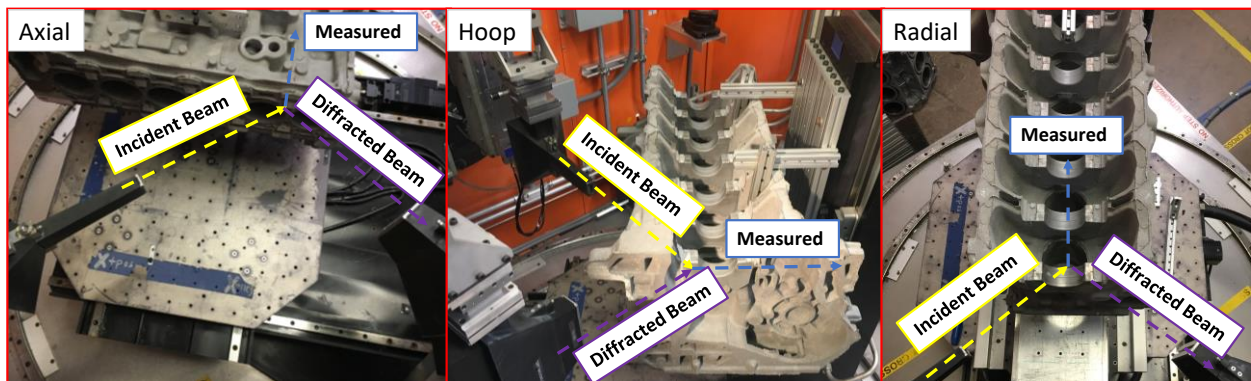


Figure 3.4-4. Orientation of casting for the axial, hoop, and radial components of strain

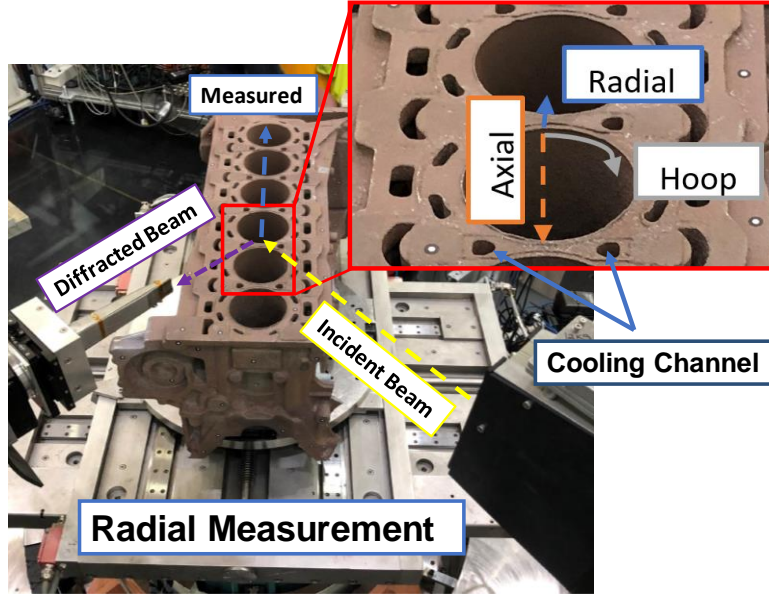


Figure 3.4-5. Radial measurement of strain in I6 engine block showing all three orientations of measurements

The three residual stress components, $\sigma_{R,H,A}$, for the radial, hoop, and axial directions are then calculated from the three strain components using the generalized Hooke's law given in Equation 14:

$$\sigma_{R,H,A} = \frac{E_{hkl}}{1+\nu_{hkl}} \left[\varepsilon_{R,H,A} + \frac{\nu_{hkl}}{1-2\nu_{hkl}} (\varepsilon_R + \varepsilon_H + \varepsilon_A) \right] \quad (14)$$

where E and ν are the materials hkl-specific modulus of elasticity and Poisson's ratio, respectively. Spatial alignment of the spectrometers was performed with the standard precision of 0.1 mm. Wavelength calibration was executed with accuracy of 0.0001 Å using ultra-high purity nickel powder with known diffraction angles and interplanar spacing for crystallographic planes. Instrument set-up and calibration were performed as outlined in ISO/TS procedures [198].

To determine the evolution of strain and stress throughout each step of Nematik's manufacturing process, residual stress mapping using neutron diffraction was performed on the cylinder bridge of five sand-cast, inline 6-cylinder Al engine blocks. The five engine blocks were in the following conditions: i) as-cast with stainless steel bore chills remaining in place (TSR + Chills), ii) as-cast with the stainless steel bore chills removed (TSR), iii) T4 heat-treated (T4), iv) T7 heat-treated (T7), and v) production-ready T7 engine block with pressed-in Fe liners and final machining (T7LM) (see Figure 3.4-6). Since the top of the cylinder bridge is exposed to the greatest level of thermomechanical loading during in-service operation, Nematik has incorporated an ~10 mm tall,

3 mm wide cooling channel in each of the cylinder bridges. Preliminary finite element simulations have shown that the inter-bridge cooling channel may greatly reduce the thermal load experienced by the cylinder bridge during engine operation [183]; however, the effect that the channel has on the residual stress has not been studied.

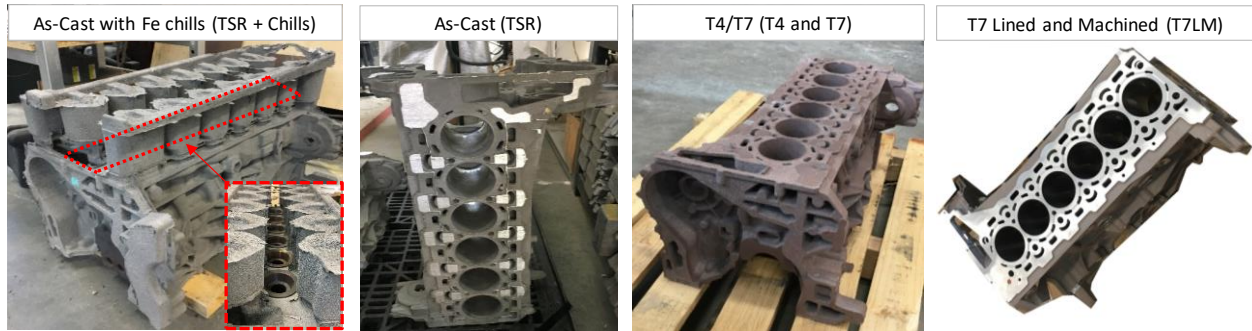


Figure 3.4-6. Engine block samples used for the completion of this study

The first experiment (TSR block) was performed at the Oak Ridge National Laboratories (ORNL) in Oak Ridge, USA and the second (TSR + Chills and T7 blocks) and third (T4 and T7LM blocks) were performed at the Australia Nuclear Science and Technology Organization (ANSTO) in Lucas Heights, Australia. The analysis was performed from the top ($z = 6$ mm) to bottom ($z = 146$ mm) of the middle bridge as well as a bridge nearest the edge of non-sectioned engine blocks (Figure 3.4-7).



Figure 3.4-7. Location of scan lines

Due to the high attenuation of the neutron beam in the blocks containing the stainless steel chills, some of the orientations of strain could not be fully measured in the TSR + Chills engine block. Consequently, it was necessary to remove some of the steel along the neutron beam path (see Figure 3.4-8). To ensure the residual stress in the Al cylinder bridge was not significantly affected after removing material from the chill, the outer and inner wall of the cylinder chill remained fully intact.

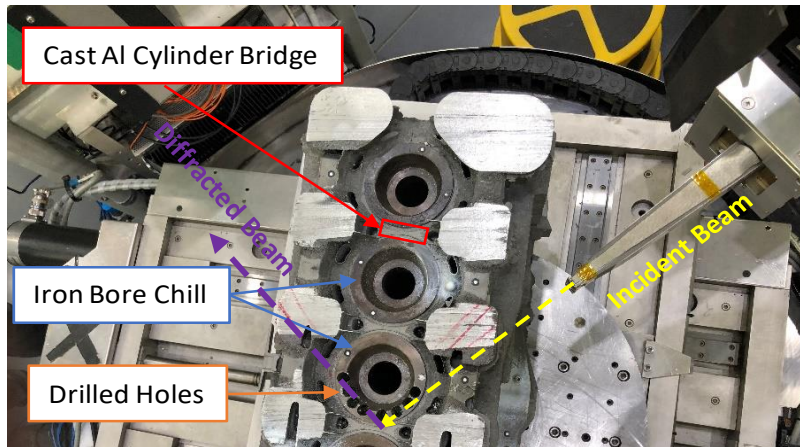


Figure 3.4-8. Removal of iron from neutron beam path for the TSR +Chills engine block

3.4.1 Residual Strain/Stress in Bore-Chilled Engine Block

3.4.1.1 Residual Strain in the TSR + Chills Engine Block

The residual strain profiles for the TSR + Chills engine block are shown below in Figure 3.4-9. The high solidification cooling rates ($\sim 5\text{-}14\text{ }^{\circ}\text{C/s}$ [180]), facilitated by the integration of stainless steel bore chills, led to the evolution of compressive strain (i.e., negative strain) for all orientations during solidification. The differences in physical properties between the intermetallics and the Al matrix results in varying degrees of deformation during casting which is increased with faster cooling rates [199]. C. Dong et al. [199] found that increasing the cooling rate from 0.5 to $40\text{ }^{\circ}\text{C/s}$ led to an increase of the compressive stress in their alloy from approximately 200 MPa to 400 MPa .

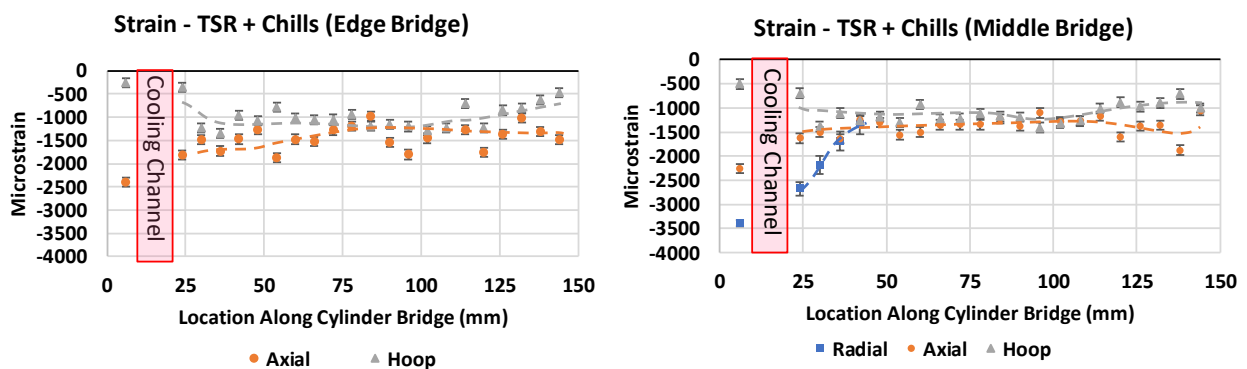


Figure 3.4-9. Residual strain profiles for TSR + Chills engine block; left) edge bridge, right) middle bridge

Unlike the ribbed surface of cast-in Fe liners, which is present to promote mechanical interlocking between the Al wall and the Fe liner, the smooth surface of the Fe bore chills allows for a more

facilitated contraction of the solidifying Al. This is presumed to be one of the primary factors, in addition to the increased cooling rate, for the observed compression in the TSR + Chills block which is dissimilar to the observed tensile strain in Al engine blocks with cast-in Fe liners [8], [35], [36], [200].

In more detail, qualitatively, this phenomenon can be explained as followed. In the sand-casting process described in these earlier studies, the pre-heated liners could quickly reach the solidification temperatures of Al. Following this, the temperature differences between different parts of the casting system (liner, aluminum, and interior surfaces of the sand mold) were relatively small, leading to the mostly volumetric solidification of aluminum around the cast-in Fe liner. The accelerated rate of contraction of aluminum (relative to the iron), which was constrained by the liner, led to the formation of tensile forces in the aluminum cylinder.

In the modified Nema-Cosworth process presented here, aluminum solidification initiates around the thermally-massive stainless steel chills, rapidly forming a cylindrical solid shell around the chill. The smooth surface of the tapered chill prevents interlocking and, as already mentioned, allows for relative sliding motion at the chill-shell interface, thereby preventing formation of tension in the aluminum shell. As the process evolves, the large amount of material surrounding the cylinder bridge contracts towards the center of the bridge, bringing the hoop orientation into compression. It is exactly this contraction in the hoop direction that is causing the observed compression in the radial orientation. As both sides of the engine block are contracting inwards in the hoop direction (toward the center of the bridge), the contracting material and compressive forces have nowhere to go except to redistribute outward in the radial direction. However, since the material near the center of the bridge has completely solidified and is now fixed rigidly in place by the iron chills, the outward motion is restricted, leading to the observed compression (see Figure 3.4-10).

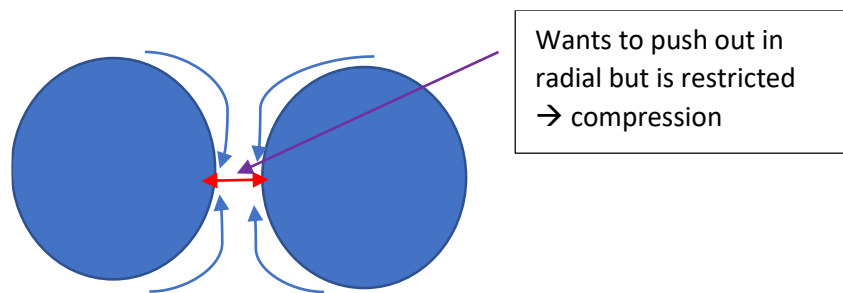


Figure 3.4-10. Graphical representation of compression forming in radial orientation

The homogenous cooling applied by the Fe chills has resulted in similar strain profiles for both the middle and edge cylinder bridge. For example, at the top of the bridge, the hoop and axial orientations of both bridges experience approximately -400 to $-500 \mu\epsilon$ and -2300 to $-2400 \mu\epsilon$, respectively. Progressing down the cylinder bridge, the hoop and axial strains appear to merge toward approximately $-1200 \mu\epsilon$ from the 50 mm to the 110 mm depth, where further down the bridge, the strains begin to diverge in opposing directions. The magnitude of strain in the axial and hoop orientation is comparable to previous ND stress experiments, although in compression rather than in tension [194]. However, the strain in the radial direction appears to be much greater than typically observed, reaching approximately $-3400 \mu\epsilon$ at the top of the bridge. The driving factor behind the increased magnitude of radial strain is thought to be caused by the greatly reduced wall thickness in the radial orientation, as compared to the axial and hoop directions. One of the reasons for the gradual decrease in the magnitude of radial strain from the 25 to 42 mm position is likely the tapered wall thickness of cylinder bridge (i.e., ~ 10 mm and 19 mm at the top and bottom, respectively). The larger wall thickness at the bottom permits a greater distribution of the forces at this location as compared to the top and, therefore, results in the observed decrease in strain. This claim is supported by the results presented by Carrera et al. [34] which indicated that an increase in wall thickness from 3.4 mm to 4.8 mm led to a 40 MPa reduction of stress in their engine block. It should be noted that due to the high attenuation of neutrons in Fe, the radial measurements of strain could only be obtained from the 6 to 42 mm position of the middle bridge (measured from the top of the cylinder bridge).

3.4.1.2 Residual Strain in the TSR Engine Block with Chills Removed

Prior to heat treatment, the stainless steel bore chills are mechanically removed from the engine blocks. The effect that this operation has on the magnitude of strain is shown in Figure 3.4-11A and B. The removal of the bore chills released a significant portion of the axial strain at the top of the cylinder bridge, reducing its magnitude from ~ -2400 to $\sim -600 \mu\epsilon$. As the chills are mechanically pressed out of the engine block, the material around the cylinder bores is partially pulled along the axial direction. However, the further away from the free surface (i.e., away from the top deck of the engine block), the harder it is for the strain to be released. Thus, the axial strain from the 30 mm to the 146 mm remains relatively unchanged.

In general, the hoop orientation of strain has been reduced at most of the locations along the cylinder bridge except for the top position (i.e., 6 mm). Also, the strain towards the bottom quarter of the bridge hovers around $\sim 0 \mu\epsilon$. The lack of strain release at the top of the cylinder bridge is likely due to the initially low magnitude of strain present at this location prior to removing the Fe chills. Conversely, the removal of the Fe chill led to a large shift in the nature of the radial strain from highly compressive to moderately tensile, particularly at the top of the bridge. This suggests that the mechanical interactions between the stainless steel bore chills and the Al bridge are locking the radial stress in place, and it is not until the chills are removed that the stress can be released. Unlike the axial and hoop orientations, which can glide more readily against the smooth bore chills, the flow and contraction of the material during solidification and subsequent cooling in the radial direction oppose one another and are bound between two adjacent Fe chills. Similar to the strain in the TSR + Chills block, the strain in both the middle and edge bridge of the TSR block is nearly identical, owing to Nemak's thermally balanced manufacturing process which results in homogenous microstructure throughout the cylinder bridges.

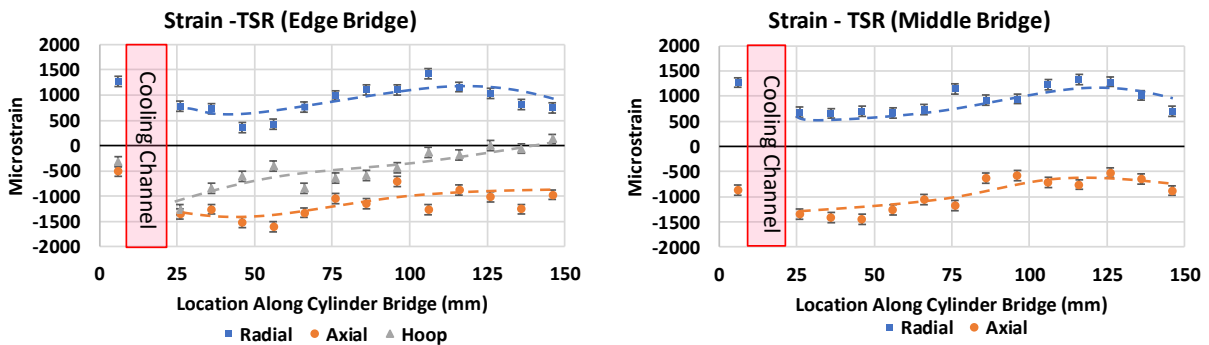


Figure 3.4-11. Residual strain profiles for TSR engine block; left) edge bridge, right) middle bridge

3.4.1.3 Residual Strain in T4 and T7 Treated Engine Blocks

The effect of the T4 heat treatment on the residual strain is shown below in Figure 3.4-12. In general, the magnitude of strain in all three orientations was greatly reduced throughout most of the cylinder bridge. For instance, the maximum magnitude of strain is now less than $1000 \mu\epsilon$, which is considerably lower than observed for the TSR + Chills ($\sim 3400 \mu\epsilon$) and the TSR ($\sim 1700 \mu\epsilon$) blocks. The cause for this strain reduction is thought to be driven by the solutionizing step of the T4 process, in that, during the elevated temperature holding, the yield strength of the alloy is reduced, allowing plastic flow to occur more readily and the relaxation of the material. The shift

toward tensile strain is likely caused by the forced air quenching process that occurred immediately after solution heat treatment. Since the cylinder bridge is the thinnest section in the engine block, the start of the quenching process forces the cylinder bridge to contract more quickly than the surrounding material. However, since the engine block is completely solid, the large mass surrounding the cylinders locks the bridge in place and prevents it from contracting. This locking causes tensile stresses to be exerted on the cylinder bridge, resulting in the overall tensile residual stress profile in this region. The bridge is less constrained in the axial orientation, but it can be implied that the overall reorientation of the contraction forces brings the bridge to some added axial tension, and at the same time somewhat reduces the radial tension.

It is important to note that, unlike the V6 Al block with cast-in gray iron liners [36], the residual strain profiles were relatively uniform and significantly lower in magnitude in this I6 engine block. It is likely that uniformity and lower stresses are due to the absence of the ribbed interface of the gray iron liners which interlocked the contraction of the dissimilar metals in the V6 engine block.

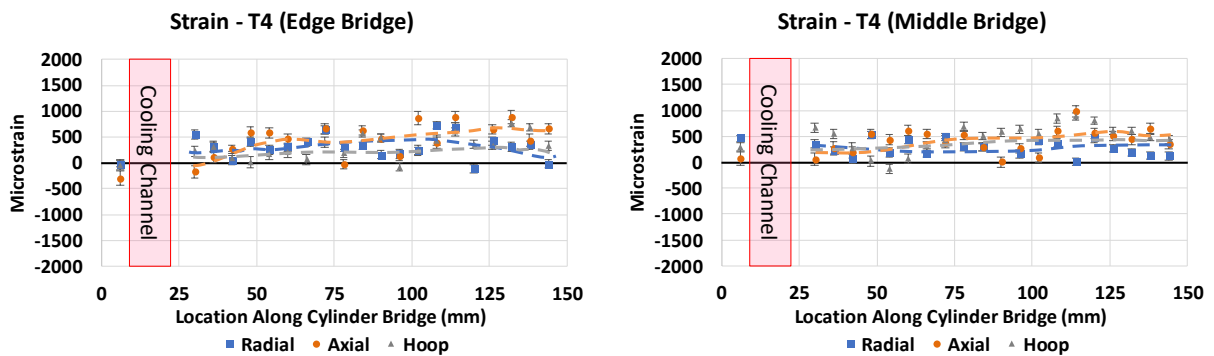


Figure 3.4-12. Residual strain profiles for T4 engine block; left) edge bridge, right) middle bridge

Figure 3.4-13 shows the strain profiles for two-cylinder bridges in the T7 engine block. Similar to the TSR and T4 bridges, a large resemblance between to the two T7 bridges, particularly for the axial and hoop orientations, was observed. The elevated temperature over aging (210 °C) portion of the T7 heat treatment seems to have redistributed the strain along most of the cylinder, as compared to the T4 heat treated block. It was observed that the upper middle section (~30-75 mm) of the cylinder transitioned from tension to compression for the axial and hoop orientations. An explanation behind this observation is offered later in the next subsection, in the discussion of the stress profiles.

The low magnitude of strain that is present along the entire cylinder bridge is a great achievement that fortifies the benefits that can be achieved through use of the modified NemaK-Cosworth manufacturing process and the elimination of the Fe liners from the casting process. For example, the compressive strain that is seen between cylinder depths of 6 and 50 mm, for the axial and hoop orientation, is particularly beneficial; during in-service operation the stress that develops during combustion is primarily tensile in nature. Thus, the compressive strain may be thought as a mode of “pre-stressing” and will likely lead to improved performance during in-service operation.

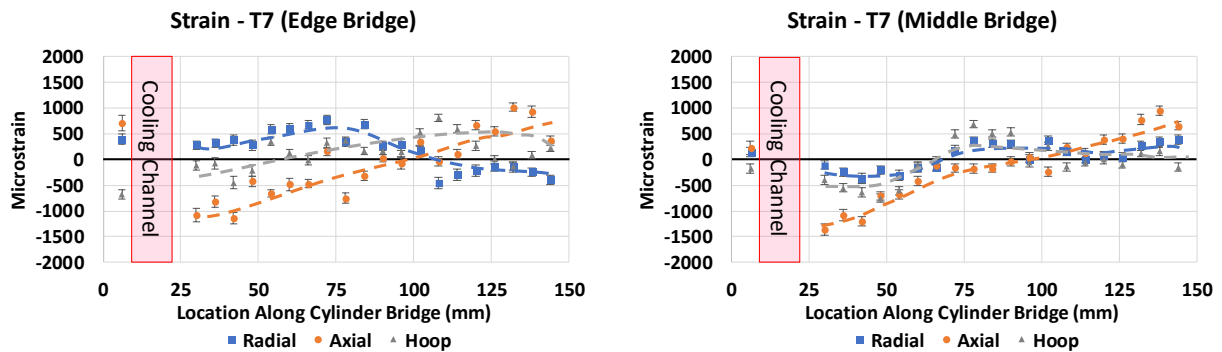


Figure 3.4-13. Residual strain profiles for T7 engine block; left) edge bridge, right) middle bridge

3.4.1.4 Residual Strain in the T7 Treated Engine Block with Pressed-in Liners

One of the primary goals of this study was to characterize the effects of the integrating stainless steel bore chills and the use of pressed-in cylinder liners rather than cast-in liners. It has been well published that the CTE mismatch between the Al engine block and the cast-in liners introduces a considerable amount of residual stress during solidification, heat treatment, and subsequent cooling [35], [40], [194]. Figures 7-9 clearly show that this issue has been resolved by removing the liners from the casting process. However, without an additional protective layer inside the cylinder, the Al alloy walls would quickly wear during in-service operation. For this reason, the bores of the engine block are first machined and then heated to 150 °C to allow for the insertion of a thin (~2mm thick) press-fit iron liner. The increase in temperature temporarily enlarges the bores, allowing for facilitated insertion of the liners, and results in a retaining force between the Fe liners and the Al cylinder block. This is exactly what is shown in Figure 3.4-14. The two adjacent Fe liners resist the contraction of the Al bridge (contraction of a hole during cooling results in a smaller internal diameter) during cooling, and both liners apply an opposing radial force onto the bridge, resulting in the observed increase in compressive strain in the radial

orientation. The strain in the axial and hoop directions are much less affected by the insertion of the liners and, thus, are very similar in magnitude as compared to the linerless T7 block (see Figure 3.4-13). The minor differences in the axial and hoop strain is likely attributed to the removal of material during the machining process.

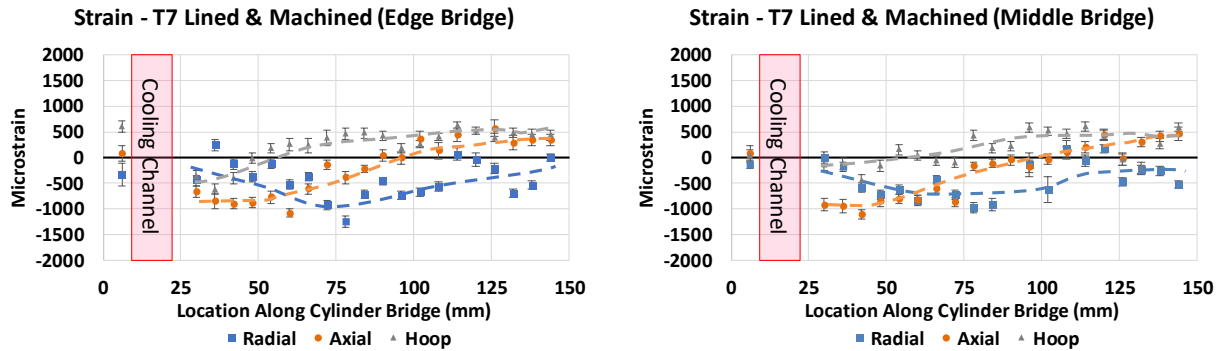


Figure 3.4-14. Residual strain profiles for T7LM engine block; left) edge bridge, right) middle bridge

Although the strain profiles shown in Figures 6-10 provide a thorough indication of the how the strain evolves throughout each of Nemak’s manufacturing process, it is difficult to directly compare these values to the alloy’s useable strength. For this reason, the residual stress was calculated using Equation 14 and the results are presented in following sections.

3.4.1.5 Residual Stress Evolution

Since the three orientations of strain are linked to the stress in the material via Hooke’s law, the discussion around the trends of the stress profiles is similar to that presented in the residual strain section of this study. Thus, less emphasis will be placed on the mechanisms behind the evolution of stress.

Figure 3.4-15 shows the stress profiles in the TSR + Chills block. The high attenuation of neutrons in Fe prevented the accurate measurement of radial strain below the 42 mm position. For this reason, we may only calculate the stress within the 6 to 42 mm position. It was observed that very high magnitudes of compressive stress were present in all three orientations, reaching maximums of about -350 to -500 MPa. Although the magnitude of strain in the axial and hoop orientation for this engine block were comparable to literature, and likely tolerable, the effect of Poisson’s ratio can clearly be observed. The high magnitude of radial strain ($\sim -3500 \mu\epsilon$) contributes greatly to the stress experienced in the hoop and axial orientations. The decreasing magnitude of stress from the

top to approximately the 42 mm position may be caused by the tapered cylinder wall (i.e., 10 mm at the top and 19 mm at the bottom) which leads to the distribution of compressive forces over a larger area, resulting in a smaller magnitude of stress.

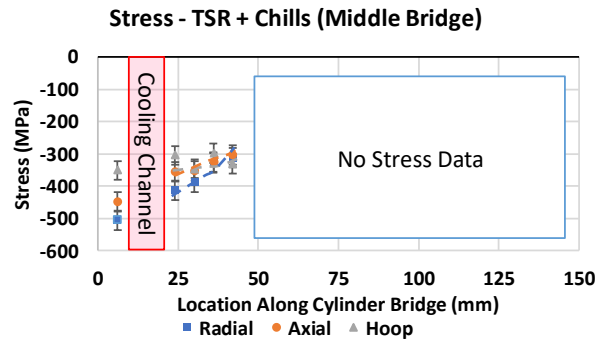


Figure 3.4-15. Residual stress profiles for TSR + Chills engine block

The residual stress profiles for the TSR block is shown below in Figure 3.4-16. As expected, the stress profiles of the edge bridge follow a similar trend as compared to the strain profiles shown in Figure 3.4-11. The radial orientation of stress is tensile above the cooling channel (maximum of ~100 MPa), and below the lower half of the cylinder bridge (maximum ~75 MPa). Although the cooling channel provides additional cooling to the cylinder bridge during operation, it seems to be acting as a stress concentrator. This claim is supported by our measurements above and below the cooling channel which show a considerable shift in the strain/stress. It can be expected that up to approximately 20-30 MPa of stress may be introduced during normal operation of typical unmodified diesel engines [22], [42], [201]. Thus, even with the combined contribution of operational and residual stress, the magnitude of tensile stress in the cylinder bridge is still well below the material’s room temperature as-cast yield strength of ~210 MPa [180].

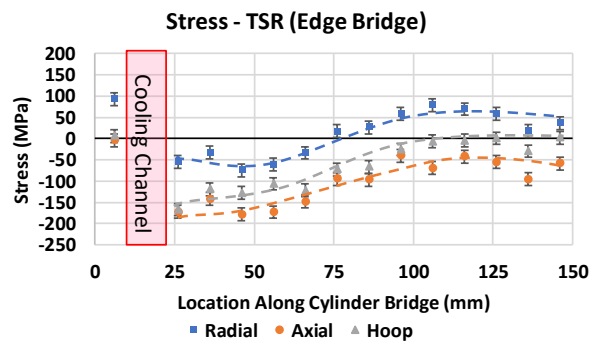


Figure 3.4-16. Residual stress profiles for TSR engine block

The combined contribution of the tensile strain that has likely evolved during the quenching portion of the T4 heat treatment led to an increase in tensile stress at all locations of the cylinder bridge, except for the section above the cooling channel. The maximum magnitude of residual stress in the T4 engine block reached ~150 MPa, which was approximately 30% lower than reported for the solution heat-treated V6 engine block that was produced with cast-in gray iron liners [36].

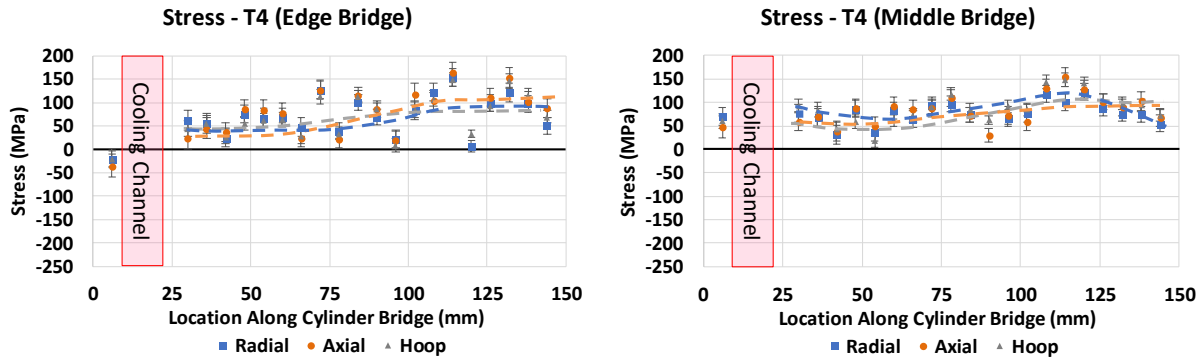


Figure 3.4-17. Residual stress profiles for T4 engine block; left) edge bridge, right) middle bridge

To further improve the performance of the I6 engine blocks, a T7 heat treatment was applied to the engine block. The T7 temper improves the dimensional stability of the casting during service, thereby reducing cylinder bore distortion and the associated negative side effects (i.e., blow-by and oil consumption). The aging process seems to have shifted the stress from tension to compression at the 30 to 70 mm position (compare Figure 3.4-17 and Figure 3.4-18), whereas, the tensile stress in the bottom half of the cylinder bridge has relaxed and reduced in magnitude. Apparently, the relatively long elevated temperature overaging process led not only to stabilization of the microstructure, but also to a new redistribution of the residual forces locked in the component. Figure 3.4-18 indicates that following artificial aging, the resulting stress profiles somewhat resemble again the profiles observed in the TSR engine block, with the upper middle portion of the cylinder bridge (below the cooling channel) being in compression. Seemingly, the fast cooling rates associated with the quenching process resulted in a quasi-stable stress distribution throughout the component, which was reduced in magnitude during aging and re-modified in the slow cooling to room temperature. The tensile stress at the top of the cylinder bridge remains mostly unchanged and reached a maximum magnitude of 61 MPa which is slightly improved as compared to the T4 block (~69 MPa).

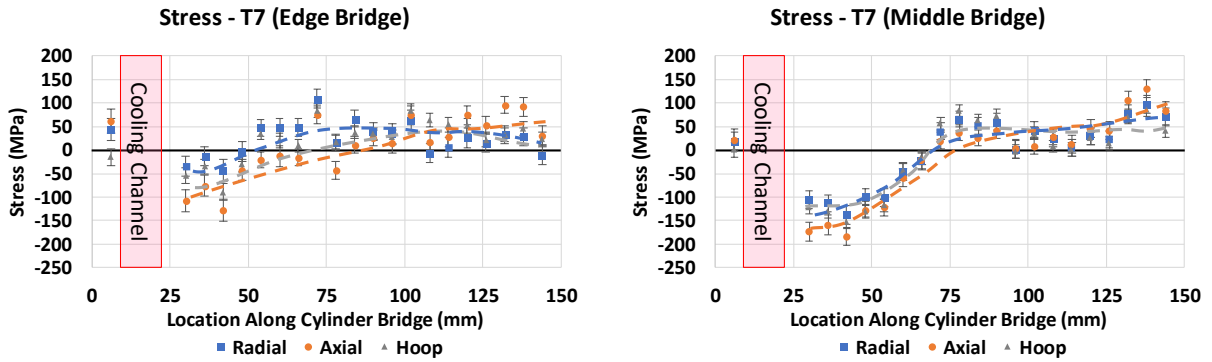


Figure 3.4-18. Residual stress profiles for T7 engine block; left) edge bridge, right) middle bridge

Finally, Figure 3.4-19 shows the residual stress in the production-ready, sand-cast Al engine block which has been machined and has had the Fe liners mechanically inserted into the cylinder bores. Comparing Figure 3.4-18 and Figure 3.4-19, no significant change has occurred in the stress present in the axial and hoop directions. However, the insertion process, including pre-heating of the engine block, has shifted the radial stress at the upper middle to middle section toward a slightly higher magnitude of compression. As mentioned in the section on strain, this shift is likely attributed to the temporary radial enlargement of the Al cylinder bore during heating and a subsequent compressive radial force applied by the liner onto the Al cylinder bridge during cooling.

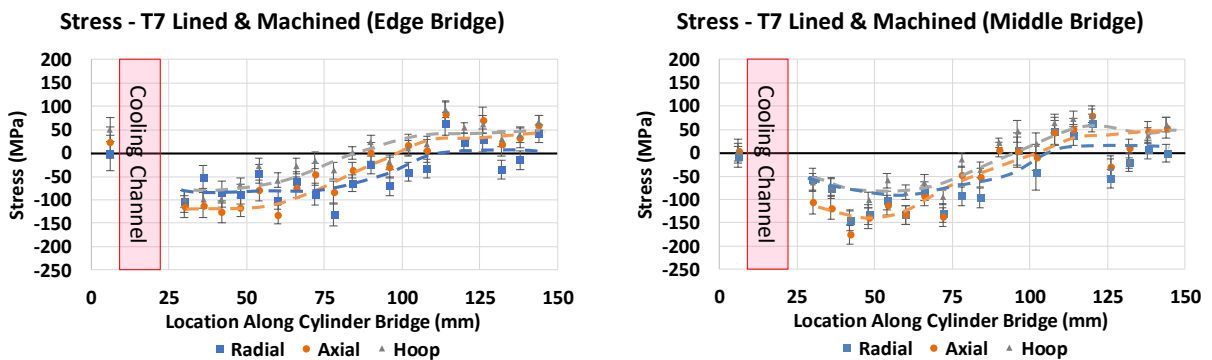


Figure 3.4-19. Residual stress profiles for production ready T7LM engine block; left) edge bridge, right) middle bridge

The magnitude of stress at the top of the cylinder bridge was observed to vary between -10 and +50 MPa, suggesting that, in addition to the ~20-30 MPa operational stress for diesel engines, a considerable amount of the alloy’s room temperature strength remains useable at this critical location of the cylinder bore. However, as mentioned in section 2.2, the room temperature YS

quickly degrades at elevated temperatures, especially when exposed for long durations. Thus, it is necessary to determine the elevated temperature strength of the A319 alloy.

3.5 Fitness-For-Service Evaluation of A319 Alloy

3.5.1 Tensile: A319 Alloy from I6 Engine Block

To further evaluate the effects of the tapered cylinder wall, tensile samples were extracted from the cylinder wall of the TSR engine block. A high precision waterjet and mill were used to machine the samples to the dimensions listed in the ASTM standards B557M – 15 [202]. Four samples were taken from the cylinder wall: Top, Middle, Lower Middle, and Bottom. A tensile sample was unable to be extracted from the Upper Middle location, as described in the microstructural analysis section, due to a cooling channel situating at this location. An MTS extensometer, with a 25.4 mm gauge length, was used to measure the axial strain while the MTS Landmark Servo hydraulic material test system pulled the samples at a constant strain rate. The results were used to determine the UTS, YS at 0.2% strain, Young's modulus, and elongation.



Figure 3.5-1. Tensile test setup including MTS extensometer

Due to the lack of testing material, only singular tensile tests could be performed for each of the locations. The results from the tensile test indicate that the YS, UTS, and elongation are very similar throughout the entire depth of the cylinder bridge. This similarity is likely due to the fine and relatively uniform microstructure. The decrease in the Young's modulus in the Middle, Lower Middle, and Bottom section may be attributed to the gradual transition of the morphology of $\text{Al}_{15}(\text{Fe},\text{Mn})_3\text{Si}_2$ from polygonal to Chinese script [203].

Tensile Test of Cylinder Wall

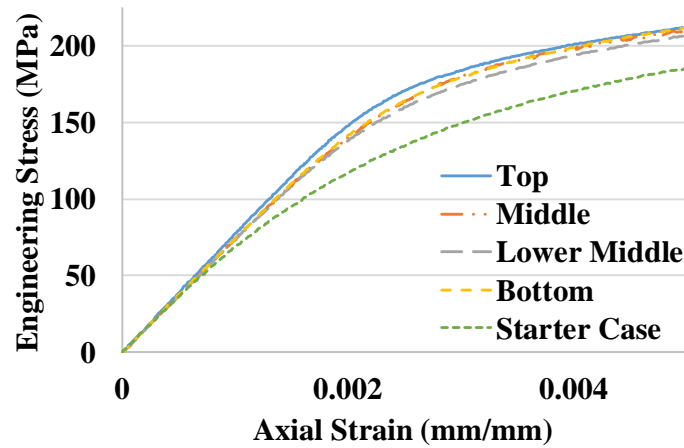


Figure 3.5-2. Stress - strain curve for cylinder web of as-cast engine block (after TSR)

Table 3.5-1. Room temperature tensile test results of TSR A319 alloy (taken from cylinder bridge of I6 engine block)

Specimen Location	Ultimate Tensile Strength (MPa)	Yield Strength (MPa)	Young's Modulus (GPa)	Elongation (%)
Top	286	209	76.7	3.1
Middle	285	209	71.7	3.1
Lower Middle	275	205	71.6	2.5
Bottom	286	211	72.3	3.1
Starter Bracket	202	187	59.9	0.7

The results shown in Figure 3.5-2 and Table 3.5-1 indicate that the chills have significantly improved all of the mechanical properties of the alloy, as compared to the non-chilled starter bracket. When compared to the average mechanical properties of the entire cylinder bridge, a reduction of approximately 28%, 10%, 18%, and 72% can be seen for the alloy's UTS, YS, Young's modulus, and elongation, respectively. Although large elongations are usually not sought after for powertrain components, it is common for the automotive industry to target a minimum of 1%.

The poor mechanical performance of the starter bracket is likely attributed to a few factors, the first being the large grain size (~600 μm in the starter case vs. ~100 μm in the cylinder bridge), and the second being that an observable increase in the size and volume fraction of porosity that

was seen in the starter case. Porosity can act as localized stress concentrators and can significantly diminish a material's mechanical properties [30], [31]. Studies performed by Fahad et al. [204] and Michalik et al. [205] indicated that both the porosity size and volume fraction increase with a decreasing cooling rate. Lastly, Vandersluis et al. indicated that the Fe-containing phases (see Figure 3.3-3F, δ -Al₃FeSi₂ and δ -Al₃Cu₂Fe) have detrimental effects on mechanical properties due to their brittleness, hardness, and poor bonding to the Al matrix [182].

The results from the tensile tests in this study are similar to the mechanical properties of A319 alloys listed in literature. J. Ferguson et al. describes that the Young's modulus of a T7 heat-treated A319 alloy had a magnitude of approximately 74 GPa [206]. In addition, a study conducted by M. Salleh et al. indicated that the UTS and YS for their A319 alloy had a magnitude of ~295 and ~201 MPa, respectively [207].

Although room temperature tensile tests of the TSR alloy provide some evidence of the expected performance of the alloy, it is well known that the temperature of Al alloys quickly degrade as the temperature is increased [106]. This property reduction is one of the reasons why the T7 heat treatment is applied to Al alloys, in addition to stress relief. The purpose of the aging portion of the T7 heat treatment is to precipitate-strengthen the alloy and to stabilize the microstructure. However, in reality, the microstructure of the currently used Al powertrain alloys will usually still undergo some type of alteration, generally worsening the structure. Thus, to determine how the engine block will actually perform at a temperature near the operating temperature (i.e., 225 °C), tensile samples were extracted from the cylinder bridge of the T7 heat-treated engine block and subjected to an elevated temperature tensile test at 250 °C.

The elevated temperature tensile strength for each alloy was evaluated using an MTS hydraulic material test system equipped with a 100 kN load frame, grips rated for 26 kN, a tri-chambered resistance furnace, three PID-controlled 0.04" k-type thermocouples, and an extensometer (see Figure 3.5-3). Due to the temperature restrictions of the grips (~175 °C), it was necessary to manufacture custom extensions that would allow the grips to remain relatively cool even as the temperature in the furnace was increased to 250 and 300 °C. Similarly, custom extension arms were also necessary to protect the extensometer. To compensate for the additional length of the extensometer arms, many trial tests were conducted, and a precise correction factor (i.e., offset of less than +/- 1%) was established and implemented for the tests presented in this study.

Prior to commencing the tensile tests, each sample was conditioned for 200 hours at the corresponding testing temperature (i.e., 250 or 300 °C). Conditioning stabilizes the alloy's microstructure and provides more realistic data of how the alloys will perform in their design purpose (i.e., engine blocks, cylinder heads and turbochargers). After conditioning, each sample was placed in the test cell (see Figure 3.5-3) and heated at a rate of 0.5 °C/s until the desired temperature was reached. Once the controller reached the selected temperature, the system was held for 30 minutes or until the temperature of the sample and extension arms reached a steady-state and the thermally-induced strain was no longer increasing. The temperature for each of the experiments was controlled using a PID controller with a precision of ± 0.5 °C. Following the procedures outlined in the ASTM standards for high elevated temperature tensile testing, a strain rate of 0.005 mm/mm/min was applied until failure (equivalent to the sample breaking or a 90% reduction of the max force).

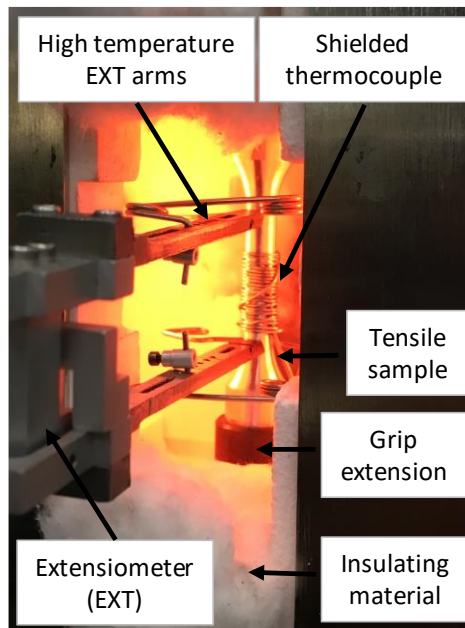


Figure 3.5-3. Experimental setup for elevated temperature tensile tests

Although 250 °C is likely above the average temperature that the current engine block alloy will experience during operation, the elevated temperature provides a good indication of how the alloy will perform in extreme conditions. The engineering stress vs. engineering strain plot for the 250 °C tensile test is shown below in Figure 3.5-4. The YS and UTS at 250 °C were determined to be 85 and 98 MPa, respectively. Interestingly, these values compare well to the unconditioned results presented in [106]. The similarity between the unconditioned and conditioned properties

could be associated with the relatively high cooling rates experienced by the engine block samples or because at 250 °C, the T7 A319 alloy is not largely affected by the conditioning process. The latter may be attributed to the high artificial aging temperature (i.e., 210 °C) of the T7 heat treatment which is relatively close to the conditioning temperature. Moreover, the addition of Ni to the A319 alloy may have also played a role by leading to the formation of precipitates with greater thermal stability (i.e., $\text{Al}_7\text{Cu}_4\text{Ni}$ as compared to Al_2Cu). The Young's modulus and elongation were determined to be 63.7 GPa and 11.5 %, respectively. The Young's modulus is not reported in [106]; however, the elongation is. A relatively large discrepancy in the elongation was observed between the non-conditioned [106] values and the conditioned values (this study) at 250 °C. Specifically, in the non-conditioned state, the T7 A319 alloy was reported to have an elongation of about 2.5%. This suggests that although the conditioning process did not have much of an effect on the YS and UTS, it may have increased the elongation. Rincon et al, [106] observed similar magnitudes of elongation for their samples tested at temperatures above 300 °C. It was observed that when the temperature of the tensile test was increased from 250 °C to 300 °C, the mode of fracture transitioned from brittle to ductile. In addition, the amount of cracked intermetallics (i.e., Al_2Cu , $\text{Al}_{15}(\text{Fe}, \text{Mn})_3\text{Si}_2$ and Si) greatly increased between 250 and 300 °C. It is likely that the high temperature conditioning process provided sufficient time and energy for the particles to crack, thus alleviating the intergranular stress in the intermetallics and leading to the increase in the elongation. Comparing the YS and UTS of the conditioned T7 A319 alloy to the maximum tensile residual stress in the T7LM engine block (i.e., +65 MPa, see Figure 3.4-19), and accounting for operational stress, it is possible that at 250 °C, the material's yield strength would not be sufficient, particularly when a factor of safety is introduced. Fortunately, with the added rigidity and strength associated with the pressed-in Fe liners, it is likely that the engine block in its current state will perform sufficiently for the lifetime of the engine, so long as the operating temperature remains below 250 °C.

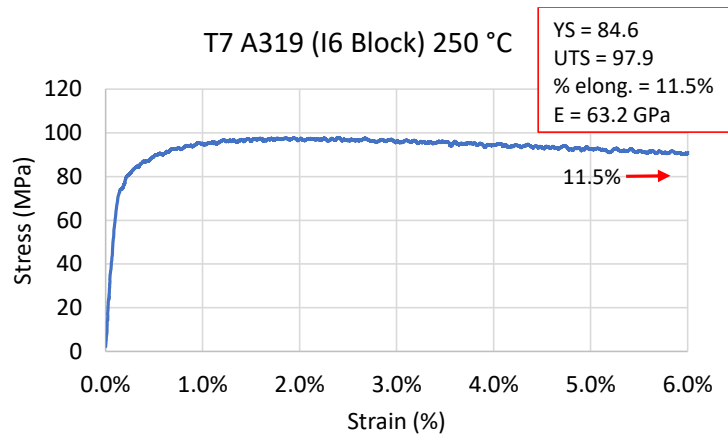


Figure 3.5-4. 250 °C tensile tests for T7 A319 alloy, extracted from cylinder bridge of an I6 engine block

In addition to the 250 °C tensile tests, additional samples were extracted, conditioned, and tested at 300 °C to evaluate how the alloy would perform if used for the next generation of engines. The YS and UTS of the alloy decreased dramatically to 39 (-54%) and 45 (-54%) MPa, respectively. One of the primary factors contributing to such a large decrease in the alloy’s performance is likely due to precipitate coarsening of the metastable λ' -Al₅Cu₂Mg₈Si₆ intermetallics. Lee et al. observed a decrease in the hardness of the T6 Al-12.5%Si-4.5%Cu-1.0%Mg alloy from 107 HRF to ~60 HRF after only 20 hours of isothermal heat treatment at 300 °C [208]. It is clear from these results that the temperature threshold for the T7 A319 alloy is well below 300 °C. If the temperature of the I6 engine block were to increase to 300 °C, the magnitude of tensile residual stress in the engine block would surpass the material’s yield strength prior to any operational loading.

In addition to the decrease in YS and UTS, the elastic modulus was decreased by approximately 22%, reaching only 49.3 GPa. The modulus of elasticity is a direct indication of the material’s stiffness. A material with a high elastic modulus has a greater stiffness and will have a much lower magnitude of strain for a given load. Conversely, the same load on a material with a low elastic modulus will result in a greater amount of strain, and therefore, a much lower dimensional stability. In the context of this study, it is important to note that dimensional stability is critical for powertrain components that rely on tight tolerances such as bearing and piston ring clearances and valve seats in combustion engines.

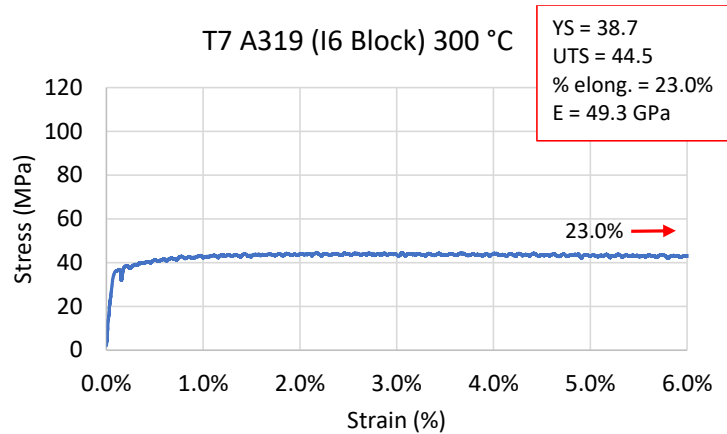


Figure 3.5-5. Elevated temperature tensile tests for T7 A319 alloy, extracted from cylinder bridge of an I6 engine block

Table 3.5-2. Tensile test results of conditioned (200 hours) T7 A319 alloy

	YS		UTS		Young's		Shear Modulus		Elongation	
	(MPa)		(MPa)		(GPa)		(GPa)*		(%)	
Temp. (°C)	250	300	250	300	250	300	250	300	250	300
T7 A319	84.6	38.7	97.9	44.5	63.7	49.3	23.9	18.5	11.5	23.0

*Calculated: $G = E/(2(1+\nu))$

3.5.2 Creep: A319 Alloy from I6 Engine Block

As described in section 2.2.1.2, creep plays a large role in the premature failure of components that operate at elevated temperatures. Subjecting a material to a single constant load for an extended period of time, either to failure (i.e., fracture or extensive elongation), or for a specific number of hours, provides an indication of how the alloy will perform for a particular application; however, a significant amount of information is missing (i.e., stress exponent n_a and activation energy Q_a). For this reason, a more practical and informative approach is to follow a staircase creep experiment [66]. The basics steps of a staircase creep experiment include subjecting the sample to an applied load (σ_1), holding for an extended period of time, releasing the load, holding for a short period of time, and then increasing the load above σ_1 and holding. These steps are repeated until the material fails. The amount that the applied stress is increased after each cycle is largely dependent on the material's mechanical properties.

Figure 3.5-6 displays the result from the staircase creep test at 250 °C. The experimental setup was identical to the tensile test experiments described above. At 250 °C, the staircase loads were 22

MPa (48 hours), 30 MPa (24 hours), 40 MPa (24 hours), 50 MPa (24 hours), 55 MPa (24 hours), 60 MPa (24 hours) and 65 MPa (fracture). The lowest load, 22 MPa, corresponds to a stress slightly greater than the current peak cylinder pressures in diesel engines (i.e., 15-20 MPa) [22], [23], [95]. The remaining loads were incrementally increased and based on the alloy's performance in the elevated temperature tensile tests. As mentioned in section 2.2.1.2, the steady-state creep rate ($\dot{\epsilon}_s$) is a critical parameter that must be included in alloy selection for elevated temperature applications like engine blocks. The $\dot{\epsilon}_s$ for each of the applied stresses is shown below Table 3.5-3.

At 22 MPa, the $\dot{\epsilon}_s$ was very low (i.e., $\sim 6.00E-09 \text{ s}^{-1}$), and thus, is more susceptible to thermal/load fluctuations. Accurate determination of the steady-state creep rates at such low values requires that the load be held for much longer than the 48 hours (on the order of weeks). As a result, an error bar is included on the $\dot{\epsilon}_s$ for the 22 MPa load with a magnitude corresponding to the fluctuations in the strain rate (i.e., $4E-09 \text{ s}^{-1}$).

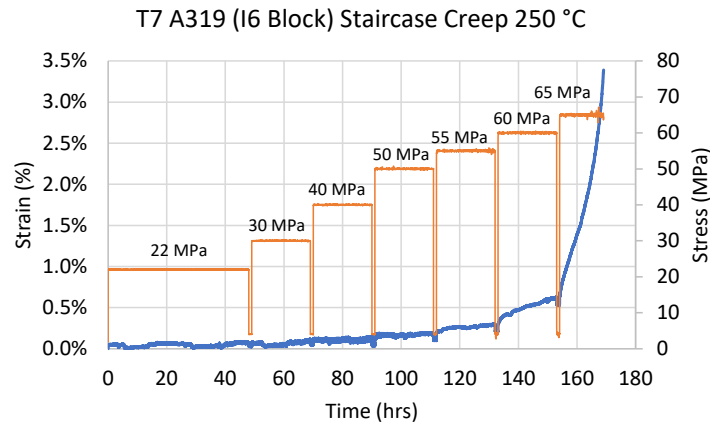


Figure 3.5-6. Staircase creep results of T7 A319 alloy (taken from cylinder bridge of engine block). Sample was conditioned at 250 °C for 200 hours prior to initiating test

It was observed that the $\dot{\epsilon}_s$ was insignificantly affected until the load was increased from 22 to 55 MPa. At these loads, the deformation mechanism map for pure Al (see Figure 2.2-6) suggests that the strain rate is governed by high temperature dislocation creep; however, the apparent stress exponent, $n_a = 0.8$ (see Figure 3.5-9), is an indication of diffusional creep (i.e., Nabarro-Herring, Coble, or Harper Dorn) [52].

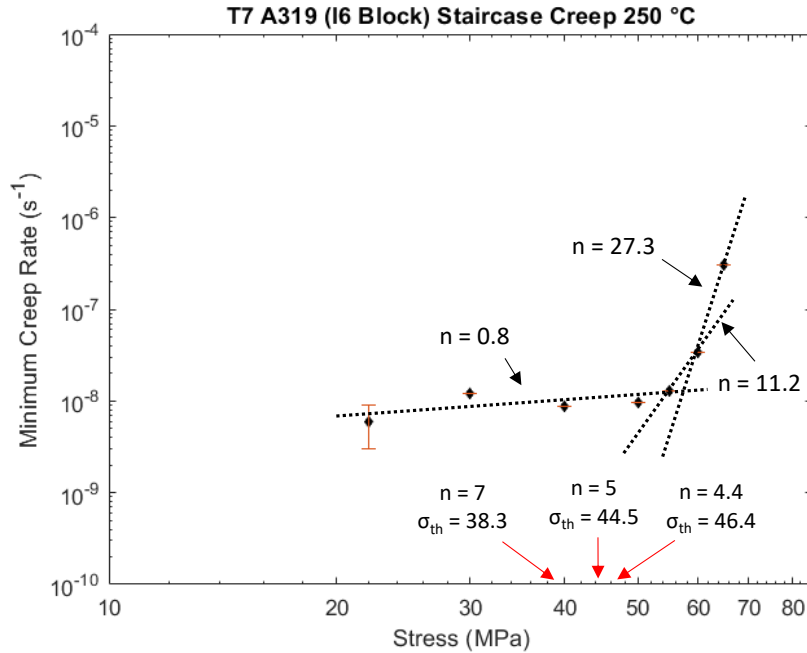


Figure 3.5-7. Minimum creep rate as a function of applied stress for the T7 A319 alloy at 250 °C. Note apparent stress exponent n_a and threshold stress σ_{th}

Raising the load to 60 MPa increases the $\dot{\epsilon}_s$ to $3.444\text{E-}08 \text{ s}^{-1}$ and raises the apparent stress exponent to $n_a = 11.8$, giving indications of power-law breakdown dislocation creep. At 65 MPa, a well-established steady-state creep rate is not apparent, and thus, a minimum creep rate is reported (i.e., $3.044\text{E-}07 \text{ s}^{-1}$). Such a large increase in the creep rate momentarily shifts the creep mechanism into dislocation glide ($n_a = 27.3$) [209] before entering plasticity and fracturing. Due to the relatively low ductility of the A319 alloy, such a large $\dot{\epsilon}_s$ results in the relatively quick necking of the sample, leading to complete fracture in ~ 10 hours. Such a high apparent stress exponent gives evidence of a threshold stress, as described in section 2.2.1.2.

The experimental data resulting in abnormally elevated apparent stress exponents were, therefore, re-examined with introduction of the σ_{th} . The σ_{th} was estimated by plotting $\dot{\epsilon}_s^{1/n}$ vs. σ and extrapolating the data to $\dot{\epsilon}_s = 0$. A stress exponent of $n = 4.4, 5,$ and 7 were used to determine the best linear fit (see Figure 3.5-8). Similar to the results presented in [210] for a T7 A319 alloy, a stress exponent of 7 results in the greatest linear fit (i.e., $R^2 = 0.929$), suggesting that creep is controlled by lattice diffusion with a constant grain substructure [58].

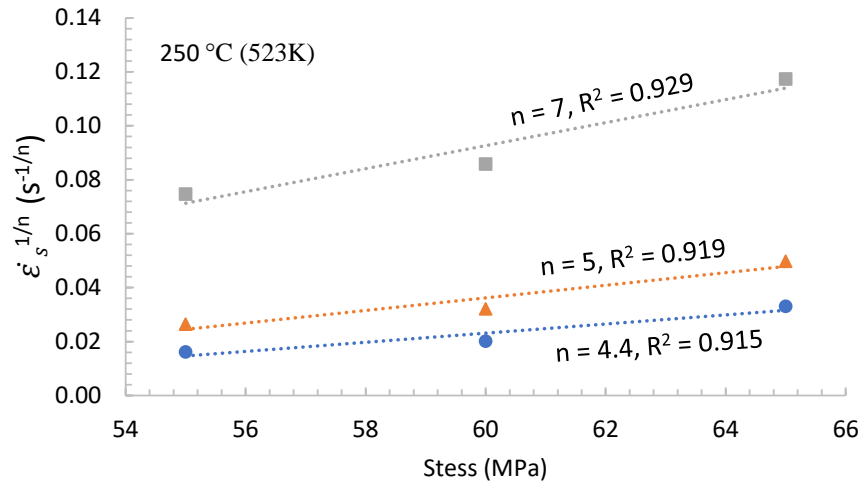


Figure 3.5-8. A plot of $\dot{\epsilon}_s^{-1/n}$ vs. σ for the T7 A319 alloy at 250 °C

As a result, the σ_{th} was estimated to be 38.3 MPa (see red arrows in Figure 3.5-7), which is considerably greater than the σ_{th} reported in [210] for $n = 7.9$ (i.e., 25 MPa). Although $n = 7$ resulted in the greatest linear fit of $\dot{\epsilon}_s^{-1/n}$ vs. σ , the estimated threshold stress at $n = 4.4$ (46.4 MPa) and $n = 5$ (44.5 MPa) appear to be closer to the actual threshold stress where dislocation creep begins to dominate. As seen in Figure 3.5-7, the creep rate remains relatively constant and low in magnitude until the stress is increased to ~50 MPa which more closely correlates with the results in [210]). It should be noted that the relatively large stress increment (i.e., $\Delta\sigma = 5$ MPa) adds a degree of error associated with the estimation of the threshold stress. Thus, for a more accurate determination of the threshold stress, smaller stress increments should be taken between the transition of diffusion creep to dislocation creep (i.e., 50 to 60 MPa).

The staircase creep results for the T7 A319 alloy at 300 °C are shown below in Figure 3.5-9. It was observed that raising the temperature to 300 °C has a negligible effect on the $\dot{\epsilon}_s$ at 22 and 30 MPa, suggesting that the threshold stress at 300 °C remains above 30 MPa (see discussion below). Similar to the low loads at 250 °C (see Table 3.5-3), the apparent stress exponent, $n_a = 0.8$ (see Figure 3.5-11), suggests that diffusional creep is the rate-controlling mechanism.

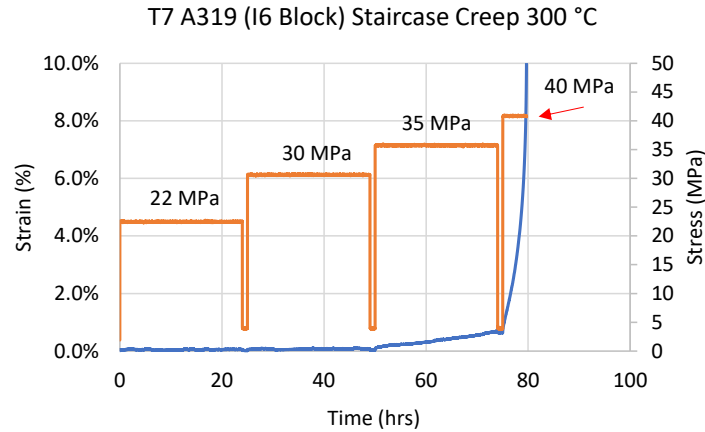


Figure 3.5-9. Staircase creep results of T7 A319 alloy (taken from cylinder bridge of engine block) Note: Sample was conditioned at 300 °C for 200 hours prior to initiating test

Increasing the load to 35 MPa abruptly increases the creep rate by a full magnitude, reaching $6.46\text{E-}08 \text{ s}^{-1}$. As a result, the apparent stress exponent increases to $n_a = 15.4$, indicating power-law breakdown dislocation creep [209]. Raising the load to 40 MPa is close to the material's yield strength and, thus, provides sufficient stress to disturb the equilibrium of work hardening vs. thermal softening (i.e., the steady-state creep rate). As a result, a true $\dot{\epsilon}_s$ was not observed, but instead, the minimum creep rate is reported. Such a large increase of the $\dot{\epsilon}_s$, raised the apparent stress exponent substantially, reaching $n_a = 26.7$. This value of n_a suggests that the creep mechanism has shifted through dislocation glide and finally into plasticity, leading to rapid fracturing of the sample. Similar to the discussion for the 250 °C creep tests, the high apparent stress exponent suggests that a threshold stress is present. Similar to the creep results at 250 °C, a stress exponent of $n = 7$ resulted in the greatest linear fit of $\dot{\epsilon}_s^{1/n}$ vs σ ($R^2 = 0.951$, see Figure 3.5-10).

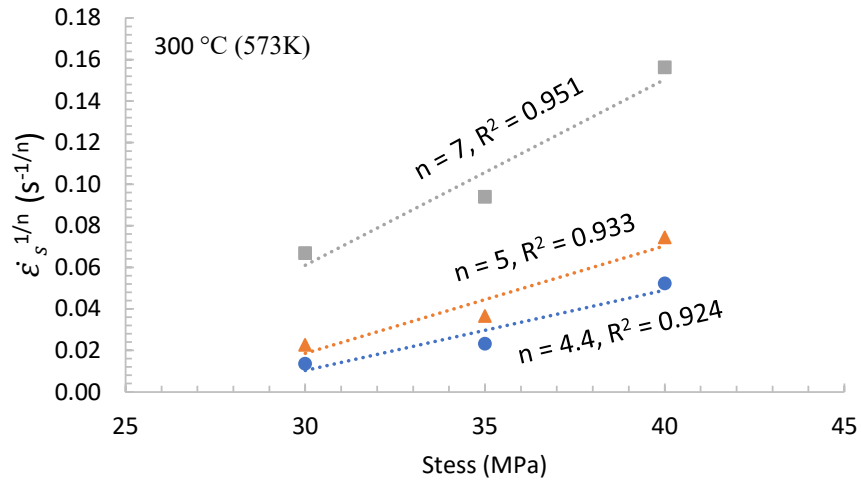


Figure 3.5-10. A plot of $\dot{\epsilon}_s^{-1/n}$ vs. σ for the T7 A319 alloy at 300 °C

Following the same procedure listed above, the threshold stress was determined to be 23.2 MPa. Similar to the results at 250 °C, the threshold stress corresponding to an $n = 7$ appears to be underestimated and suggests that the threshold stress at $n = 4.4$ (i.e., 27.4 MPa) seems more appropriate based on the measured creep rates shown in Figure 3.5-11. The 50 °C temperature increase lowers the onset stress for dislocation creep by nearly 50%, which is likely attributed to the poor coarsening resistance of the $\text{Al}_5\text{Cu}_2\text{Mg}_8\text{Si}_6$ phase and the increased rate of cracking of the eutectic Si and $\text{Al}_{15}(\text{Fe},\text{Mn})_3\text{Si}_2$ particles at 300 °C.

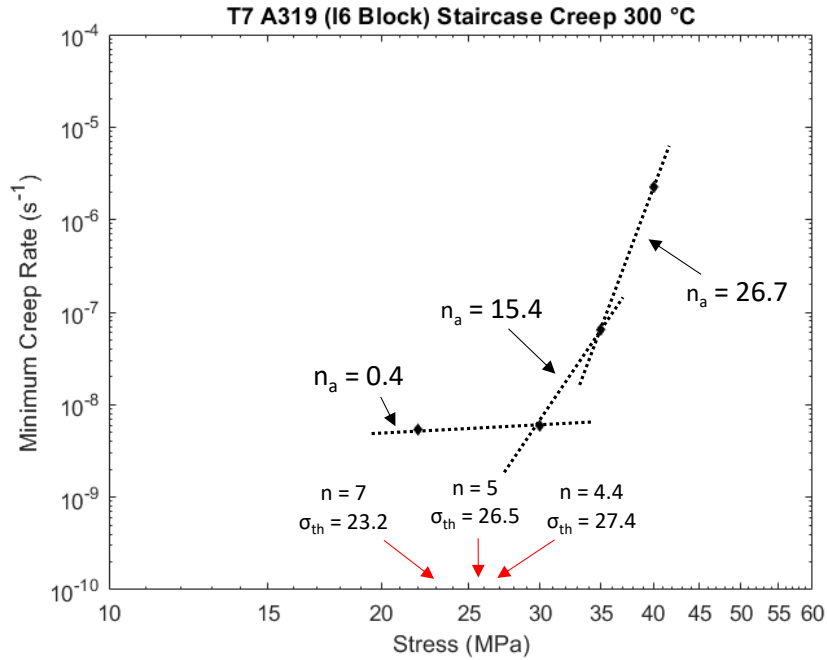


Figure 3.5-11. Minimum creep rate as a function of applied stress for the T7 A319 alloy at 300 °C. Note apparent stress exponent n_a and threshold stress σ_{th}

Table 3.5-3. Steady-state creep rate for T7 A319 extracted from cylinder bridge of I6 engine block (units: $10^{-8}/s$)

T7 A319	22 (MPa)	30 (MPa)	35 (MPa)	40 (MPa)	50 (MPa)	55 (MPa)	60 (MPa)	65 (MPa)
250 °C	0.600	0.633	-	1.179	0.971	1.295	3.444	30.670
300 °C	0.532	0.598	6.461	227.700	-	-	-	-

Figure 3.5-12 displays the minimum creep rate as a function of the reciprocal of the absolute temperature for the 40 MPa loads at 250 and 300 °C. The purpose of this chart is to display the effect that the load and temperature have on the activation energy for creep. In literature, the activation energy is commonly compared to the activation energy of self-diffusion of pure aluminum (~143 kJ/mol). At 40 MPa, the activation energy is 102 kJ/mol, suggesting that dislocation core diffusion creep or power-law creep [209]. These results correlate well with the apparent stress exponent.

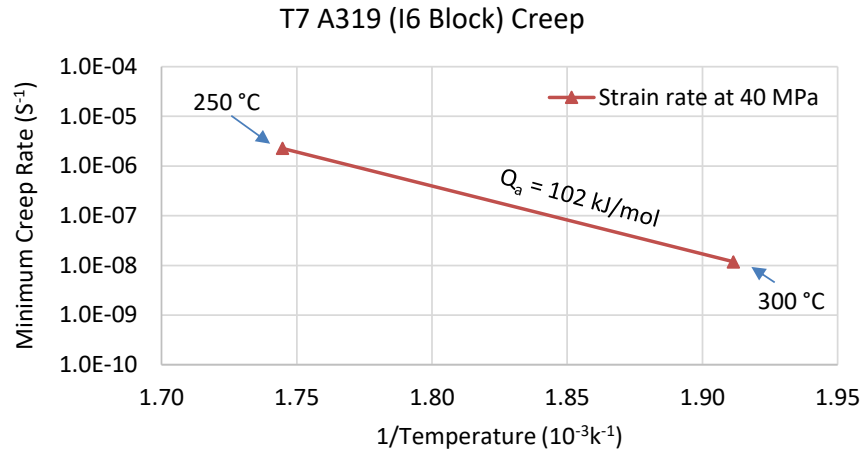


Figure 3.5-12. Minimum creep rate plotted against the reciprocal of the absolute temperature. Note apparent activation energies, Q_a

Dislocation core diffusion should not result in significant deformation and, thus, this alloy may perform adequately at 300 °C with an applied stress of 40 MPa. However, even though the sample failed at 100% of its YS, the poor YS and ductility of the A319 alloy suggests that this alloy, in its current state, may only be used for applications which operate at stresses below 35 MPa. Thus, this alloy will not be able to tolerate the increase pressure and temperature of next generation combustion engines.

3.6 Chapter Summary

OSM, SEM/EDXS, neutron diffraction, and fitness-for-service testing were used to study, for the first time, the effects that integrated bore chills and the use of pressed-in iron liners, as opposed to cast-in iron liners, have on the evolution of residual stress in the cylinder bridge of sand-cast I6 aluminum engine blocks.

The rapid and well distributed cooling of the cylinder bridges, as a direct result of the thermally massive bore chills, resulted in a highly consistent and homogenous microstructure throughout the entire depth of the cylinder bridge. Besides the slightly larger SDAS and the moderate shift in the morphology of the $Al_{15}(Fe,Mn)_3Si_2$ phase from rod-like to Chinese script, no other major microstructure differences were observed from the top to the bottom of the cylinder bridge. This consistency led to nearly identical room temperature mechanical properties for the entire cylinder bridge (differences of less than ~5%).

The maximum magnitudes of stress at four depths along the cylinder bridge (i.e., top, upper middle, lower middle and bottom) of this I6 block, in comparison to a V6 Al block with cast-in gray iron liners, are presented in Table 2.1-1. The use of stainless steel bore chills refined the microstructure along the entire depth of the cylinder by homogenizing and increasing the cooling rate during solidification and subsequent cooling. However, it was observed that the use of stainless steel bore chills still induced a considerable amount of stress in the cylinder bridge. Fortunately, by mechanically removing the chills, a substantial release of stress occurs. Once subjected to the T4 heat treatment (i.e., solutionized and quenched), the stress profiles in all three orientations (i.e., radial, axial, and hoop) almost completely shift to tension. This shift is presumed to be primarily caused by the quenching portion of the T4 treatment due to the variation in material thickness between the thin cylinder bridge (fast cooling) and the thicker surrounding material (slower cooling). In both the TSR and T4 state, it is likely that the combined magnitude of operational and residual stress would not exceed the room temperature YS of the alloy (~210 MPa [180]). However, to improve the alloy's geometric stability, the T4 engine blocks were overaged to a T7 temper. The T7 heat treatment also led to a reduction of the tensile residual stress at the top, lower middle and bottom section of the cylinder bridge.

Table 3.6-1. Residual stress evolution in sand-cast Al (A319) engine blocks (units in MPa)

Engine Type		Bore Chills and Pressed-in Fe Liners (this study)					Cast-in Fe Liners [36], [40]		
		TSR + Chills	TSR	T4	T7	T7LM	TSR*	T4	T7
Top	Radial	-505	93	69	44	0	-65	25	17
	Axial	-447	-4	48	61	23	63	55	9
	Hoop	-351	6	60	-15	51	158	120	21
Upper middle	Radial	-300	-75	31	-44	-84	38	-75	55
	Axial	-303	-168	38	-128	-126	160	45	101
	Hoop	-330	-167	43	-90	-99	225	100	103
Lower middle	Radial	-	59	66	35	-71	55	-80	41
	Axial	-	-41	72	15	-31	160	35	102
	Hoop	-	-26	72	27	-20	202	-10	149
Bottom	Radial	-	36	55	-11	41	-95	-125	49
	Axial	-	-58	68	31	60	15	5	106
	Hoop	-	2	73	24	65	88	-30	157

* Average between TSR A (470°C) and TSR B (500°C)

One of the primary goals for this work was to evaluate the effects of using pressed-in liners instead of cast-in liners. Thus, the residual stress in a production ready, machined, and Fe-lined T7 engine block was also evaluated. In general, the axial and hoop orientations of stress were not significantly affected (compare Figure 3.4-18 and Figure 3.4-19). However, the radial orientation of stress shifted toward compression, particularly at the upper middle and lower middle sections. Similar to how the compressive stress was formed in the TSR + Chills block, it is believed that preheating the engine block prior to insertion of the thin (~2 mm) Fe liners temporarily enlarges the Al cylinder bore and, thus, once the block returned to ambient temperature, both of the adjacent Fe liners apply a force onto either side of the cylinder bridge bringing the center of the bridge into compression.

Comparing the residual stress results from this work to a previous study [36] that utilized neutron diffraction to determine the stress in a sand-cast engine block with cast-in Fe liners, clearly shows the effectiveness of the recently developed Nema-Cosworth casting process as well as the effectiveness of pressed-fit Fe liners, as opposed to cast-in liners. The magnitude of residual stress in almost all sections of the engine block with pressed-in liners is considerably lower than its predecessor which was produced with cast-in liners. For example, in the TSR condition, the use of pressed-in liners results in a maximum tensile stress at the top of the cylinder bridge of only 93 MPa, whereas the stress produced with cast-in liners reaches ~130-200 MPa. Combined with operating loads of up to ~20-30 MPa, as well as stress concentrators such as porosity or intermetallics with detrimental morphologies, it is likely that the stress in the cast-in Fe-lined block would surpass the material's YS. Moreover, as mentioned previously, the mechanical properties of the A319 alloy are largely affected by the operating temperature, particularly after elongated exposure.

Thus, to determine the feasibility of utilizing the A319 alloy for the development of the next generation of engines, high temperature fitness-for-service tests were conducted. The tensile tests of the conditioned samples, extracted from the cylinder bridge of the I6 block, revealed that, at 250 °C, the material may not be able to tolerate the combined thermo-mechanical loading and residual stress. With a YS of 85 MPa, approximate cylinder pressure/thermally induced stress of 22 MPa, and a residual stress of 51 MPa, the T7 A319 at the top of the cylinder bridge has just 12 MPa left of useable strength. Such a small margin of error surely results in an insufficient safety factor for the automotive industry. Moreover, the alloy's relatively high susceptibility to creep further reduces the viability of this alloy for performing above its designed operating temperature.

At 300 °C, tensile and creep tests clearly demonstrate that this magnitude of temperature is far exceeding the thermal stability of the strengthening intermetallics. More than 50% of the alloy's strength is reduced after increasing the temperature from 250 to 300 °C. As a result, operational and residual stresses push the total stress 33 MPa beyond ($39 - 22 - 51 = -33$ MPa) the YS of the T7 A319 alloy, indicating that the T7 A319 alloy cannot function sufficiently at 300 °C. The large reduction in performance is likely due to the dissolution of Cu-bearing intermetallics as well as the thermally-induced cracking of the Si and $Al_{15}(Fe,Mn)_3Si_2$ precipitates.

Although manufacturers have developed methods for partially reducing residual stress formations (heat treatment) and homogenizing the microstructure and mechanical properties (casting process and integration of chills), this is only prolonging the insufficient reserve of high-temperature strength required for enhancing engines' performance and efficiency. The need for improved performance and efficiency is already driving the operating pressures and temperatures of powertrain components above the physical limits of the currently used powertrain alloys. Thus, it is necessary to begin developing a replacement alloy with improved mechanical properties, particular at elevated temperatures.

Chapter 4: Development of Next Generation Powertrain Alloys

As discussed in Chapter 2 and demonstrated in Chapter 3, the use of Al alloys for powertrain applications has allowed manufacturers to remove substantial mass from the powertrain system; however, the insufficient thermal stability of the currently used alloys (i.e., A319, A356, A380, and A390) leads to rapid weakening of the material at elevated temperatures. Thus, focused on improving the high temperature strength and creep resistance of Al alloys, this chapter evaluates the effects that RE elements, combined with conventional Al-alloying elements like Si, Mg, and Cu, have on the microstructure of Al alloys. The work presented in this chapter uses thermodynamic simulation software (ThermoCalc™), scanning electron microscopy, energy-dispersive X-ray spectroscopy, and one of the methods of neutron diffraction, specifically neutron powder diffraction, to characterize the size, shape and composition of the phases in Al-RE alloys and to determine how the RE additions affect the temperature-dependent evolution of phase during solidification.

The compositions of the alloys included in this chapter are presented in Table 3.6-1. The compositions of the two binary Al-Ce alloys were selected to study both hypoeutectic (Al-6%Ce) and hypereutectic (Al-16%Ce) Al-Ce alloys. Based on the available [165], [211] literature and preliminary data, it was found that the concentration of Ce should remain below the eutectic composition to obtain the greatest ratio of ductility and strength while minimizing the precipitation of brittle primary $Al_{11}Ce_3$ crystals. To further improve the mechanical properties of the Al-Ce system, a 10 wt.% Mg addition was introduced. A 10 wt.% Mg addition was selected to have the greatest YS, while maintaining castability (see Figure 2.3-3 and section 2.3.2).

In hopes of developing the first commercially viable Al-RE alloy for powertrain applications, the effects that RE mischmetal additions to two conventional powertrain alloys were studied. As mentioned in sections 2.3.1 and 2.3.2, RE mischmetal is a more cost-effective addition over pure REs while having little effect on the alloy's mechanical properties [116]. To maintain castability, while precipitating the greatest number of RE-bearing intermetallics, the Si:RE ratio should be near 2:1. As a result, a 3.5%RE, and 8%RE mischmetal addition was introduced to the hypoeutectic A356 (~Al-7%Si) and hypereutectic A390 (~Al-19%Si) alloys, respectively. Since the ratio of Cu:RE should remain near 1:1.5 to 1:2 (see section 2.3.2), the Si:RE ratio is slightly higher in the A390 alloy as compared to the A356 alloy (see section 2.3.2). Both the A356 and

A390 alloys are used in current powertrain applications, but like many conventional Al alloys, the alloys suffer from poor thermal stability and, thus, they are restricted to applications which operate under 250 °C (see section 2.2.2).

Table 3.6-1. Alloy composition in wt.%

Alloy	Al	Ce	Mg	Si	Cu	Fe	Mn	Ti	La	Nd	Pr
Al-6%Ce	Bal.	5.82-6.13	-	-	-	-	-	-	-	-	-
Al-16%Ce	Bal.	15.86-16.32	-	-	-	-	-	-	-	-	-
Al-8%Ce-10%Mg	Bal.	7.84-8.16	9.5-10	0.15	0.05	0.15	0.25	0.25	-	-	-
A356+3.5%RE ^{*a}	Bal.	1.83	0.49	7.28	0.03	0.13	0.1	0.2	0.92	0.58	0.19
A390+8%RE ^{*a}	Bal.	4.18	0.66	18.94	4.26	0.97	max 0.10	-	2.1	1.33	0.43
A356 ^a	Bal.	-	0.49	7.28	0.03	0.13	0.1	0.2	-	-	-

*RE in the form of mischmetal (~52% Ce, 26% La, 16% Nd, Bal.% Pr)

^a contains trace amounts of Ni , Cr , Sr , Sn, and Zn

The Al samples discussed in this chapter were produced at Eck Industries' manufacturing facility in Manitowoc, Wisconsin. The alloys were melted in a gas-fired furnace and poured into ASTM standard steel tensile molds preheated to 400 °C. The T6 heat treatment consisted of solutionizing at 537 °C for 8 hours, followed by quenching in 71-82 °C water. The quenched samples were held at room temperature for 12 hours, aged at 154 °C for 4 hours, and then cooled in air to room temperature.

This chapter can broadly be separated into the following sections:

1. Thermodynamic simulations using ThermoCalc software
 - a. Equilibrium
 - b. Non-equilibrium solidification (Scheil)
2. Metallography
 - a. Scanning electron microscopy
 - b. Energy dispersive X-ray spectroscopy

3. Solidification analysis using in-situ neutron diffraction

The subsequent sections aim to answer the following questions:

- 1) What phases are present in Al-RE-, Al-RE-Mg-, and Al-Si-RE-based alloys?
- 2) How do the RE additions affect the solidification characteristics of Al alloys?
- 3) What Al-RE alloy system shows the greatest potential for superior fitness-for-service performance as compared to conventional Al alloys?

4.1 Thermodynamics (ThermoCalc™)

A better understanding of which phases are expected to be present at specific temperatures can help the development process of alloys with specific strengthening intermetallics and optimal casting characteristics. Moreover, this information can be used to optimize heat treatment parameters, either to dissolve unwanted phases or to purposely precipitate intermetallics which are known to improve the alloy's performance. Table 4.1-1 displays the name of the abbreviated phases listed in the ThermoCalc simulations (left column) and their corresponding stoichiometries as shown in ThermoCalc (right column).

Table 4.1-1. List of phases shown in ThermoCalc simulations

Nomenclature	Stoichiometry
FCC_A1	Aluminum
AlMg_Beta	$(\text{Mg})_{89}(\text{Al,Zn})_{140}$
Al13CeMg6	$(\text{Al})_{0.67}(\text{Ce})_{0.05}(\text{Mg})_{0.28}$
Al11Ce3	$(\text{Al,Mg})_{0.79}(\text{Ce})_{0.21}$
Diamond_A4	Diamond Si
Al2Cu_C16	$(\text{Al,Ni,Mn,Fe})_2(\text{Al,Si,Cu,Ni,Mn,Fe})_1, \text{Al}_2\text{Cu}$
Al4Ce3Si6	$(\text{Al})_4(\text{Ce})_3(\text{Si})_6$
AlCeSi2	$(\text{Al})_1(\text{Ce})_1(\text{Si})_2$
Al15Si2M4	$(\text{Al})_{16}(\text{Mn,Fe})_4(\text{Si})_1(\text{Al,Si})_2, \text{Al}_{15}(\text{Fe,Mn})_3\text{Si}_2$
AlCeSi	$(\text{Al,Si})_2(\text{Ce})_1, \text{Ce}(\text{Al}_{1.2}\text{Si}_{0.8})$
Al7Cu2Fe	$(\text{Ni,Fe})_1(\text{Cu})_2(\text{Al})_7$
Al9Fe2Si2	$(\text{Al})_{0.6}(\text{Fe})_{0.15}(\text{Si})_{0.1}(\text{Al,Si})_{0.15}, \text{Al}_9\text{Fe}_2\text{Si}_2/\text{Al}_5\text{FeSi}$
Al11La3_LT	$(\text{Al})_{11}(\text{La})_3$
Al6Mn	$(\text{Al,Cu,Zn})_6(\text{Cu,Mn,Fe})_1$
LASi2_A2	$(\text{La})_{0.33}(\text{Si})_{0.67}$
LASi2_A1	$(\text{La})_{0.36}(\text{Si})_{0.64}$
Q_AlCuMgSi	$(\text{Al})_5(\text{Cu})_2(\text{Mg})_8(\text{Si})_6$
Al31Mn6Ni2	$(\text{Al})_{31}(\text{Mn})_6(\text{Ni})_2$
Al3Ti_LT	$(\text{Al,Si,Ti})_3(\text{Al,Ti})_1$
T_Phase	$(\text{Mg})_{26}(\text{Al,Mg})_6(\text{Al,Cu,Mg,Zn})_{48}(\text{Al})_1$
Al7Cu4Ni	$(\text{Al})_1(\text{VA,Cu,Ni,Fe})_1$
Mg2Si_C1	$(\text{Mg})_2(\text{Si,Sn})_1$
AlSi3Ti2	$(\text{Al,Si})_{0.2}(\text{Si})_{0.47}(\text{Ti})_{0.33}$
Al10CeFe2	$\text{Al}_{10}\text{CeFe}_2$
Al8CeM4	$(\text{Al})_{0.62}(\text{Ce})_{0.08}(\text{Al,Cu,Mn,Fe})_{0.31}$
Al13Fe4	$(\text{Al,Cu})_{0.63}(\text{Mn,Fe,Zn})_{0.23}(\text{VA,Al,Si,Zn})_{0.14}$
Al3Ti_D022	$(\text{Al,Si,Mn,Ti})_3(\text{Al,Mn,Ti})_1$
Al13Cr4Si4:	$(\text{Al})_{13}(\text{Cr})_4(\text{Si})_4$

The ThermoCalc simulations were performed following two solidification models, i) equilibrium solidification and ii) non-equilibrium solidification (i.e., Scheil model). Equilibrium solidification occurs when the process is slow enough for the system to be in equilibrium at all temperatures. Scheil's model contains the following three assumptions:

- 1) Diffusion of all elements in the liquid phase is infinitely fast
- 2) Diffusion of all elements in the solid phases is zero
- 3) The liquid/solid interface is in thermodynamic equilibrium

In actual practice, the solidification process follows neither equilibrium nor non-equilibrium cooling; however, depending on the experimental setup, the process may deviate towards one of the two modes, and thus, it is important to study both models.

4.1.1 Thermodynamics Al-6%Ce and Al-16%Ce

The binary Al-Ce phase diagram is shown below in Figure 4.1-1. The dashed red lines correspond to the composition of the hypoeutectic Al-6%Ce and the hypereutectic Al-16%Ce alloys described in this study (wt.% will be used for the remainder of this section unless otherwise stated). Based on the binary phase diagram, the Al-6%Ce and Al-16%Ce alloys should consist of primary α -Al + eutectic Al-Al₁₁Ce₃ and primary Al₁₁Ce₃ + eutectic Al-Al₁₁Ce₃, respectively. According to the phase diagram, the equilibrium and Scheil solidification charts (see Figure 4.1-1, Figure 4.1-2, and Figure 4.1-3), the liquidus and solidus temperatures of the Al-6%Ce alloy were determined to be ~650 and 640 °C, respectively.

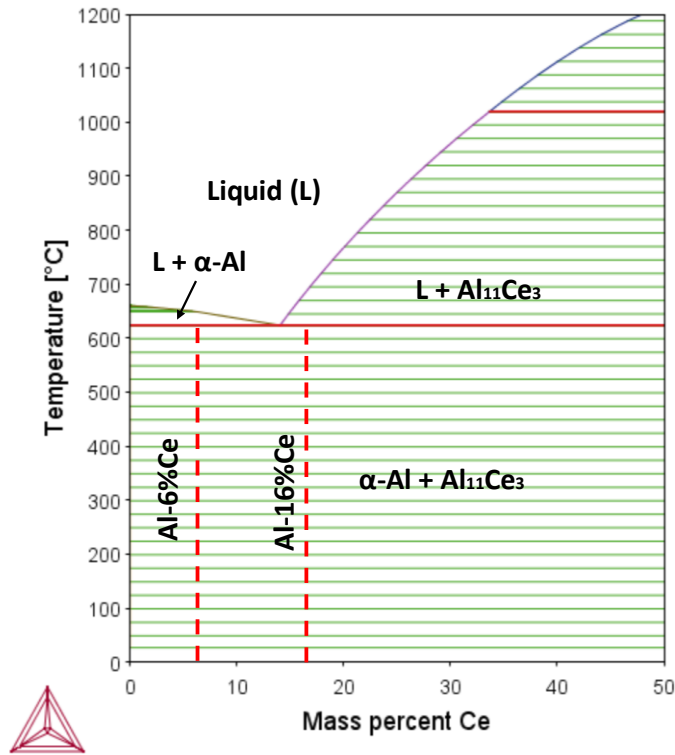


Figure 4.1-1. Binary Al-Ce phase diagrams calculated using ThermoCalc™ software

The liquidus temperature of the Al-6%Ce alloy was determined to be ~650 °C which is just below that of pure Al (~660 °C), markedly higher than an Al-6%Si alloy (~622 °C) and, slightly higher than an Al-6%Cu alloy (~645 °C). The Al-6%Si and Al-6%Cu alloys are not included in this study but are discussed here to compare the effects that Ce has on the solidification characteristics of Al as compared to more conventional alloying elements like Si and Cu. More importantly is the 63 and 93 °C increase in the Al-6%Ce alloy's solidus temperature as compared to the Al-6%Si alloy (i.e., 640 °C as compared to 577 °C) and the Al-6%Cu alloy (i.e., 640 °C as compared to 548 °C), respectively. Such a large increase of the melting temperature is expected to result in greater thermal stability of the Al-Ce alloy. Moreover, the solidification range of the Al-6%Ce alloy is ~36 °C less than an Al-6%Si alloy (i.e., 9 °C as compared to 45 °C) and 88 °C less than for the Al-6%Cu alloy. Generally, the shorter the solidification range, the lower the probability of forming porosity [139]. In addition, such a short solidification range essentially instantaneously freezes the microstructure and is expected to result in a very fine microstructure. No major differences were observed between the equilibrium and non-equilibrium diagrams for the Al-6%Ce. In fact, in both cases, the mass fraction of eutectic Al₁₁Ce₃ reached 10.24% (see Table 4.1-2).

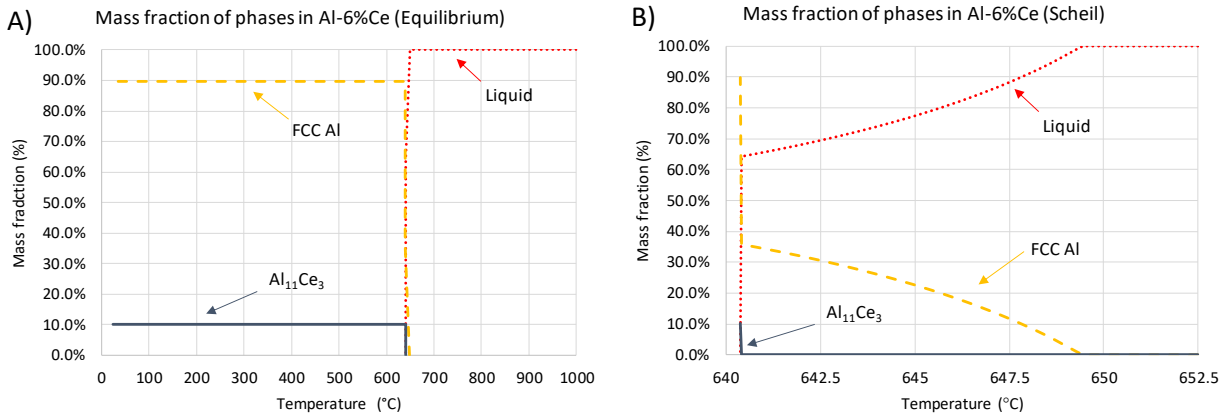


Figure 4.1-2. Mass fraction of phases in Al-6%Ce alloy, A) Equilibrium, B) Non-equilibrium Scheil solidification

Table 4.1-2. Mass fraction of phases in Al-6%Ce alloy

Phases	Mass Fraction (%)	
	Equilibrium (25 °C)	Scheil (640 °C)
FCC Al	BAL.	BAL.
Eutectic Al ₁₁ Ce ₃	10.24	10.24

Raising the Ce concentration to 16 wt.% resulted in a considerable increase in the alloy's liquidus temperature, reaching approximately 753 °C. Consequently, the solidification range also increased from 9 °C (Al-6%Ce) to 113 °C. Comparing this to the solidification range of a hypereutectic Al-16%Si alloy (i.e., ~54 °C), it appears that Ce concentrations above the eutectic composition (i.e., ~14 wt.% Ce) have a greater effect on increasing the liquidus temperature as compared to Si additions. Since the eutectic Cu composition in Al is ~33 wt.%, the solidification range of an Al-Cu decrease with Cu concentration is up to 33 wt.%. As a result, the large increase in the solidification range of the Al-16%Ce alloy has surpassed that of an Al-16%Cu alloy (i.e., ~113 °C vs ~67 °C). It should be noted that an Al alloy with such a high Cu concentration would not be economically feasible in practice and, thus, is only discussed for demonstration purposes. As mentioned previously, the large increase in the solidification range of the Al-16%Ce alloy may result in a higher quantity of porosity. In addition to raising the solidification range, the hypereutectic concentration of Ce also leads to the formation of primary Al₁₁Ce₃. This is clearly shown in the equilibrium diagram (see Figure 4.1-3), where a gradual formation of primary Al₁₁Ce₃ occurs between 753 and 640 °C (0 to 13.5%) which is followed by the instantaneous

growth of eutectic $\text{Al}_{11}\text{Ce}_3$ (13.5% to 27.3%). This phenomenon is also observed in the Scheil diagram. Similar to primary Si in hypereutectic Al-Si alloys, primary $\text{Al}_{11}\text{Ce}_3$ has been observed to form as large brittle precipitates [20], which have a negative impact on the alloys' toughness and ductility.

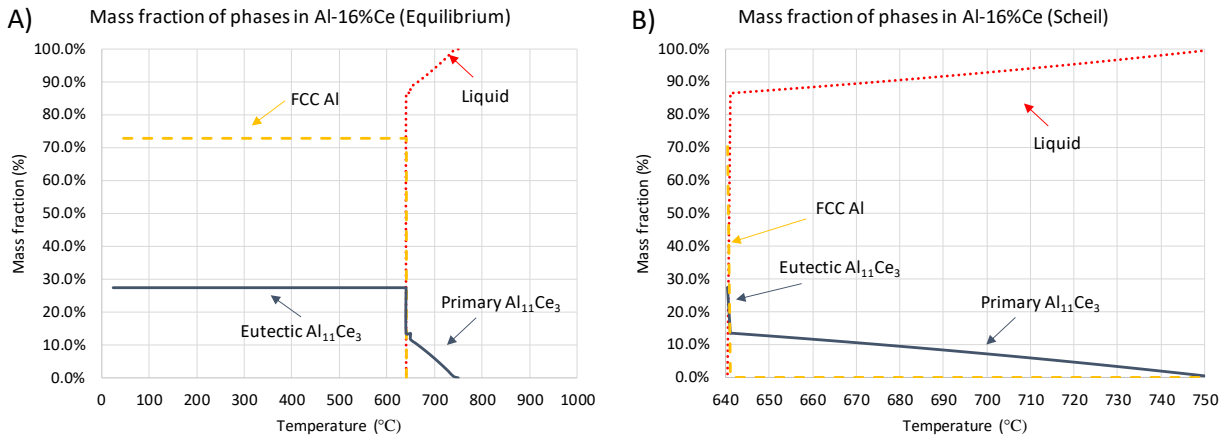


Figure 4.1-3. Mass fraction of phases in Al-16%Ce alloy, A) Equilibrium, B) Non-equilibrium Scheil solidification

Table 4.1-3. Mass fraction of phases in Al-16%Ce alloy

Phases	Mass Fraction (%)	
	Equilibrium (25 °C)	Scheil (640 °C)
FCC Al	BAL.	BAL.
Primary $\text{Al}_{11}\text{Ce}_3$	13.49	13.43
Eutectic $\text{Al}_{11}\text{Ce}_3$	13.81	13.87
Total $\text{Al}_{11}\text{Ce}_3$	27.30	27.30

4.1.2 Thermodynamics Al-8%Ce-10%Mg

In conventional Al alloys, Mg is commonly added to provide strengthening via precipitation of hardening intermetallics or through solid solution strengthening with the Al matrix. Thus, this section aims to characterize the effects of Mg on an Al-Ce based alloy (i.e., Al-8%Ce-10%Mg alloy). The particular Ce content of the alloy was selected to provide an optimal ratio of strength and ductility by raising the Ce composition closer to the Al-Ce eutectic concentration. In addition, the relatively high Mg concentration was chosen to dissolve the maximum amount Mg in the Al matrix, thereby providing the greatest contribution from solid solution strengthening.

The simulated isothermal (25 °C) ternary phase diagram of the Al-Ce-Mg system is shown below in Figure 4.1-4. At the nominal composition of Al-8%Ce-10%Mg (wt.%), FCC Al is accompanied by a high mass fraction of β -AlMg (~26.74%) and $Al_{11}Ce_3$ (~13.67%). The $Al_{11}Ce_3$ is known for its near nano-scale structure and high thermal stability [9], [122]; however, the β -AlMg phase has a very poor thermal stability and its phase fraction begins to rapidly decrease with temperatures above ~100 °C [9].

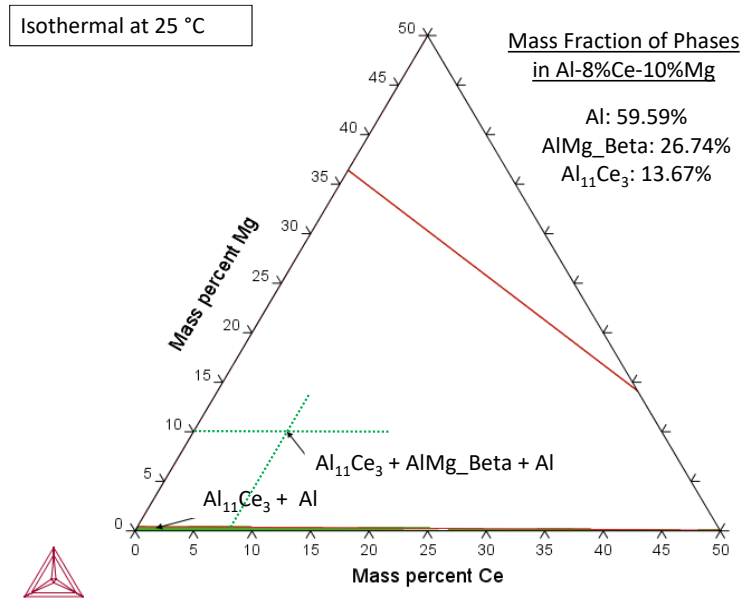
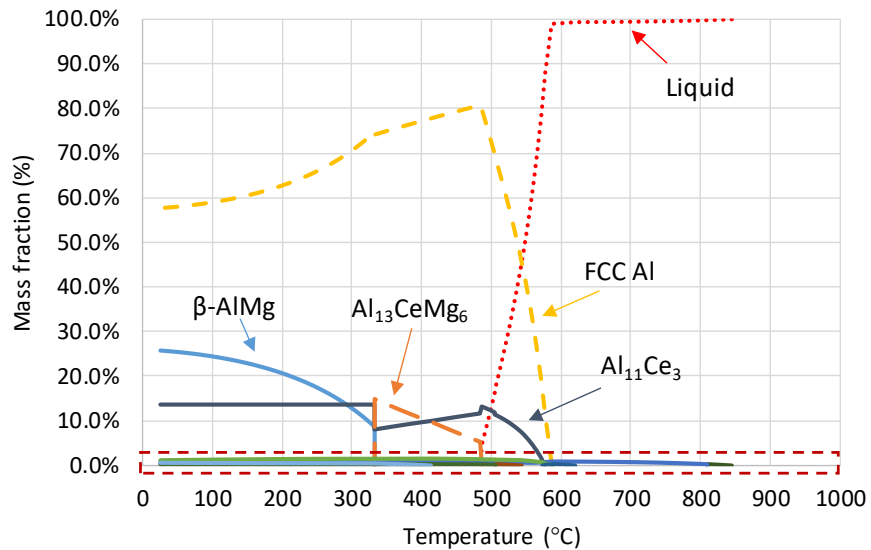


Figure 4.1-4. Ternary phase diagram of Al-8%Ce-10%Mg alloy at 25 °C

Due to the high purity of binary alloys, the cost associated with their production is not feasible for industrial applications. Thus, the Al-8%Ce-10%Mg alloy was produced using a commercial 535 aluminum alloy as the base metal which resulted in the minor addition of Si, Cu, Fe, Mn, and Ti as listed in Table 3.6-1. The resulting equilibrium solidification diagram is shown in Figure 4.1-5. The simulation suggests that the liquidus and solidus temperature of the Al-8%Ce-10%Mg alloy are ~846 °C and ~484 °C, respectively. However, the mass fraction of solid phases remains below 0.7% (comprised of Al_3Ti and Al_8CeM_4 (metastable)) until the nucleation temperature of Al (i.e., ~586 °C). The Mg addition appears to have decreased the nucleation temperature of Al by ~64 °C. Further, the solidus was determined to be 484 °C, nearly 157 °C lower than for the Al-6%Ce alloy. Clearly, the Mg addition has greatly increased the solidification range of the alloy (i.e., 102 vs. 9 °C), as compared to the Al-6%Ce alloy. It is likely that this will lead to a higher volume fraction of porosity.

A) Mass fraction of phases in Al-8%Ce-10%Mg (equilibrium)



B) Mass fraction of phases in Al-8%Ce-10%Mg (equilibrium)

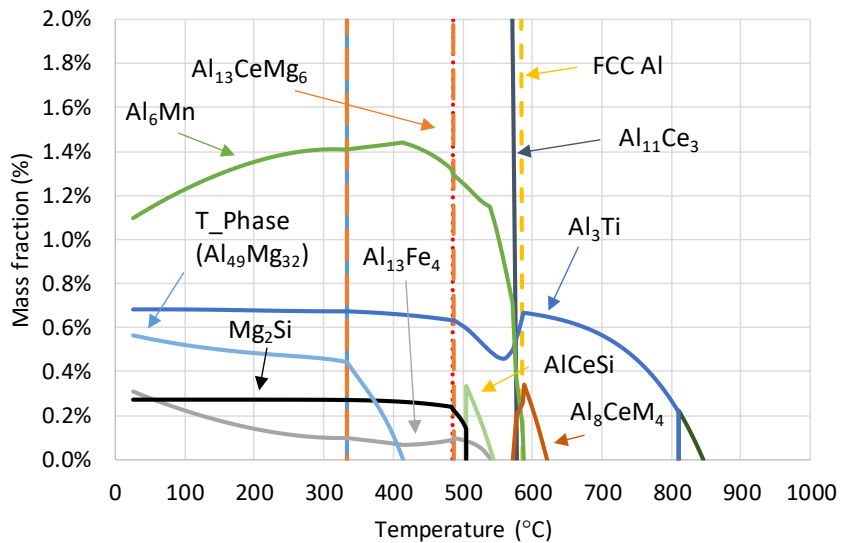


Figure 4.1-5. Mass fraction of phases in Al-8%Ce-10%Mg alloy A) full solidification process, B) progression of minority phase solidification (equilibrium solidification)

As the alloy cools from the liquidus to solidus temperature, the amount of liquid is replaced with a congruent growth of FCC-Al and $\text{Al}_{11}\text{Ce}_3$. Further cooling of the alloy from 446 °C to 332 °C decreases the amount of FCC-Al and $\text{Al}_{11}\text{Ce}_3$ while the mass fraction of an $\text{Al}_{13}\text{CeMg}_6$ phase increases from 0% to approximately 14%. Cooling the alloy one more degree results in a complete

breakdown of the $\text{Al}_{13}\text{CeMg}_6$ phase into $\beta\text{-AlMg}$ and back into $\text{Al}_{11}\text{Ce}_3$. This morphological change of the $\text{Al}_{13}\text{CeMg}_6$ phase suggests that it is a metastable phase that should not be observed in the microstructure at room temperature.

At the end of solidification and subsequent cooling to room temperature, the alloy primarily consists of FCC-aluminum, $\beta\text{-AlMg}$ (25.75%) and $\text{Al}_{11}\text{Ce}_3$ (13.64%). Although the $\text{Al}_{11}\text{Ce}_3$ phase has shown greater temperature stability, the work presented in [9] suggests that the $\beta\text{-AlMg}$ phase begins to coarsen above 100 °C. Moreover, the presence of $\beta\text{-AlMg}$ removes a considerable amount of the available Mg for solid solution strengthening the alloy. Fortunately, some of the Mg is also present as a hardening precipitate, specifically, Mg_2Si . Mg_2Si is known to improve the strength of Al alloys; however, its contribution decreases exponentially above 170 °C and, thus, its presence is only beneficial for moderate temperature applications. In addition, the poor thermal stability of the T phase (see Table 4.1-1 for composition) lowers the alloy's resistance to elevated temperatures.

Due to the impurity elements in the 535 Al-base alloy, several low mass fraction phases are also present in the microstructure. Although low in mass fraction, the presence of some of these minority phases can be deleterious to the mechanical properties of the alloys. For example, the $\text{Al}_{13}\text{Fe}_4$ phase commonly forms with a needle-like morphology which acts as a stress concentrator and crack initiation site, both of which impair the alloy's toughness and ductility. The mass fraction of all phases present in the alloy is shown in Table 4.1-4.

Table 4.1-4. Mass fraction of phases in Al-8%Ce-10%Mg alloy

Phases	Mass Fraction (%)	
	Equilibrium (25 °C)	Scheil (446 °C)
FCC Al	BAL.	BAL.
AlMg beta	25.75	10.56
Al ₁₃ CeMg ₆	0 (14.88)*	6.32
Al ₁₁ Ce ₃	13.64	10.70
Al ₆ Mn	1.44	0.24
Al ₃ Ti_LT	0.68	0.44
T_Phase	0.57	0.45
Al ₈ CeM ₄	0 (0.34)*	0.34
AlCeSi	0 (0.34)*	0.22
Al ₁₃ Fe ₄	0.31	0.15
Mg ₂ Si_C1	0.27	0.16
Al ₃ Ti_D022	0 (0.22)*	0.22
Al ₁₀ CeFe ₂	0 (0.22)*	0.36

Note: (max values)

*Metastable at specific temperature (see Figure 4.1-5)

According to the non-equilibrium mode of solidification, the liquidus and solidus temperature of the alloy are 846 °C and 446 °C, respectively. Similar to the discussion above, only a small fraction of solid phases exists above the initial nucleation of Al (i.e., 586 °C). Following this initial growth of FCC Al, Al₁₁Ce₃ precipitates begin to nucleate below 577 °C. Due to the assumptions associated with the Scheil model, there is no diffusion in the solid phase and, thus, the mass fraction of these two phases continue to grow until the alloy has completely solidified. At approximately 487 °C, a gradual growth of the Al₁₃CeMg₆ phase is observed up to approximately 6.3%. From 449 °C to 446 °C, a near instantaneous growth of the β-AlMg (~10.6%) is observed. Similar to the equilibrium solidification, the impurities in the 535 alloy led to several minority phases, each with a mass fraction between 0.15% and 0.45% (see Table 4.1-4.).

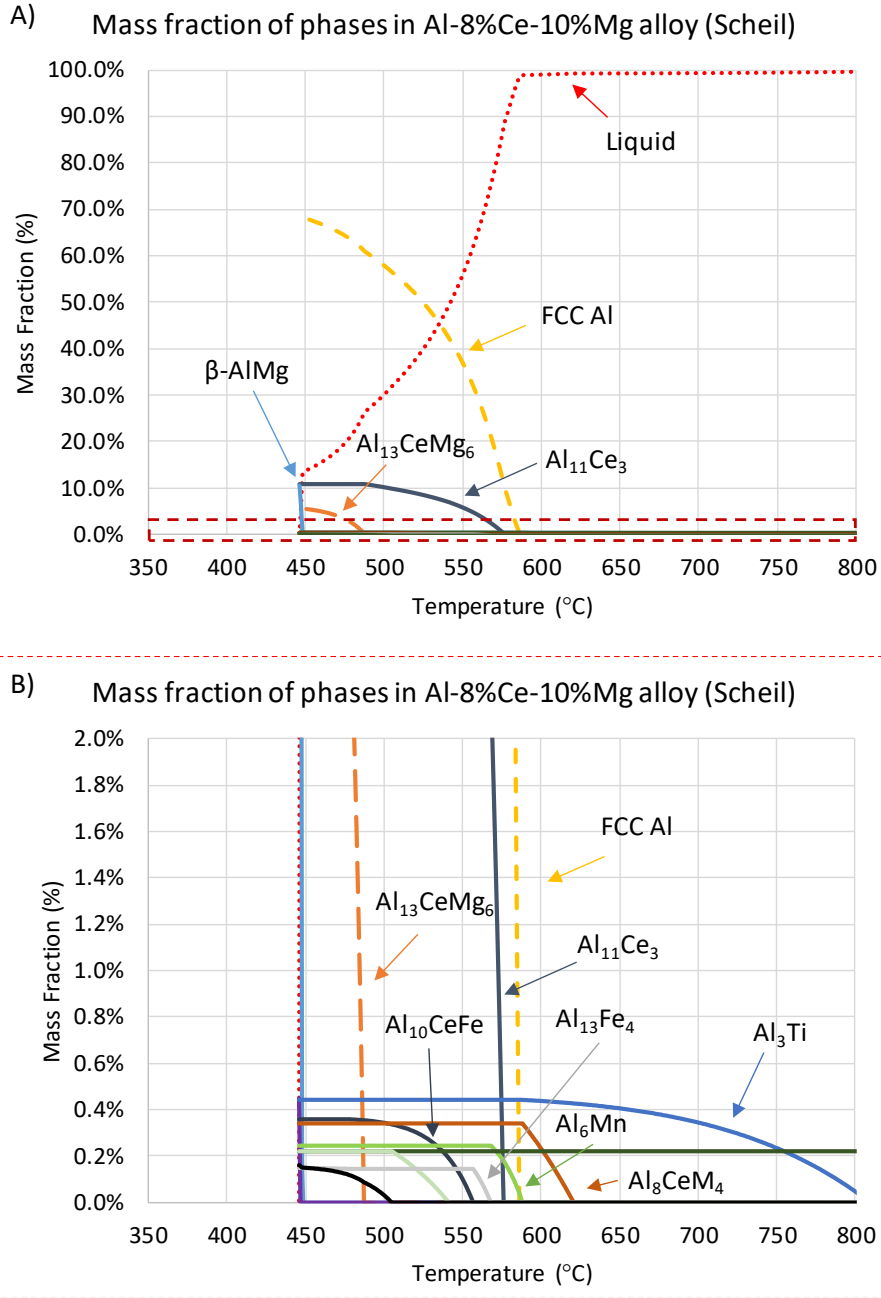


Figure 4.1-6. Mass fraction of phases in Al-8%Ce-10%Mg alloy A) full solidification process, B) progression of minority phase solidification (non-equilibrium Scheil solidification)

Combined with the poor thermal stability of the β -AlMg phase, the prolonged solidification range may increase the localized density of microstructural defects, and consequently, the benefits from the solution-strengthened Al-Mg matrix will be likely be offset. Consequently, the performance of this alloy may not be sufficient at the planned testing temperatures of 250 and 300 °C.

4.1.3 Thermodynamics of A356 and A356RE

Focused on further improving the tensile properties and heat treatability of Al alloys containing rare earth elements, Z. Sims et al. developed an Al-Ce-Si-Mg alloy [122]. They reported that addition of Si and Mg improved the heat treatability of the alloy and resulted in improved room temperature YS and UTS values in the T6 condition. Moreover, they report that the microstructure consists of a high-volume fraction of thermally stable AlCeSi intermetallics which should result in a greater magnitude of property retention at elevated temperatures.

To diversify the supply chain and lower production costs, some manufacturers have begun utilizing rare earth mischmetal as opposed to pure cerium metal (as used in the Al-6%Ce, Al-16%Ce and Al-8%Ce-10%Mg alloys described in the previous section). Using RE mischmetal as a substitute for Ce metal has also shown to result in greater yield strengths with only a slight decrease in the UTS [116]. Although the UTS is an important parameter when considering alloys for powertrain applications, a higher YS is more desirable, as this lowers the chance of permanent dimensional distortion.

Thus, this chapter aims to evaluate the effects that RE mischmetal has on the thermodynamics of Al-Si-RE alloys, specifically on the commercially available powertrain alloy, A356. Unlike the A319-type powertrain alloy, A356 has considerably greater ductility and, thus, the reduction of ductility caused by the presence of the hard RE-bearing intermetallics should be offset. A certain magnitude of ductility is desired for powertrain components as it provides automotive manufacturers with an additional safety factor since the component should show signs of distortion prior to cracking. In addition to the benefits associated with greater ductility, the lower concentration of Cu in the A356 alloy, as compared to A319 (less than 0.1 wt.% as compared to nearly 3 wt.%), decreases the alloy's density and coefficient of thermal expansion, thereby enabling production of lighter and more geometrically stable castings.

Beginning with the RE-free A356 alloy (composition listed in Table 3.6-1), the equilibrium solidification diagram below suggests that at room temperature, the A356 alloy will primarily consist of FCC-Al, eutectic Si (6.58%), $Q_{Al_5Cu_2Mg_8Si_6}$ (0.98%), $Al_9Fe_2Si_2$ (0.74%), Al_3Ti_{LT} (0.55%), Mg_2Si (0.43%), and a small concentration of minority phases. It should be noted that the current version of ThermoCalc™ only contains La and Ce and, thus, the effects of the Nd and Pr in the RE mischmetal are not available. The presence of $Q_{Al_5Cu_2Mg_8Si_6}$ and Mg_2Si can improve

the mechanical properties of Al alloys, depending on their morphology and the temperature of the environment (see Chapter 2). On the other hand, the $\text{Al}_9\text{Fe}_2\text{Si}_2$ phase is very brittle and its needle-like morphology acts as a stress concentrator and crack initiation site, leading to impaired toughness and ductility. Consequently, it is common for manufacturers to introduce Mn to the alloy to transform this phase to the more morphologically favorable $\alpha\text{-Al}_{15}(\text{Fe},\text{Mn})_3\text{Si}_2$.

It appears that the extremely slow cooling rate associated with equilibrium solidification, as well as the low Mn concentration (0.1 wt.%) in the A356 alloy, has resulted in only a partial transformation of the harmful $\text{Al}_9\text{Fe}_2\text{Si}_2$ phase. Future considerations should include raising the Mn concentration in this alloy to lower the mass fraction of the $\text{Al}_9\text{Fe}_2\text{Si}_2$ phase.

The nucleation temperature of Al and the solidus temperatures of the A356 alloy were determined to be ~ 614 °C and 562 °C, respectively. As compared to the Al-6%Ce alloy, the solidus temperature has decreased quite significantly (i.e., 562 vs. 641 °C) and the solidification range has increased (i.e., 9 vs. 52 °C). However, the solidification range is nearly half that of the Al-8%Ce-10%Mg alloy, which is likely due to the minimal amount of Mg in the A356 alloy.

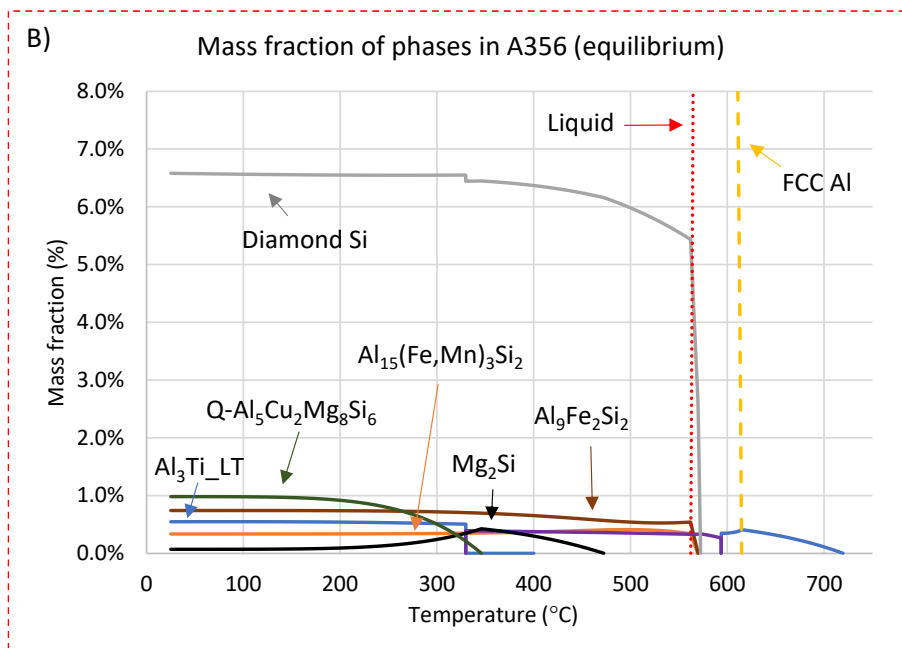
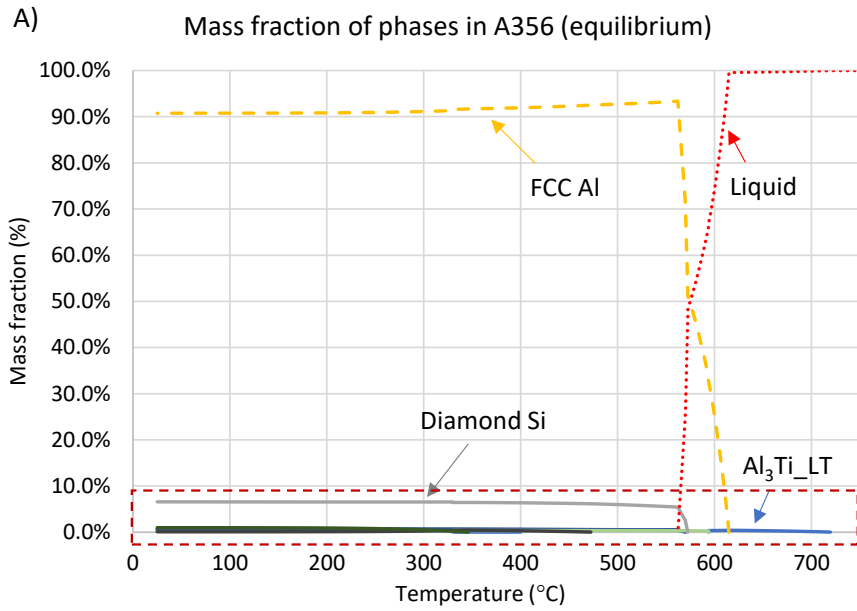


Figure 4.1-7. Mass fraction of phases in A356 alloy A) full solidification process, B) progression of minority phase solidification (equilibrium solidification)

Table 4.1-5. Mass fraction of phases in A356 alloy

Phases	Mass Fraction (%)	
	Equilibrium (25 °C)	Scheil (533 °C)
FCC Al	BAL.	Bal.
Diamond (Si)	6.58	5.47
Q _{Al₅Cu₂Mg₈Si₆}	0.98	-
Al ₉ Fe ₂ Si ₂	0.74	0.43
Al ₃ Ti_LT	0.55	0.40
Mg ₂ Si	0.43	0.16
Al ₁₅ (Fe,Mn) ₃ Si ₂	0.41	0.37
AlSi ₃ Ti ₂	0 (0.39)*	-
Al ₁₈ Fe ₂ Mg ₆ Si ₁₀	-	0.26

Note: (max values)

The evolution of phases under non-equilibrium conditions is shown below in Figure 4.1-8. Nearly all of the same phases shown in the equilibrium chart above were observed in the Scheil model; however, the presence of a new Al₁₈Fe₂Mg₆Si₁₀ phase was observed. The stoichiometry of this phase suggests that is the commonly reported π -Al₉FeSi₃Mg₅ [212]. This phase has a slightly less detrimental effect on the mechanical properties of Al alloy as compared to the Al₉Fe₂Si₂ phase; however, it is still considered less favorable as compared to Al₁₅(Fe,Mn)₃Si₂.

The Q_{Al₅Cu₂Mg₈Si₆} shown in the equilibrium chart was not observed in the non-equilibrium chart. This is believed to be attributed to the low Cu concentration in the A356 alloy as well as the high solubility of Cu in FCC Al (~5 wt.%) at these elevated temperatures. The mass fraction of each intermetallic is listed in Table 4.1-5.

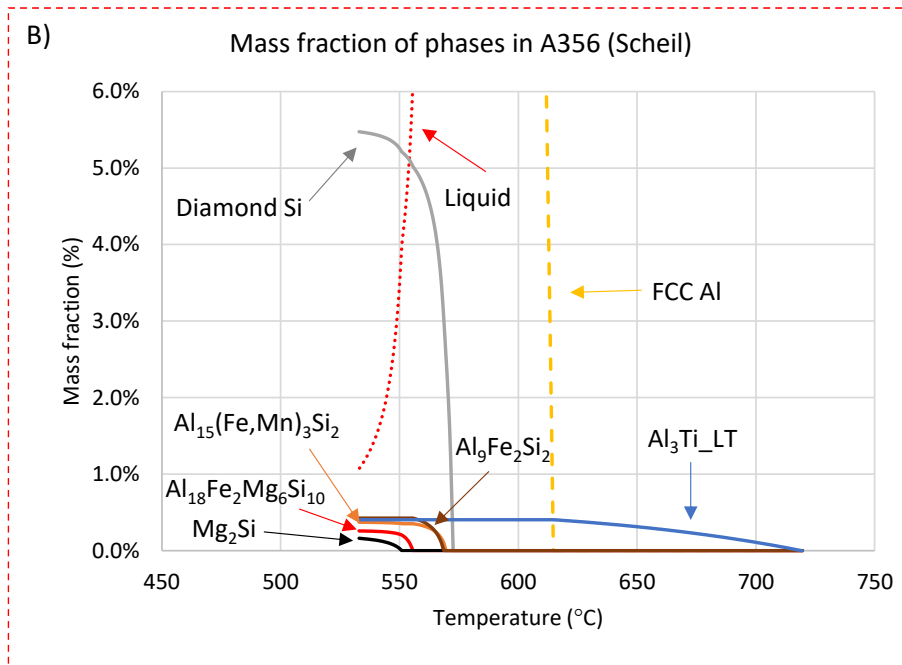
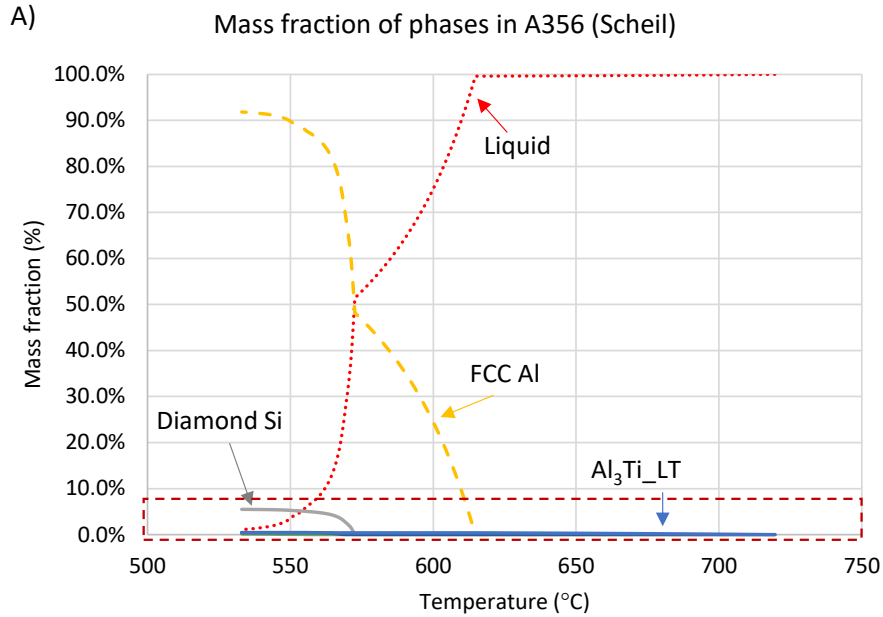


Figure 4.1-8. Mass fraction of phases in A356 alloy A) full solidification process, B) progression of minority phase solidification (non-equilibrium Scheil solidification)

The equilibrium solidification diagram for the A356RE alloy is shown below in Figure 4.1-9. The simulation suggests that, at room temperature, the alloy should consist of Al, eutectic Si, $\text{Al}_4\text{Ce}_3\text{Si}_6$, $\text{Al}_{11}\text{La}_3$, $\text{Al}_5\text{Cu}_2\text{Mg}_8\text{Si}_6$, $\text{Al}_9\text{Fe}_2\text{Si}_2$, $\text{Al}_3\text{Ti_LT}$, Mg_2Si , and $\text{Al}_{15}(\text{Fe},\text{Mn})_3\text{Si}_2$. The mass fraction of each phase is listed in Table 4.1-6. In addition to these phases, some metastable phases were also

observed to form during the solidification process, specifically AlCeSi, AlCeSi₂, LaSi₂_A1, LaSi₂_A2, and AlSi₃Ti₂.

Due to the high melting temperature of the La-Si phases, a small mass fraction of the LaSi₂_A1 phase was observed above 1000 °C (i.e., ~0.6%) which transforms into LaSi₂_A2 at 822 °C. Subsequently, the nucleation of the AlCeSi phase begins at 811 °C. This phase reaches a maximum mass fraction of 2.23% at 612 °C before temporarily transforming into AlCeSi₂ and then, finally, into Al₄Ce₃Si₆ which reaches a maximum mass fraction of 3.03%. The Al₄Ce₃Si₆ phase has been reported to improve the thermal stability of Al-Si-RE alloys [9] and is one of the reasons for the impressive increase in elevated temperature strength of the A356 system [213]. In addition to the Al₄Ce₃Si₆ phase, the presence of La in the RE mischmetal led to the formation of Al₁₁La₃. This phase has nearly identical properties as the Al₁₁Ce₃ phase, and its presence further improves the alloy's thermal stability [214].

Combating the positive benefits from the thermally-stable Al₁₁La₃ and Al₄Ce₃Si₆ phases, ~0.74% of the harmful Al₉Fe₂Si₂ phase was observed. The Al₉Fe₂Si₂ phase is also commonly reported as Al₅FeSi. The nucleation of this phase begins at ~570 °C which is followed by a rapid increase in the mass fraction to 0.53%. Subsequently, the mass fraction of this phase slowly increases until about 140 °C, after which the mass fraction remains relatively unchanged. Congruently, the more desirable Al₁₅(Fe,Mn)₃Si₂ phase begins to nucleate just prior to the onset of the Al₉Fe₂Si₂ phase, reaching a maximum mass fraction of 0.43%. This suggests that due to the low amount of Mn in the alloy (i.e., 0.1 wt.%), the Al₉Fe₂Si₂ phase is the preferential Fe phase to form. This supports the work done by N. Below et al. [215].

The nucleation and solidus temperature of FCC-Al was observed to be 617 and 562 °C, respectively. The moderate solidification range (i.e., 55 °C) of FCC-Al suggests that porosity, caused by slow solidification, should not be a considerable issue.

Due to moderate Mg concentration in the A356RE alloy, it was expected that the Al₉FeMg₃Si₅ would be observed in the solidification diagram but, instead, part of the Mg forms a solid solution with the Al matrix and the rest is present in the Q_Al₅Cu₂Mg₈Si₆ phase. Fortunately, the Q_Al₅Cu₂Mg₈Si₆ phase improves the thermal stability of the alloy and is much more desirable as compared to the Al₉FeMg₃Si₅ phase.

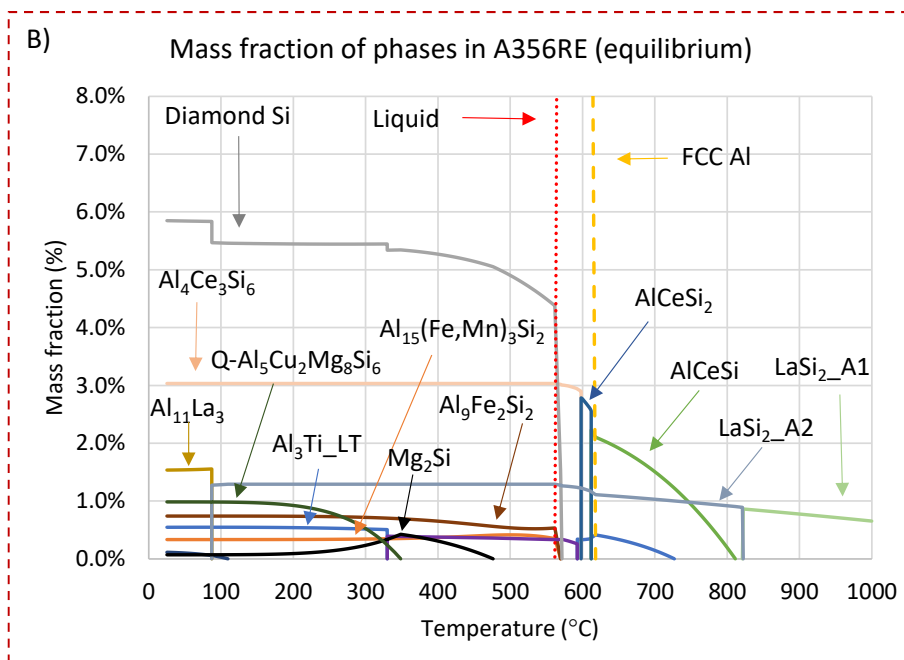
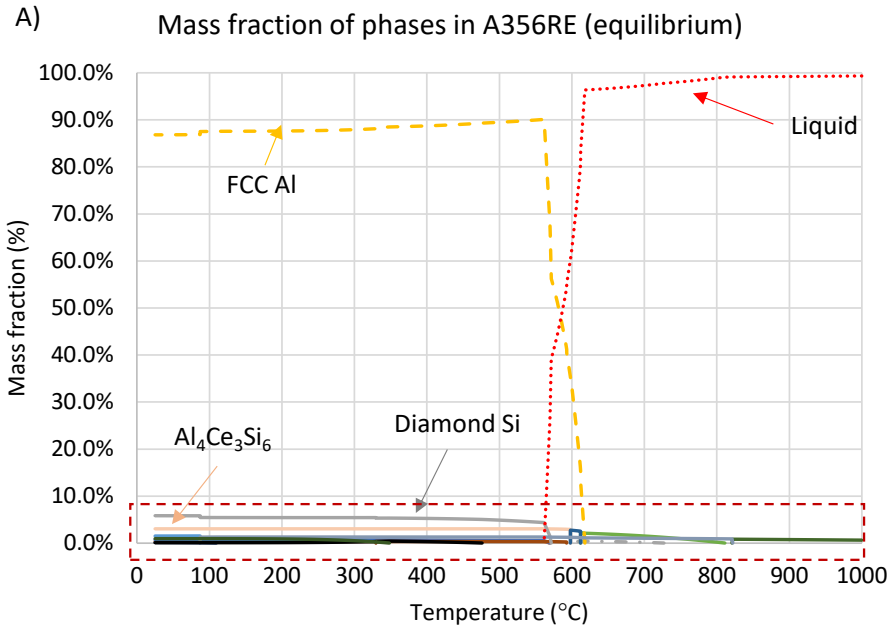


Figure 4.1-9. Mass fraction of phases in A356RE alloy A) full solidification process, B) progression of minority phase solidification (equilibrium solidification)

Table 4.1-6. Mass fraction of phases in A356RE alloy

Phases	Mass Fraction (%)	
	Equilibrium (25 °C)	Scheil (532 °C)
FCC Al	BAL.	BAL.
Diamond (Si)	5.85	4.69
Al ₄ Ce ₃ Si ₆	3.03	0.15
AlCeSi ₂	0 (2.79)*	0.25
AlCeSi	0 (2.23)*	2.22
Al ₁₁ La ₃	1.56	-
LaSi ₂ _A2	0 (1.29)*	0.40
Q_Al ₅ Cu ₂ Mg ₈ Si ₆	0.98	-
LaSi ₂ _A1	0 (0.86)*	0.86
Al ₉ Fe ₂ Si ₂	0.74	0.43
Al ₃ Ti_LT	0.55	0.41
Mg ₂ Si	0.43	0.16
Al ₁₅ (Fe,Mn) ₃ Si ₂	0.42	0.37
AlSi ₃ Ti ₂	0 (0.39)*	-
Al ₁₈ Fe ₂ Mg ₇ Si ₁₀	-	0.26

Note: (max values)

*Metastable at specific temperature

The Scheil diagram for the A356RE alloy is shown below in Figure 4.1-10. Due to the assumptions associated with Scheil solidification, the AlCeSi phase could not transform in the AlCeSi₂ or Al₄Ce₃Si₆ phases. Similarly, the growth of the Q_Al₅Cu₂Mg₈Si₆ phase was also halted by the assumption that zero diffusion occurs in the solid state. The non-equilibrium mode of solidification appears to have resulted in the formation of the Al₉FeMg₃Si₅ phase (i.e., Al₁₈Fe₂Mg₆Si₁₀ phase). The presence of this phase suggests that, depending on the cooling rate, this phase may or may not be present in the microstructures. However, it is likely that a combination of equilibrium and non-equilibrium solidification will occur, and thus, it is expected that some of this phase will be present at room temperature. The Scheil diagram indicates that this phase begins to nucleate at 556 °C and reaches a maximum mass fraction of 0.26% by 532 °C. In addition to this phase, the Al₉Fe₂Si₂ phase was also observed; however, in a considerably lower amount (~0.43%).

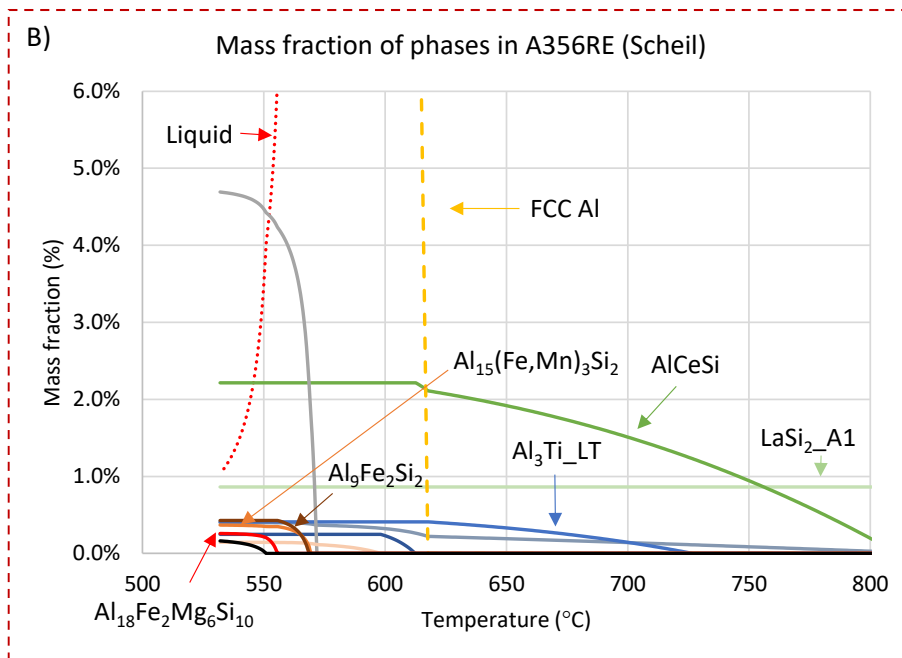
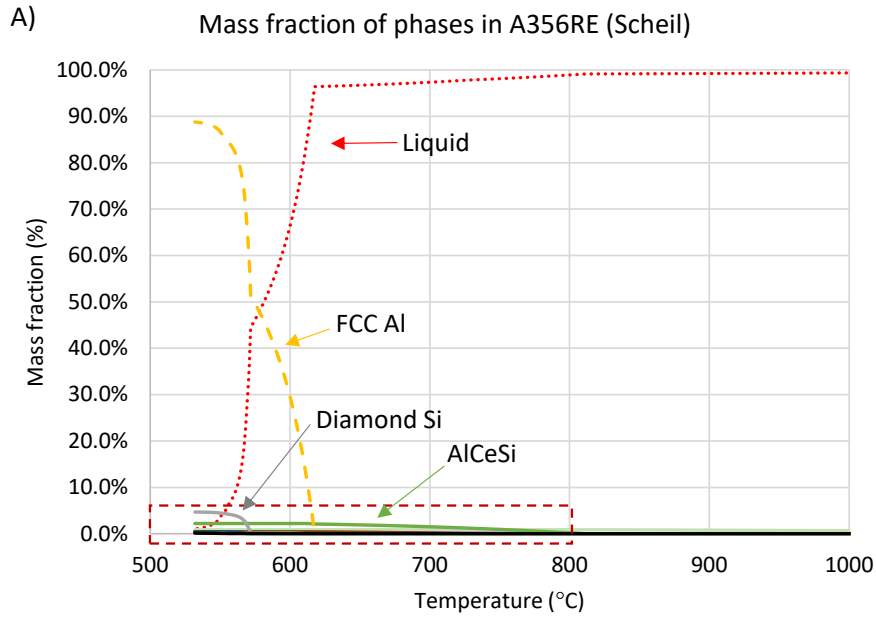


Figure 4.1-10. Mass fraction of phases in A356RE alloy A) full solidification process, B) progression of minority phase solidification (non-equilibrium Scheil solidification)

The relatively short solidification range of the A356RE alloy is expected to result in minimal microstructural defects like porosity. Moreover, the presence of the thermally stable AlCeSi phases will surely improve the thermal stability of the A356 alloy.

4.1.4 Thermodynamics A390 and A390RE

In addition to studying the effects of RE elements on the hypoeutectic Al-Si alloy, the solidification characteristics of a hypereutectic Al-Si powertrain alloy, A390, was also investigated. The equilibrium solidification diagram for the A390 alloy is shown below in Figure 4.1-11. The hypereutectic Si content in this alloy lead to a dual stage growth of Si, the first being the slow growth of primary Si from ~678 °C to ~560 °C which is then followed by more rapid growth of eutectic Si until ~500 °C. This primary growth of Si leads to a greatly prolonged solidification range (i.e., approximately 178 °C) which is more than triple the solidification temperature range of the hypoeutectic A356 alloy. To add to this, a much greater mass fraction of the harmful $\text{Al}_9\text{Fe}_2\text{Si}_2$ phase (i.e., ~3.60%) may be present in the microstructure at room temperature (see Table 4.1-7). Fortunately, two strengthening intermetallics are present in the alloy, namely Al_2Cu (7.14%) and $\text{Q_Al}_5\text{Cu}_2\text{Mg}_8\text{Si}_6$ (2.12%).

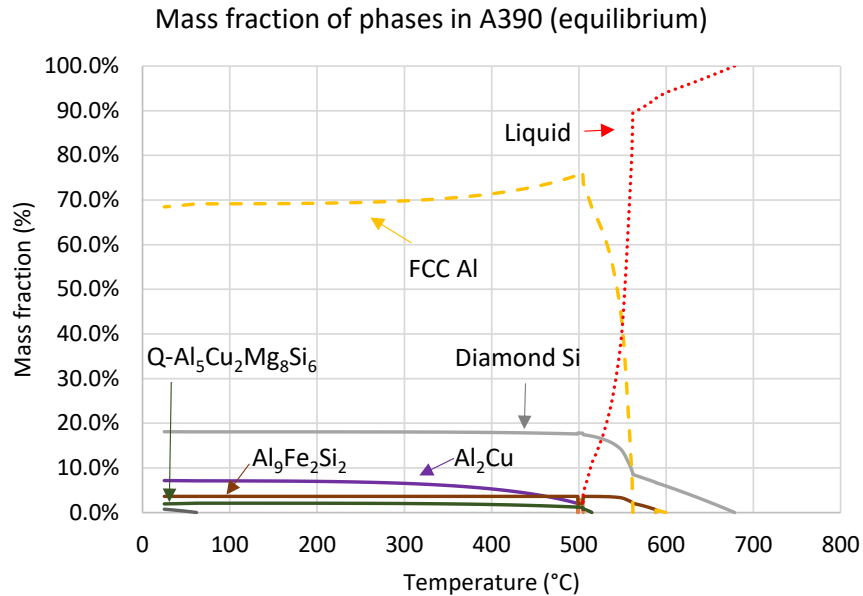


Figure 4.1-11. Mass fraction of phases in A390 alloy (equilibrium solidification)

Table 4.1-7. Mass fraction of phases in A390 alloy

Phases	Mass Fraction (%)	
	Equilibrium (25 °C)	Scheil (462 °C)
FCC Al	BAL.	BAL.
Diamond (Si)	18.07	17.07
Al ₂ Cu	7.14	5.10
Al ₉ Fe ₂ Si ₂	3.60	2.98
Al ₇ Cu ₂ Fe	0 (3.03)*	
Q_ Al ₅ Cu ₂ Mg ₈ Si ₆	2.12	1.46
AlFeSi_T4	0 (0.57)*	0.57

Note: *(max values)

The simulated non-equilibrium solidification of the A390 alloy did not reveal a significant difference in the type of phases in the alloy (see Figure 4.1-12). However, it was observed that the mass fraction of the strengthening phases, Al₅Cu₂Mg₈Si₆ and Al₂Cu, decreased (see Table 4.1-7). This decrease was presumed to be attributed to the higher solubility of Cu in the Al matrix at these elevated temperatures as compared to the ambient temperature shown for the equilibrium solidification.

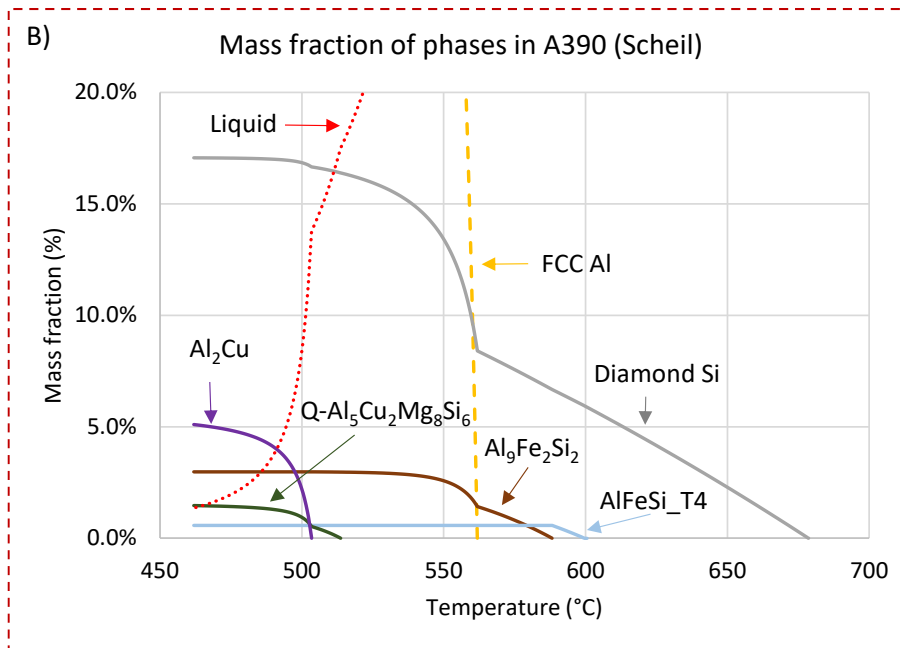
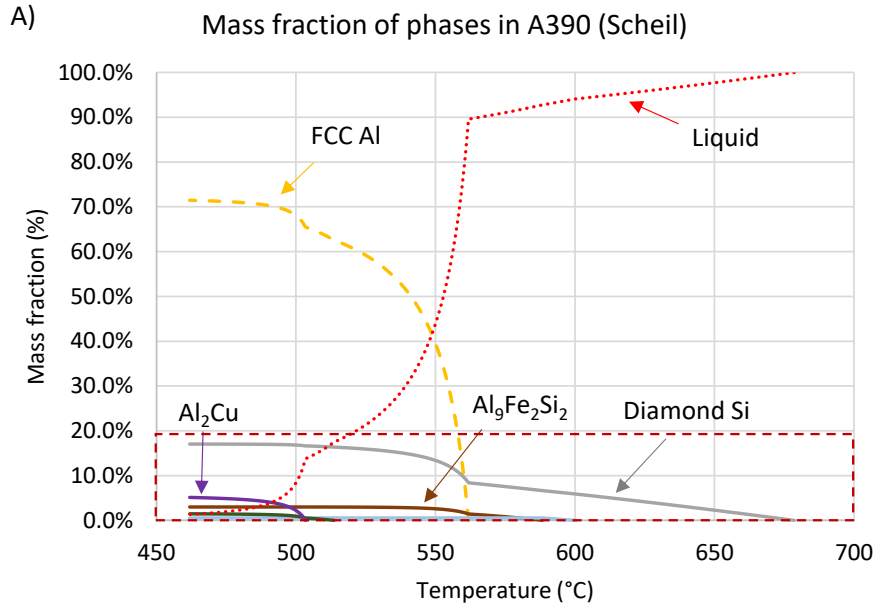


Figure 4.1-12. Mass fraction of phases in the A390 alloy A) full solidification process, B) progression of minority phase solidification (non-equilibrium Scheil solidification)

The extremely long solidification range of the A390 alloys suggests that the likelihood of producing defect-free castings is much lower than for the A356 type alloy. Moreover, as discussed in Chapter 2, the hypereutectic concentration of Si results in the formation of primary silicon, a very hard but brittle phase which can impair the alloy's toughness.

Similar to the A356RE alloy, the addition of the RE mischmetal to the A390 alloy led to a number of RE-bearing phases during and after solidification; however, the solidus and liquidus temperature remained relatively unchanged.

All of the LaSi and AlCeSi phases that were observed in the A356RE alloy were also observed in the A390RE alloy but in much higher quantity. However, the higher Ce concentrations appears to have led to the short presence of a new metastable precipitate (i.e., CeSi₂) between 680 and 646 °C. No other new RE-bearing phases were observed as compared to the A356RE alloy.

The elevated concentration of Cu in this alloy led to the formation of Al₂Cu in similar quantities as compared to the A390 alloy. This phase is known to improve the mechanical properties of Al alloys up to about 200-225 °C; however, further increasing the temperature can lead to coarsening and dissolution of the phase.

The high concentration of impurity iron led to a considerable increase in the mass fraction of the harmful Al₉Fe₂Si₂ phase as compared to the A356RE alloy (3.60 vs 0.74%). The RE addition has not affected the mass fraction of Fe-bearing phases in the A390 alloy.

Similar to the A356RE alloy, the presence of La forms two metastable LaSi phases well above 1000 °C. It is these phases which form the desirable Al₁₁La₃ phase.

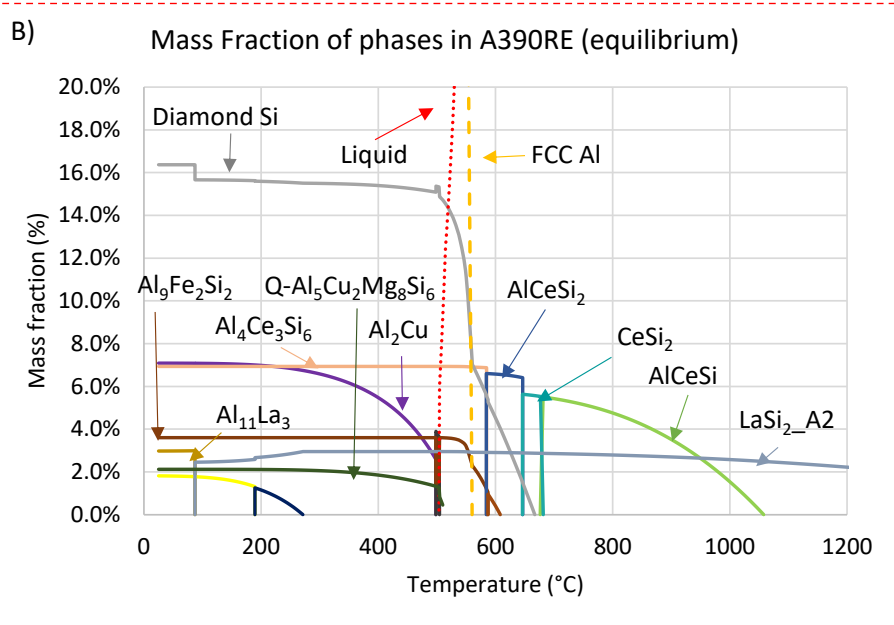
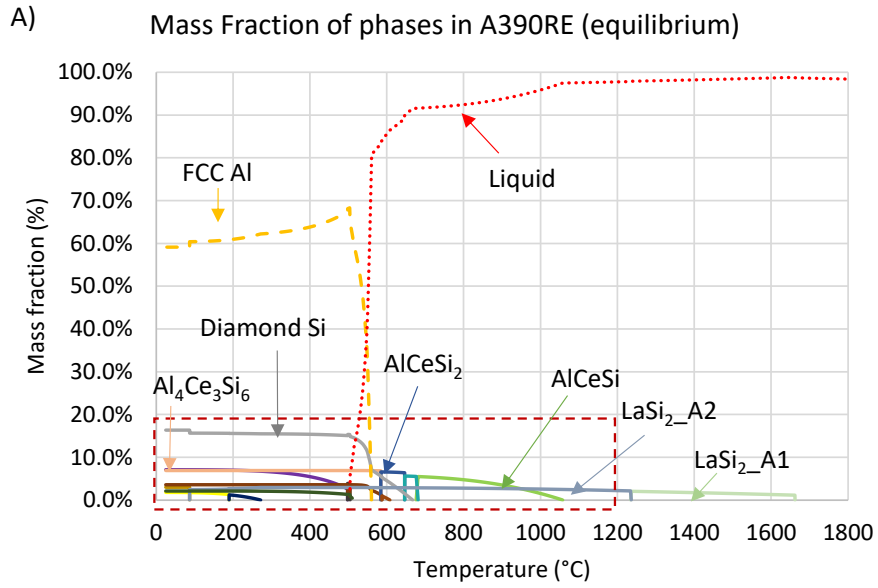


Figure 4.1-13. Mass fraction of phases in A390RE alloy A) full solidification process, B) progression of minority phase solidification (equilibrium solidification)

Table 4.1-8. Mass fraction of phases in A390RE

Phases	Mass Fraction (%)	
	Equilibrium (25 °C)	Scheil (458 °C)
FCC Al	BAL.	BAL.
Diamond (Si)	16.37	15.09
Al ₂ Cu ₁₆	7.08	5.19
Al ₄ Ce ₃ Si ₆	6.93	0.06
AlCeSi ₂	0 (6.60)*	0.20
CeSi ₂	0 (5.63)*	0.13
AlCeSi	0 (5.50)*	5.48
Al ₇ Cu ₂ Fe	0 (3.89)*	-
Al ₉ Fe ₂ Si ₂	3.60	2.59
Al ₁₁ La ₃	2.99	-
LaSi ₂ _A2	0 (2.95)*	2.07
Q_Al ₅ Cu ₂ Mg ₈ Si ₆	2.12	1.49
LaSi ₂ _A1	0 (2.07)*	2.07
Al ₁₅ (Fe,Mn) ₃ Si ₂	0.42	-
AlSi ₃ Ti ₂	0 (0.39)*	-
AlFeSi_T4	-	0.93

Note: (max values)

The non-equilibrium solidification chart for the A390RE alloy is below in Figure 4.1-14. A nearly identical solidus temperature was observed as compared to the RE-free alloy. Due to the complex nature of the AlCeSi phases, the mass fraction of these phases has changed significantly as compared to the equilibrium solidification results shown in Table 4.1-8.

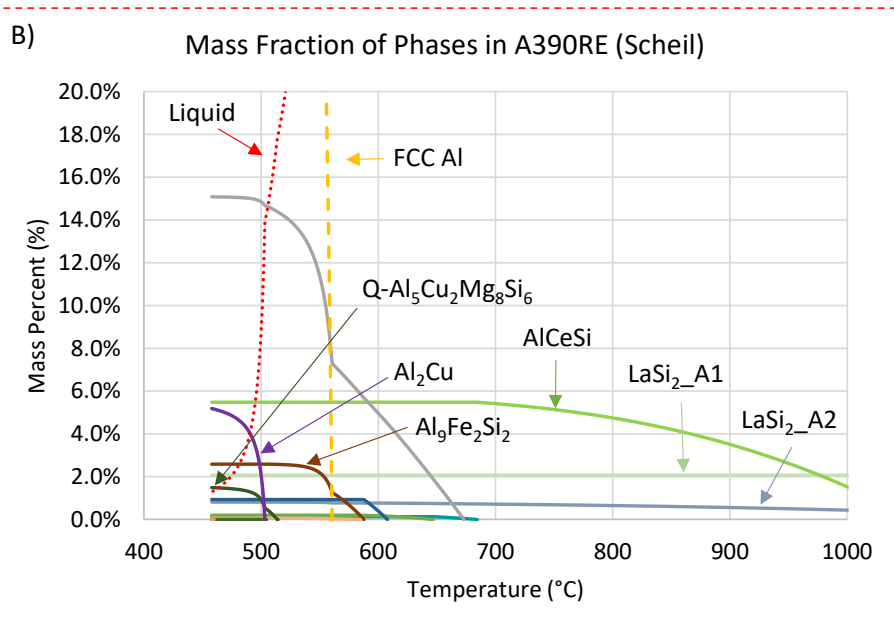
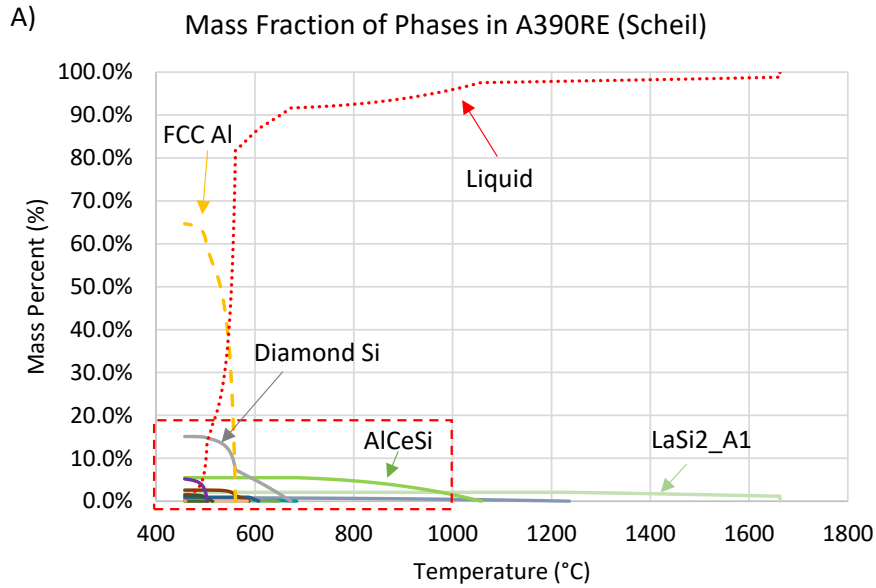


Figure 4.1-14 Mass fraction of phases in A390RE alloy A) full solidification process, B) progression of minority phase solidification (non-equilibrium Scheil solidification)

Similar to the RE-free A390 alloy, the prolonged solidification range of this alloy may result in a large number of microstructural defects during the casting process. If sufficiently high cooling rates can be attained, these defects may have a less pronounced effect. However, this attribute limits the use of this alloy to permanent mold castings or chilled sand castings.

The following information summarizes the key information from the simulation results:

- 1) The RE additions do not significantly affect the solidification characteristics of Al and Si in the A356 and A390 alloys.
- 2) Depending on the solidification mode (i.e., equilibrium or non-equilibrium), the mass fraction of certain phases may differ significantly.
- 3) The RE additions led to a number of RE-bearing phases ($\text{Al}_4\text{Ce}_3\text{Si}_6$, AlCeSi , and $\text{Al}_{11}\text{Ce/La}_3$) that are known to have good thermal stability above the target engine operating temperature of 300 °C.
- 4) The presence of impurity Fe in the A356 and A390 alloys leads to the precipitation of harmful Fe-bearing phases ($\text{Al}_9\text{Fe}_2\text{Si}_2$ and $\text{Al}_{18}\text{Fe}_2\text{Mg}_7\text{Si}_{10}$). These phases are known to have a poor bonding with the Al matrix and their needle-like morphologies act as a stress concentrator and crack initiation site, thereby decreasing the mechanical properties of the alloy.
- 5) The high mass fraction of Fe phases and long solidification range of the A390RE alloy suggest that this alloy may perform poorly during the fitness-for-service tests.

4.2 Metallography of Al-RE Alloys

To complement the results presented in the thermodynamic simulation chapter above, this section describes the results from a comprehensive metallography analysis. This section begins by identifying the morphology and composition of primary and secondary intermetallics in a series of Al-Ce- and Al-RE-based alloys using SEM and EDS. Following this, the solidification kinetics for each are characterized as a function of temperature using in-situ neutron diffraction.

Sample preparation for the Al-RE alloys followed the same procedures as outlined in section 3.2. The results from the SEM/EDS analyses were compared to literature [1, 12], the binary Al-Ce and ternary Al-Ce-Mg phase diagrams, the crystal structures listed in the Inorganic Crystal Structures Database (ICSD) [187], and the simulated equilibrium and non-equilibrium solidification charts in the previous section.

4.2.1 Binary Al-6%Ce and Al-16%Ce alloys

Microstructural analyses were performed on the Al-6%Ce and Al-16%Ce to characterize the microstructure of hypoeutectic and hypereutectic Al-Ce alloys. The results from the SEM/EDXS

analysis of the Al-6%Ce alloy indicate that primary α -Al is surrounded by thin, interconnected eutectic Al-Al₁₁Ce₃ (see Figure 4.2-1). As expected, the microstructure shows no presence of primary Al₁₁Ce₃ crystals since the Ce content in this alloy is approximately 8 wt.% below the eutectic composition. Due to the near-instantaneous freezing of the Al-6%Ce alloy, the average size of the eutectic Al₁₁Ce₃ phase is on the nano scale.

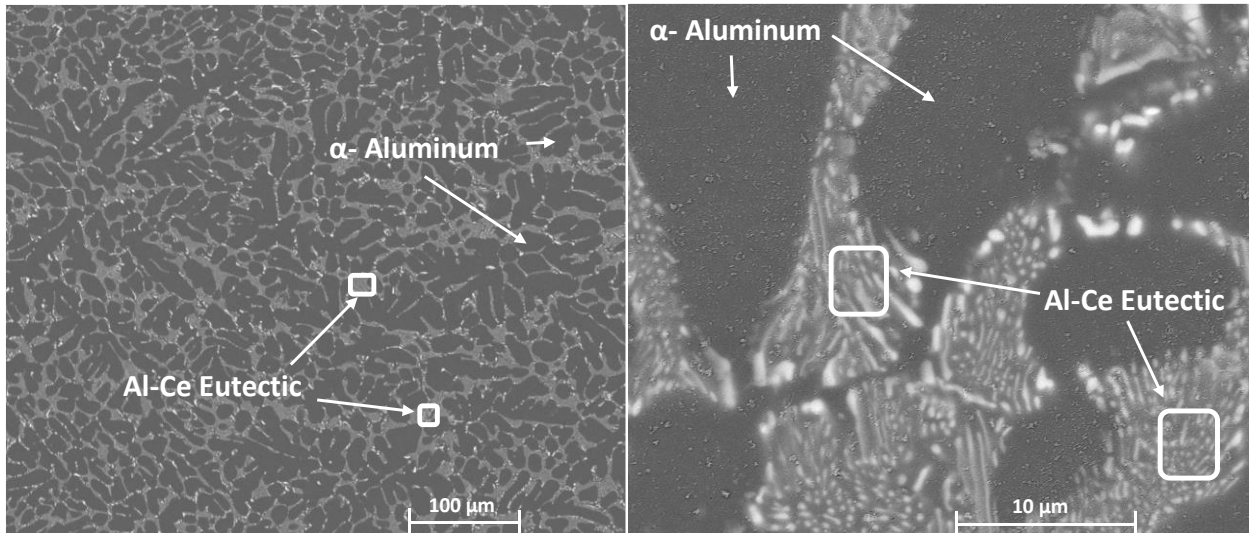


Figure 4.2-1. SEM micrograph of Al-6%Ce alloy, left) 500x, right) 5000x

A few Al-Ce-O oxides were also observed throughout the microstructure (see Figure 4.2-2). The composition of the oxide varied significantly from location to location; however, the range of at.% for each element is shown in Table 4.2-1. The geometry and porous structure of the oxide shell likely has a strong impact on the material's mechanical properties; however, further investigation into the full effect that these oxides have on properties of the Al-Ce alloys is outside of the scope of this study. It should be noted that very few oxides were found in the microstructure (i.e., less than 0.1 vol. %), and it is believed that they have formed during melt processing [216].

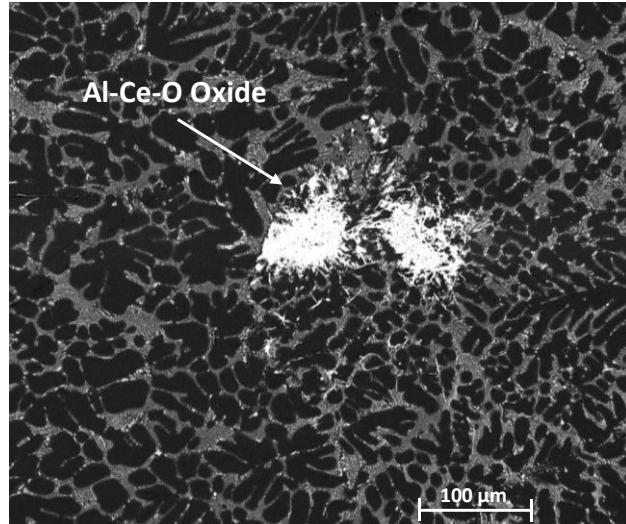


Figure 4.2-2. SEM micrograph of oxide in Al-6%Ce alloy, 500x

Table 4.2-1. Composition of intermetallics in Al-6%Ce alloy

Phase	Al (at. %)	Ce (at. %)	O (at. %)
α -Al Matrix	100	-	-
Al-Ce Oxide	11-29	36-50	33-38

Figure 4.2-3 displays the microstructure of the Al-16%Ce alloy (the microstructure shown in Figure 4.2-3 was chosen to clearly display each of the intermetallics and is not representative of the actual volume fraction of the phases). Analogous to the microstructure of the Al-6%Ce alloy, the interdendritic regions of primary α -Al consist of fine interconnected eutectic Al-Al₁₁Ce₃. The fine structure (i.e., approximate thickness of 1 μ m and smaller) and high thermal stability of the eutectic Al₁₁Ce₃ phase is likely the primary factor driving the improved high-temperature properties that were reported in [9], [20], [122], [165], [211].

Due to the high Ce concentration in the Al-16%Ce alloy, primary Al₁₁Ce₃ crystals were also observed in the microstructure with a large blocky and needle-like morphology. A higher magnification reveals that significant microcracking is present in the primary Al₁₁Ce₃ precipitates (see right side of Figure 4.2-3). It has been postulated that during cooling and contraction of the Al matrix and the Ce-containing intermetallics, the large difference in the coefficient of thermal expansion between Al and Ce (i.e., $\sim 24 \times 10^{-6}/^{\circ}\text{C}$ for Al vs $\sim 9 \times 10^{-6}/^{\circ}\text{C}$ for Ce) may lead to localized tensile and compressive intergranular forces; however, the claim has been unsupported in literature to date. The formation of these microcracks may be attributed to the development of intergranular

stress during the solidification of the Al-16%Ce alloy. This observation suggests that increasing the level of Ce content above the Al-Ce eutectic composition may result in an increase in the material's brittleness and a reduction of its toughness. This is supported with the tensile test results performed by D. Weiss [20], which indicate that increasing the Ce content from 6 wt.% to 16 wt.% result in a reduction in the alloy's elongation from 25 to 3.5%, respectively. Although the phases presented in this study are not pure Al and pure Ce, comparing the CTE values for each element provides a partial indication of the expected CTE of the $\text{Al}_{11}\text{Ce}_3$ intermetallic. In addition, to further investigate the CTE of the $\text{Al}_{11}\text{Ce}_3$ intermetallic, the volumetric CTE was calculated using ThermoCalc™ and the results support the initial claim that the $\text{Al}_{11}\text{Ce}_3$ has a lower CTE than the Al matrix (i.e., 26% apparent volumetric CTE reduction of Al-6%Ce, as compared to pure Al (0.00007 (Al-16%Ce) vs. 0.00011 (pure Al) $^{\circ}\text{C}^{-1}$) as compared to pure Al. In addition, and following the procedure explained by E. Vandersluis et al. [217], the neutron diffraction data presented in section 4.3.1 was used to calculate the CTE of the Al matrix and $\text{Al}_{11}\text{Ce}_3$ precipitate. The average CTE for the Al (111) and $\text{Al}_{11}\text{Ce}_3$ (112) reflections was calculated to be $28.2\text{E-}06$ and $15.6\text{E-}06$ $^{\circ}\text{C}^{-1}$, respectively. To the best of the authors' knowledge, this is the first confirmation of the thermal expansion coefficient of $\text{Al}_{11}\text{Ce}_3$.

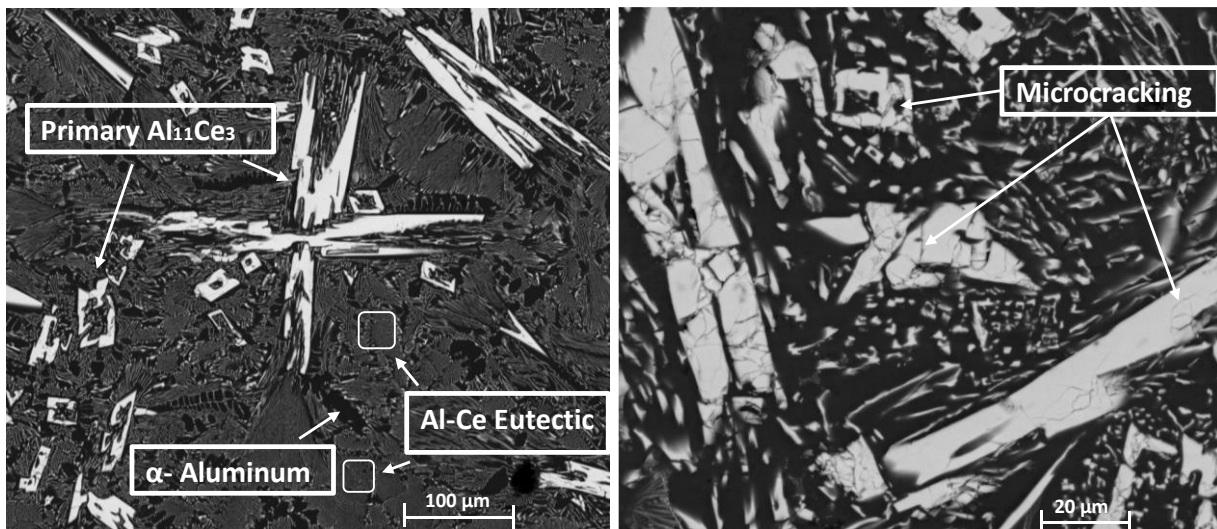


Figure 4.2-3. SEM micrograph of Al-16%Ce, (left) 500x, (right) 2000x. Note microcracking in the primary $\text{Al}_{11}\text{Ce}_3$ crystals

To determine if the stress within the $\text{Al}_{11}\text{Ce}_3$ intermetallics is affected by the additional Ce content in the Al-16%Ce alloy, the full-width-half-maximum (FWHM) of the strongest ND peak for the $\text{Al}_{11}\text{Ce}_3$ intermetallic (i.e., 112 reflection) was investigated (see Figure 4.2-4). The FWHM

correlates to Type 2 and Type 3 stresses (i.e., damage accumulation) in a material. For example, a previous study [218] evaluated the damage accumulation in the Al (111) plane of an A206 alloy by comparing the FWHM during a 120 MPa and a 140 MPa tensile load at 225 °C. The study indicated that after the load was increased to 140 MPa, the sample entered the tertiary stage of creep, which resulted in a rapid increase in creep strain and a congruent broadening of the neutron peak (approximate FWHM increase of 0.05°). Therefore, the observed 0.03° FWHM decrease between the Al₁₁Ce₃ (112) peak of the Al-6%Ce and Al-16%Ce alloy suggests that the stress in the Al₁₁Ce₃ precipitate in the Al-16%Ce alloy surpassed the phase's strength and led to a release of stress by cracking the intermetallic. The brittleness of this intermetallic is likely one of the primary factors causing the reduction in elongation that was reported by D. Weiss [20].

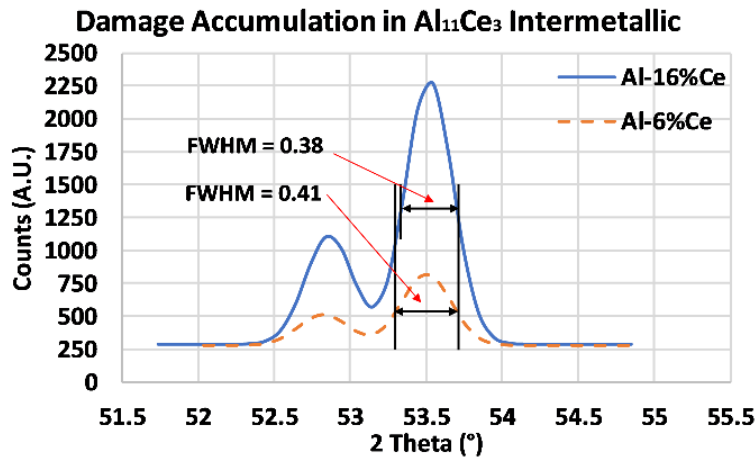


Figure 4.2-4. FWHM peak broadening for Al₁₁Ce₃ intermetallic in Al-6%Ce and Al-16%Ce alloy

To complement the SEM/EDXS results, X-Ray diffraction was performed with a Bruker D8-Advance X-ray diffractometer using a Bragg-Brentano configuration and a generator voltage and amperage of 40kV and 40 mA, respectively. A copper K α_1 and K α_2 radiation and a LynxEye silicon strip detector were used to obtain the diffraction pattern, and a nickel filter was used to remove the CuK β wavelength. Small samples were cut from the larger as-cast specimen provided by Eck industries. The cut samples were sequentially ground and polished to 1 μ m as described in the microstructural analysis section above. Room temperature XRD scans were performed for approximately 30 minutes on each of the alloys using a wavelength of 1.54 Å across diffraction angles of 5° to 90° while the specimen rotated on a platform. The XRD data was evaluated using

the Bruker EVA software, and the diffraction patterns were compared to the International Center for Diffraction Data database.

The XRD results of the Al-6%Ce alloy are shown in Figure 4.2-5A. The diffraction peaks were indexed as Al and $\text{Al}_{11}\text{Ce}_3$. The XRD pattern for the Al-16%Ce alloy is shown in Figure 4.2-5B. Other than an increase in Al-Ce peak intensities, no significant variations were observed between the Al-6%Ce and Al-16%Ce alloys. The results correlate well with the SEM and EDS observations.

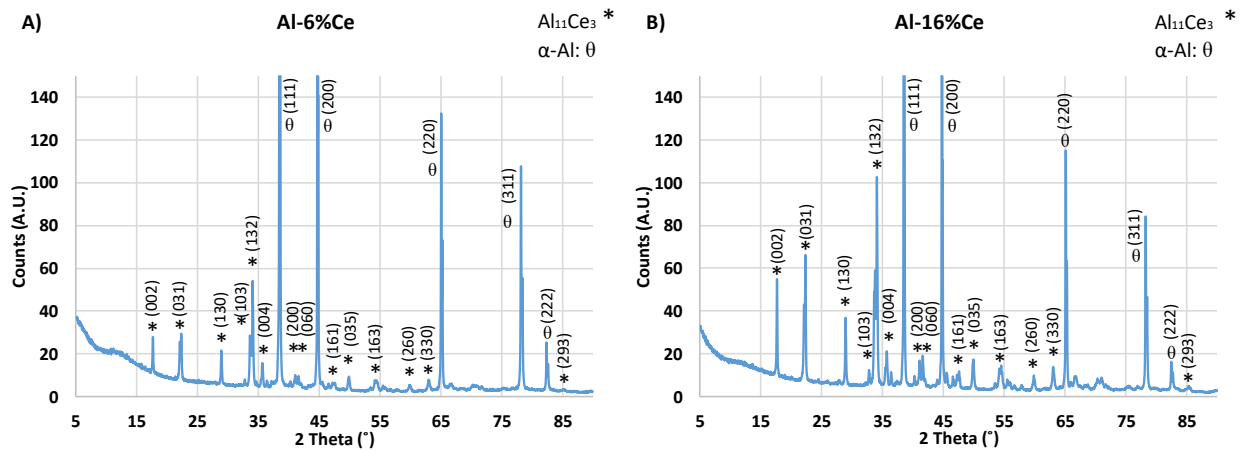


Figure 4.2-5. XRD diffraction pattern for the A) Al-6%Ce and B) Al-16%Ce alloy

4.2.2 Al-8%Ce-10%Mg

SEM/EDS analyses were performed on the Al-8%Ce-10%Mg alloy to determine the effects that the Mg addition has on the microstructure of the Al-Ce system. Figure 4.2-6 is a SEM micrograph of the Al-8%Ce-10%Mg alloy, and Table 4.2-22 shows the EDS elemental composition results for the phases. The Mg-rich Al matrix surrounds a few primary $\text{Al}_{11}\text{Ce}_3$ precipitates (~1 vol.%) and a high-volume fraction of Chinese script $\text{Al}_{11}\text{Ce}_3$ (~35 vol.%). The microstructure of an Al-12%Ce alloy, as described by Sims et al. [122], consists of primary crystals surrounded by fine interconnected eutectic Al-Ce; however, the Chinese script Al-Ce intermetallic in the Al-8%Ce-10%Mg is much larger, more randomly dispersed throughout the microstructure, and less connected to the surrounding Chinese script Al-Ce precipitates. Similarly, P. Minárik et al. [219], found that the microstructure of a Mg-4%Li-4-Al-2%RE alloy contains the coarser Chinese script $\text{Al}_{11}\text{Ce}_3$ intermetallic. Taken together, these results suggest that the Mg content in the Al-8%Ce-10%Mg is a factor in the alternation of the fine and interconnected morphology of the eutectic Al-

Ce to individualized intermetallic particles that are more randomly dispersed throughout the microstructure. In addition, the lack of the larger Chinese script $\text{Al}_{11}\text{Ce}_3$ intermetallics in the Al-16%Ce alloy (see Figure 4.2-3) further supports this claim.

The increased rate of growth of the FCC-Al towards the end of the Scheil solidification analysis (see Figure 4.1-6) suggests that the relatively high concentration of Mg in the Al matrix, as compared to the theoretical solubility of Mg in Al, can be partially attributed to the dissolution of the minority Mg-containing intermetallics into the matrix. Because the Mg content in this alloy is considerably greater than the theoretical solubility of Mg in Al at room temperature, an irregularly shaped AlMg precipitate (~5 vol.%) was also observed in the microstructure (Figure 4.2-6). A comparison of the EDS composition results of this phase to the ThermoCalc results suggests that this phase is β -AlMg [220] with dissolved oxygen. The $\text{Al}_{13}\text{CeMg}_6$ phase shown in the non-equilibrium solidification analysis (Figure 4.1-5) was not observed in the microstructure of this alloy. This is likely attributed to the assumptions associated with Scheil solidification which state that no diffusion occurs in solid phases once they are formed. Moreover, it has been reported that the decomposition of $\text{Al}_{13}\text{CeMg}_6$ back into $\text{Al}_{11}\text{Ce}_3$ and β -AlMg occurs between approximately 400 to 320 °C [221]. The Fe-containing intermetallics shown in Figure 4.1-5 and Figure 4.1-6 are not observed in the microstructure.

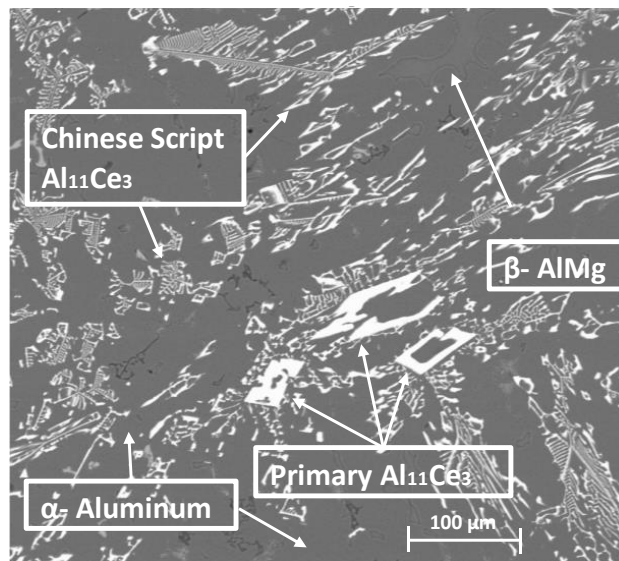


Figure 4.2-6. SEM micrograph of the Al-8%Ce-10%Mg alloy, 500x

Table 4.2-2. Composition of intermetallics in Al-8%Ce-10%Mg

Phase	Al (at. %)	Ce (at. %)	Mg (at. %)	O (at. %)	Fe (at. %)
α -Al Matrix	89-94	-	6-11	-	-
Primary $\text{Al}_{11}\text{Ce}_3$	78-80	20-22	-	-	-
Chinese Script $\text{Al}_{11}\text{Ce}_3$	78-80	20-22	-	-	-
β -AlMg	56-60	-	31-35	6-10	-
β -AlMg* (Figure 4.2-7)	50-59	-	25-32	7-21	1-3

A closer look at the β -AlMg phase reveals that the small amount of Fe (~0.15 wt. %) in this alloy, in combination with higher levels of impurity oxygen, modifies a portion of the phase's structure, changing its surface to a more fibrous type (see β -AlMg* Figure 4.2-7 and Table 4.2-2). The O and Fe content in this phase has increased to a maximum of ~20 at. % and ~2.5 at. %, respectively. The non-homogenous structure of this phase is expected to have a negative effect on the material's mechanical properties.

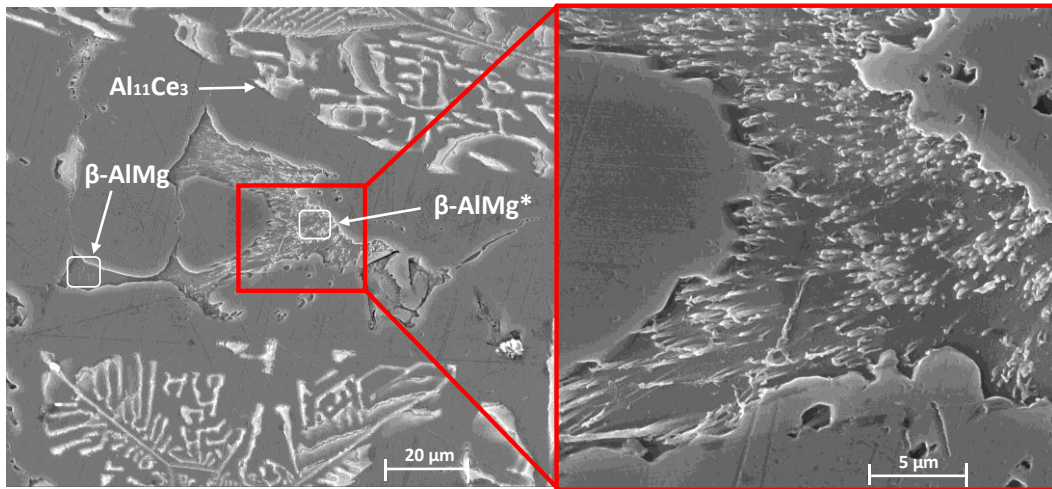


Figure 4.2-7. Non-homogenous structure of the β -AlMg phase in Al-8%Ce-10%Mg alloy

Figure 4.2-8A displays the results obtained from the XRD analysis of the Al-8%Ce-10%Mg alloy. Similar to the binary alloys, the Al matrix and $\text{Al}_{11}\text{Ce}_3$ phase were also identified. Other than a change in peak intensities and a slight shift in the peak position of α -Al (caused by the strain induced by the presence of dissolved Mg in the Al matrix), no major differences were observed.

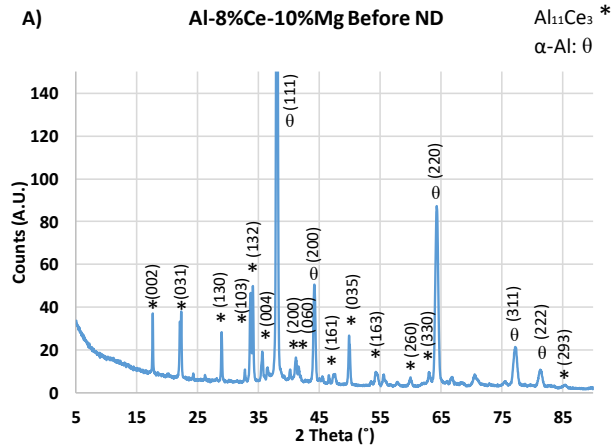


Figure 4.2-8. XRD diffraction pattern for the Al-8%Ce-10%Mg alloy

To analyze the 3D structure of the intermetallics in the Al-8%Ce-10%Mg alloy, X-Ray micro-computed tomography (XMCT) imaging (Zeiss/Xradia X-400, in Composite Research Network at University of British Columbia-Okanagan Campus, CRNO) was performed. The sample-detector and X-ray-source-sample distances were 7 and 200 mm, respectively. Rotational steps of 0.144° were conducted to scan a complete 360° of the sample. For each sample, 2500 2D X-ray radiographs were recorded with a resolution of 700 nm. To process and visualize the 2D images, Avizo 9.3. software was used [222]. The procedure undertaken for the X-ray Micro-CT analysis is described in more detail in [223], [224]. Figure 4.2-9 illustrates the X-ray Micro-CT system used in this research study.

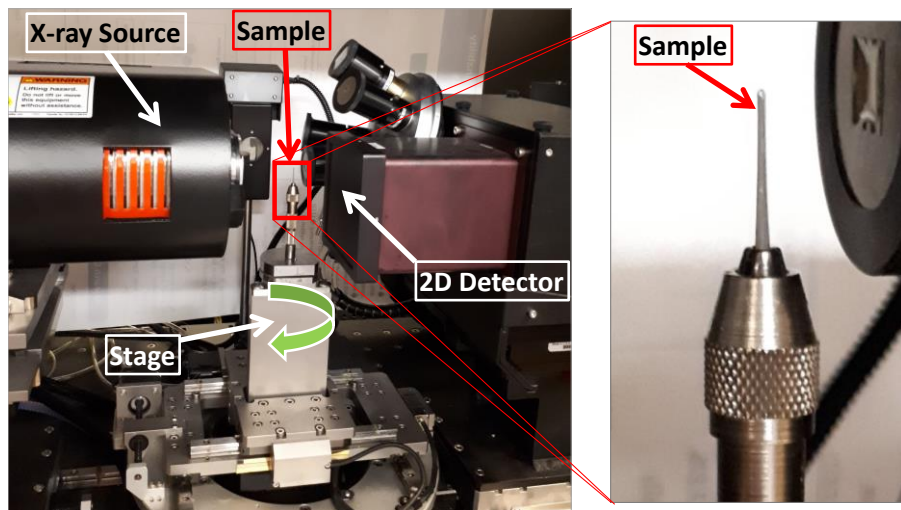


Figure 4.2-9. X-ray micro computed tomography machine (X-Ray Micro-CT, Zeiss/Xradia X-400) [21]

Due to the similar densities between the Al matrix and β -AlMg precipitates, the distinction between these two phases was not possible. However, the high density of the Ce in the $\text{Al}_{11}\text{Ce}_3$ phase provided sufficient contrast against the remaining phases. Figure 4.2-10 displays the 3D structure of the Chinese script $\text{Al}_{11}\text{Ce}_3$ intermetallic. The XMCT analysis was capable of reconstructing the branches of this intermetallic, as seen in the SEM micrograph (see Figure 4.2-6).

It is believed that these branches may act as a barrier against dislocation motion which may improve the material's strength as compared to the binary Al-Ce alloys. However, it is likely that the large size of these $\text{Al}_{11}\text{Ce}_3$ crystals ($\sim 100\text{-}400\ \mu\text{m}$) will reduce the benefits from this phase. As discussed in chapter 2, the smaller and more homogeneously dispersed the precipitate, the greater the resistance to dislocation motion.

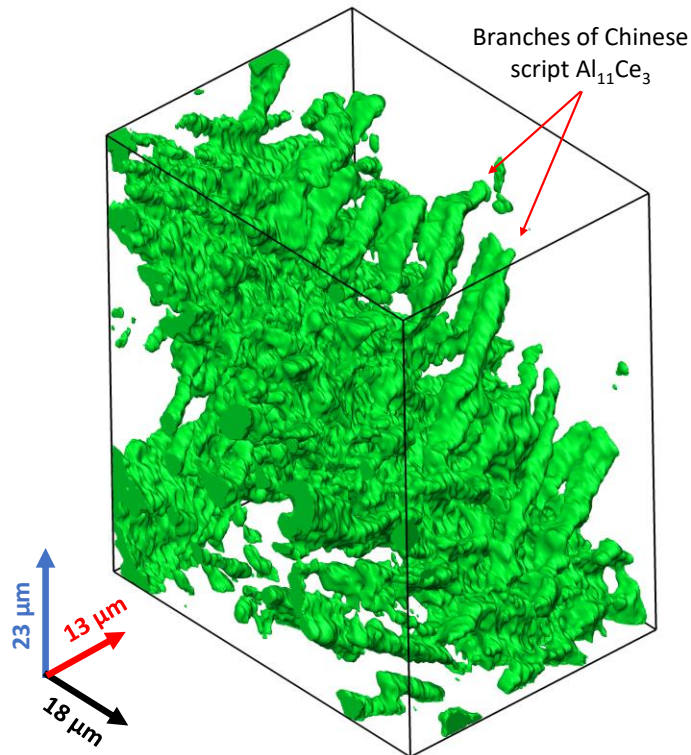


Figure 4.2-10. XMCT results for $\text{Al}_{11}\text{Ce}_3$ intermetallics in Al-8%Ce-10%Mg alloy

4.2.3 T6 A356 and A356RE (as-cast + T6)

This section describes the effects that a 3.5 wt.% RE mischmetal addition has on the microstructure of the A356 series Al alloy (see Table 3.6-1 for alloy composition). The heat-treated alloys were subjected to a T6 heat treatment, consisting of solutioning at 538 °C (1000 °F) for 8 hours,

quenching in water at 71 to 82 °C (160-180 °F), holding at room temperature for 12 hours, aging for 4 hours at 154 °C (310 °F), and then cooling in air to room temperature.

Figure 4.2-11 displays the microstructure of the T6 A356 alloy. The majority of the alloy's microstructure consists of dendritic α -Al grains and spheroidized eutectic Si particles. The microstructure is consistent with published literature on similar alloys. In addition to Al and Si, needle-like AlFeSiMg intermetallics (similar size, shape and composition as π -Al₉FeMg₃Si₅) were also observed throughout the microstructure but in relatively low volume fraction (1.20±0.25 vol.%).

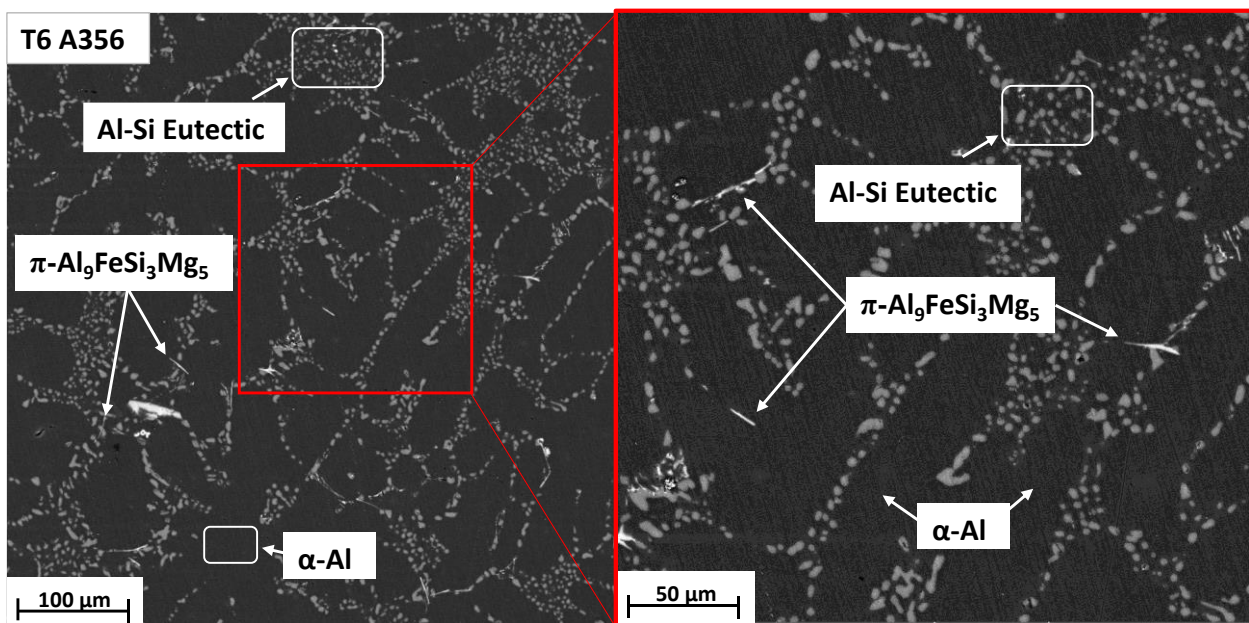


Figure 4.2-11. SEM micrograph of the T6 A356 alloy, left) 500x and right) 1000x

Figure 4.2-12 displays the microstructure of the as-cast rare earth-reinforced A356 alloy (i.e., A356RE). Similar to the observations reported in [225], the majority of the microstructure consists of primary α -Al, eutectic Al-Si, and a blocky Al-Si-Ce-La-Nd-Pr (shown as AlSiRE) phase. The eutectic Si particles are present in a fibrous/rod-like blocky morphology rather than the large plate-like structure that is more commonly observed in unmodified Al-Si alloys [135]. This is likely due to the presence of Sr in the alloy.

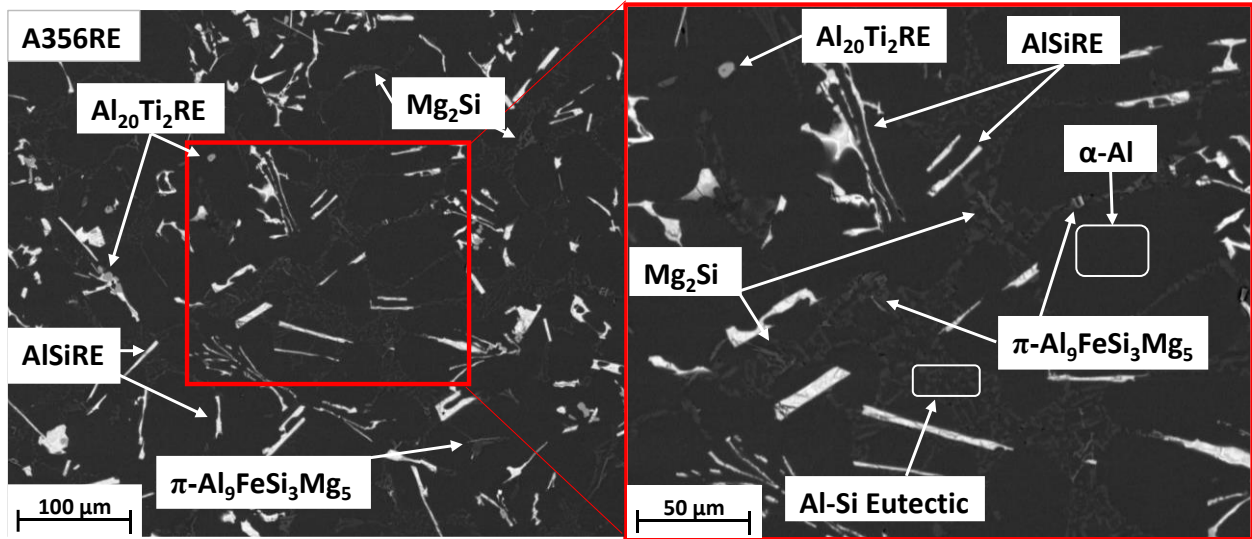


Figure 4.2-12. Microstructure of the as-cast A356RE alloy, left) 500x and right) 1000x

Similar to the A319 alloy discussed in chapter 3 (see Figure 3.3-6 and Figure 3.3-8), the contrast between the Al-matrix and eutectic Si particles is not clearly shown in Figure 4.2-12. As a result, an optical micrograph is shown below in Figure 4.2-13 (note the fibrous/rod-like structure of the Si particles).

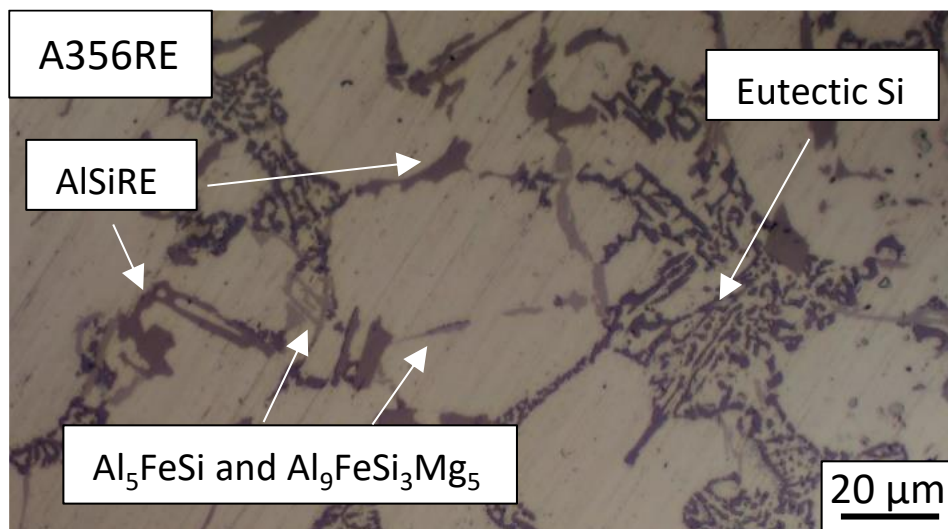


Figure 4.2-13. Optical micrograph of as-cast A356RE alloy

In addition to the AlSiRE phase (4.37 ± 0.37 vol.%), a polygonal $\text{Al}_{20}\text{Ti}_2\text{RE}$ (0.70 ± 0.30 vol.%), irregular, blocky Mg_2Si (2.00 ± 0.34 vol.%), and needle-like $\pi\text{-Al}_9\text{FeMg}_3\text{Si}_5$, and $\beta\text{-Al}_5\text{FeSi}$ intermetallics (combined 0.35 ± 0.16 vol.%) are also observed in the microstructure. The size of the AlSiRE phase ranges from approximately 5 to 75 μm , whereas the size of $\text{Al}_{20}\text{Ti}_2\text{RE}$, Mg_2Si , and

Fe intermetallics are more commonly observed between 5 to 10 μm . The morphology of the AlSiRE intermetallic is similar to the τ_1 phase (i.e., $\text{Ce}(\text{Si}_{1-x}\text{Al}_x)_2$, where $x = 0.1-0.9$) published by Z. Sims et al. [9] and E. Elgallad et al. [138]. However, the heavier rare earth elements (i.e., Nd and Pr) in the mischmetal are also present in the two intermetallics (see Table 4.2-3 for EDS composition analysis). Z. Sims suggests that the near-zero solubility of Ce in Al and Si [131], the strong bonding of vacancies to cerium [132], and the enthalpy of formation of the τ_1 phase (i.e., minimum of -67 kJ/mol near $x = 0.5$) all contribute to the high thermal stability of the AlSiRE intermetallic. A closer look at the AlSiRE precipitate revealed similar microcracking as observed in the primary $\text{Al}_{11}\text{Ce}_3$ particles in an Al-16%Ce alloy [226]. The geometry of the microcracks can act as a stress concentrator and may lead to a reduction of the alloy's ductility.

Figure 4.2-14 displays the microstructure of the T6 heat-treated alloy (i.e., T6 A356 +3.5wt.%RE). Similar to the as-cast alloy, the microstructure of the T6 alloy consists of primary α -Al, eutectic Al-Si, AlSiRE (5.27 ± 0.72 vol.%), $\text{Al}_{20}\text{Ti}_2\text{RE}$ (0.78 ± 0.35 vol.%), π - $\text{Al}_9\text{FeMg}_3\text{Si}_5$, and β - Al_5FeSi (combined 1.85 ± 0.83 vol.%) phases. The size and composition of the intermetallics has changed insignificantly; however, it appears that the Mg_2Si phase is no longer present in the heat-treated alloy's microstructure. Congruently, the volume fraction of the Fe phases has increased by approximately 1.5 vol.%. It is likely that during the solutionizing stage of the T6 temper, the Mg_2Si phase dissolves preferentially over the π - $\text{Al}_9\text{FeMg}_3\text{Si}_5$ due to the low diffusivity of Fe in Al and the low melting temperature of Mg_2Si . Further, when a relatively high amount of Mg (i.e., greater than ~ 0.40 wt.%) is present in Al-Si-Mg alloys with Fe impurities, the π - $\text{Al}_9\text{FeMg}_3\text{Si}_5$ phase is more stable, leading to a reduction of available Mg for precipitation of Mg_2Si . [97]–[99].

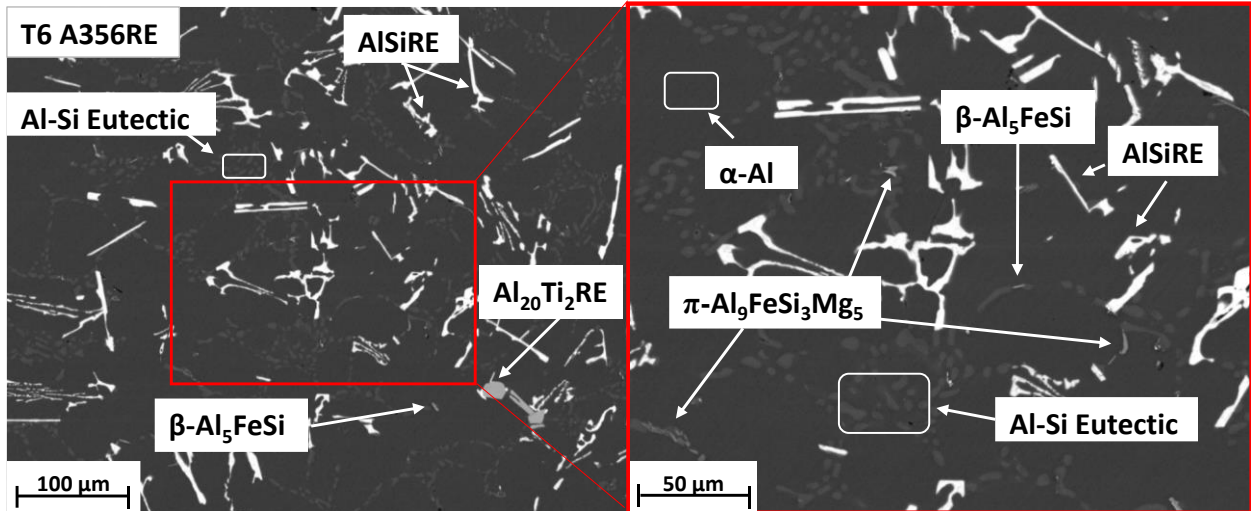


Figure 4.2-14. Microstructure of the T6 A356RE alloy, left) 500x and right) 1000x

When comparing the shape of the eutectic Si particles between the as-cast and T6 samples, it was observed that the heat treatment resulted in spheroidization of the individual particles (see Figure 4.2-15). It is well published that spheroidized Si particles can result in greatly improved mechanical properties and, therefore, it is expected that this alloy will outperform the as-cast sample [227], [228]. Further, this observation suggests that the RE additions are not impairing the alloy's responsiveness to commercial heat treatments.

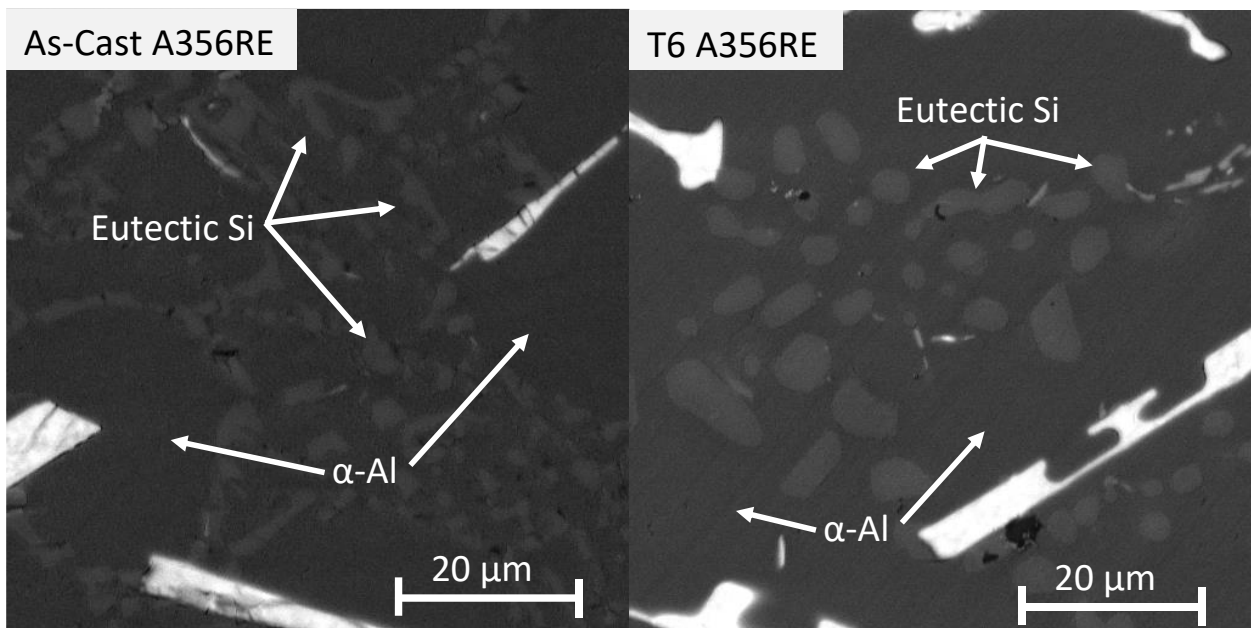


Figure 4.2-15. SEM micrographs A356RE alloy: left) as-cast, right) T6 heat-treated

Table 4.2-3. EDS elemental analysis of phases present in A356 and A356RE alloys (at.%)

	Al	Si	Ce	La	Nd	Pr	Fe	Mg	Ti
α -Al matrix	Bal.	1.2	-	-	-	-	-	-	-
AlSiRE*	Bal.	37-39	9-10	5-6	2-4	0-1	-	-	-
Al ₂₀ Ti ₂ RE*	Bal.	2	3	0.7-0.8	0.7-0.8	-	-	2	7-8
Mg ₂ Si	-	33-36	-	-	-	-	-	64-66	-
Al ₉ FeSi ₃ Mg ₅	Bal.	19-22	-	-	-	-	2-3	7-8	-

*Present in RE-modified alloys

Similar to the Al-8%Ce-10%Mg alloy, an XMCT analysis was performed on the T6 A356RE alloy. Due to the low volume fraction of the Al₂₀Ti₂RE phase and the minimal difference in densities between Al and Si, these phases were unable to be identified. However, the analysis provided a clear 3D reconstruction of the AlSiRE phase (see Figure 4.2-16). From the SEM micrographs, the phase appears to be in a block or rod-like morphology; however, the phase was more predominantly found with a plate-like structure. As compared to the Chinese script Al₁₁Ce₃ phase found in the Al-8%Ce-10%Mg alloy, the plate-like AlSiRE phase is much smaller in size (average size = 50-100 μ m as compared to 200-400 μ m). Moreover, the random orientation and significant dispersion of this AlSiRE phase are expected to further improve the mechanical properties of the alloy.

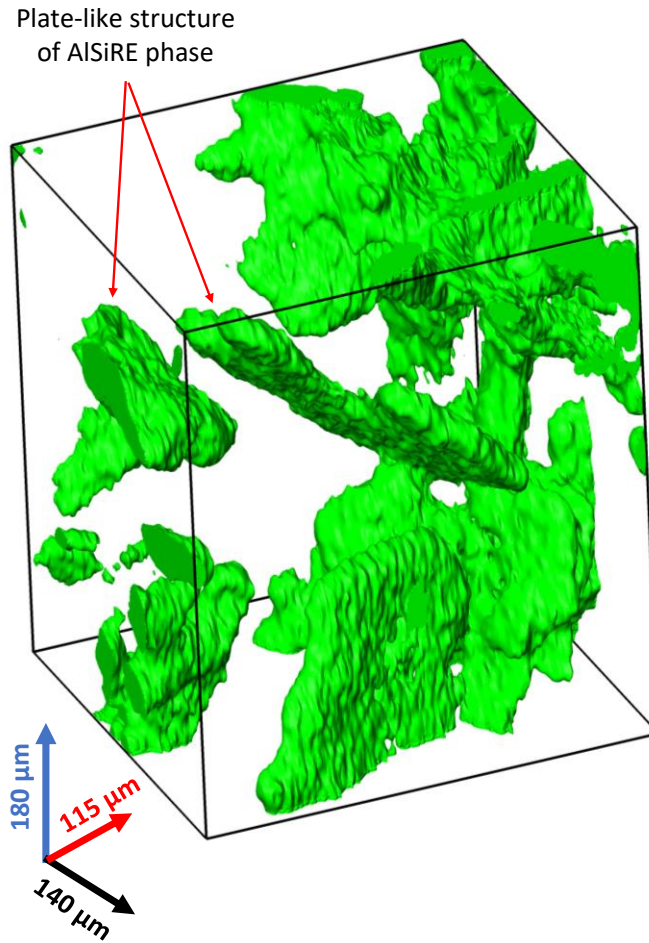


Figure 4.2-16. XMCT results of AlSiRE phase in T6 A356RE alloy

4.2.4 A390RE

Figure 4.2-17 and Figure 4.2-18 display the microstructure of the A390 alloy with 8 wt.% RE mischmetal. The majority of the microstructure consists of blocky primary Si crystals, eutectic Al-Si, Al dendrites, and a few RE-bearing intermetallics. The compositions of the phases are listed in Table 4.2-4.

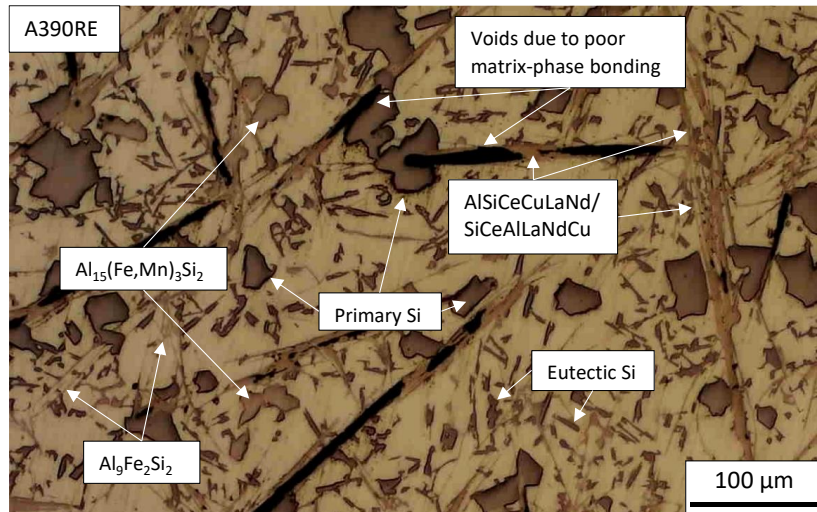


Figure 4.2-17. Optical micrograph of A390RE alloy

The additional 11 wt.% Si and 4 wt.% Cu in the A390RE alloy, as compared to the A356 alloy, appears to have transformed the structure of the AlSiRE intermetallic (see Figure 4.2-14) to a fibrous, twin-layered structure comprised of alternating SiCeAlLaNdCu and AlSiCeCuLaNd layers. The composition of the slightly darker outer core is close to that of the AlSiRE phase in the A356RE alloy but has a higher concentration of Cu. The Cu in this phase is not likely forming as a part of its structure but, instead, is forming a solid solution with Ce. The high solubility of Cu in Ce is believed to be one of the primary factors for the lack of Al₂Cu in this alloy; ThermoCalc calculated the mass fraction to be as high as 5.19-7.08%, depending on solidification mode (see

Table 4.1-8). Moreover, according to the non-equilibrium solidification simulation (see Figure 4.1-14), $\text{Al}_5\text{Cu}_2\text{Mg}_8\text{Si}_6$ begins to form $\sim 15^\circ\text{C}$ before Al_2Cu and thus, this phase likely consumes the remaining available Cu that is not accounted for in the SiCeAlLaNdCu and AlSiCeCuLaNd phases.

The layers of the SiCeAlLaNdCu and AlSiCeCuLaNd phases are not well connected to one another and several voids/porosities can be observed. Along with the fibrous structure of these large phases, the voids can act as stress concentrators which facilitate crack initiation once exposed to an external load. Following the microstructural preparation process, it was observed that many of these twin-layered compounds were pulled out of the microstructure (see Figure 4.2-17), further elucidating the poor bonding of these phases with the Al matrix.

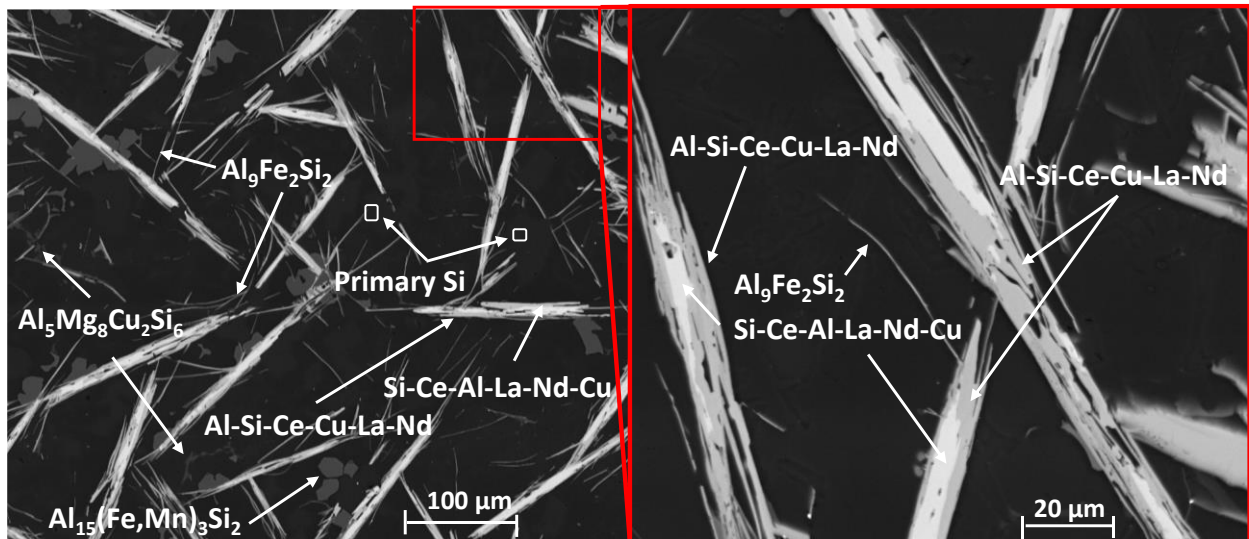


Figure 4.2-18. SEM micrograph of A390RE alloy

Table 4.2-4. EDS elemental analysis of phases present in A390RE alloy (at.%)

	Al	Si	Ce	La	Nd	Pr	Fe	Mg	Cu	Mn
α -Al Matrix	Bal.	-	-	-	-	-	-	-	0.56	-
AlSiCeCuLaNd	Bal.	32.5	11.5	4.5	2.5	0.75	-	-	9.50	-
SiCeAlLaNdCu	Bal.	48.5	18.5	8.0	4.2	1.50	-	-	2.50	-
Al ₅ Mg ₈ Cu ₂ Si ₆	Bal.	25.5	-	-	-	-	-	30.0	7.20	-
Al ₁₅ (Fe,Mn) ₃ Si ₂	Bal.	10.5	-	-	-	-	11.0	-	0.75	3.50
Al ₉ Fe ₂ Si ₂	Bal.	16.7	-	-	-	-	11.3	-	1.0	1.10

In addition to the RE-bearing phases, Chinese script Al₅Mg₈Cu₂Si₆, polygonal Al₁₅(Fe,Mn)₃Si₂, and needle-like Al₉Fe₂Si₂ intermetallics were also observed. As mentioned in Chapter 2, the Al₅Mg₈Cu₂Si₆ has a greater thermal stability than Al₂Cu and should improve the alloy's temperature resistance. Although the Mn addition in this alloy resulted in the formation of the more desirable Al₁₅(Fe,Mn)₃Si₂ phase, the concentration of Mn was not high enough to completely transform the Al₉Fe₂Si₂ phase.

The results from the SEM/EDS analysis correlate to the ThermoCalc results. The lack of Al₂Cu in the alloy's microstructure is the primary difference between the two sets of results. This is presumed to be attributed to the relatively high concentration of Cu in the large RE-bearing fibrous phases. Since the fibrous phases nucleate and grow at a much higher temperature than the Al₂Cu and Al₅Mg₈Cu₂Si₆, and since Cu has a high solubility in Ce, it is likely that they contain a much higher Cu concentration than predicted in the simulated solidification models, thereby reducing the available Cu for forming Al₂Cu and Al₅Mg₈Cu₂Si₆. The size and structure of the twin layered, void-filled constituent, as well as the high volume fraction of needle-like Al₉Fe₂Si₂ precipitates, is expected to greatly hinder the performance of this alloy during the fitness-for-service testing.

4.3 Solidification Analyses Using In-Situ Neutron Diffraction

The in-situ ND experiments were performed at the C2 powder diffractometer at the Canadian Nuclear Laboratories (CNL) in Chalk River, Ontario, and the high-resolution neutron powder diffractometer, Echidna, at the Australian Nuclear Science and Technology Organization (ANSTO) at the OPAL reactor source in Australia [229]. Following the procedure first described

by D. Sediako et al. [230], each sample was machined down to 40 mm in length and 10.5 mm in diameter with a 2 mm diameter hole drilled on one end with a depth of 10 mm. This hole enabled the insertion of a K-type thermocouple to monitor the temperature of the sample as it solidified. A PID controller was used to control a stepwise temperature sequence of the sample to within ± 0.5 °C. Each sample was mounted into a graphite crucible and aligned to the neutron beam in the furnace sample chamber (see Figure 4.3-1). The furnace volume was purged with argon gas with a constant low flowrate of approximately 100 SCCM to ensure no oxidation would occur during the melting of the sample. The samples were then heated to approximately 25 °C above the alloy's liquidus temperature, determined by the equilibrium model ThermoCalc simulations, to ensure the entire sample was completely molten. The sample then followed a preset solidification sequence with decremental temperature steps of 5-10 °C around the alloy's liquidus and solidus temperatures, as well as the nucleation temperatures of the intermetallics. Each temperature of interest was held for ~30 to 60 minutes. A monochromatic incident neutron beam with a wavelength of between 2.37 to 2.44 Å (facility-dependent) was used, and a wide-angle detector collected neutrons counts within a 80-160° span of diffraction angles (2θ). The longer wavelengths broaden the peaks, making them easier to process when calculating fraction solid. Applying Bragg's law for diffraction, as shown in Equation 6, the resulting ND data produced quantifiable neutron peaks for different phases on different crystallographic planes during the solidification process. The individual reflections for each intermetallic were indexed against the crystal structures list in the Inorganic Crystal Structure Database (ICSD) [187].

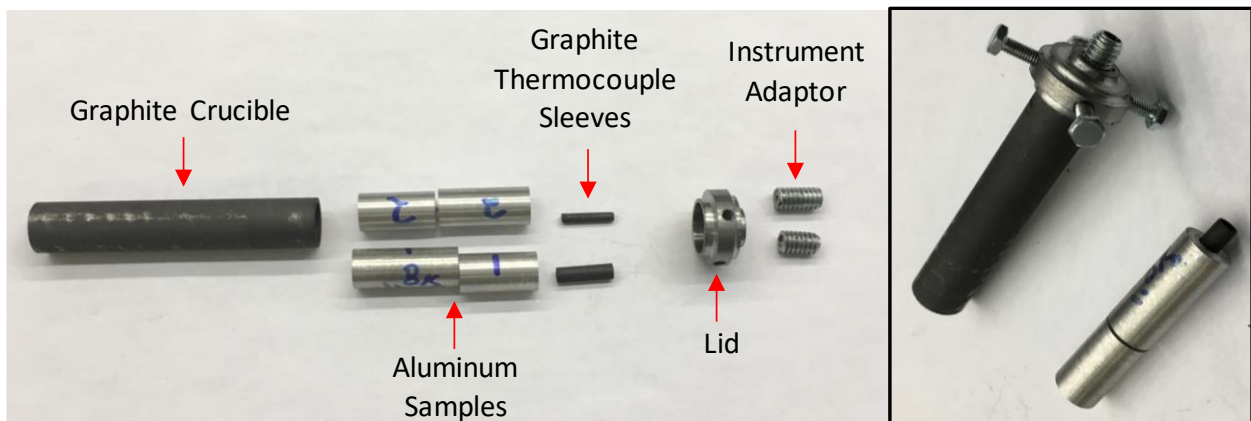


Figure 4.3-1. Sample setup used in ND solidification experiment

The ND data resulted in a diffraction pattern for each temperature step with several peaks occurring at different scattering angles. In order to obtain the solidification characteristics for each of these

phases, integration of the peak intensities was required. It was also required to differentiate the background intensity from the total peak intensity for each phase. With the background intensity subtracted from total peak intensity, the fraction solid at each temperature step was determined by normalizing the data and accounting for the temperature dependency of the peak intensity from liquidus to solidus. In solid materials, the peak intensity is inversely related to temperature due to the thermally activated motion of atoms in the sample material (which contributes to inelastic neutron scattering). This means the peak intensity increases with decreased temperature even though the fraction solid is unchanged. If not corrected, this may lead to values of fraction solid “in excess” of 100% in the lower temperature regions. Therefore, a correction factor, also known as the Debye-Waller factor, must be subtracted from the previously calculated fraction solid. Since the thermal motion of atoms is reduced in solid material, as compared to liquids and gases, the influence of Debye-Waller factor is much less pronounced [231]–[233]. For this reason, a second order polynomial function, representing the fraction solid evolution of each temperature below the solidus, was extrapolated to all temperatures to adjust the total fraction solid curve, as presented in [234]. With this function, the Debye-Waller correction factor was calculated and subtracted from the previously determined fraction solid evolution, and a corrected fraction solid curve was plotted. A detailed description of the phase solidification analysis is described by E. Vandersluis et al. [235].

4.3.1 Neutron Diffraction of Al-6%Ce and Al-16%Ce

The room-temperature ND pattern for the Al-6%Ce alloy is shown below in Figure 4.3-2A. The chart presents the scattering intensity before the alloy has undergone the melting-solidification experiment. Similar to the XRD results, the ND peaks were indexed as orthorhombic $\text{Al}_{11}\text{Ce}_3$ and FCC-Al.

The ND pattern for the Al-16%Ce alloy is shown below in Figure 4.3-2B. A few of the peaks that were not visible in the Al-6%Ce alloy can now be seen in the diffraction pattern of the Al-16%Ce alloy. The additional Al-Ce peaks became detectable due to the increased Ce content in the hypereutectic alloy, leading to a higher weight fraction of Al-Ce intermetallics and, correspondingly, to a stronger diffraction. These peaks are likely present in the Al-6%Ce diffraction pattern but are masked by the high background intensities caused by inelastic neutron scattering during solidification and cooling of the alloy.

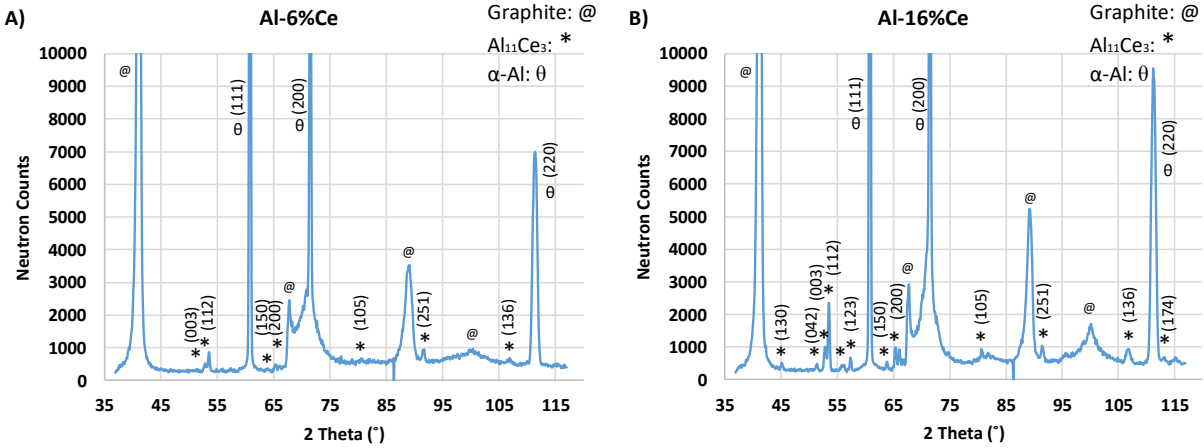


Figure 4.3-2. Full neutron diffraction pattern of A) Al-6%Ce and B) Al-16%Ce alloys prior to solidification experiment

Figure 4.3-3 displays the Al (111) reflection during cooling of the Al-6%Ce alloy, revealing a shift to higher angles, consistent with thermal contraction during cooling. For visual clarity, not all of the data collected are shown in Figure 4.3-3. As the temperature increases, the size of the Al peak reduces, which corresponds to a reduction of the amount of solid Al. At 655 °C the peak completely disappears, indicating that this is the liquidus temperature of the Al-6%Ce alloy. As compared to the ThermoCalc results presented in Figure 4.1-2, the liquidus temperature of the Al-6%Ce alloy is ~6 °C above the simulated results.

Normalizing the area under the peaks to the background allows for the characterization of the solidification process, as explained in detail in [235], [236]. The results from this process are shown as a fraction solid chart (see figure on right in Figure 4.3-3). The fraction solid chart displays the near instantaneous solidification of the alloy, where it takes just 10 °C to reach 100% solid (i.e., fraction solid of 1 in Figure 4.3-3). The temperature at which the material is 100% solid represents the alloy's solidus temperature, which in this case is 645 °C. Similar to the liquidus temperature, this is 5 °C above the calculated solidus temperature for this alloy. Identical results were observed for the Al (200) and Al (220) reflections.

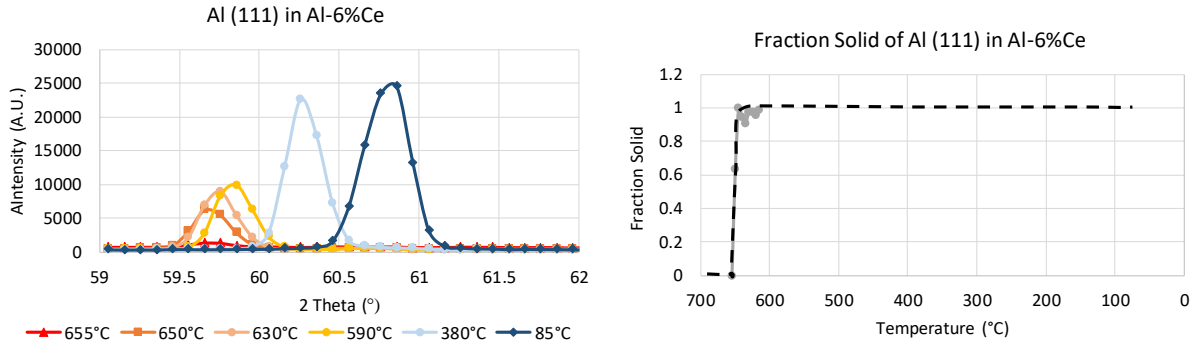


Figure 4.3-3. Temperature-dependent neutron powder diffraction data of the Al-6%Ce alloy showing the Al (111) reflection (left) and the corresponding solid fraction (right). Data are shown as points with the solid and dashed line guiding the eye

Due to the low intensity of the $\text{Al}_{11}\text{Ce}_3$ peaks, the fraction solid as a function of temperature could only be calculated for the (112) reflection of the $\text{Al}_{11}\text{Ce}_3$ intermetallic (see Figure 4.3-4). Identical to α -Al, the nucleation temperature of the $\text{Al}_{11}\text{Ce}_3$ was determined to be 655 °C. In addition, the point at which the phase reached 100% solid was also determined to be 645 °C. Due to the short solidification temperature range and 5 °C interval step, the difference in the 0% and 100% fraction solid temperatures between the Al and $\text{Al}_{11}\text{Ce}_3$ were masked. In reality, these temperatures should differ slightly.

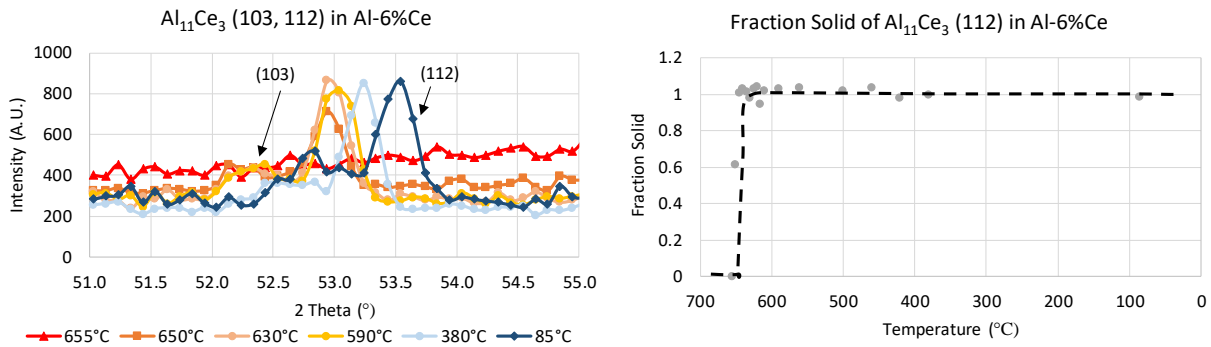


Figure 4.3-4. Temperature-dependent neutron powder diffraction data of the Al-6%Ce alloy showing the $\text{Al}_{11}\text{Ce}_3$ (112) reflection (left) and the corresponding solid fraction (right). Data are shown as points with the solid and dashed line guiding the eye

Similar to the Al-6%Ce alloy, the fraction solid, as a function of temperature, for the α -Al (111) and $\text{Al}_{11}\text{Ce}_3$ (112) reflections was calculated. Although the peak intensity of the Al and $\text{Al}_{11}\text{Ce}_3$ phases changed as compared to the Al-6%Ce alloy, the temperature at which the phases were 0% and 100% solid did not. Referring to the binary Al-Ce phase diagram (Figure 4.1-1), it was

expected that the liquidus temperature of the Al-16%Ce alloy would be slightly higher than for the Al-6%Ce alloy; however, this was not the case. Due to the higher concentration of Ce in the Al-16%Ce alloy, the fraction solid for the $\text{Al}_{11}\text{Ce}_3$ (200) reflection was also calculated and follows the same trend as the (112) reflection.

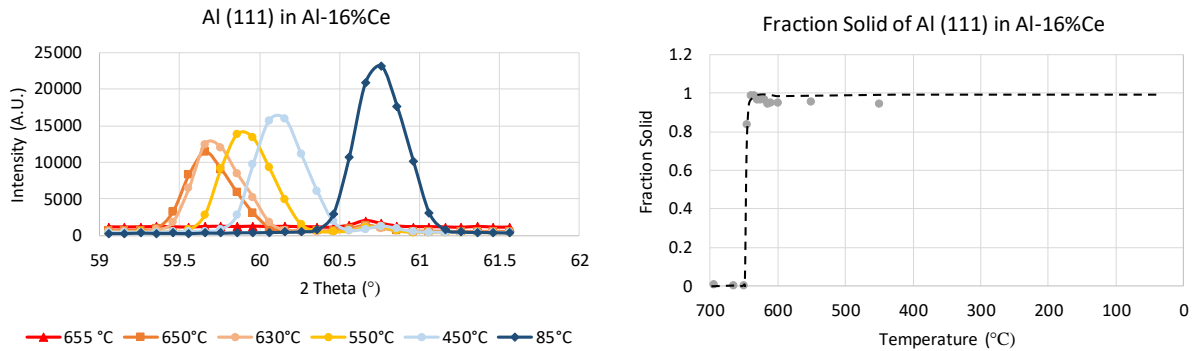


Figure 4.3-5. Temperature-dependent neutron powder diffraction data of the Al-16%Ce alloy showing the Al (111) reflection (left) and the corresponding solid fraction (right). Data are shown as points with the solid and dashed line guiding the eye

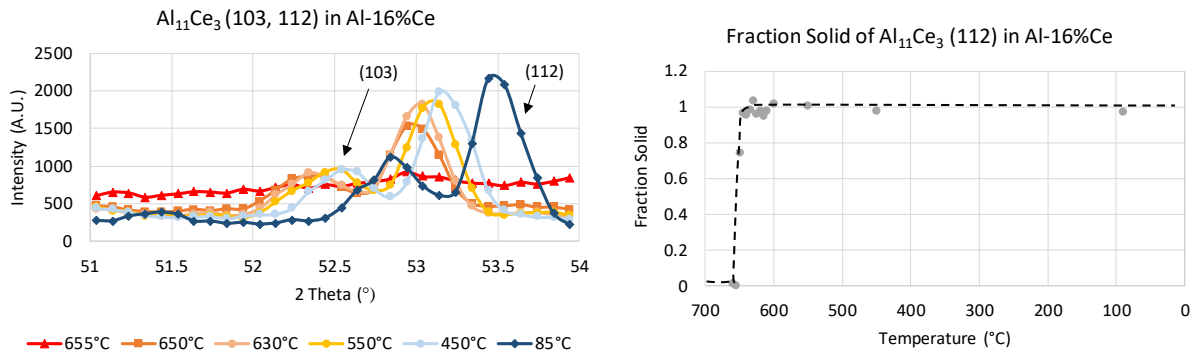


Figure 4.3-6. Temperature-dependent neutron powder diffraction data of the Al-16%Ce alloy showing the $\text{Al}_{11}\text{Ce}_3$ (112) reflection (left) and the corresponding solid fraction (right). Data are shown as points with the solid and dashed line guiding the eye

4.3.2 Neutron Diffraction Al-8%Ce-10%Mg Alloy

The neutron diffraction pattern for the Al-8%Ce-10%Mg alloy, prior to commencing the ND solidification experiment, is shown below in Figure 4.3-7. In general, the ND pattern is similar to that seen in the binary Al-Ce alloys; however, the intensity of a few Al-Ce peaks has increased (i.e., at 45° and 57°). In addition, the $\text{Al}_{11}\text{Ce}_3$ peak at 115° and the $\text{Al}_{11}\text{Ce}_3$ (251) peak at 88° , shown in ND patterns of the binary alloys, is no longer present in the Al-8%Ce-10%Mg pattern. It was observed that the position of the Al peaks has shifted toward lower angles in the Al-8%Ce-10%Mg

alloy as compared to the binary Al-Ce alloys. For example, the Al (111) reflection has decreased from $\sim 60.8^\circ$ (Al-6%Ce and Al-16%Ce alloys) to $\sim 60.2^\circ$ (Al-8%Ce-10%Mg alloy). It is believed that the peak shift is attributed to the dissolved Mg (6-11 at.%) in the Al matrix which induces lattice strain, leading to a larger d-spacing and, thus, a shift of the peak position to lower 2-theta angles.

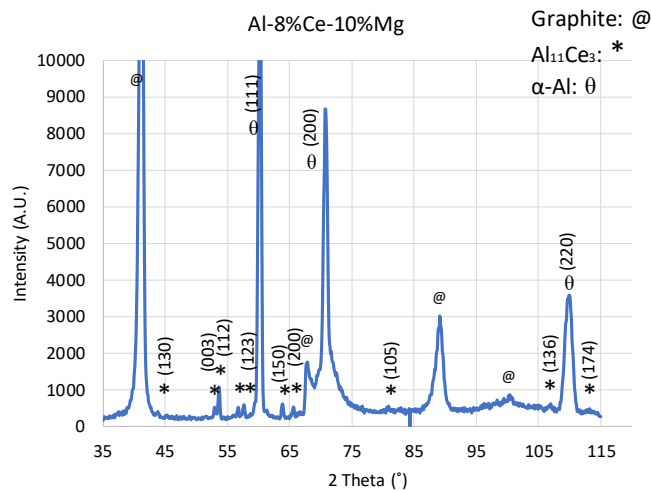


Figure 4.3-7. Full neutron diffraction pattern for the Al-8%Ce-10%Mg alloy prior to solidification

The temperature-dependent ND pattern and fraction solid chart of the Al (111) reflection are shown below in Figure 4.3-8. The ND solidification experiment revealed that FCC-Al begins to nucleate at approximately 600 °C and reaches 100% solid at approximately 500 °C. The nucleation temperature correlates well with the average values of the equilibrium and Scheil calculations. Moreover, the temperature at which the phase reaches 100% solid is only slightly higher than predicted by ThermoCalc's equilibrium model ($\sim 490^\circ\text{C}$).

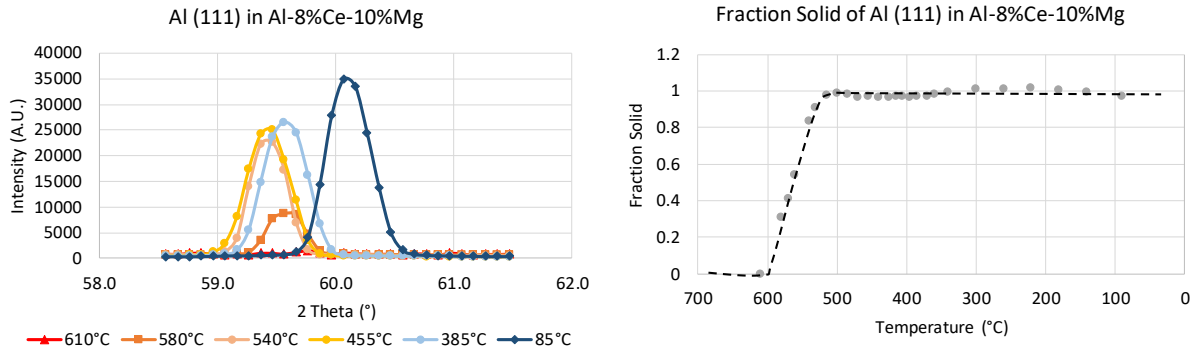


Figure 4.3-8. Temperature-dependent neutron powder diffraction data of the Al-8%Ce-10%Mg alloy showing the Al (111) reflection (left) and the corresponding solid fraction (right). Data are shown as points with the solid and dashed line guiding the eye

Typically, when the temperature of the material is decreased, the interplanar spacing also decreases, and thus, the 2-theta angle increases. This is exactly what we observed for the binary Al-Ce alloys; the peak position of the Al (111) reflection shifted towards higher angles with increasing temperatures. However, for the Al-8%Ce-10%Mg alloy, the peak position of Al first shifts towards lower angles from 610 to 515 °C and then follows the normal rightward angle shift from 515 to 85 °C (see left side of Figure 4.3-9). This initial shift toward lower angles is believed to be caused by the increasing concentration of Mg in the matrix. As the temperature decreases to the solidus temperature and below (i.e., 515-500 °C), the Mg begins to expel from the Al matrix to form Mg-containing intermetallics such as β -AlMg. This claim is supported by the ThermoCalc results shown on the right side of Figure 4.3-9, which indicate that the Mg content in FCC-Al increases from ~3% at 590 °C to ~10% at 490 °C. Beyond 490 °C, the amount of Mg in FCC decreases and, thus, the peak position of Al can return to shifting towards higher angles as the temperature decreases.

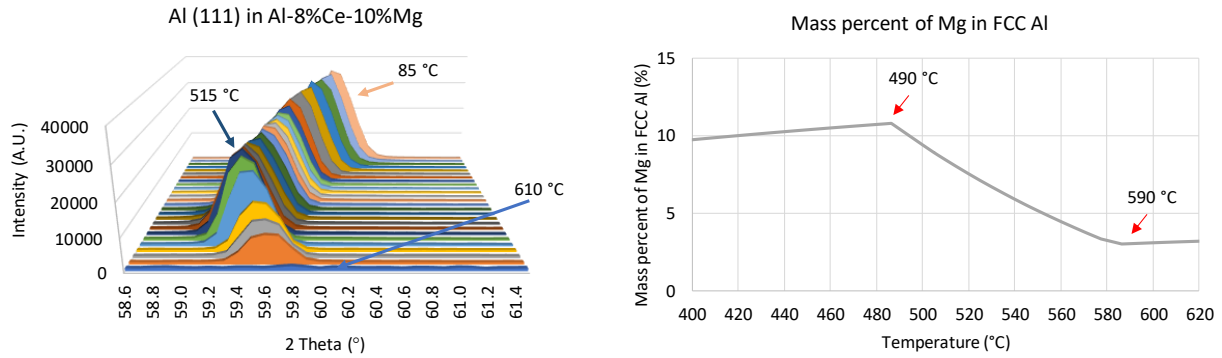


Figure 4.3-9. Progression of Al (111) reflection towards higher angles at lower temperatures in Al-8%Ce-10%Mg alloy (left) and calculated mass percent of dissolved Mg in Al as a function of temperature (right)

According to the Scheil and equilibrium solidification calculations (see Figure 4.1-5 and Figure 4.1-6), the nucleation temperature of the $Al_{11}Ce_3$ phase is ~ 576 °C. Thus, at the highest temperature of the ND experiment (i.e., 610 °C), the $Al_{11}Ce_3$ phase should not be present in the diffraction pattern. However, at 610 °C, a peak was observed near the peak position of the $Al_{11}Ce_3$ (112) reflection (see Figure 4.3-11). Indexing the peak positions of the phases shown in the ThermoCalc results (see Table 4.1-4 and Figure 4.1-5), suggests that this peak corresponds to the Al_8CeMn_4 (002) reflection. This correlates well with the ThermoCalc results, which suggest that the Al_8CeMn_4 phase begins to grow once the $Al_{11}Ce_3$ has almost completely melted (see Figure 4.3-10).

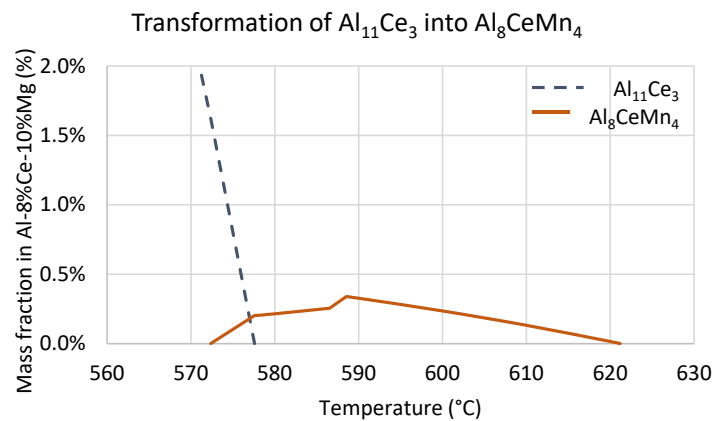


Figure 4.3-10. Transformation of $Al_{11}Ce_3$ into Al_8CeMn_4 for Al-8%Ce-10%Mg alloy (data from ThermoCalc simulation)

Since the peak from the Al_8CeMn_4 phase is present above the liquidus temperature of the $\text{Al}_{11}\text{Ce}_3$ phase, the fraction solid as a function of temperature for this reflection could not be accurately calculated. A similar trend was observed for the $\text{Al}_{11}\text{Ce}_3$ (200) reflection (peak at 610 °C corresponds to Al_8CeMn_4 (231)).

Fortunately, there was no peak at 610 °C for the $\text{Al}_{11}\text{Ce}_3$ (150) reflection (see Figure 4.3-12). Moreover, the nucleation temperature of the (150) reflection correlates much more closely to the ThermoCalc results. For example, based on the ND experiment, the nucleation temperature was determined to be ~560-570 °C and the ThermoCalc calculations suggest ~577 °C. The phase reaches 100% solid between 500 and 515 °C which is just slightly higher than predicted by the equilibrium model.

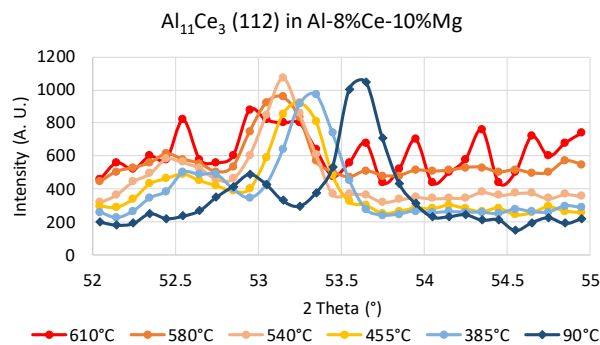


Figure 4.3-11. Temperature-dependent neutron powder diffraction data of the Al-8%Ce-10%Mg alloy showing the $\text{Al}_{11}\text{Ce}_3$ (112) reflection

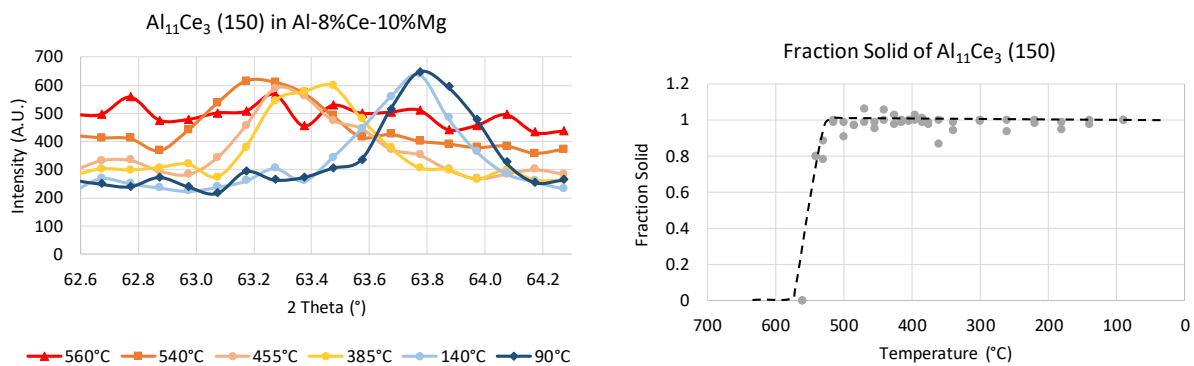


Figure 4.3-12. Temperature-dependent neutron powder diffraction data of the Al-8%Ce-10%Mg alloy showing the $\text{Al}_{11}\text{Ce}_3$ (150) reflection (left) and the corresponding solid fraction (right). Data are shown as points with the solid and dashed line guiding the eye

4.3.3 Neutron Diffraction of A356RE

The full neutron powder diffraction patterns for the A356RE and T6 A356RE alloys prior to the solidification experiment are shown in Figure 4.3-13. The peaks were indexed to Al, Si, Ce($\text{Al}_{1.2}\text{Si}_{0.8}$), $\text{Al}_4\text{Ce}_3\text{Si}_6$, $\text{Al}_{20}\text{Ti}_2\text{Ce}$, $\text{Al}_9\text{FeSi}_3\text{Mg}_5$, Mg_2Si , and $\text{Al}_9\text{Fe}_2\text{Si}_2$. These results correlate very well with the ThermoCalc and SEM/EDS results. The presence of both the Ce($\text{Al}_{1.2}\text{Si}_{0.8}$) and $\text{Al}_4\text{Ce}_3\text{Si}_6$ phases suggests that during the casting process of this alloy, the solidification mode contains both equilibrium and non-equilibrium characteristics. The Ce($\text{Al}_{1.2}\text{Si}_{0.8}$) phase has a greater number of peaks with higher intensities as compared to the $\text{Al}_4\text{Ce}_3\text{Si}_6$ phase, suggesting that the process leans towards non-equilibrium solidification.

Several of the strongest AlSiRE reflections were masked by Al, Si, and graphite and, consequently, the solid fractions curves could not be calculated for these phases. The ND results confirm that the AlSiRE phase shown in the SEM micrographs (see Figure 4.2-12 and Figure 4.2-14) are indeed the Ce($\text{Al}_{1.2}\text{Si}_{0.8}$) reported in [9]. However, the peak positions for each of the Ce($\text{Al}_{1.2}\text{Si}_{0.8}$) peaks shifted slightly from measured 2θ positions shown in the ICSD. These shifts are presumed to be attributed to the additional RE elements (i.e., Nd, and Pr) dissolved in the phase, causing a slightly enlargement of the phase's lattice and, thus, shifting the ND peak position to lower 2-theta angles. According to the Hume-Rothery rules for solid solutions, the comparable, but decreasing atomic radius (i.e., $\text{La} = 2.74 \text{ \AA} \rightarrow \text{Ce} = 2.70 \text{ \AA} \rightarrow \text{Pr} = 2.67 \text{ \AA} \rightarrow \text{Nd} = 2.64 \text{ \AA}$), as well as the similar electronegativities (i.e., $\text{La} = 1.10 \rightarrow \text{Ce} = 1.12 \rightarrow \text{Pr} = 1.13 \rightarrow \text{Nd} = 1.14$) and crystal structures of Pr and Nd to Ce and La, support the claim that both Pr and Nd could be present as substitutional elements [237], [238].

The diffraction patterns for the as-cast and T6 alloys are nearly identical; however, some small variations were observed. The T6 heat treatment appears to have reduced the intensity of the Mg_2Si peaks and, in fact, the (229) reflection was not observed in the ND pattern of the T6 A356RE alloy. These results correlate well with the lower volume fraction of Mg_2Si in the T6 alloy as compared to the as-cast (see Figure 4.2-12 and Figure 4.2-14). Similarly, some of the $\text{Al}_9\text{FeSi}_3\text{Mg}_5$ peaks have decreased in intensity or were not observed in the diffraction pattern. It is possible that the peaks may still be present but are just masked by the background.

Figure 4.3-16 displays the Al (111) reflection during cooling of the A356RE alloy, revealing a shift to higher angles consistent with thermal contraction during cooling. Similar to previous

differential scanning calorimetry results [138], the liquidus and solidus temperatures of primary α -Al are approximately 610 and 550 °C, respectively (see Figure 4.3-16B). Therefore, it appears the additional Ce (~0.9 % increase), Nd (~0.6 % increase), and Pr (~0.2 % increase) in this alloy had negligible effect on the solidification temperature of Al as compared to the Al-7%Si-1%Ce-1%La alloy described in [138]. Figure 4.3-16C and D shows the Si (111) reflection during cooling of the A356RE alloy, where the additional RE content also had a negligible effect on the eutectic temperature of Si (~565-550 °C). Due to the high ratio of the background intensity to the peak intensity of the minority intermetallics, the fraction solid for these phases could not be calculated.

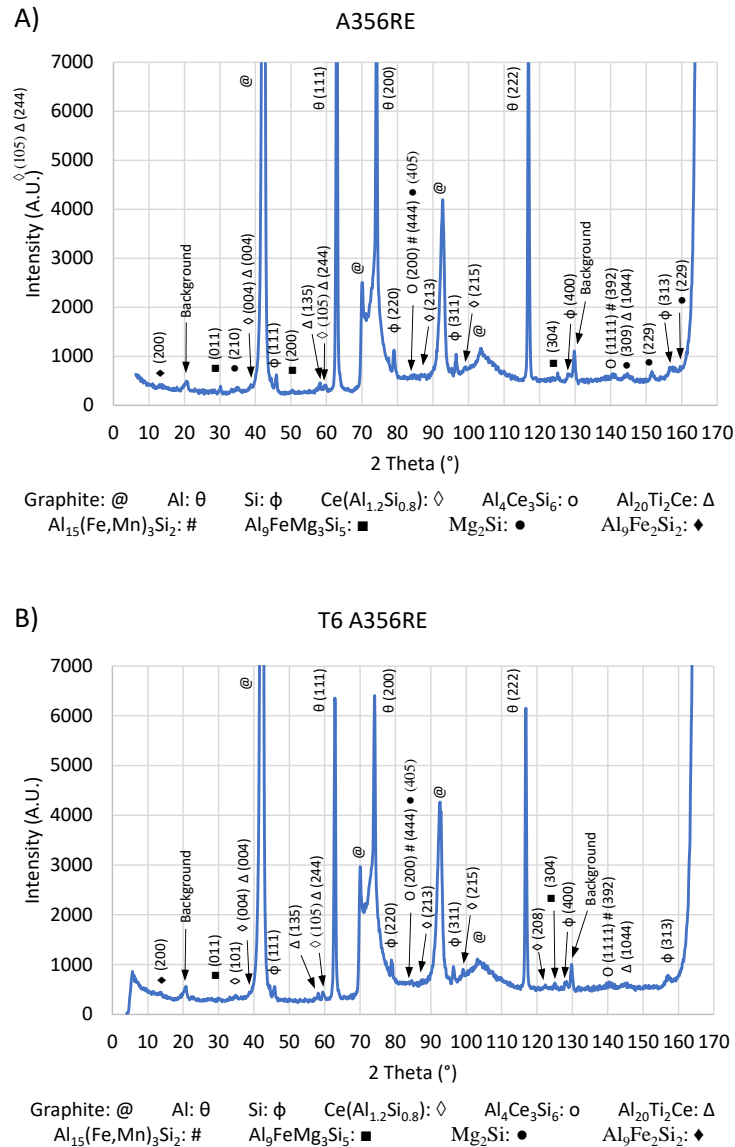


Figure 4.3-13. Full neutron diffraction pattern for A) A356RE and B) T6 A356RE alloys prior to solidification experiment

To estimate the weight fraction of intermetallics in the T6 A356RE alloy, a Rietveld refinement using GSASII was performed (see Figure 4.3-14). The Rietveld method was first introduced in 1969 by Hugo Rietveld to quantitatively analyze neutron diffraction powder patterns [239]. The details of the process are described in detail by H. Reitveld [239] and L. McCusker et al. [240]; however, the basis of the Rietveld method involves using a least-squares method to fit a calculated profile to a powder pattern. Some of the refinable parameters in GSASII include the lattice parameters for each phase, site occupancies of atoms in the unit cell, crystallite size and strain, and

the scale factor (relative intensity of each phase). The accuracy (goodness of fit) of the fitted profile is evaluated using a weighted profile R-factor R_{wp} [241]. The lower the R_{wp} , the better the fit. Due to the relatively high ratio of background intensity and the presence of crystalline and amorphous graphite peaks (caused by the graphite crucible), the accuracy of the Rietveld analysis presented in this dissertation is somewhat limited.

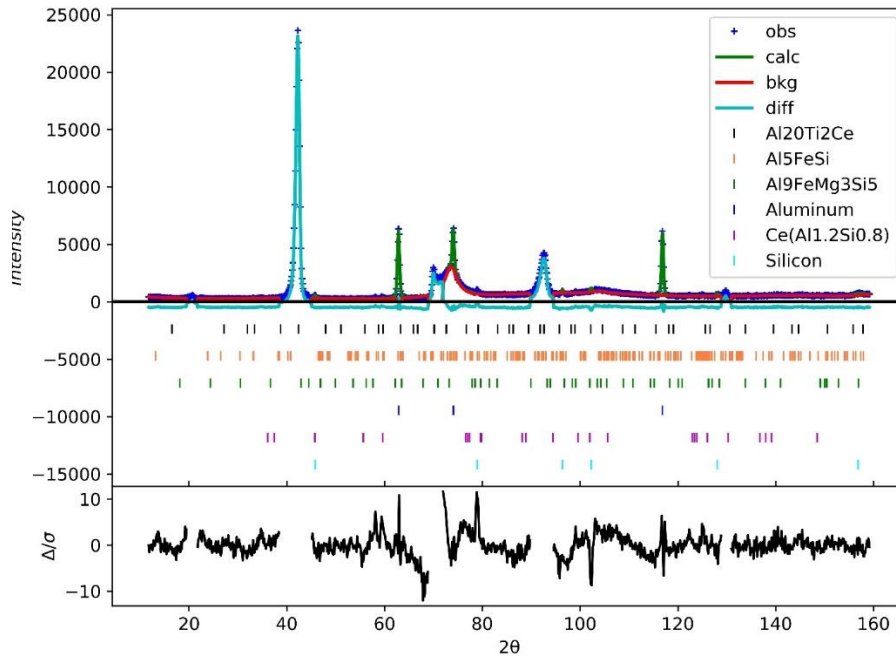


Figure 4.3-14. Rietveld refinement of T6 A356RE alloy using GSASII

Regardless of the inadvertent error, the Rietveld refinement of the T6 A356RE alloy correlates well with the SEM/EDS and ThermoCalc results, and the R_{wp} value was acceptably low (7.7%). The peaks in the powder data were indexed to Al, Si, Ce($\text{Al}_{1.2}\text{Si}_{0.8}$), Al_5FeSi , $\text{Al}_9\text{FeMg}_3\text{Si}_5$, and $\text{Al}_{20}\text{Ti}_2\text{Ce}$, and their corresponding mass fractions are shown in Table 4.3-1. The larger wt.% of Ce($\text{Al}_{1.2}\text{Si}_{0.8}$) calculated by the Rietveld method is likely attributed to the fact that the ThermoCalc database anticipated several additional RE-containing intermetallics, which were not observed in the microstructure during the SEM/EDS analysis. Similarly, the wt.% of Al_5FeSi is greater than predicted by the ThermoCalc simulations due to the lack of the $\text{Al}_{15}(\text{Fe},\text{Mn})_3\text{Si}_2$ present in the actual microstructure. Moreover, the Gibbs free energy of Al_5FeSi is slightly more negative than $\text{Al}_{15}(\text{Fe},\text{Mn})_3\text{Si}_2$ (-29.9 vs. -25.9 kJmol^{-1}), suggesting that the growth of Al_5FeSi will occur more spontaneously than $\text{Al}_{15}(\text{Fe},\text{Mn})_3\text{Si}_2$.

Table 4.3-1. Comparison of results from Reitveld refinement and ThermoCalc

Phase	Rietveld Refinement (wt.%)	ThermoCalc (wt.%)
Al	BAL.	BAL.
Si	5.4	4.7-5.9
Ce(Al _{1.2} Si _{0.8})	4.2	2.22-2.23
Al ₅ FeSi	1.8	0.43-0.74
Al ₉ FeMg ₃ Si ₅	0.7	-
Al ₂₀ Ti ₂ Ce	0.3	-

The temperature-dependent neutron diffraction powder data and corresponding fraction solid for the Al (111) reflection are shown below in Figure 4.3-15. It was observed that the Al was completely liquid at 615 °C, and a peak was present at 600 °C. This suggests that the liquidus temperature is likely about 610 to 615 °C, which correlates well with the ThermoCalc results (i.e., 617 °C). The fraction solid of the Al grows quite rapidly in the first 10 °C below the alloy’s nucleation temperature, and then a slightly slower rate of growth occurs until about 550-560 °C where the Al reaches 100% solid. These results correlate well with the ThermoCalc results. Similar observations were made for the (200) and (220) Al planes.

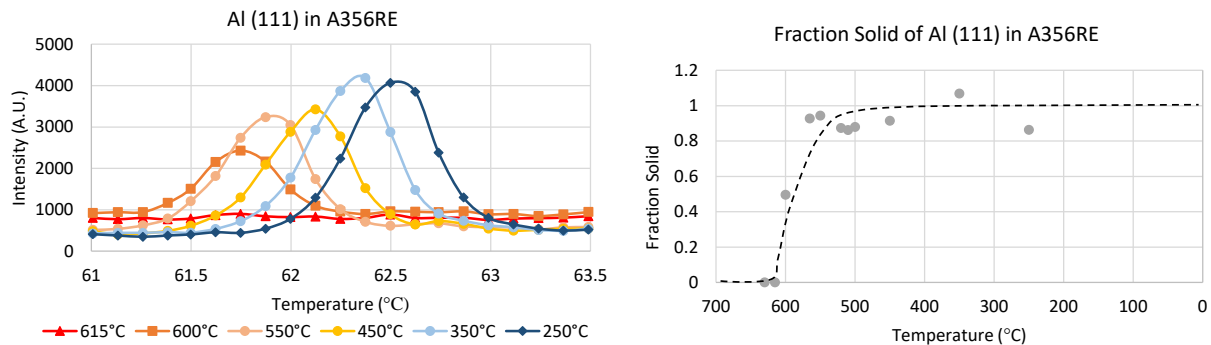


Figure 4.3-15. Temperature-dependent neutron powder diffraction data of the A356RE alloy showing the Al (111) reflection (left) and the corresponding solid fraction (right). Data are shown as points with the solid and dashed line guiding the eye

Similar to the results for the Al (111) reflection, the fraction solid data for the Si (111) reflection correlates well with the ThermoCalc results. For example, the nucleation temperature of Si was

determined to be ~ 575 °C, the same temperature found in the ThermoCalc data. The hypoeutectic composition of Si in the A356RE alloy is indicative by the near-instantaneous growth of Si, reaching 100% solid by ~ 540 - 550 °C. Due to the low coefficient of thermal expansion of Si, the peak shift associated with a temperature change is much lower for the Si phase as compared to the Al phase.

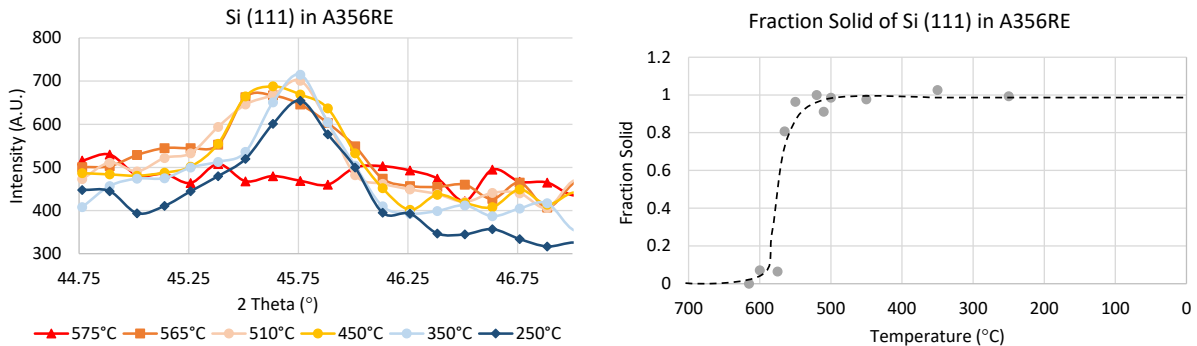


Figure 4.3-16. Temperature-dependent neutron powder diffraction data of the A356RE alloy showing the Si (111) reflection (left) and the corresponding solid fraction (right). Data are shown as points with the solid and dashed line guiding the eye

Connecting the results from the Rietveld refinement with the normalized intensities that were observed with in-situ neutrons, the corresponding mass fraction as a function of temperature could be calculated. The result for the Al (111) and Si (111) reflections are shown below in Figure 4.3-17.

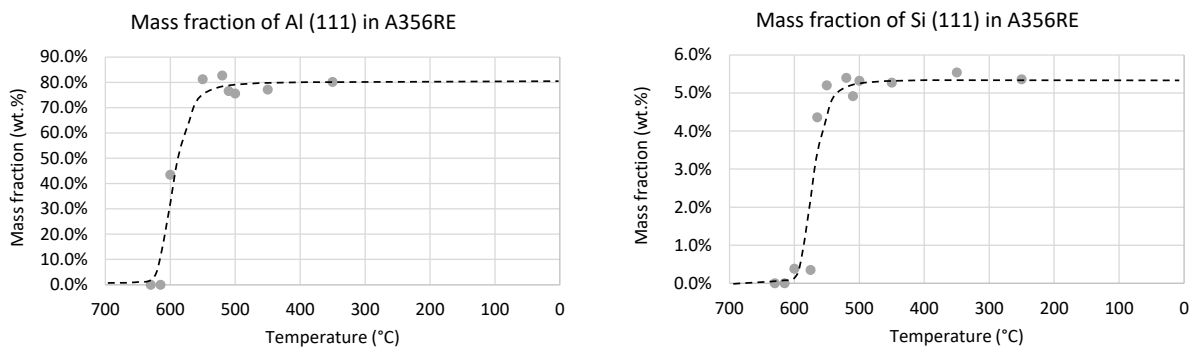


Figure 4.3-17. Calculated mass fraction as a function of temperature for left) Al (111) and right) Si (111) reflection in A356RE alloy

To obtain more than just the solidification characteristics, several data points were collected during the heating process of the samples to determine if any phase changes could be observed. The high background intensity masked a large portion of this data; however, not all was hidden. Figure 4.3-18 provides evidence of the relatively poor thermal stability of the Mg_2Si precipitate at

moderate to high temperatures. The ambient 100 and 130 °C data clearly contain distinguishable peaks corresponding to the (229) reflection of Mg₂Si. At 250 °C, the peak is no longer present, suggesting that this phase has either dissolved or transformed into another intermetallic. This observation helps explain the lack of Mg₂Si in the T6 A356RE alloy as compared to the as-cast A356RE alloy. The already low volume fraction of Mg₂Si in the as-cast alloy may be dissolving or transforming into another phase during the elevated-temperature solution heat treatment or aging portion of the T6 heat treatment. It is difficult to know which phase could be forming at the expense of Mg₂Si based solely off the ND and ThermoCalc results; however, it is possible that the Mg from this phase is simply dissolving back into solution with the Al matrix. The actual mechanisms falls outside the scope of this dissertation.

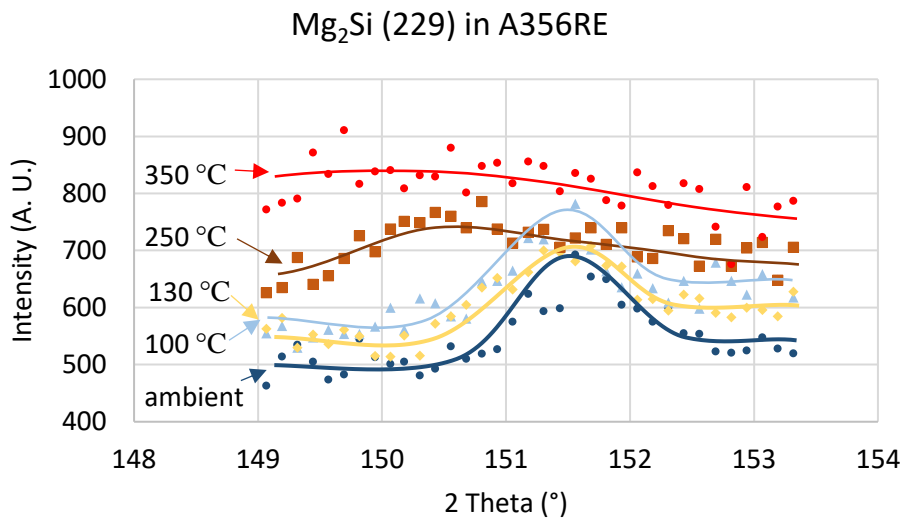


Figure 4.3-18. Dissolution of Mg₂Si phase during heating of the A356RE alloy

The SEM/EDS and ND results clearly indicate that the amount of Mg₂Si has been reduced following the T6 heat treatment. For ambient temperature applications, this would weaken the alloy at room temperature; however, as demonstrated in Figure 4.3-18, the benefits associated with the Mg₂Si phase would likely diminish at current and next-generation engine operating temperatures (250-300 °C). As a result, the dissolution of this phase during heat treatment may, in fact, improve the alloy's thermal stability through formation of more thermally stable intermetallics or through solid solution strengthening the Al matrix.

Due to the high ratio of background intensity to peak intensity, the fraction solid curves for the RE-containing intermetallics could not be determined. However, the progression of peak

intensities for the $\text{Al}_{20}\text{Ti}_2\text{RE}$ and AlSiRE phase was still observed (see Figure 4.3-19). Also seen in the figure below, a small peak corresponding to the $\text{Al}_{20}\text{Ti}_2\text{Ce}$ (135) reflection was observed at approximately 58° . Although low in intensity, it appears that the peak is no longer present at 575°C , suggesting that it has either transformed or completely melted. However, the peak corresponding to the $\text{Ce}(\text{Al}_{1.2}\text{Si}_{0.8})$ (105) reflection at $\sim 59.5^\circ$, can be observed all the way up until the highest temperature of 830°C . This is $\sim 20^\circ\text{C}$ above the simulated liquidus temperature (i.e., 811°C) of this intermetallic, suggesting that the additional RE-elements, which could not be included in the ThermoCalc simulations, may be further improving the thermal stability of this precipitate.

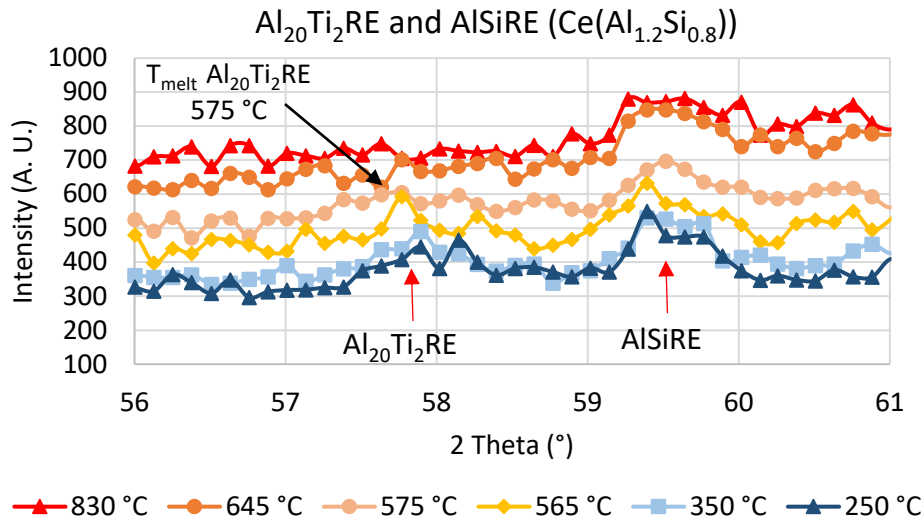


Figure 4.3-19. Progression of peak intensities for $\text{Al}_{20}\text{Ti}_2\text{RE}$ and AlSiRE phases during solidification of A356RE alloy

4.3.4 Neutron Diffraction of A390RE

The complete neutron powder diffraction pattern for the A390RE alloy is shown below in Figure 4.3-20. Similar to the A356RE alloy, the Al, Si, $\text{Ce}(\text{Al}_{1.2}\text{Si}_{0.8})$, $\text{Al}_9\text{Fe}_2\text{Si}_2$, and $\text{Al}_{15}(\text{Fe},\text{Mn})_3\text{Si}_2$ phases were indexed to the ND peaks at room temperature. Due to the high Cu and Si content in the A390RE alloy, an additional phase (i.e., $\text{Al}_4\text{Cu}_2\text{Mg}_8\text{Si}_7$) was also observed in the powder pattern. These results correlate well with the ThermoCalc and SEM/EDS results presented in Figure 4.1-13, Figure 4.1-14, Figure 4.2-18, and Table 4.2-4. The $\text{Al}_4\text{Ce}_3\text{Si}_6$ shown in the equilibrium ThermoCalc simulations (Figure 4.1-13) was not present in the ND powder pattern but, instead, several $\text{Ce}(\text{Al}_{1.2}\text{Si}_{0.8})$ reflections were observed (shown as AlCeSi in ThermoCalc

plots). Similar to the A356RE alloy, this suggests that the A390RE casting followed non-equilibrium solidification.

Similar to the A356RE alloy, the peak positions of the $Ce(Al_{1.2}Si_{0.8})$ phase shifted slightly due to the presence of other RE elements and high concentration of Cu. The results from the ND study of the A390RE alloy reveal that the large fibrous, twin-layered phase is likely the same AlSiRE phase that was observed in the A356RE alloy but its morphology has changed. It is not well understood if the higher Si, RE or Cu concentration is the reason behind this morphology transformation, but it is likely that a combination of their elevated presence factors into that transformation.

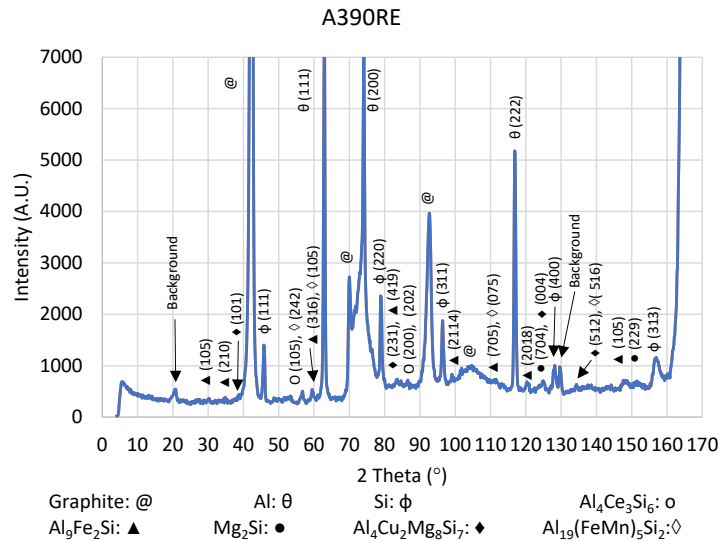


Figure 4.3-20. Full neutron diffraction pattern for the A390RE alloy prior to solidification experiment

Contrary to the gradual solidification of the Al in the A356RE alloy, the complete solidification of Al in the A390RE alloy is nearly instantaneous (~ 565 - 550 °C, see Figure 4.3-21). Conversely, it was observed that the solidification of Si occurred in two stages. First, the relatively slow solidification of primary Si crystals occurred from approximately 650 to 565 °C. Following this, the remaining Si rapidly solidifies in the form of eutectic Si between approximately 565 and 550 °C (see Figure 4.3-22). This prolonged solidification of the alloy increases the susceptibility of porosity formation which is deleterious to the alloy's mechanical properties [139]. Moreover, the addition of large amounts of RE significantly increases the volume fraction of RE-based intermetallics (see Figure 4.2-18), leading to a reduced feedability of the Al during solidification

and the formation of shrinkage porosity. Therefore, additional care should be taken to minimize the formation of porosity during casting.

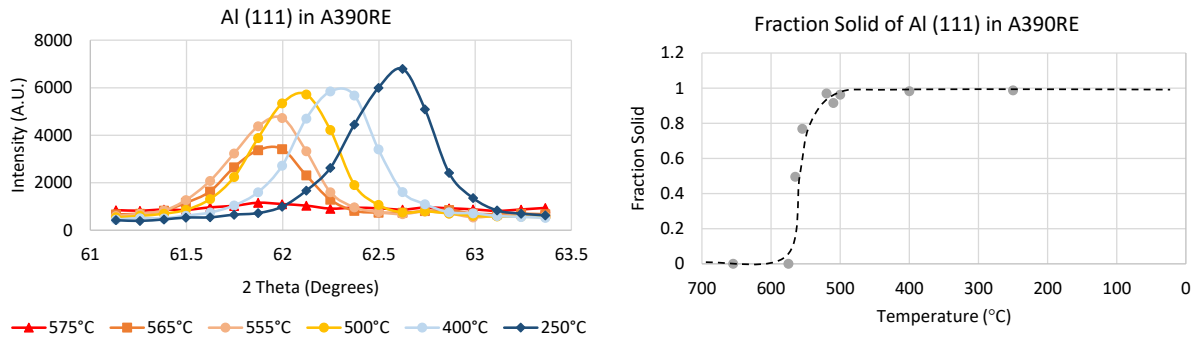


Figure 4.3-21. Temperature-dependent neutron powder diffraction data of the A390RE alloy showing the Al (111) reflection (left) and the corresponding solid fraction (right). Data are shown as points with the solid and dashed line guiding the eye

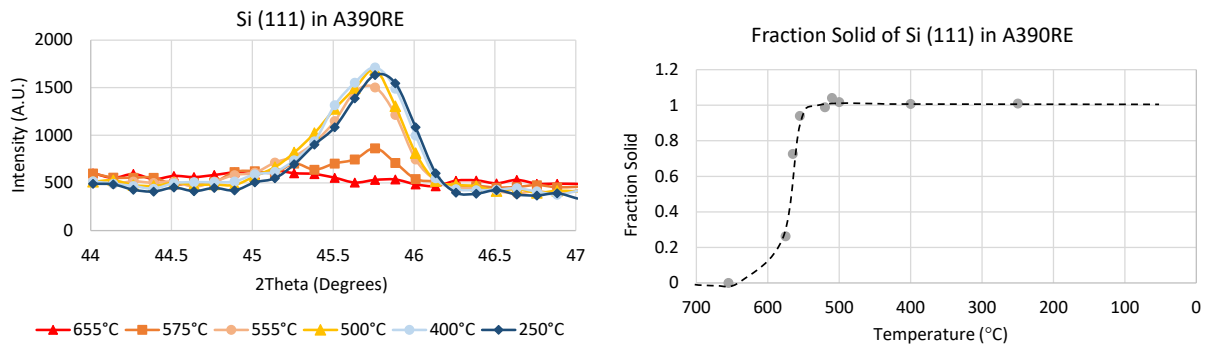


Figure 4.3-22. Temperature-dependent neutron powder diffraction data of the A390RE alloy showing the Si (111) reflection (left) and the corresponding solid fraction (right). Data are shown as points with the solid and dashed line guiding the eye

4.4 Chapter Summary

This chapter discussed the effects that Ce and RE mischmetal has on the expected solidification characteristics (ThermoCalc simulations), microstructure and evolution of phases during solidification of Al alloys. The key points for each alloy are as follows:

Al-6%Ce

The thermodynamic analysis of the Al-6%Ce alloy revealed a nearly instantaneous solidification of the alloy (i.e., 9 °C difference between liquidus and solidus). This suggests that the microstructure of hypoeutectic Al-Ce alloys should consist of very fine phases (i.e., $\text{Al}_{11}\text{Ce}_3$) and minimal defects. This was confirmed from the SEM micrographs which displayed the near-nano-scale lamellar structure of the eutectic $\text{Al}_{11}\text{Ce}_3$ phase. The in-situ solidification studies suggest that this phase has a high thermal stability; its presence was clearly visible until the temperature increased above 650 °C. The neutron results correlate well with the predicted liquidus temperature of the phases.

Al-16%Ce

The thermodynamic analysis of the Al-16%Ce alloy revealed that the solidification range of the alloy greatly increased (i.e., 113 °C vs. 9 °C), rendering it susceptible to porosity formation. However, the SEM/EDS analysis showed minimal porosity. The hypereutectic Ce content resulted in the formation of relatively large brittle primary $\text{Al}_{11}\text{Ce}_3$ crystals. It has been postulated that, due to the difference in thermal expansion coefficients between the Al and $\text{Al}_{11}\text{Ce}_3$, large intergranular stresses may have formed, leading to the observed microcracking. This cracking is believed to be the primary cause for the reported [20] reduction of ductility in hypereutectic Al-Ce alloys. Thus, to obtain the benefits associated with Ce, without inducing stress concentrations and crack initiation sites (microcracks and sharp edge morphology of $\text{Al}_{11}\text{Ce}_3$), the amount of Ce addition should remain below the eutectic concentration.

Al-8%Ce-10%Mg

The addition of Mg to the Al-Ce system resulted in a large increase in the alloy's solidification range, a Mg-supersaturated Al matrix, a change in the morphology of the $\text{Al}_{11}\text{Ce}_3$ eutectic phase from a thin, interconnected lamellar structure to an individualized Chinese script shape, and a large volume fraction of thermally unstable $\beta\text{-AlMg}$ pools. Moreover, the presence of Mg appears to have led to a slight undercooling of the alloy, leading to the precipitation of a few primary $\text{Al}_{11}\text{Ce}_3$. The branch-like structure of the Chinese script phase is expected to act as a barrier against dislocation motion, thereby strengthening the alloy. However, its relatively large size reduces the contribution from Orowan-strengthening and its irregular morphology may lead to stress

concentrations. Together with the poor coarsening resistance of the β -AlMg pools and high susceptibility of porosity formation, it is expected that this alloy may perform poorly in the elevated temperature fitness-for-service tests.

A356/A356RE (as-cast and T6)

The 3.5 wt.% RE addition to the A356 alloy had little effect on the simulated nucleation and solidus temperature of primary Al. However, the RE addition led to several RE-bearing intermetallics, including $\text{Al}_4\text{Ce}_3\text{Si}_6$, AlCeSi_2 , AlCeSi , $\text{Al}_{11}\text{La}_3$, and LaSi_2 . The SEM/EDS analysis revealed the presence of only one RE-containing Al-Si phase (i.e., AlSiRE) which had a similar composition as $\text{Ce}(\text{Al}_{1.2}\text{Si}_{0.8})$ (shown as AlCeSi in ThermoCalc plots), but with additional RE elements. Due to the limitations of the current version of ThermoCalc, Nd and Pr could not be added to the simulations. However, the EDS results suggest that a combined total of ~10 at.% of these elements is present in this AlSiRE phase.

The in-situ neutron diffraction experiment revealed the high thermal stability of the AlSiRE phase, showing the presence of a peak at the highest temperature of 830 °C. This corresponds to a temperature 20 °C higher than the simulated melting temperature of this intermetallic, suggesting the additional RE elements (Pr and Nd) may be improving the thermal stability of this phase.

The Rietveld refinement of the T6 A356RE alloy quantified the approximate weight fraction of intermetallics in the alloy. The results correlate well with the SEM/EDS and simulated ThermoCalc results. As a result, the mass fraction of some of the intermetallics was quantified as a function of temperature.

The XMCT results revealed that the 3D structure of the phase can also be present as a plate rather than just the reported block-like structure. Combined with the high thermal stability of this phase, strong bonding with vacancies, and significant distribution, it is expected that the AlSiRE phase will improve the A356 alloy's tensile strength and creep resistance at elevated temperatures.

A390/A390RE

The ThermoCalc simulations suggested that the A390 and A390RE alloys would consist of several intermetallics, including a large mass fraction of Al_2Cu . However, this phase was not observed in

the actual microstructure. The lack of Al_2Cu is believed to be caused by the high solubility of Cu in Ce-containing phases.

The high Si and Cu concentration in the A390RE appears to have transformed the plate-like structure of the AlSiRE phase into a twin-layer, fibrous structure which frequently contained large voids and porosities. Together with the long solidification range of this alloy, it is not expected that this alloy will perform sufficiently during the elevated-temperature tensile and creep tests. The analysis of the A390 alloy suggest that the REs, in the presence of high Cu and Si concentrations, may lead to unfavorable microstructures and, therefore, unfavourable mechanical properties.

The observations from this chapter lead to the following questions:

- 1) How do the RE additions affect alloys' creep resistance and strength retention at elevated temperatures?
- 2) How does the fitness-for-service performance of the RE-modified A356 and A390 alloys compare to the currently used powertrain alloy, T7 A319?

Chapter 5: Fitness-For-Service Properties of Al-RE Alloys

The lack of high-temperature strength of conventional powertrain alloys has been the driving factor behind a few recent studies which have investigated the effects that REs have on the mechanical properties of Al powertrain alloys. For example, E. Aghaie et al. [167] characterized the effects that small additions (0.1 to 1 wt.%) of Ce have on the room and elevated-temperature mechanical properties of an as-cast B319 alloy (Al-Si-Cu-Mg based). The study indicated that 0.1 wt.% of Ce resulted in the greatest increase in the room-temperature YS (i.e., 150 to 165 MPa) and UTS (214 to 234 MPa). In addition, at 250 °C, the B319 alloy's YS and UTS improved from 110 and 139 MPa to 125 and 149 MPa, respectively. It should be noted that the samples described in the aforementioned study were not conditioned prior to conducting the tensile test. In another study, M. Ibrahim [166] studied the effects that Ce and La have on the room-temperature mechanical properties of an A356 alloy. . The study characterized the individual effects that 1.0 wt.% of Ce, 1.0 wt.% La, and 1.0 wt.% Ce + 1.0 wt.% La have on the YS and UTS of the A356 alloy in the as-cast, T6 and T7 heat-treated state. The results from the study suggest that the T6 heat treatment provides the greatest improvement to the mechanical properties of the alloy; however, the RE additions seem to have had a negative effect on the YS and UTS. For example, the YS and UTS of the alloy was reduced from 260 and 320 MPa to 240 and 275 MPa, respectively, after the introduction of 1.0 wt.% Ce and 1.0 wt.% La. The study suggests that the higher volume fraction of the RE intermetallics increases the alloy's brittleness and, therefore, deteriorates the tensile properties. This study provides an indication of the effects that REs have on the microstructure and room-temperature properties of the A356 alloy system; however, the elevated-temperature tensile and creep properties were not studied. Further, the published high-temperature properties of RE-modified Al alloys are largely restricted to non-conditioned samples and, therefore, the results are not representative of the actual in-service performance of the alloy. Thus, this chapter characterizes the effects that REs have on the mechanical properties of aluminum alloys that would determine their fitness-for-service feasibility for the next generation of diesel engines.

Similar to the experimental procedure written in section 3.5, the Al-RE alloys were subjected to elevated-temperature (~250 and 300 °C) tensile and creep tests following the ASTM standard E8M and B139 [61], [62]. The dimensions of the creep and tensile samples are shown below in Figure 5-1.

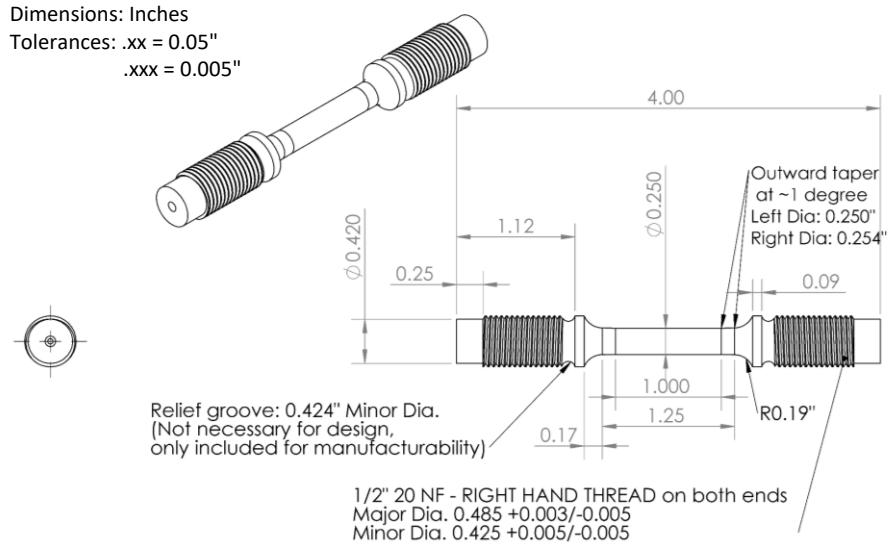


Figure 5-1. Geometry of tensile and creep samples

All of the samples described in this section were pre-conditioned at the testing temperature for 200 hours. It should be noted that the machining process of the hypereutectic A390RE alloy revealed the alloy's extreme brittleness as well as its susceptibility to porosity. Several A390RE samples, both prior to and after conditioning, were broken during the machining process, regardless of the machining intensity. It is believed that this is due to the presence of the brittle primary Si crystals, the very large and non-homogenous structure of the fibrous phases, as well as the elevated amount of porosity. For this reason, the FFS testing for the A390RE alloy was excluded from this study. Future work will include modification of the alloy's chemistry.

5.1 Tensile: Al-8%Ce-10%Mg

The results from the elevated-temperature tensile tests of the Al-8%Ce-10%Mg alloy are shown below in Figure 5.1-1. At 250 °C, the YS and UTS of the alloy were determined to be ~90 and 98 MPa, respectively. These values, particularly the UTS, are considerably lower than the values presented by D. Weiss et al. [211] who found that the YS and UTS at 260 °C were 97 and 137 MPa, respectively. The primary cause for this reduction of strength is believed to be the conditioning process that was performed on the alloys presented in this dissertation. The coarsening resistance of the β -AlMg pools, shown in Figure 4.2-6 and Figure 4.2-7, is known to be very poor. Thus, during the 200- hour conditioning process, it is likely that the AlMg pools begin to coarsen and even dissolve, causing the strength provided by the AlMg precipitates to diminish. This is supported by the ThermoCalc results (see Figure 4.1-5) which suggest that the β -

AlMg phase begins to dissolve above ~30-50 °C. It is not 100% accurate to look at solidification simulations in reverse (i.e., in the direction of low to high temperatures); however, this can provide some indication of how the precipitate will react to an increase of temperature. According to Figure 4.1-5 (i.e., the equilibrium solidification results for the Al-8%Ce-10%Mg alloy), at 25 °C, approximately 26% of the microstructure should consist of β -AlMg. The amount of β -AlMg decreases to ~17% when the temperature of the system increases to 250 °C.

The same reasoning is suggested for the increasingly poor performance of the alloy at 300 °C. The poor thermal stability of β -AlMg is believed to cause precipitate coarsening and dissolution back into the matrix, reducing the materials YS and UTS by ~37% and 32%, respectively. Increasing the temperature to 300 °C has tripled the elongation (i.e., from 3.4 to 10.1%). Although ductility is an important factor in powertrain components (provides an “artificial” safety factor), too much ductility can result in poor dimensional stability and can limit the alloy’s applicability for components which rely on tight tolerances.

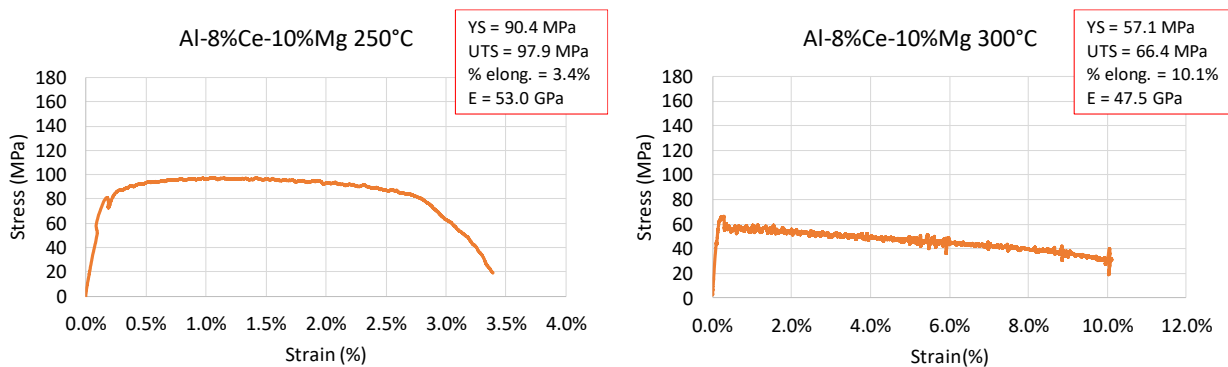


Figure 5.1-1. Tensile test results for Al-8%Ce-10%Mg alloy at left) 250 °C and right) 300 °C (Conditioned for 200 hours)

5.2 Tensile: T6 A356 and A356RE (As-Cast and T6)

The results from the room and elevated-temperature tensile tests of the T6 A356, as-cast A356RE and T6 A356RE alloys are shown below in Figure 5.2-1 to Figure 5.2-5. An indication of the alloy’s thermal stability will be provided by comparing the results to the room-temperature properties. Since the as-cast A356RE alloy is not intended for commercial use, and is only under investigation to observe the effects of heat treatment, a room-temperature tensile test was not performed on this alloy.

The published room-temperature YS, UTS, elongation, and Young's modulus for T6 A356 are ~150-170 MPa, 228-250 MPa, 3.0-5%, and 72.4 GPa, respectively [242]. These values correspond well with the values obtained during the room-temperature tensile test of the T6 A356 alloy (see Figure 5.2-1), with the exception of YS which was considerably higher than reported in literature.

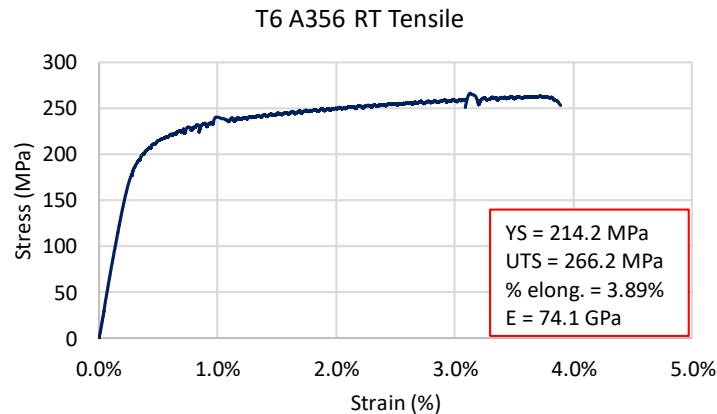


Figure 5.2-1. Room-temperature tensile test results for T6 A356 alloy

Increasing the temperature of the tensile test to 250 °C reduced the YS and UTS by 60-75%, reaching just 55 and 59 MPa, respectively. It is possible that since eutectic Si is, essentially, the only strengthening phase, the Si particles act as the main load-bearing phase and, thus, are susceptible to cracking once the applied stress and temperature increase. Moreover, the elevated-temperature conditioning process has likely resulted in the cracking of the Si particles and the Fe-bearing phases prior to subjecting any external load. At 250 °C, the rate of particle cracking for both phases nearly doubles as compared to room temperature [243]. This effect is amplified after the conditioning temperature is increased to 300 °C which is presumed to be the primary reason for the further reduction of the alloy's strength (i.e., decreased by another ~50%). As compared to the room-temperature properties, the YS and UTS at 300 °C have decreased by 83-87%. The massive increase in the elongation, the reduction of the elastic modulus (lowers the material's geometrical stability), and the poor strength retention at 250 and 300 °C, indicate that, in the current state, the T6 A356 alloy is not suitable for elevated temperature applications.

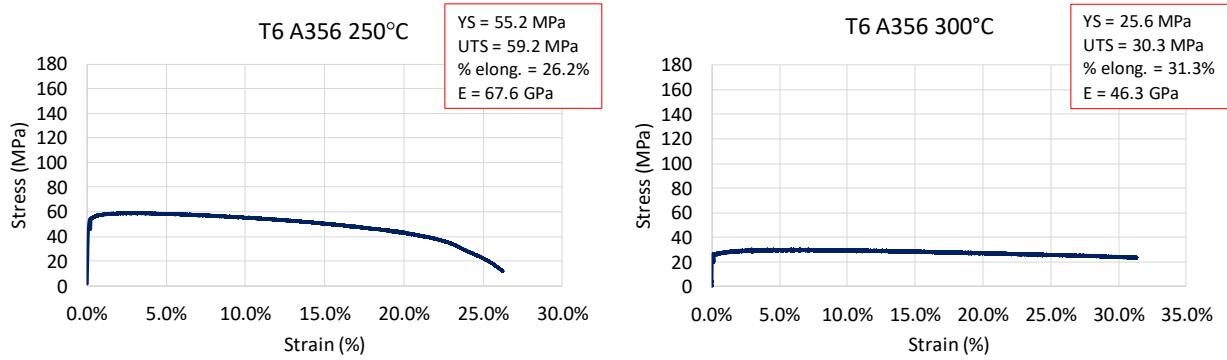


Figure 5.2-2. Tensile test results for T6 A356 alloy at left) 250 °C and right) 300 °C (conditioned for 200 hours)

The tensile test results for the as-cast A356RE alloy are shown below in Figure 5.2-3. At 250 °C, the YS of the A356RE was the same as the T6 A356 alloy; however, the UTS was improved by approximately 17%, reaching ~70 MPa. The increase in the strength is believed to be attributed to the presence of the hard and thermally stable AlSiRE phase (see Figure 4.2-15). The hard AlSiRE phase is also the reason for the reduced elongation, from 26 to 9%. More impressive is the strength retention once the temperature is increased to 300 °C. Not only are the YS and UTS nearly twice that of the T6 A356 alloy at 300 °C, but the as-cast A356RE alloy has retained more than 90% of its strength at 300 °C. These results clearly demonstrate the benefits associated with RE additions. Currently, the as-cast A356RE alloy performs superiorly without the need for a costly heat treatment.

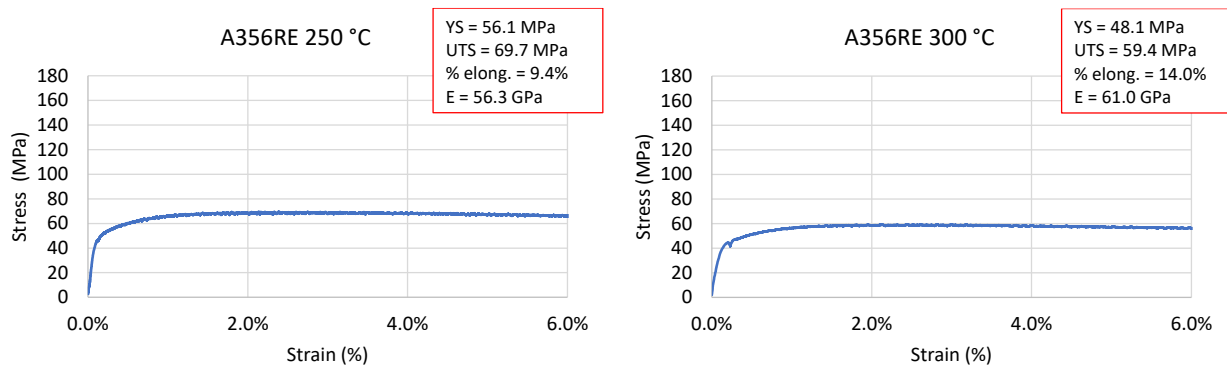


Figure 5.2-3. Tensile test results for as-cast A356RE alloy at left) 250 °C and right) 300 °C (conditioned for 200 hours)

The room-temperature tensile test results for the T6 A356RE alloy is shown below in Figure 5.2-4. As compared to the RE-free T6 A356 alloy, the YS and UTS appear to have decreased quite

substantially, reaching ~192 and 223 MPa, respectively. This corresponds well with the reported characteristic trait that RE additions above 1 wt.% result in an impairment of the room-temperature strength of the A356 alloy [166]. The Young's modulus has remained relatively unchanged; however, the elongation has decreased by more than 2%. It is likely that the hard RE-bearing intermetallics are the primary cause for the reduction of the elongation.

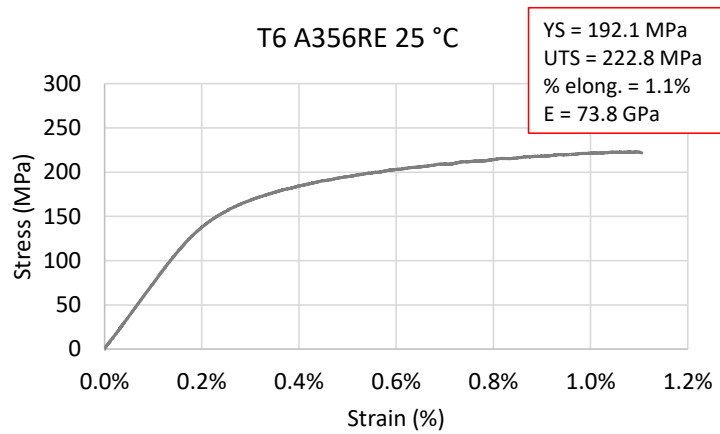


Figure 5.2-4. Room-temperature tensile test results for T6 A356+3.5% alloy

Although the room-temperature performance of the T6 A356RE alloy has decreased as compared to the RE-free T6 A356 alloy, the elevated-temperature tensile test results for the T6 A356RE alloy elucidate the effectiveness of RE mischmetal for improving the thermal stability of the A356 alloy. More than 75% of the alloy's YS is retained after increasing the temperature to 250 °C, reaching a maximum magnitude of ~147 MPa. Further, approximately 60% of the alloy's strength is retained after the temperature is increased from 250 to 300 °C. The high thermal stability of the RE-containing phases results in the retention of approximately 50% of the alloy's strength when the temperature is increased from 25 to 300 °C. Moreover, the elongation has remained at an appropriately low magnitude, unlike the RE-free T6 A356 alloy which saw more than 30% elongation at 300 °C.

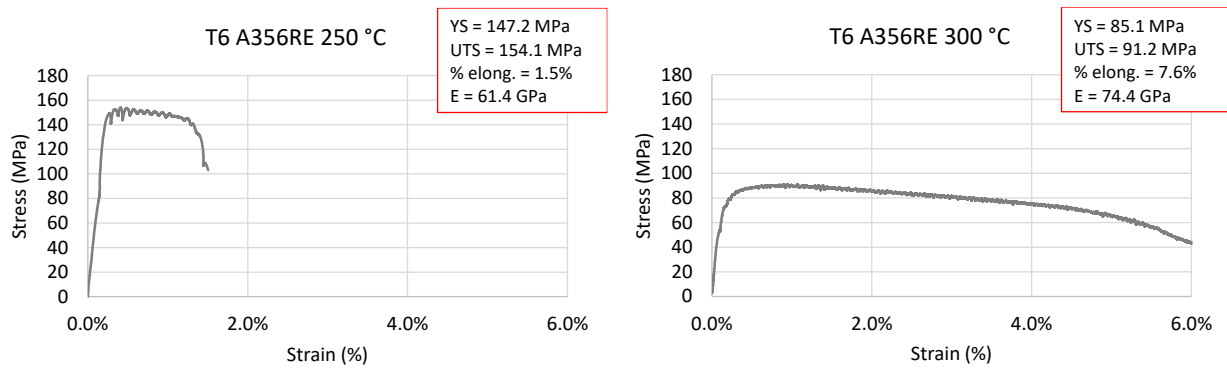


Figure 5.2-5. Tensile test results for T6 A356RE alloy at left) 250 °C and right) 300 °C (conditioned for 200 hours)

The decrease in the strength and the increase in the elongation of the T6 A356RE alloy at 300 °C are believed to be attributed to the increased rate of intermetallic cracking during the conditioning process [106]. This is supported by the SEM micrographs shown below in Figure 5.2-6 which clearly demonstrate that the 250 °C conditioning process leads to insignificant microstructural changes, whereas the 300 °C conditioning process clearly results in a considerable amount of Si fracturing and a notable degree of AlSiRE particle cracking.

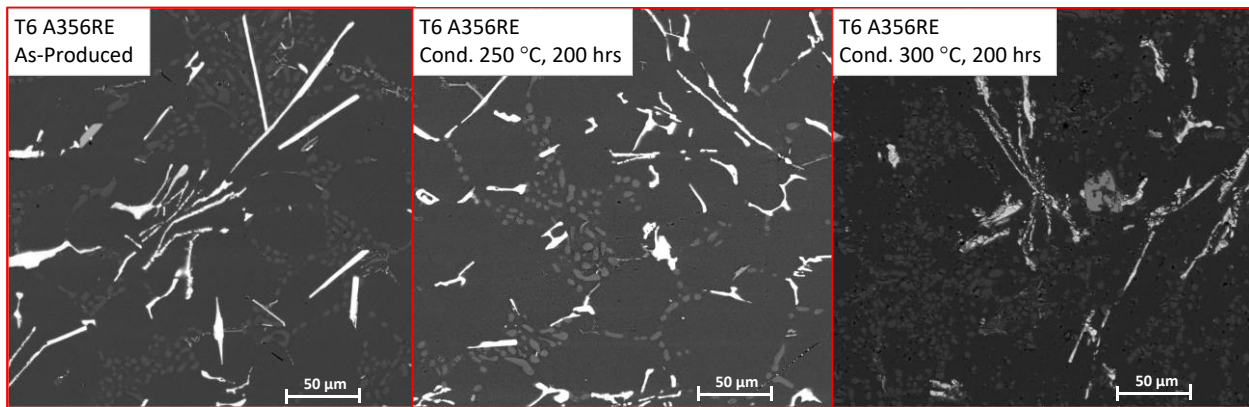


Figure 5.2-6. SEM micrographs of T6 A356RE alloy throughout the conditioning process

5.3 Creep: Al-8%Ce-10%Mg

The creep results for the Al-8%Ce-10%Mg alloy are shown below in Figure 5.3-1. At 250 °C, with an applied stress of 22 MPa, the Al-8%Ce-10%Mg alloy entered steady-state creep after approximately 10 hours; the minimum creep rate was determined to be $\sim 1.169\text{E-}08 \text{ s}^{-1}$. At 100 hours, the total creep strain was approximately 0.62%, which is much greater than the approximate target of 0.1%. It was expected that the branch-like structure of the Chinese script $\text{Al}_{11}\text{Ce}_3$ precipitates would act as a barrier against dislocation movements; however, the poor performance

of the alloy during the creep test says otherwise. It is likely that the large size of these $\text{Al}_{11}\text{Ce}_3$ crystals minimizes the Orowan mechanism, resulting in facilitated gliding and climbing of dislocation within the large precipitate-free pockets of the Al matrix. Similar to the mechanisms explained for the alloy's poor tensile test performance, the 300 °C conditioning process has surely led to a substantial reduction of the volume fraction of the thermally unstable $\beta\text{-AlMg}$ precipitates, leading to fewer intermetallics available for halting dislocation motion. The reduction of available precipitates is believed to be one of the driving factors for the insufficient performance of the Al-8%Ce-10%Mg alloy at both 250 and 300 °C. The results from the 300 °C creep test indicate that the alloy enters tertiary creep after just 12 hours, leading to the complete failure of the sample in under 20 hours. Although the sample quickly transitioned to tertiary creep, the brief steady-state creep rate was $\sim 7.621\text{E-}07 \text{ s}^{-1}$. The activation energy at 22 MPa, between 250 and 300 °C, was calculated as $\sim 208 \text{ kJmol}^{-1}$, which is moderately higher than for self-diffusion of pure Al (i.e., $\sim 143 \text{ kJmol}^{-1}$ [244]). It should be noted that the difference of the activation energy for the Al-8%Ce-10%Mg alloy, as compared to pure Al, is likely associated to the temperature-dependence of the elastic modulus of Al [210] and the presence of incoherent and semi-coherent precipitates [245], [246]. Along with the poor tensile performance of the Al-8%Ce-10%Mg alloy, the creep performance indicates that this alloy is not suitable for current or next-generation engines.

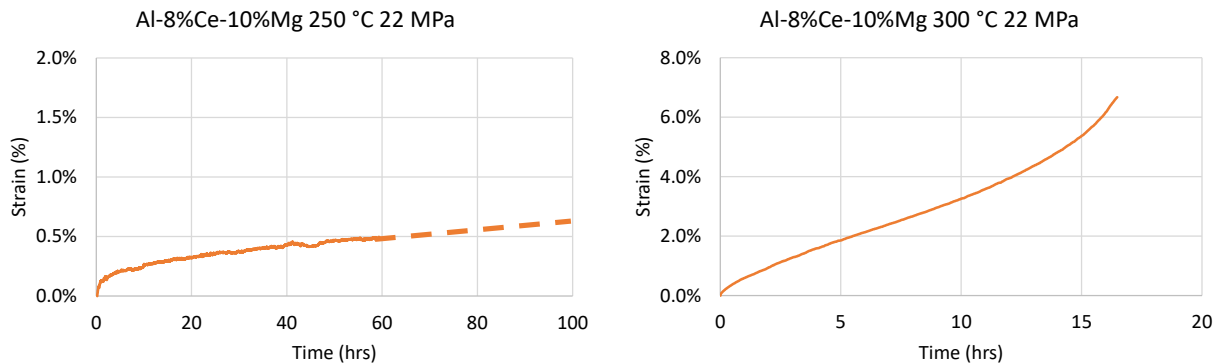


Figure 5.3-1. Creep test results for Al-8%Ce-10%Mg alloy at left) 250 °C and right) 300 °C (conditioned for 200 hours)

5.4 Creep: T6 A356 and A356re (As-Cast and T6)

The creep results for the T6 A356 alloy are shown below in Figure 5.4-2. To extract additional information from the creep tests for this alloy, a staircase creep experiment was also performed. Based on the tensile strength obtained from the tensile tests, the applied stress was progressively

increased from 22 MPa toward the material's yield strength. Each load was held for 24 hours and then released for 1 hour. The minimum creep rates for each load at 250 and 300 °C are shown in Table 5.4-1. At 22 MPa, the T6 A356 alloy performed considerably better than the Al-8%Ce-10%Mg alloy. In fact, with an applied load of 22 MPa at 250 °C, the creep after 100 hours was within the target creep of ~0.1%. The creep rate remained relatively low until the load was increased to 40 MPa, after which, the sample quickly transitioned to tertiary creep then failed. Once the temperature was increased to 300 °C, the sample began to enter tertiary creep in approximately 15 hours, elucidating the poor thermal stability of the alloy. Even at the low load of 22 MPa, the brief steady-state creep rate was three magnitudes larger than it was at 250 °C.

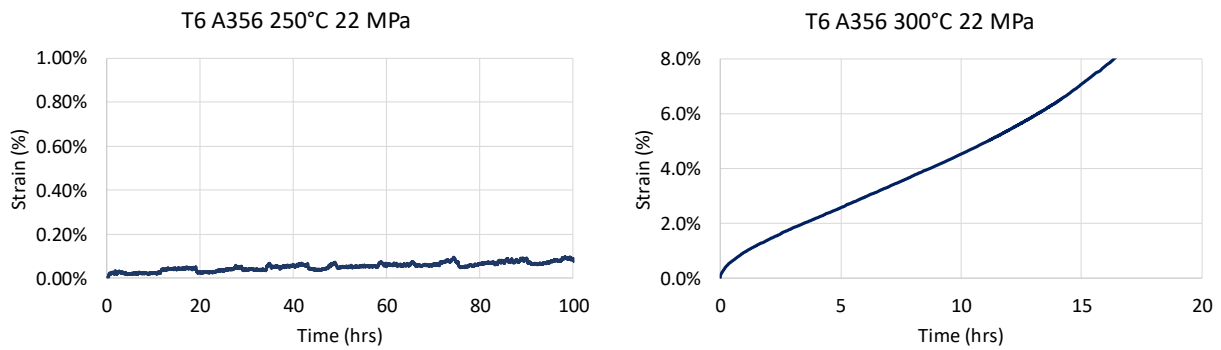


Figure 5.4-1. Creep test results for T6 A356 alloy at left) 250 °C and right) 300 °C (conditioned for 200 hours)

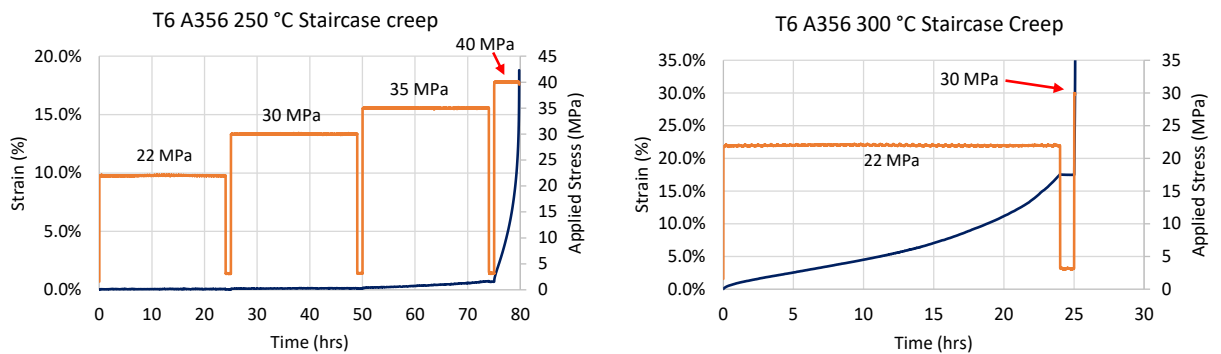


Figure 5.4-2. Creep test results for T6 A356 alloy at left) 250 °C and right) 300 °C (conditioned for 200 hours)

Table 5.4-1. Steady-state creep rates for T6 A356 alloy (units: $10^{-8}/s$)

T6 A356	22 MPa	30 MPa	35 MPa	40 MPa
250 °C	0.20	0.48	5.76	394.31 ^f
300 °C	106.21	fracture	-	-

^f:fracture

As described in sections 2.2.1.2 and 3.5, a staircase creep test allows for the determination of the apparent stress exponent n_a and activation energy Q_a , which provide additional information regarding which mechanisms are controlling the creep rate (see Figure 5.4-4). At 250 °C, from 22 to 30 MPa, $n_a = 2.8$, which suggests that creep rate is governed by viscous drag/climb [247], [248]. However, the activation energy at 22 MPa was determined to be 312 kJmol^{-1} . This elevated magnitude of activation energy suggests that the dislocations are thermally activated which facilitates the bypassing of precipitates by a combination of gliding and cross slipping [209]. Increasing the load from 30 to 35 MPa results in a rapid increase in the stress exponent to $n_a = 16.1$, suggesting that the power-law has broken down and that dislocation creep is now the predominant creep mechanism. Raising the load from 35 to 40 MPa increases the strain rate by nearly 2 magnitudes (i.e., $E-08$ to $E-06 \text{ s}^{-1}$), and doubles the creep exponent to $n = 31.6$, resulting in the quick failure of the sample. An n_a value of 31.6 suggests that the rate-controlling mechanism has transitioned from dislocation creep to dislocation glide [209]. Similar to the T7 A319 alloy, such high apparent stress exponents are indicative of a threshold stress (see section 2.2.1.2). Plotting $\dot{\epsilon}_s^{1/n}$ vs. σ , with a true stress exponent of $n = 4.4, 5,$ and 7 , the best linear fit corresponds to an $n = 7$ ($R^2 = 0.931$, see Figure 5.4-3), representing lattice diffusion controlled creep with a constant subgrain structure [58]. Extrapolating the trendlines into $\dot{\epsilon}_s = 0$.

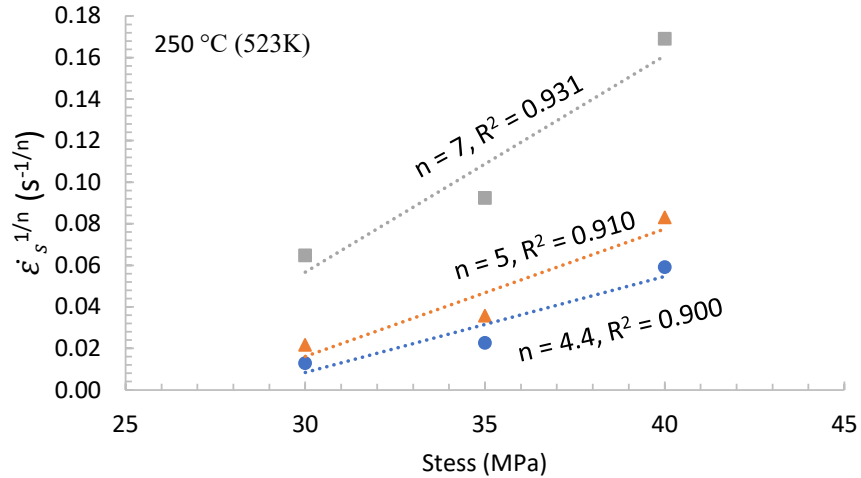


Figure 5.4-3. A plot of $\dot{\epsilon}_s^{1/n}$ vs σ for the T6 A356 alloy at 250 °C

As a result, the threshold stress was determined to be 24.6 MPa (see Figure 5.4-4). Similar to the T7 A319 alloy, the threshold stress at $n = 7$ appears to be under-estimated, and it is more likely that the threshold stress correlates more closely to $n = 4.4$ (28.1 MPa) or $n = 5$ (27.4 MPa). Similar to the discussion about the threshold stress for the T7 A319 alloy, the relatively large stress increments add uncertainty to the estimated threshold value, and thus, future experiments should be performed with smaller increments between 30 and 35 MPa.

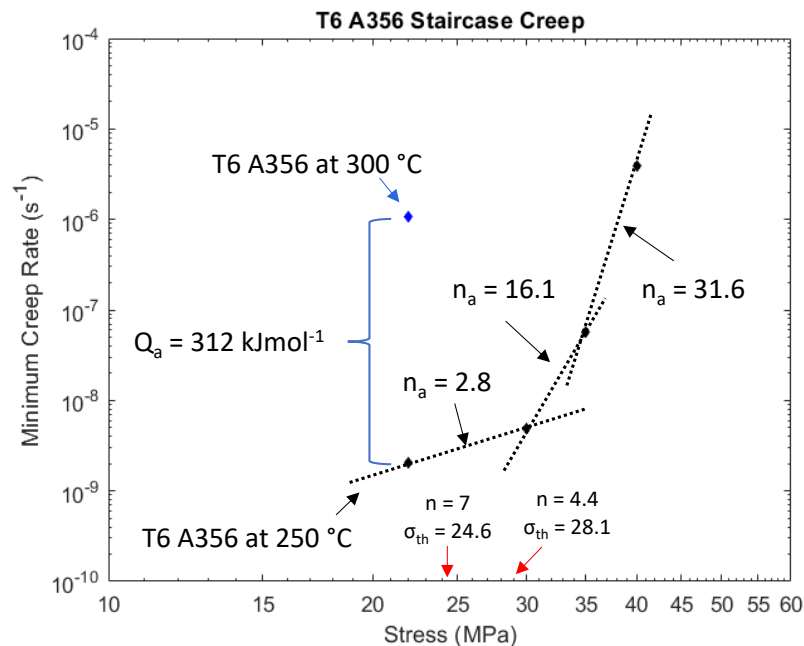


Figure 5.4-4. Minimum creep rates as a function of applied stress for T6 A356 alloy. Note apparent stress exponent n_a and threshold stress σ_{th}

The low $\dot{\epsilon}_s$ at 22 MPa and 250 °C suggests that the T6 A356 would likely perform sufficiently under these operating conditions; however, this is not the case at 300 °C. By increasing the temperature to 300 °C, the $\dot{\epsilon}_s$ increased by more than two full magnitudes, reaching 1.02E-06 s⁻¹. Moreover, the poor tensile performance of this alloy at 300 °C further restricts the feasibility of using this alloy for elevated-temperature applications. Similar to the Al-8%Ce-10%Mg alloy, the T6 A356 alloy is also unfit for current or next-generation engines.

The creep results for the as-cast A356RE alloy are shown below in Figure 5.4-5. At first glance, it seems that the as-cast A356RE is performing slightly worse than the T6 A356 at 250 °C since the total strain of the RE-modified alloy at 100 hours is ~0.2%, as compared to 0.1%. However, the steady-state creep rates at 22 MPa for both alloys are essentially the same (i.e., 2.015E-09 for A356RE and 2.038E-09 s⁻¹ for T6 A356). This suggests that the strain associated with primary creep is larger in the as-cast A356RE alloy as compared to the T6 A356 alloy. This is likely due to the lower stiffness of the A356RE alloy (E = 56.3 GPa) as compared to the T6 A356 alloy (E = 67.6 GPa) (see Figure 5.2-2 and Figure 5.2-3).

Similar to the tensile test results, the performance of the A356RE alloy in the 300 °C creep test is considerably better than in the T6 A356 alloy. For example, the strain after 20 hours at 22 MPa for the A356RE and T6 A356 alloys was ~0.3% and 12%, respectively. Moreover, the steady-state creep rate is two magnitudes smaller than the T6 A356 alloy (i.e., 1.874E-08 s⁻¹ vs. 1.062E-06 s⁻¹). Comparing the results from both 250 and 300 °C reveals that the activation energy reduces by nearly 50%, reaching ~111 kJmol⁻¹. This suggests that the creep rate is controlled by a dislocation core-diffusion mechanism [209]. Since the as-cast A356RE alloy was not intended for commercial applications, a staircase creep experiment was not performed.

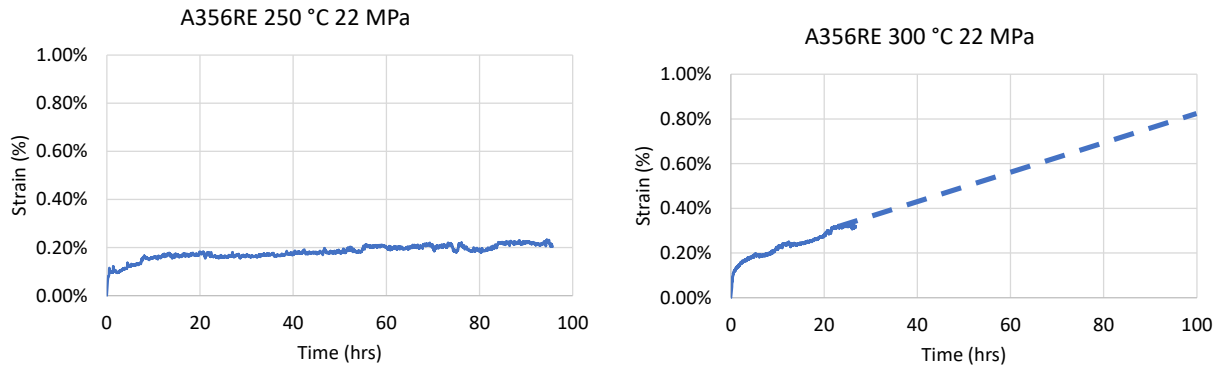


Figure 5.4-5. Creep test results for as-cast A356RE alloy at left) 250 °C and right) 300 °C (conditioned for 200 hours)

The T6 heat treatment of the A356RE alloy has clearly improved the creep resistance of the alloy at 250 °C (see Figure 5.4-6). First, the increased modulus of elasticity of the T6 alloy has reduced the amount of strain cause by the primary stage of creep which helped lower the total strain after 100 hours to ~0.1%. In addition, the steady-state creep rate has decreased to $1.287\text{E-}09 \text{ s}^{-1}$ (~35% lower than the as-cast A356RE and T6 A356 alloys).

Once the temperature was increased to 300 °C, the performance of the T6 sample decreased considerably. Not only did the strain rate increase by 20 times (i.e., from $1.287\text{E-}09$ to $2.510\text{E-}08 \text{ s}^{-1}$), but the strain rate was actually ~33% higher than the as-cast A356RE alloy. This was not expected since the T6 alloy performed much better than the as-cast sample during the 300 °C tensile test.

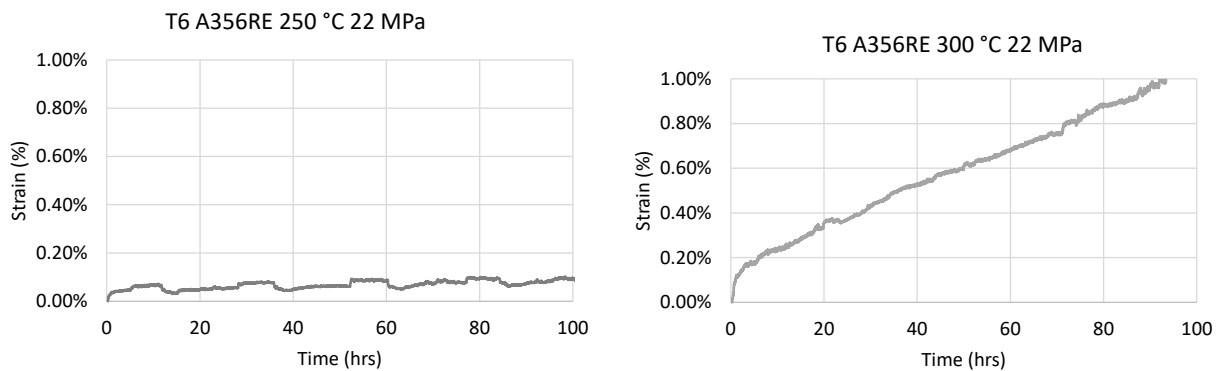


Figure 5.4-6. Creep test results for T6 A356RE alloy at left) 250 °C and right) 300 °C (conditioned for 200 hours)

Upon further investigation of the fracture surfaces of RE-modified A356 samples, it was observed that very large black clusters were present in the T6 A356RE samples (see Figure 5.4-7). An SEM/EDS analysis of the cluster revealed that it is a large agglomeration of RE elements. It is believed that these clusters may be present due to two factors: i) formation of an oxide layer on the RE mischmetal which prevents it from breaking down and melting during casting and/or ii) insufficient stirring during the casting process. Mechanically removing the cluster revealed a large pocket filled with Al dendrites.

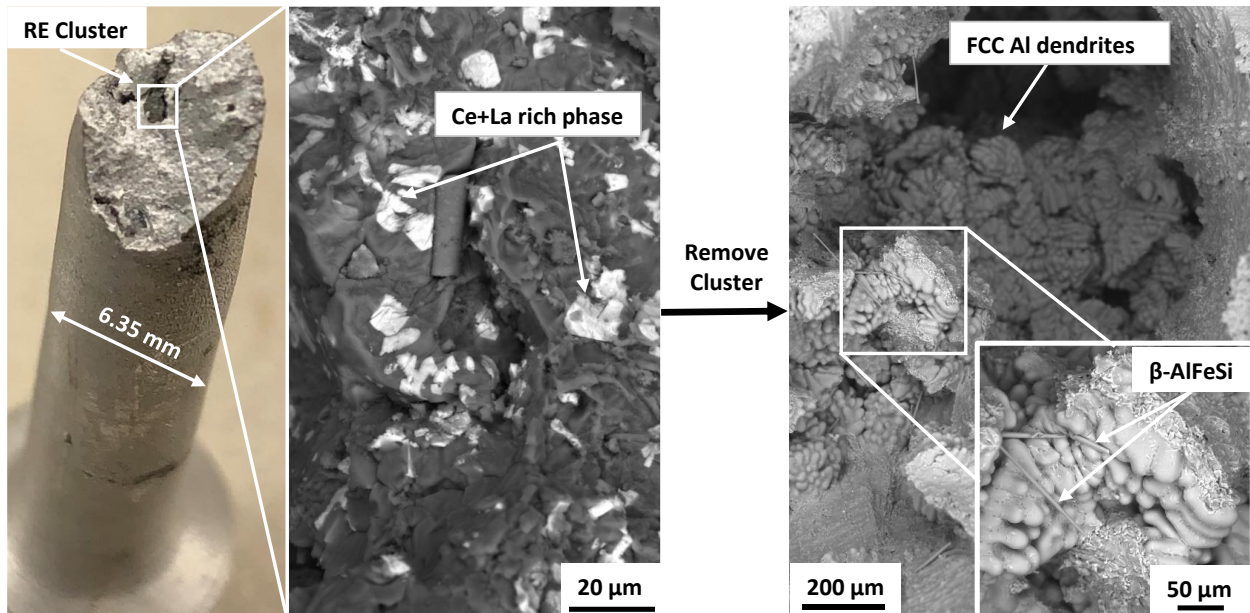


Figure 5.4-7. RE cluster in A356RE alloys

The irregular geometry of the exposed dendrite arms would undoubtedly act as a stress concentrator; the pocket reduces the effective cross-sectional area of the sample. In addition to the poor wetting of the clusters with the Al matrix, these reasons are believed to be the primary causes for the poor creep results at 300 °C. Although the alloy performed well at 250 °C, it was suspected that these clusters may also be present in the sample. Thus, it was necessary that additional samples of A356RE alloys were cast and tested.

5.5 Modified A356RE (A356RE-A and A356RE-B)

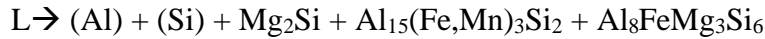
The additional samples of A356RE alloys were mixed with an impeller speed of 250 RPM, degassed and cleaned with argon for 20 minutes, and then poured into the preheated ASTM tensile mold. The “cleaned” A356RE alloy is designated as A356RE-A for the remainder of this section.

In addition to casting A356RE-A, additional samples were cast with a modified chemistry in hopes of further improving the material's fitness-for-service properties (designated as A356RE-B for the remainder of this section).

Although the A356RE samples contained good distribution of strength-enhancing, temperature-resistant phases, which are believed to be one of the reasons for the improved tensile strength and temperature resistance of the A356 alloy, the naturally occurring Fe impurities in the A356 base material led to the formation of unwanted Fe-bearing intermetallics, specifically β -Al₅FeSi and π -Al₉FeMg₃Si₅. Among the two phases, β -Al₅FeSi has the most detrimental effect on the alloy's strength and fracture toughness [249]. Two of the main reasons for this are that the needle-like geometry of the β -Al₅FeSi phase acts as a stress concentrator, it has a large aspect ratio (high interfacial energy), and it also lowers the feedability of the molten alloy during casting by blocking the interdendritic flow channels towards the end of solidification [212], [215], [250]. Insufficient feeding of the material during solidification can lead to a higher volume fraction of porosity and, thus, even greater magnitudes of stress concentration. Moreover, it has been reported that β -Al₅FeSi acts as a nucleation poisoning site, thereby leading to larger grain sizes and lower mechanical properties [251]. Fortunately, modification of the Mn and/or Mg concentration can result in the transformation of these two harmful Fe-bearing intermetallics into the more morphologically favorable α -Al₁₅(Fe,Mn)₃Si₂ phase. The Chinese script or polygonal morphology of the α -Al₁₅(Fe,Mn)₃Si₂ phase lowers stress concentrations and interfacial energies and generally result in improved mechanical properties. Not only does the morphology of the Al₁₅(Fe,Mn)₃Si₂ phase reduce stress concentrations as compared to the needle-like Fe-phases (improving the alloys toughness), it has been reported that when this phase forms in the microstructure, it generally forms in higher volume fractions as compared to the other Fe-bearing intermetallics. It is expected that the rise in intermetallic volume fraction will improve the material's strength via Orowan mechanisms. Taylor et al. [212] describe the transformation of the β -Al₅FeSi phase into α -Al₁₅(Fe,Mn)₃Si₂ as a neutralization or iron correction.

N. Belov et al. report that there exists two possible invariant reactions for Si-rich Al-Si-Mg-Fe-Mn alloys (see reactions below) [215]. The reactions suggest that, even though a Mn addition can transform the most detrimental phase, Al₅FeSi, into Al₁₅(Fe,Mn)₃Si₂, the AlFeMgSi phase will likely still be present (it should be noted that literature suggests two common stoichiometries for

the AlFeSiMg phase: i) Al₉FeMg₃Si₅ and ii) Al₈FeMg₃Si₆). However, given that this phase forms in the presence of Mg, it is postulated that lowering the Mg content should minimize the amount of the phase to a reasonable level.



Thus, focused on eliminating or minimizing the amount of the Al₉FeSi₃Mg₅ and Al₅FeSi phases in the A356RE samples, the Mn concentration was increased from 0.1 to 0.41 wt.% while the Mg content was reduced from 0.49 to 0.25 wt.% (see table below).

Table 5.5-1. Composition of cleaned and modified A356RE alloys

Alloy	Al	Mg	Si	Cu	Fe	Mn	Ti	Ce	La	Nd	Pr
A356RE-A ^a	Bal.	0.49	7.11	0.01	0.13	0.10	0.20	1.83	0.92	0.58	0.19
A356RE-B ^a	Bal.	0.25	6.15	0.01	0.13	0.41	0.20	1.83	0.92	0.58	0.19

^a contains trace amounts of strontium and boron

To verify that the casting process for both alloys was similar, the SDAS for each alloy was measured using an optical microscope. The average SDAS for over 50 Al grains for A356RE-A and A356RE-B were $39.1 \pm 6.5 \mu\text{m}$ and $36.4 \pm 7.5 \mu\text{m}$, respectively. The minimal change between both alloys confirms that the solidification cooling rates for both samples were essentially equal. Such a small difference in the SDAS will likely have a negligible effect on the material's mechanical properties, especially when considering the standard deviations and, thus, the differences between the two alloys is presumed to be directly caused by the chemistry modification.

5.5.1 Thermodynamic Simulations

Since the composition of the original A356RE alloy and A356RE-A are essential equal, this section will only present the simulated results for A356RE-B; the ThermoCalc simulation results provided in section 4.1.3 should be referred to for A356RE-A. The equilibrium solidification diagram for A356RE-B (high Mn, low Mg alloy) is shown below in Figure 5.5-1. The results from the equilibrium simulation suggest that the chemistry modification greatly increases the volume

fraction of the $\text{Al}_{15}(\text{Fe},\text{Mn})_3\text{Si}_2$ phase (i.e., from 0.42% to 1.75%) while reducing the mass fraction of the $\text{Al}_9\text{Fe}_2\text{Si}_2$ by ~65% (i.e., from 0.74% to 0.48%) (compare Table 4.1-6 and Table 5.5-2)

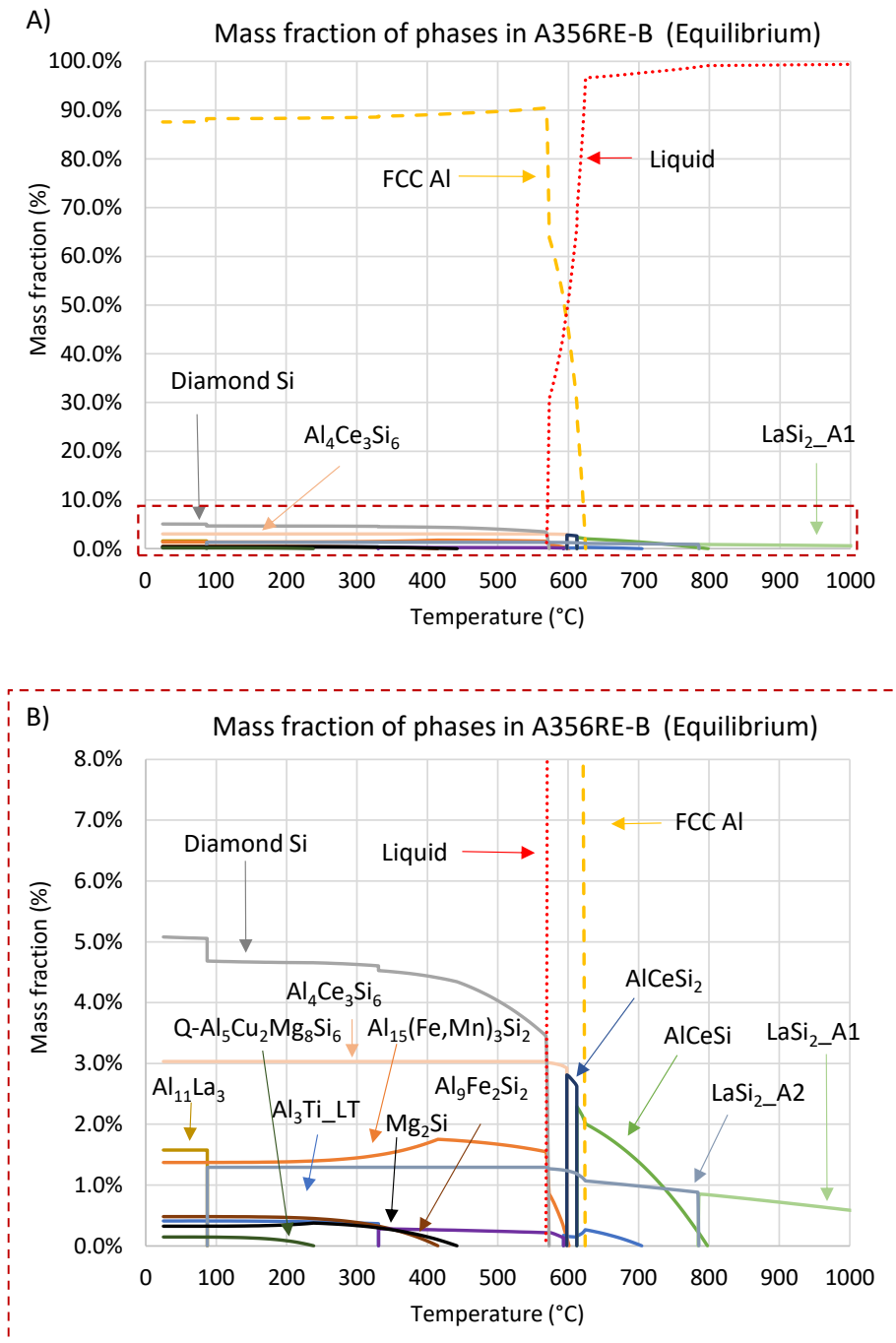


Figure 5.5-1. Mass fraction of phases in the A356RE-B alloy A) full solidification process, B) progression of minority phase solidification (equilibrium solidification)

The chemistry modification had an insignificant effect on the mass fraction of RE-containing phases and the nucleation and solidus temperature of FCC-Al (i.e., increased by only ~5-6 °C).

Although the $\text{Al}_5\text{Cu}_2\text{Mg}_8\text{Si}_6$ was not actually observed in the microstructure of the A356RE alloy, the composition change appears to have reduced the nucleation temperature of this phase by nearly 100 °C. In addition, the solidification path of Mg_2Si has also changed. Instead of its mass fraction increasing from 25 to 340 °C and then decreasing to 0% by ~480 °C, as shown in Figure 4.1-9 for the A356RE alloy, its mass fraction in A356RE-B gradually increases from 25 to 230 °C and then decreases until 0% by 440 °C.

Table 5.5-2. Mass fraction of phases in A356RE-B

Phases	Mass Fraction (%)	
	Equilibrium (25 °C)	Scheil (554 °C)
FCC Al	BAL.	BAL.
Diamond (Si)	5.08	3.92
$\text{Al}_4\text{Ce}_3\text{Si}_6$	3.03	0.12
AlCeSi_2	0 (2.81)*	0.20
AlCeSi	0 (2.29)*	2.28
$\text{Al}_{11}\text{La}_3$	1.58	-
$\text{LaSi}_2\text{-A2}$	0 (1.29)*	0.41
$\text{Q-Al}_5\text{Cu}_2\text{Mg}_8\text{Si}_6$	0.15	-
$\text{LaSi}_2\text{-A1}$	0 (0.85)*	0.85
$\text{Al}_9\text{Fe}_2\text{Si}_2$	0.48	0.08
$\text{Al}_3\text{Ti-LT}$	0.41	0.26
Mg_2Si	0.37	0.07
$\text{Al}_{15}(\text{Fe},\text{Mn})_3\text{Si}_2$	1.75	1.23
AlSi_3Ti_2	0 (0.28)*	-
$\text{Al}_{18}\text{Fe}_2\text{Mg}_6\text{Si}_{10}$	-	0.20

Note: (max values)

*Metastable at specific temperature

The Scheil simulation of A356RE-B reveals similar observations as described for the equilibrium simulation. The mass fraction of the $\text{Al}_9\text{Fe}_2\text{Si}_2$ was further decreased, reaching only 0.08%, and the amount of $\text{Al}_{15}(\text{Fe},\text{Mn})_3\text{Si}_2$ reached similar levels (i.e., 1.32%). The slightly lower mass fraction of $\text{Al}_{15}(\text{Fe},\text{Mn})_3\text{Si}_2$ is caused by the precipitation of the undesirable $\text{Al}_9\text{FeMg}_3\text{Si}_5$ phase (shown as $\text{Al}_{18}\text{Fe}_2\text{Mg}_6\text{Si}_{10}$).

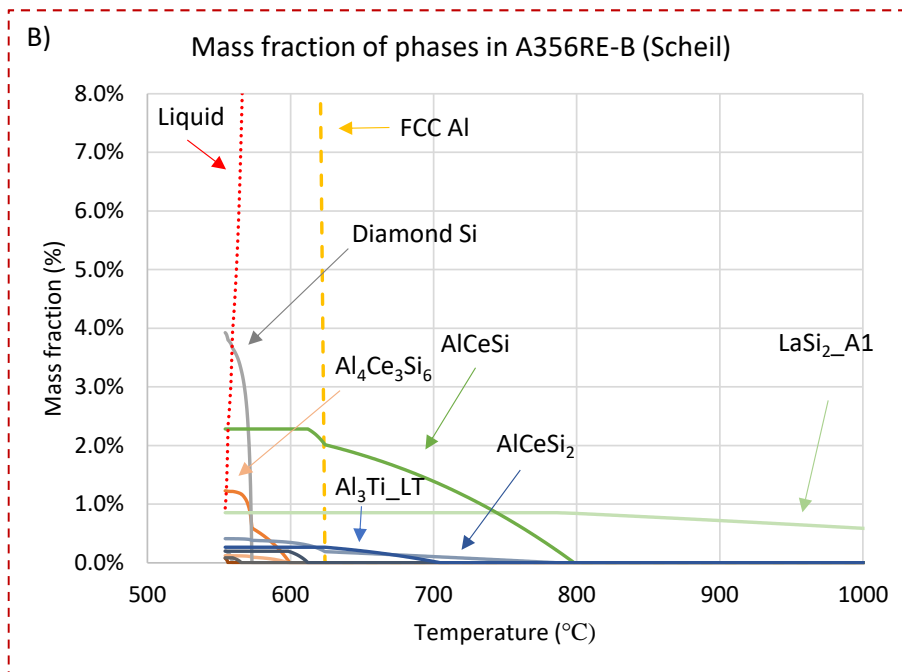
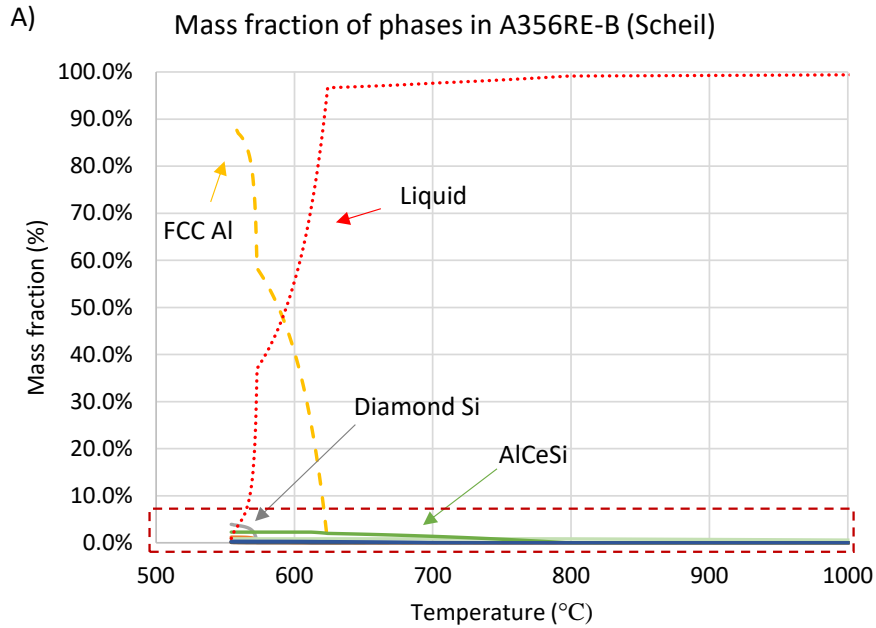


Figure 5.5-2. Mass fraction of phases in the A356RE-B alloy A) full solidification process, B) progression of minority phase solidification (non-equilibrium solidification)

The thermodynamic simulations of A356RE-B suggest that the modified Mn and Mg concentration should result in a lower concentration of harmful Fe-bearing intermetallics while having little negative effect on the RE-bearing intermetallics or solidification characteristics of the alloy.

5.5.2 Microstructure of A356RE-A and A356RE-B

Optical and SEM micrographs of A356RE-A are shown below in Figure 5.5-3 and Figure 5.5-4. The microstructure of A356RE-A is nearly identical to the original A356RE alloy. The measured area fraction of this phase was determined to be 4.85 ± 1.23 %, marginally higher than the A356RE alloy. Due to the high Mg and low Mn content in A356RE-A, both the $\text{Al}_9\text{FeMg}_3\text{Si}_5$ and the Al_5FeSi phases were observed and their combined area fraction reached 2.9 ± 0.85 %.

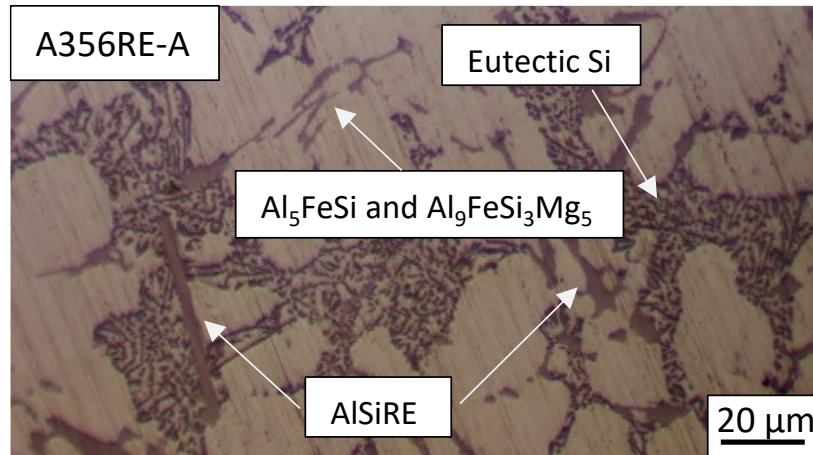


Figure 5.5-3. Optical micrograph of A356RE-A

The morphology of the $\text{Al}_9\text{FeMg}_3\text{Si}_5$ phase is blocky and interconnected, and this phase is present in a larger volume fraction as compared to the more harmful needle-like Al_5FeSi phase. The $\text{Al}_{11}\text{La}_3$ and $\text{Q_Al}_5\text{Cu}_2\text{Mg}_8\text{Si}_6$ phases shown in the simulated solidification charts (see Figure 4.1-9 and Figure 4.1-10), were not observed in the microstructure. This is believed to be attributed to the high concentration of La and Mg in the AlSiRE and $\text{Al}_9\text{FeSi}_3\text{Mg}_5$ phase, respectively.

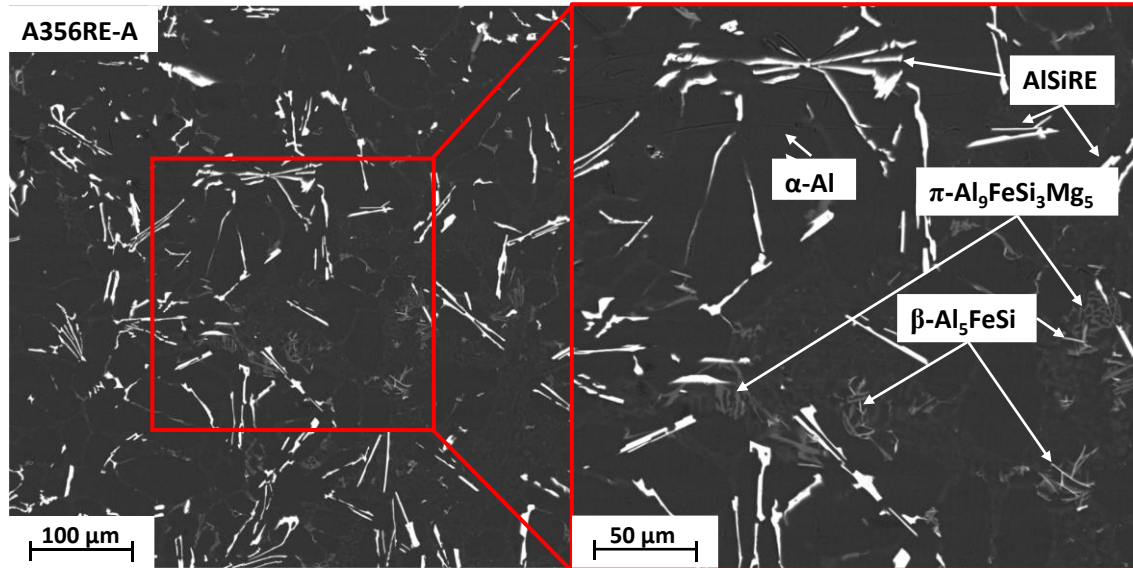


Figure 5.5-4. SEM micrograph of A356RE-A left) 500x, right) 1000x

Table 5.5-3. Composition of phases in A356RE-A (at.%)

	Al	Si	Fe	Mg	Ce	La	Nd	Ti	Ni	Mn
Al	Bal	1.37 ±0.01	-	-	-	-	-	0.14 ±0.01	-	-
AlSiRE	Bal	37.84 ±0.96	-	-	16.03 ±3.0 8	7.12 ±2.03	6.68 ±1.36	-	-	-
Al ₂₀ Ti ₂ RE	Bal	2.13 ±0.89	-	-	3.79 ±0.2 0	-	0.48 ±0.03	7.69 ±0.20	-	-
Al ₉ FeSi ₃ Mg ₆	Bal	23.32 ±3.25	2.97 ±0.19	9.92 ±0.58	0.22 ±0.0 4	-	0.09 ±0.01	-	0.15 ±0.04	0.38 ±0.04
Al ₅ FeSi	Bal	9.88 ±3.25	2.23 ±0.85	0.74 ±0.23	0.09 ±0.0 3	-	-	-	0.19 ±0.05	0.54 ±0.21

The SEM micrograph below shows that the modified composition did, indeed, result in the partial transformation of the harmful Fe-containing phases into Al₁₅(Fe,Mn)₃Si₂ (3.54 ±0.93 %). Not all of the harmful Al₅FeSi and Al₉FeSi₃Mg₅ precipitates were transformed; however, their combined area fraction reached only 0.55±0.25%. The volume fraction of the AlSiRE phase remained essentially unchanged, reaching 4.85±1.36. The combined contribution of the temperature-

resistant AlSiRE phase and the tough $\text{Al}_{15}(\text{Fe},\text{Mn})_3\text{Si}_2$ phase is expected to improve the fitness-for-service performance of the alloy.

The SEM micrograph below (see Figure 5.5-6) clearly displays that the modified composition did, indeed, result in the partial transformation of the harmful Fe-containing phases into $\text{Al}_{15}(\text{Fe},\text{Mn})_3\text{Si}_2$ ($3.54 \pm 0.93 \%$). Not all of the harmful Al_5FeSi and $\text{Al}_9\text{FeSi}_3\text{Mg}_6$ precipitates were transformed; however, their combined area fraction reached only $0.55 \pm 0.25 \%$ as compared to the 2.9% observed in A356RE-A.

The Mn addition appears to have also reduced the interparticle spacing of eutectic Si particles while also decreasing the size of the eutectic colonies (compare Figure 5.5-3 and Figure 5.5-8). Together, these changes are expected to further improve the alloy's fitness-for-service performance via the Orowan mechanism [68].

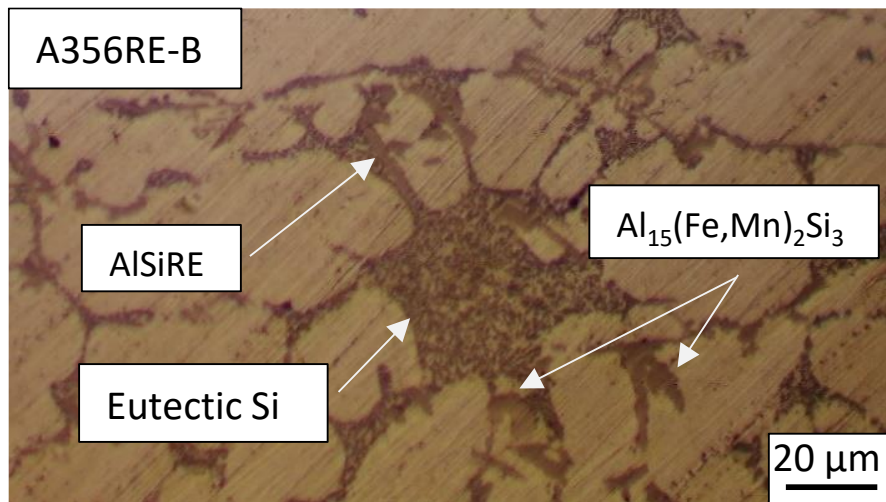


Figure 5.5-5. Optical micrograph of A356RE-B (low Mg, high Mn)

The volume fraction of the AlSiRE phase remained essentially unchanged, reaching 4.85 ± 1.36 . Moreover, similar concentration coring was observed, leading to higher Ce and La concentrations at the center of some of the AlSiRE precipitates. The concentration of RE elements in the AlSiRE phase seems to have increased slightly in A356RE-B as compared to A356RE-A (see Table 5.5-3 and Table 5.5-4). In addition, it was observed that the morphology of the AlSiRE phase appears to have shifted from the elongated rod/plate-like structure in A356RE-A toward a smaller and more interconnected Chinese script shape. The faceted growth of the AlSiRE phase in A356RE-B suggests that this alloy may have improved resistance against dislocation motion as compared to

A356RE-A. Combined with the higher area fraction of the tougher, and less stress concentrating $\text{Al}_{15}(\text{Fe,Mn})_3\text{Si}_2$ phase, it is expected that A356RE-B will perform superiorly during the elevated-temperature tensile and creep tests.

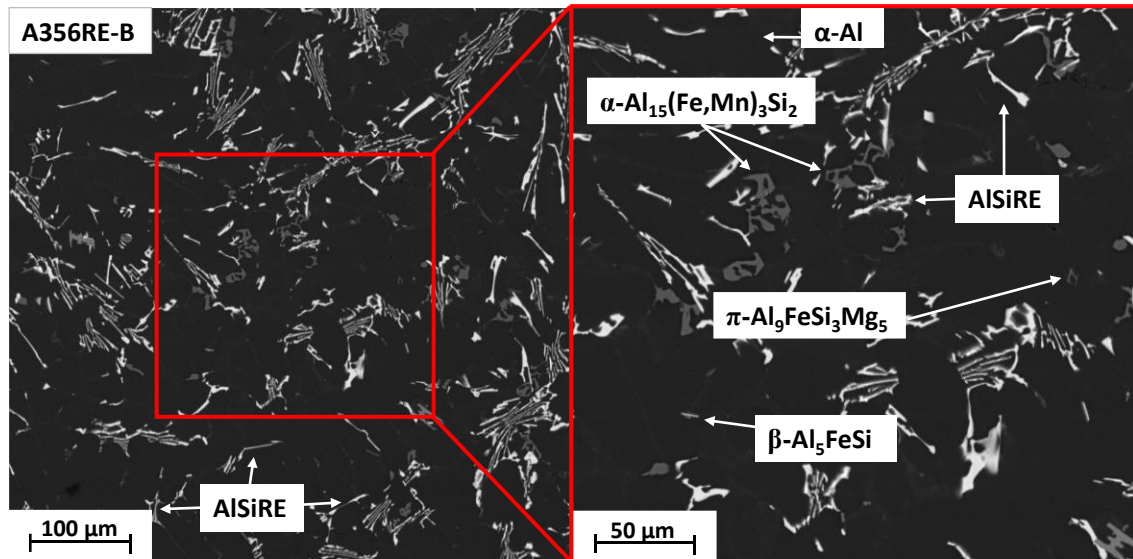


Figure 5.5-6. SEM micrograph of A356RE-B left) 500x, right) 1000x (low Mg, high Mn)

Table 5.5-4. Composition of phases in A356RE-B (at.% ± standard deviation)

	Al	Si	Fe	Mg	Ce	La	Nd	Ti	Ni	Mn
Al	Bal	1.15 ±0.06	-	-	-	-	-	-	-	0.10 ±0.05
AlSiRE	Bal	35.21 ±0.23	-	0.73 ±0.70	11.65 ±3.4 0	4.43 ±0.08	4.24 ±1.88	-	-	-
$\text{Al}_{20}\text{Ti}_2\text{RE}$	Bal	-	-	-	4.79 ±0.5 8	0.35 ±0.	0.99 ±0.99	6.66 ±0.15	-	-
$\text{Al}_9\text{FeSi}_3\text{Mg}_6$	Bal	26.74 ±1.25	3.04 ±0.47	19.86 ±0.44	-	-	-	-	2.98 ±0.56	1.84 ±0.03
Al_5FeSi	Bal	8.85 ±3.12	2.25 ±0.69	0.68 ±0.28	0.04 ±0.0 1	-	-	-	0.25 ±0.05	0.37 ±0.22
$\text{Al}_{15}(\text{Fe,Mn})_3\text{Si}_2$	Bal	12.67 ±0.26	4.21 ±0.12	-	-	-	-	-	-	11.90 ±0.15

5.5.3 Tensile: A356RE-A and A356RE-B

To determine how the microstructural differences between A356RE-A and A356RE-B (see Figure 5.5-4 and Figure 5.5-6) affect the fitness-for-service performance of the alloy system, elevated-temperature tensile and creep tests were performed on the two alloys after conditioning at their test temperature for 200 hours. The tensile results of A356RE-A at 250 °C are shown below in Figure 5.5-7. The YS and UTS were determined to be 62 and 84.3 MPa, respectively. As compared to the tensile results for the original as-cast A356RE alloy (see Figure 5.2-3), the new cleaning process (i.e., mechanical mixing + argon-purging) has increased both the YS (from 56 to 62 MPa) and UTS (from 70 to 84 MPa). In addition, the modulus of elasticity increased from 56.3 to 64.2 GPa, respectively. Powertrain components that operate at elevated temperatures require sufficient stiffness to maintain tight dimensional tolerances; however, these applications also benefit from some degree of ductility which provides automotive manufacturers with another type of safety factor (i.e., the component will deform before cracking).

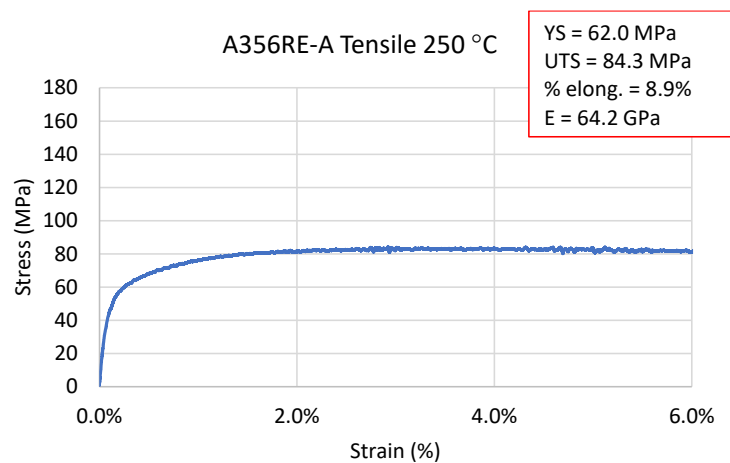


Figure 5.5-7. Tensile test results of A356RE-A at 250 °C (conditioned for 200 hours at 250 °C)

The elevated-temperature tensile test result for the A356RE-B is shown below in Figure 5.5-8. At 250 °C, the modified alloy performed considerably better than A356RE-A. Specifically, the YS, UTS, and modulus of elasticity improved by ~14 %, 9 %, and 10 % respectively. As compared to the original A356RE alloy, the YS, UTS and modulus improved by ~25%, 31%, and 26%, respectively. The improved tensile performance of A356RE-B is believed to be attributed to three events, the first being the transformation of the harmful needle-like Fe phase to the more favourable $Al_{15}(Fe,Mn)_2Si_3$. This phase transformation leads to lower stress concentrations and

interfacial energy while increasing the contribution from Orowan strengthening. Similarly, the partial transformation of the AlSiRE phase from elongated plates to smaller, faceted Chinese script improves the strength via the Hall-Petch relationship (i.e., the smaller the precipitate, the greater the resistance against dislocation motion). The last contribution to improved strength is related to the noticeable decrease in the interparticle spacing of the eutectic Si particles.

Since the performance of A356RE-B was superior than A356RE-A at 250 °C, A356RE-B was also subjected to a 300 °C tensile test. Further increasing the test temperature to 300 °C resulted in a slight decrease in the alloy's strength as compared to the original A356RE alloy (see Figure 5.2-3). It should be noted, however, that the alloy still performed considerably better than the T6 A356 (see Figure 5.2-2) and the T7 A319 (see Figure 3.5-5) alloys at 300 °C. The reason for the slight decrease in mechanical properties is believed to be associated to an increase in particle cracking of the $Al_{15}(Fe,Mn)_2Si_3$ phase. Rincon et al. [106] found that above 250 °C, the percentage of cracked $Al_{15}(Fe,Mn)_2Si_3$ particles in their A319 alloy increased exponentially. They report that increasing the temperature from 250 to 300 °C, nearly doubled the percentage of cracked particles, reaching ~25-30%.

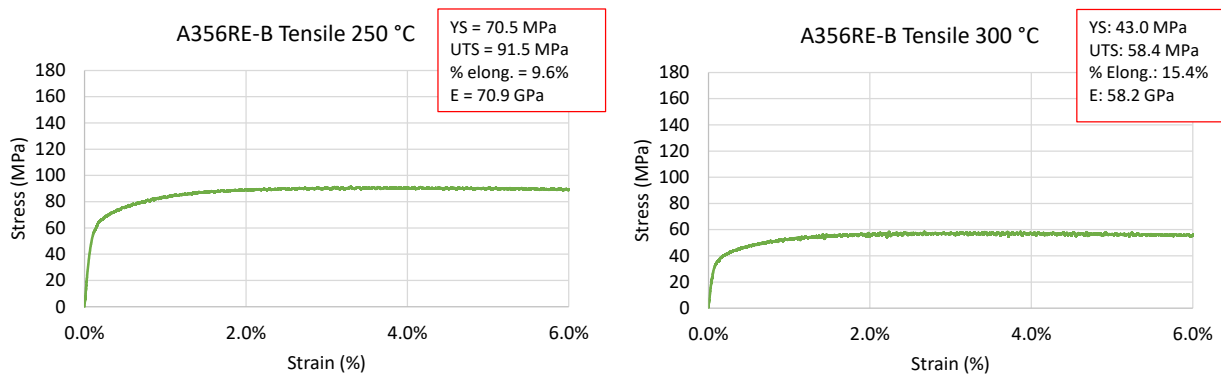


Figure 5.5-8. Tensile test results of A356RE-B (left) 250 °C, (right) 300 °C (low Mg, high Mn) (conditioned for 200 hours at test temperature)

5.5.4 Creep: A356RE-A and A356RE-B

The staircase creep results for A356RE-A are shown below in Figure 5.5-10, and the steady-state creep rates for each load are listed in Table 5.5-5. At 22 MPa, the $\dot{\epsilon}_s$ was measured to be $\sim 9.02E-10 \text{ s}^{-1}$. Such a slow $\dot{\epsilon}_s$ suggests that diffusion-based creep is the rate-controlling mechanism. It should be noted, however, that to accurately measure such low creep rates, a much longer time

interval is required (on the order of several days to weeks). One of the reasons for this is due to the precision of extensometers as well as the natural force and thermal fluctuations that occur during creep tests.

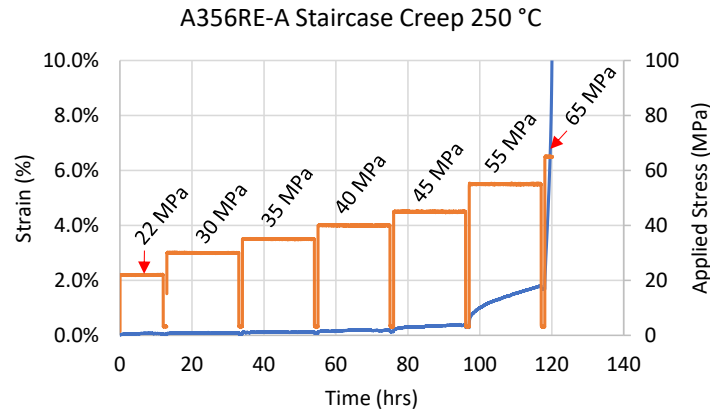


Figure 5.5-9. Staircase creep results of A356RE-A at 250 °C (conditioned for 200 hours at 250 °C)

Increasing the applied stress from 22 to 30 and finally 35 MPa resulted in only a small increase in the $\dot{\epsilon}_s$, reaching a maximum of $2.66E-09 \text{ s}^{-1}$. The calculated apparent stress exponent from 22 to 35 MPa was $n_a = 2.4$ (see Figure 5.5-10). This suggests that the diffusional creep at 22 MPa is transitioning to viscous drag and climb [247], [248]. Increasing the load to 40, 45, and finally 55 MPa quadruples the apparent stress exponent to $n_a = 10.0$, indicating that creep deformation bypassed power-law-governed dislocation climb, and transitioned to power-law breakdown dislocation creep. Such a high apparent stress exponent suggests that a threshold stress is present, which is likely present due to the high volume fraction of hard intermetallics in the alloy which pins dislocations [60]. Plotting $\dot{\epsilon}_s^{1/n}$ vs. σ reveals a similar trend as described for the T7 A319 and T6 A356 alloys. The stress exponent $n = 7$ resulted in the greatest linear fit, and the estimated threshold stress of 34.3 MPa appears to be more representative of the initiation of dislocation creep as compared to the threshold stress at $n = 7$ for T6 A356 or T7 A319. This suggests that the high-volume fraction of thermally stable AlSiRE precipitates may be shifting the creep mechanism from dislocation creep to lattice diffusion-controlled creep with a constant subgrain structure.

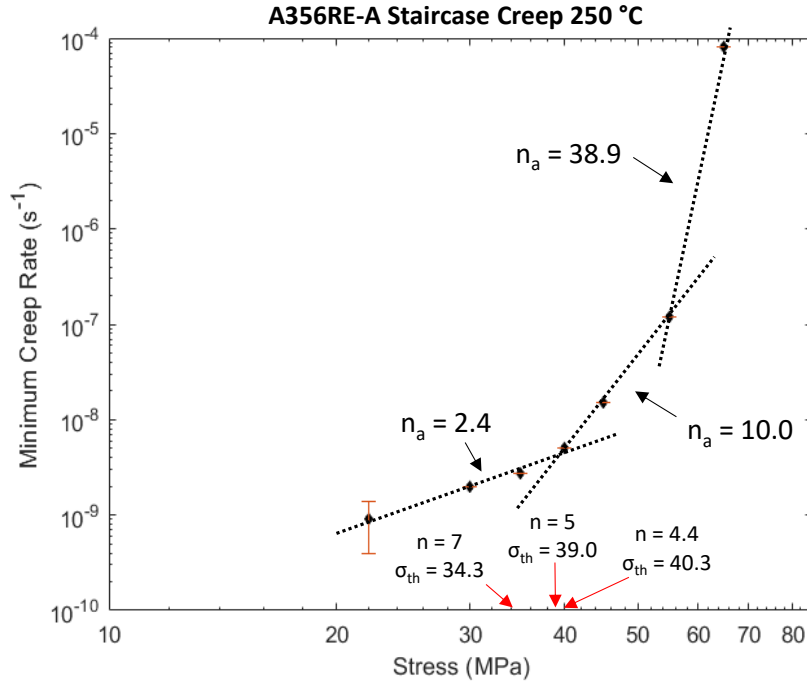


Figure 5.5-10. Minimum creep rate as a function of applied stress for A356RE-A at 250 °C. Note apparent stress exponent n_a and threshold stress σ_{th}

The following increase in the applied stress (i.e., to 65 MPa) caused rapid elongation; the sample failed in ~2 hours. A true steady-state creep did not establish; however, the brief minimum creep rate was determined to be $7.99E-06 \text{ s}^{-1}$. Such a large increase in the creep rate caused a near-instantaneous transition through dislocation glide into plasticity ($n_a = 38.9$) [209].

The effects from the chemistry modification (increased Mn, decreased Mg) are clear from the clear increase in the material's creep resistance (see Figure 5.5-11 and Figure 5.5-12). Specifically, at every load, the $\dot{\epsilon}_s$ was lower for A356RE-B than for A356RE-A (see Table 5.5-5). Moreover, A356RE-B failed at a load ~15 MPa greater than A356RE-A, reaching 100% of A356RE-B's measured YS. At 65 MPa (i.e., the fracture load of A356RE-A) the $\dot{\epsilon}_s$ for A356RE-B was more than a full magnitude lower than observed for A356RE-A, reaching just $1.12E-07 \text{ s}^{-1}$ as compared to $7.99E-06 \text{ s}^{-1}$. In fact, the creep rate for the A356RE-B was a well-established steady-state creep rate, as opposed to the brief minimum creep rate for A356RE-A.

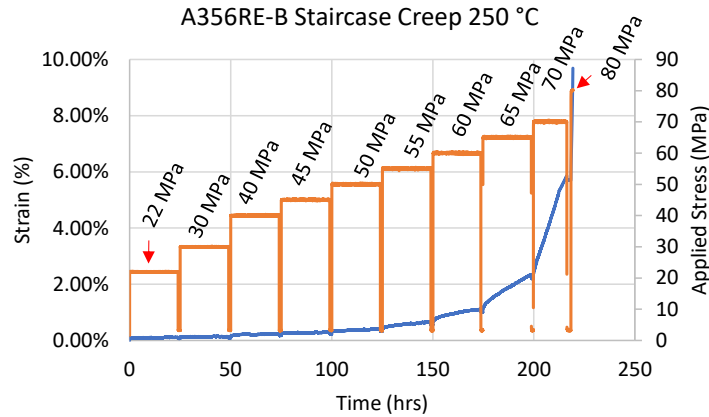


Figure 5.5-11. Staircase creep results of A356RE-B at 250 °C (low Mg, high Mn) (conditioned for 200 hours at 250 °C)

The steady-state creep rate at 22 MPa was determined to be $6.57E-10 \text{ s}^{-1}$. Similar to the discussion for A356RE-A, accurate measurement of the such a low strain rate is difficult without subjecting the load for several days to weeks. Thus, there is expected to be some minor error associated with the measurement at 22 MPa. Once the load on the A356RE-B alloy was increased from 22 to 30 MPa, the resulting creep rate was half that of A356RE-A (i.e., $1.03E-09 \text{ s}^{-1}$ vs. $2.00E-09 \text{ s}^{-1}$, respectively). The calculated apparent stress exponent was also lower, reaching only $n_a = 1.1$ (as compared to $n_a = 2.4$). Such a low n_a suggests that diffusional creep is the rate-controlling mechanism. Further increasing the load to 40 and 45 MPa only slightly raised the creep rate, reaching a maximum of $4.70E-09 \text{ s}^{-1}$. Albeit only a small increase, the calculated apparent stress exponent $n_a = 4.2$ suggests that the dominant creep mechanism has transitioned from diffusion creep to power-law-governed dislocation climb [247], [248]. This correlates well with the deformation mechanism map (see Figure 2.2-6). Increasing the applied stress from 55 to 65 MPa raises the $\dot{\epsilon}_s$ by a magnitude, reaching $3.32E-08 \text{ s}^{-1}$. As a result, the power-law breaks down and dislocation creep is the now rate-controlling mechanism ($n_a = 11.0$) [209]. This is dissimilar from the deformation mechanism map for pure Al (see Figure 2.2-6). According to the deformation map and the calculated shear modulus (26.6 GPa), the power-law should breakdown with an applied load of $\sim 133 \text{ MPa}$. This difference is likely attributed to the high-volume fraction of precipitates in A356RE-B as compared to pure Al. Further increasing the load to 70 MPa leads to a complete breakdown of the power-law, and as a result, the dislocation creep transitions to dislocation glide ($n_a = 21.2$) [209]. It should be noted that the $\dot{\epsilon}_s$ at 70 MPa was more than a full magnitude lower

for A356RE-B than at 65 MPa for A356RE-A. Finally, once the load is increased to 80 MPa, the creep enters the plasticity regime where the sample begins to neck and, ultimately, leads to failure.

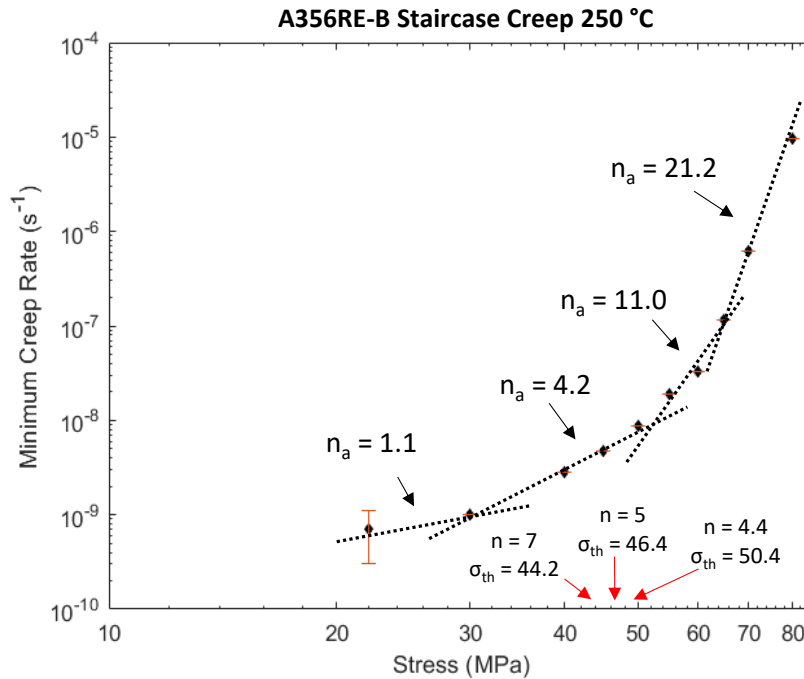


Figure 5.5-12. Minimum creep rate as a function of applied stress for A356RE-B at 250 °C. Note apparent stress exponent n_a and threshold stress σ_{th}

Similar to the A356RE-A alloy, the high apparent stress exponents suggest that there is a threshold stress in the A356RE-B alloy. Plotting $\dot{\epsilon}_s^{1/n}$ vs. σ reveals good linear fits for all three stress exponents, with $n = 7$ having the greatest fit at $R^2 = 0.983$, leading to an estimated threshold stress of 44.2 MPa.

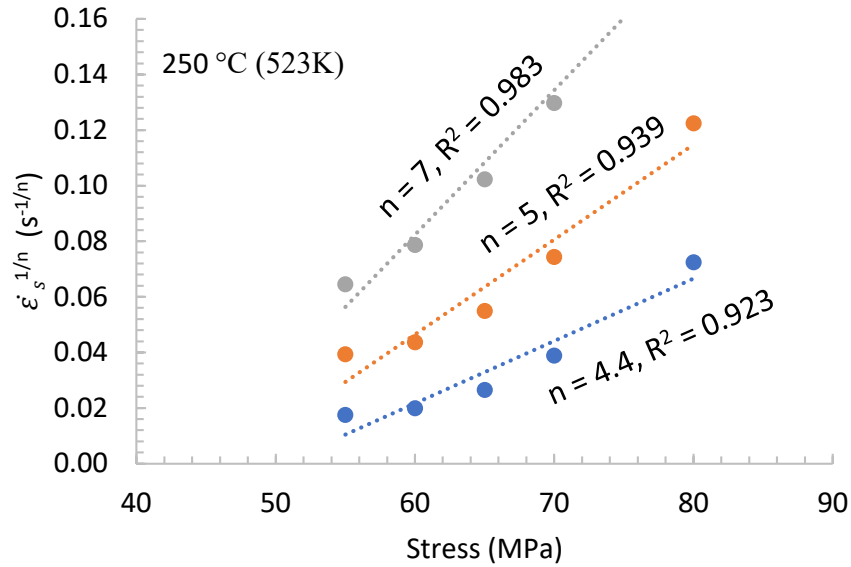


Figure 5.5-13. A plot of $\dot{\epsilon}_s^{1/n}$ vs. σ for the A356RE-B alloy at 250 °C

The chemistry modification has clearly led to an increase in the creep resistance of the alloy. Not only has the threshold stress increased by ~10 MPa, the steady-state creep rates are lower at every load. This is likely attributed to the higher volume fraction of intermetallics available for pinning dislocations, the transformation of the brittle $\text{Al}_9\text{Fe}_2\text{Si}_2$ and $\text{Al}_9\text{FeMg}_3\text{Si}_5$ into $\text{Al}_{15}(\text{Fe},\text{Mn})_3\text{Si}_2$ which imparts ductility on the matrix, as well as the size reduction and morphology modification of the AlSiRE intermetallic.

Table 5.5-5. Steady-state creep rates for A356RE-A and A356RE-B at 250 °C (units: $10^{-8}/\text{s}$)

	22 (MPa)	30 (MPa)	35 (MPa)	40 (MPa)	45 (MPa)	50 (MPa)	55 (MPa)	60 (MPa)	65 (MPa)	70 (MPa)	80 (MPa)
A356RE-A	0.09	0.20	0.27	0.50	1.53	-	12.10	-	798.58*	-	-
A356RE-B	0.07	0.10	-	0.28	0.47	0.87	1.87	3.32	11.74	62.19	965.81*

*sample failed

The creep results at 300 °C elucidate the effectiveness of the cleaning process and chemistry modification on improving the temperature resistance of the alloy (see Figure 5.5-14). With an applied load of 22 MPa, the steady creep rate was only $5.92\text{E-}09 \text{ s}^{-1}$. This is considerably lower than the original A356RE (i.e., $1.874\text{E-}08 \text{ s}^{-1}$) and the T6 A356 (i.e., $1.062\text{E-}06 \text{ s}^{-1}$) Although the

creep rate of A356RE-B more than doubled when the load was increased to 30 MPa, the rate remained relatively low. The calculated apparent stress exponent was determined to be $n_a = 2.2$, suggesting that the creep is governed by viscous drag/climb [247], [248]. Increasing the load to 40 MPa abruptly increased the steady-state creep rate to $2.09E-07 \text{ s}^{-1}$, raising the apparent stress exponent to $n_a = 10.0$, suggesting that the creep deformation is governed by power-law breakdown dislocation creep. Finally, once the load is increased to 45 MPa, the sample enters a brief minimum creep rate of $2.09E-06 \text{ s}^{-1}$ which transitions into tertiary creep after approximately 4-5 hours. Similar to the results at 250 °C, the sample remains intact until the load increases above 100% of the alloy's yield strength (i.e., ~45 MPa).

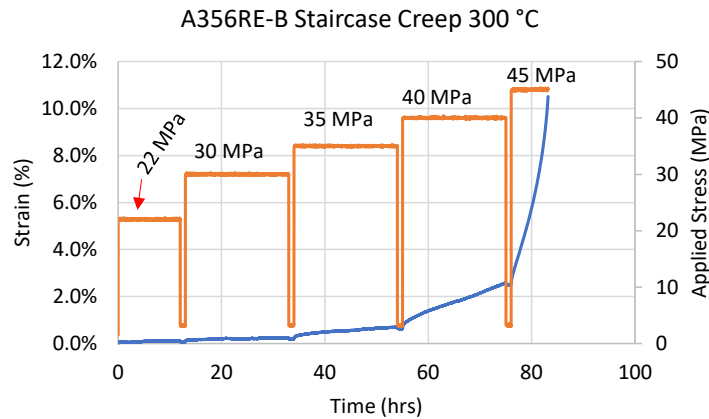


Figure 5.5-14. Staircase creep results of A356RE-B (low Mg, high Mn) (conditioned for 200 hours at 300 °C)

Similar to the results presented by A. Farkoosh and M. Pekguleryuz [63] who studied the effects of Mn on the creep resistance of Al-Si-Cu-Mg-Ni alloys, the increased Mn addition in the A356RE alloy not only lowered the steady-state creep rates for all loads but also raised the fracture load. The driving factors behind the observed improved strength and creep resistance is believed to be the transformation of Al_5FeSi and $\text{Al}_9\text{FeSi}_3\text{Mg}_5$ into $\text{Al}_{15}(\text{Fe},\text{Mn})_3\text{Si}_2$ phase, as well as the partial transformation of the elongated AlSiRE plates into a smaller, faceted Chinese script morphology. The lower aspect ratio, a stronger bonding with the Al matrix, and the more favorable morphology of $\text{Al}_{15}(\text{Fe},\text{Mn})_3\text{Si}_2$ phase lead to a decrease in the precipitate-matrix interfacial energy, lower the development of stress concentrations and improve the alloy's ductility. Moreover, this transformation increased the total volume fraction of intermetallics, leading to a greater number of

obstacles available to pin dislocation motion (Orowan strengthening), and thereby, further improving the creep resistance of the alloy.

Plotting $\dot{\epsilon}_s^{1/n}$ vs. σ reveals similarly good linear fits at all three stress exponents (see Figure 5.5-15), resulting in estimated threshold stresses for $n = 4.4, 5,$ and 7 of 28.4, 25.6, and 21.7 MPa, respectively (see Figure 5.5-16). At $n = 4.4$, the value of the threshold stress is higher than reported by A. Farkoosh et al. [63] for their Mn-modified Al-Si-Cu-Mg-Ni alloy (i.e., ~28 vs. 20 MPa). It is worthwhile to note that the Mn-modified Al-Si-Cu-Mg-Ni alloy was in the heat-treated condition, suggesting that the A356RE-B alloy is a strong competitor even in the as-cast condition.

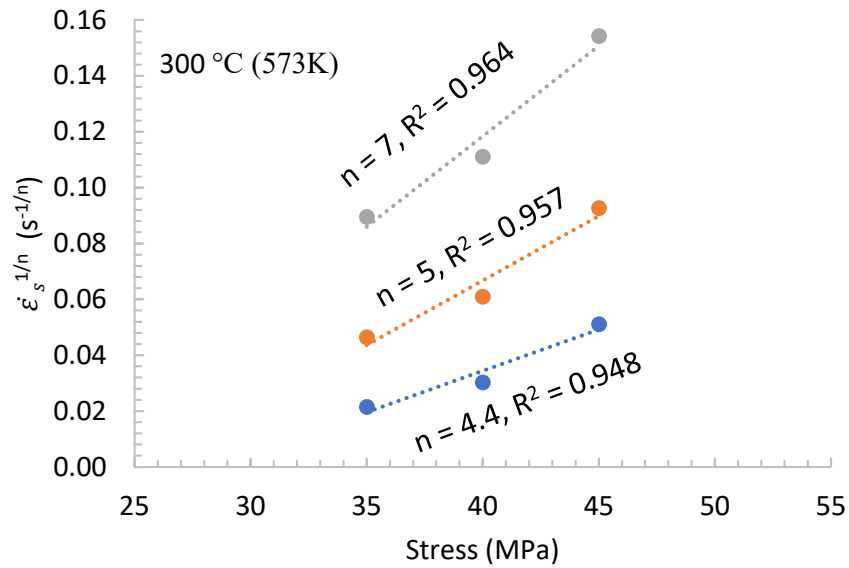


Figure 5.5-15. A plot of $\dot{\epsilon}_s^{1/n}$ vs. σ for the A356RE-B alloy at 300 °C

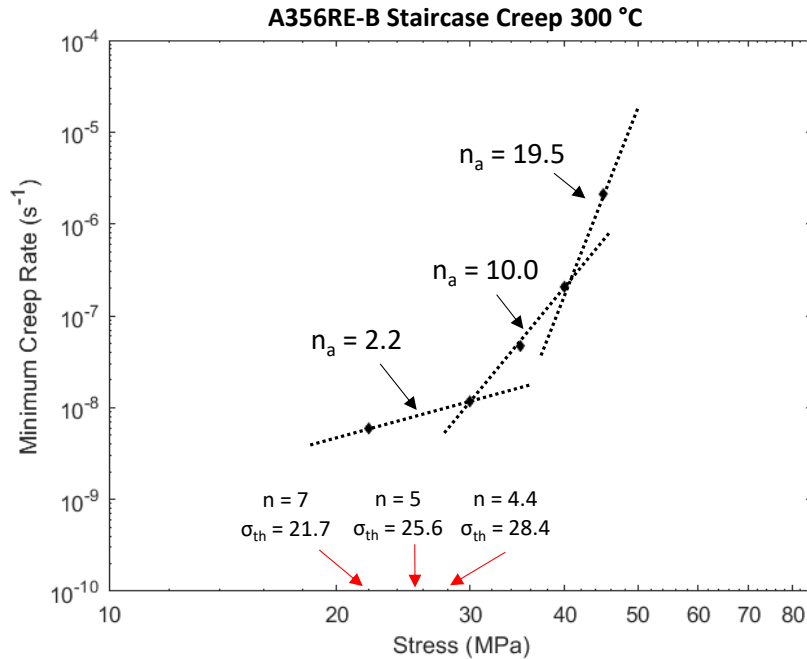


Figure 5.5-16. Minimum creep rate as a function of applied stress for A356RE-B at 300 °C. Note apparent stress exponent n_a and threshold stress σ_{th}

Table 5.5-6. Steady-state creep rates for A356RE-B 300 °C (units: $10^{-8}/s$)

A356RE-B	22 (MPa)	30 (MPa)	35 (MPa)	40 (MPa)	45 (MPa)
300 °C	0.59	1.18	4.63	20.90	208.57

In addition to the stress exponent and creep rates, the activation energies were also calculated (see Figure 5.5-17). At 22 MPa, the apparent activation energy was calculated to be $\sim 110 \text{ kJmol}^{-1}$, suggesting that dislocations move via core diffusion creep [209]. At 30 MPa, the activation energy is similar to the self-diffusion of pure aluminum (i.e., 136 kJmol^{-1}). This correlates well with the deformation mechanism map for pure Al (see Figure 2.2-6). Further increasing the load to 35 MPa nearly doubled the activation energy to 215 kJmol^{-1} . Such a large deviation from the activation energy for self-diffusion supports the claim that a threshold stress is present [252]. Once the load is increased to 40 MPa, the activation energy continues to increase to 304 kJmol^{-1} , suggesting that the creep has entered power-law breakdown creep regime where dislocations can glide and cross slip passed precipitates [209]. This correlates well with the discussion around the high apparent stress exponent at this temperature and load (i.e., $n_a = 19.5$). Such high apparent activation energies are commonly reported for dispersoid-strengthened aluminum alloys [253]–[255].

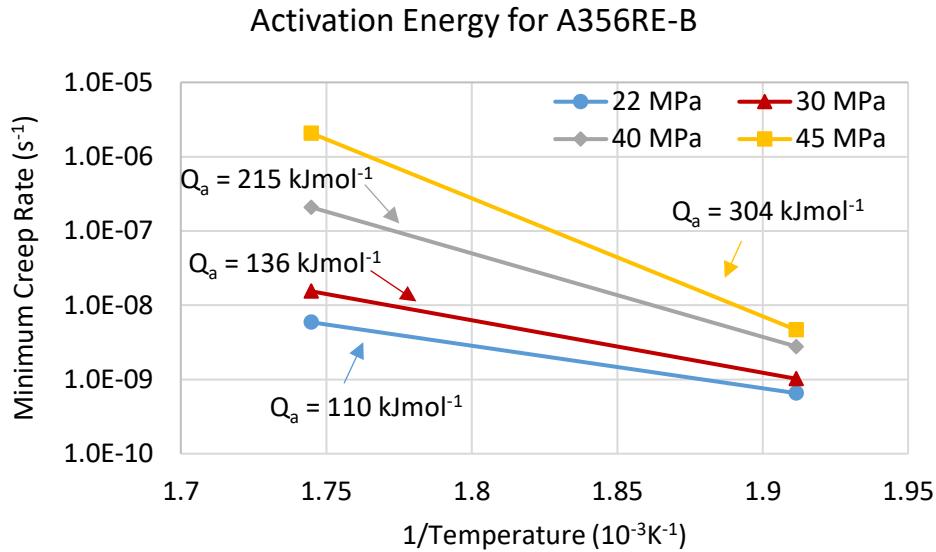


Figure 5.5-17. Minimum creep rates plotted against the reciprocal of the absolute test temperature for the A356RE-B alloy (note apparent activation energies, Q_a)

5.6 Chapter Summary

This chapter discussed the efforts of improving the fitness-for-service performance of aluminum alloys through the addition of inexpensive rare earth elements. Thermodynamic simulations and comprehensive microscopy and spectroscopy analyses were performed to determine the reasons for the performance improvement or deterioration.

First, hypoeutectic (Al-6%Ce) and hypereutectic (Al-16%Ce) binary alloys were studied. The long solidification range and high-volume fraction of brittle primary $Al_{11}Ce_3$ crystals in the Al-16%Ce alloy suggested that the Ce concentration should remain below the eutectic composition to maintain sufficient castability and mechanical properties. Following this, a 10 wt.% Mg addition was added to an Al-8%Ce alloy in hopes of improving the mechanical properties via solution strengthening of the Al matrix. Comparing the microstructure of the Al-8%Ce-10%Mg alloy to the Al-6%Ce alloy suggested that the Mg transformed the morphology of the very fine and interconnected eutectic $Al_{11}Ce_3$ to a larger and more individualized Chinese script shape. Reported room-temperature tensile results of the alloy indicated that the strength of the alloy greatly increased with the addition of Mg. However, since a considerable amount of the Mg formed as large pools of β -AlMg, the temperature resistance of the alloy was restricted and, thus, the performance of the alloy at 250 and 300 °C was poor. This observation indicated that additional

elements were required, and that the amount of Mg should be restricted to prevent the formation of the thermally unstable β -AlMg phase. This led to the shift toward Al-Si based alloys, specifically compositions close to A356 (i.e., ~Al-7%Si). The relatively high concentration of Si in this alloy system provides greater castability which is a desirable characteristic for casting complex powertrain components.

The RE-modified A356 (A356RE) samples had great machinability and the microstructure consisted of several homogeneously dispersed and relatively small precipitates. Among the Al dendrites and eutectic Si particles, a relatively high concentration of blocky AlSiRE precipitates were observed. The AlSiRE phase has great thermal stability and was expected to greatly improve the alloy's temperature resistance. However, the relatively high-volume fraction of needle-like Fe phases induces stress concentrations and, together with the phase's brittleness, was expected to offset some of the benefits provided by the AlSiRE phase. As compared to the Al-8%Ce-10%Mg alloy, the yield strength of the T6 A356RE alloy at 250 and 300 °C increased by 50 and 63%, respectively. Moreover, as compared to the RE-free T6 A356 alloy, the yield strength at 250 and 300 °C improved by 167 and 226%, respectively. In fact, in the as-cast condition, the yield strength of the A356RE alloy was equal to T6 A356 at 250 °C and nearly double at 300 °C.

Following the tensile testing, a series of creep tests were performed. At first, single load creep tests at 22 MPa (slightly greater than the peak pressure of diesel engines) were performed; however, this limited the amount of data that could be extracted. Thus, once it was established that the A356RE alloy had the greatest potential for improved creep resistance, multi-step loading creep tests (staircase creep) were performed on these samples as well as on the baseline RE-free T6 A356 samples. As expected, the RE-free T6 A356 samples performed poorly at 250 °C, entering tertiary creep and fracturing by 40 MPa. Further, at 300 °C the T6 A356 entered tertiary creep toward the end of the 22 MPa load, and fractured immediately after raising the load to 30 MPa. Together with the tensile results, the poor creep resistance of the A356 alloy clearly demonstrates that it cannot be used at these elevated temperatures.

At first glance, it appeared that the addition of REs to the A356 alloy did not significantly improve the creep resistance. However, upon investigation of the alloy's fracture surface, large clusters of REs and pockets of porosity were observed. It was postulated that the clusters formed during the casting process and, consequently, a new stirring and de-gassing method was performed, and new

samples were cast (i.e., A356RE-A). In addition, since it was necessary to cast new samples, the concentration of Mg and Mn was modified (i.e., A356RE-B) to purposely transform the harmful needle-like Fe-containing phases into the more favorable Chinese script and polygonal $Al_{15}(Fe,Mn)_2Si_3$ phase. Together with the melt cleaning, the chemistry modification resulted in a considerable improvement in the alloy's strength, even in the as-cast condition. More impressive was the large increase in the alloy's creep resistance. In the as-cast condition, the creep rate at 250 °C of the modified and cleaned A356RE alloy (A356RE-B) maintained impressively small up to approximately 55 MPa, and only fractured after the load was increased above 70 MPa (100% of its yield strength). Similarly, at 300 °C, the sample did not fail until the load was increased above 100% of the alloy's yield strength (i.e., 45 MPa).

The results from this chapter provide clear evidence that the performance of the A356 alloy can be greatly improved by the addition of rare earth elements. However, since the RE-free A356 alloy has such poor performance at elevated temperatures, at this stage it is unclear if the RE-modified A356 alloy can perform sufficiently for applications like diesel engine blocks. Thus, it is necessary to compare the results to the well-established A319 alloy (see Chapter 3) which is currently used in several high-powered engines.

The engineering stress versus engineering strain results for the tensile tests are shown below in Figure 5.6-1, and the corresponding mechanical properties (i.e., YS at 0.2% strain, UTS and elongation) are shown in Table 5.6-1. Comparing the stress vs. strain profiles shown in Figure 5.6-1, it is clear just how effective the RE additions are at improving the temperature resistance of Al-Si-based alloy (it should be noted that for clarity, Figure 5.6-1 displays the strain up to only 6%; however, the actually elongation at failure is shown in Table 5.6-1).

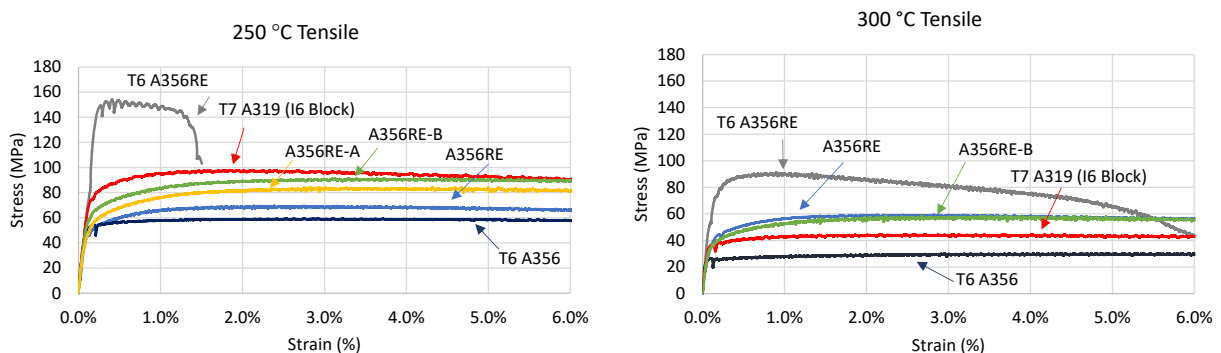


Figure 5.6-1. Summary of Tensile Test Results at left) 250 and right) 300 °C

At 250 °C, the T6 A356RE alloy demonstrated a considerably higher strength than T7 A319 (i.e., YS is 147 vs. 89 MPa and UTS is 154 vs. 98 MPa). Moreover, A356RE-B performed very similarly as compared to T7 A319, without the need for applying any costly heat treatment. Further, once the temperature of the tensile test increased to 300 °C, the improved temperature resistance of the RE-bearing alloys was clearly observed. For all three RE-containing alloys, the measured YS and UTS was higher than T7 A319, with the greatest improvement (i.e., ~117 and 104% increase in YS and UTS, respectively) being from the T6 A356RE alloy. Both as-cast RE-modified alloys performed similarly at 300 °C, and were observed to perform approximately 20-30% better than the T7 A319 alloy.

Table 5.6-1. Summary of mechanical properties at 250 and 300 °C

Alloy	YS (MPa)		UTS (MPa)		Young's Modulus (GPa)	
	250 °C	300 °C	250 °C	300 °C	250 °C	300 °C
T6 A356	63	31	66	25	68	46
T7 A319	89	39	98	45	63	49
A356RE	56	48	70	59	56	61
T6 A356RE	147	85	154	92	56	74
A356RE-A	62	-	84	-	64	-
A356RE-B	71	43	92	58	71	58

In addition to the clearly improved performance of the RE-bearing alloys during the tensile tests, the results from the elevated temperature creep tests further confirm that this alloy system is a feasible option for current and possibly next-generation powertrains. To no surprise, the RE-modified alloys performed considerably better than the base material T6 A356. Furthermore, at almost all loads at both 250 and 300 °C, A356RE-B performed notably better than T7 A319 (see Figure 5.6-2). Moreover, A356RE-B surpassed the fracture load of T7 A319 by 15 MPa, reaching over 100% of the alloy's YS. Similarly, at 300 °C, A356RE-B surpassed T7 A319's fracture load by 5 MPa with an equivalent steady-state creep rate.

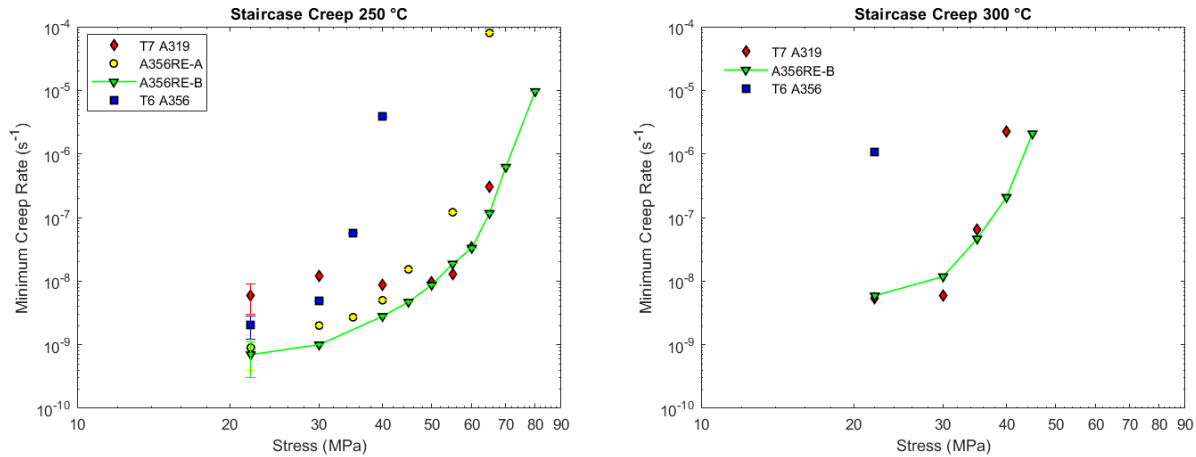


Figure 5.6-2. Summary of staircase creep results at left) 250 °C and right) 300 °C

The results of this research provide strong evidence of the benefits that RE additions have on the elevated-temperature strength retention and creep resistance of Al-Si alloys. The large improvement in the tensile properties of the A356RE alloy after the T6 heat treatment suggest that heat treating the modified A356RE alloy (i.e., A356RE-B) may result in similar strength and creep resistance enhancements. However, even without applying a costly heat treatment, the A356RE-B alloy is a viable option for replacing the A319 alloy for current and next-generation engines. The improved strength and creep resistance of A356RE-B may help the automotive industry raise the internal operating pressure in next-generation engines, leading to greater efficiencies and lower emissions.

Chapter 6: Conclusions

This dissertation was conducted to evaluate the effectiveness of adding rare earth elements to aluminum alloys, aimed at improving the elevated temperature fitness-for-service properties of next generation powertrains (i.e., engine blocks, engine heads, etc.). This was accomplished by first studying the evolution of residual stress during each stage of the manufacturing process of a high-powered diesel engine block, and then, following this, investigating the microstructure and fitness-for-service performance of the alloy (i.e., A319, Al-Si-Cu-Mg) used for the diesel engine block. The observations from the engine block study were used as a baseline to determine the feasibility of using the newly developed Al-RE alloys in similar applications. The primary conclusions that can be drawn from this dissertation are as follows:

Characterization of Residual Stress in I6 Diesel Engine Block and Evaluation of Fitness-for-Service of A319 Alloy

- 1) The use of integrated cylinder bore chills greatly increased the cooling rate experienced by the cylinder bridge, reaching upwards of 14 °C/s. Moreover, the high degree of cooling led to a homogeneous microstructure and consistent mechanical properties along the entire depth of the cylinder bridge.
- 2) Solutionizing and quenching (T4) and aging (T7), led to insignificant microstructural changes along the entire depth of the cylinder bridge. This suggests that the observed changes in residual stress are caused primarily by thermo-mechanical loading of the material as opposed to phase evolution.
- 3) The use of stainless steel bore chills during the casting process led to a significant accumulation of compressive stress in the radial, axial and hoop orientations in the cylinder bridge. However, the removal of the bore chill allowed the cylinder bridge to relax elastically and reduced the magnitude of stress at the top of the bridge in the radial, axial and hoop direction to ~100, -4, and 6 MPa, respectively.
- 4) The T4 heat treatment reduced the magnitude of radial stress at the top of the cylinder bridge but shifted the stress below the cooling channel to purely tensile in nature. The shift towards tensile stress was likely caused by the quenching portion of the T4 heat treatment, in that the thicker material adjacent to the cylinder bridge contracts more slowly than the thin cylinder wall, and pulls the center of the bridge into tension towards the end of cooling.

- 5) To further improve the dimensional stability, thermal stability, and elevated-temperature properties of the I6 engine block, the block was heat treated to a T7 temper. Compared with the stress after the T4 treatments, the T7 temper lowered the magnitude of stress at the top, lower middle, and bottom of the bridge, and shifted the upper middle section to compression. Below the cooling channel, the general trend along the length of the cylinder bridge for each orientation is a gradual shift from compression to tension.
- 6) The combined effects of pre-heating and mechanical insertion of the T7LM block did not considerably affect the axial and hoop stress; however, the radial stress in the upper half of the cylinder bridge shifted slightly toward more compression. Since the top of the cylinder bridge is typically the area exposed to the greatest level of thermo-mechanical loading, and is most prone to cracking, it is one of the locations most concerning for engine manufacturers. The results from this study indicate that the combined contribution of the in-service operational stress (~15-60 MPa for diesel engines) and the maximum residual stress at the top of the cylinder bridge that has developed during the manufacturing process (~51 MPa) will account for at least ~90% of the materials strength at 250 °C. Thus, increasing the operating pressure and, therefore, the temperature of the engine block to 300 °C is infeasible using the current T7 A319 alloy.

Microstructure and Solidification Characteristics of Al-RE Alloys

Al-Ce Alloys

- 1) Increasing the Ce content from 6% to 16% (i.e., above eutectic) in binary Al-Ce alloys leads to the formation of brittle blocky or needle-like primary $\text{Al}_{11}\text{Ce}_3$ crystals. The difference of the coefficient of thermal expansion between the Al matrix and $\text{Al}_{11}\text{Ce}_3$ may lead to the development of intergranular stress during solidification, surpassing the strength of the brittle $\text{Al}_{11}\text{Ce}_3$ crystals and resulting in the observed micro-cracking. This is likely the cause for the reported decreasing ductility of higher Ce content alloys. As a result, it is concluded that the Ce content should remain below the alloy's eutectic composition.
- 2) The morphology and high thermal stability of the $\text{Al}_{11}\text{Ce}_3$ (~650 °C) phase is likely the driving factor behind the improved high-temperature mechanical properties of the Al-Ce system as compared to more conventional Al alloys.

- 3) Addition of Mg to Al-Ce alloys may be a factor that alters the fine interconnected eutectic Al-Ce to a coarser and more randomly dispersed Chinese script. In conjunction with the solid solutionizing effect of Mg in Al, this Chinese script phase is one of the reasons for the increased strength of the alloy as compared to the binary Al-Ce alloys. However, the Mg addition also led to a considerable amount of thermally unstable Al-Mg pools.
- 4) The XRD results for all four samples (i.e., Al-6%Ce, Al-16%Ce, Al-8% Ce-10% Mg before ND, and Al-8% Ce-10% Mg after ND) appear to be nearly identical, with only a slight shift of the major α -Al peaks in the Al-8%Ce-10%Mg alloy due to the dissolution of Mg into the Al matrix.

A356 and A356RE Alloys

- 1) The addition of RE mischmetal to the A356 alloy led to the formation of blocky $\text{Al}_{20}\text{Ti}_2\text{RE}$ and plate-like AlSiRE precipitates. The AlSiRE intermetallic is presumed to be the thermally stable $\text{Ce}(\text{Al}_{1.2}\text{Si}_{0.8})$ phase with additional dissolved RE elements (up to ~10 at.% of Pr and Nd). T6 heat treatment of the A356RE alloy led to a complete spheroidization of the eutectic Si particles and appears to have increased the area fraction of π - $\text{Al}_9\text{FeMg}_3\text{Si}_5$ at the expense of Mg_2Si . The T6 heat treatment had no effect on the size, composition or morphology of the AlSiRE intermetallic.
- 2) Due to the low diffusivity of Fe in Al and the poor thermal stability of the Mg_2Si precipitate (~170 °C), the increased volume fraction of the $\text{Al}_9\text{FeMg}_3\text{Si}_5$ intermetallic may have also contributed to the improved thermal stability of the A356RE alloy, as compared to the base alloy, A356.
- 3) The peak positions of the neutron diffraction powder pattern were indexed to Al, Si, $\text{Ce}(\text{Al}_{1.2}\text{Si}_{0.8})$, $\text{Al}_{20}\text{Ti}_2\text{Ce}$, Mg_2Si , $\text{Al}_9\text{Fe}_2\text{Si}_2$, and $\text{Al}_9\text{FeMg}_3\text{Si}_5$. The peak intensities at each temperature (liquid to ambient) were normalized and a Debye-Waller correction factor was introduced to offset the thermal vibrations of atoms at the elevated temperatures. The analysis revealed that the RE additions had little effect on the solidification characteristics of Al and Si. Specifically, the solidification range for primary α -Al in the A356RE alloy is approximately 610 °C (liquidus) to 550 °C (solidus), with eutectic Si evolving in the temperature range of 565 to 550 °C. This is similar to the predicted ThermoCalc results as well as the published solidification range of A356.

- 4) Due to the presence of the harmful Fe-bearing intermetallics (i.e., β -Al₅FeSi and π -Al₉FeMg₃Si₅), the Mn and Mg concentration in the A356RE alloy was modified to 0.41 (from 0.1 wt.%) and 0.25 (from 0.49 wt.%) wt.%, respectively. The chemical modification led to a near complete transformation of the two harmful Fe phases into the more favorable Al₁₅(Fe,Mn)₃Si₂ intermetallic. In addition, this transformation increased the area fraction of the Fe phase, leading to a greater contribution from Orowan strengthening. Lastly, it appears that the modified chemistry also partially transformed the size and shape of the elongated rod/plate-like structure of the AlSiRE phase into a smaller, faceted Chinese script style morphology.

Fitness-for-Service Performance of Al-RE Alloys

- 1) The tensile performance of the A356 system was greatly improved after introducing 3.5 wt.% RE mischmetal. Specifically, the YS was increased at 250 and 300 °C by 133 and 174%, respectively. Further, by adjusting the Mn and Mg concentration to transform the harmful Fe phases, the YS was further improved at 250 °C by over 10%.
- 2) The RE addition to the A356 alloy led to a considerable increase in the alloy's creep resistance at both 250 and 300 °C. Specifically, the steady-state creep rates at every load were significantly lower in A356RE-B as compared to the T6 A356 alloy. Moreover, the fracture load for A356RE-B was nearly two times larger than for the T6 A356 alloy. The increase in creep resistance is believed to be attributed to the relatively high volume fraction of thermally stable AlSiRE intermetallics and the transformation of the brittle, stress-concentrating Al₉Fe₂Si₂ and Al₉Fe₃Mg₅Si₆ phases into Al₁₅(Fe,Mn)₃Si₂. Not only does the Al₁₅(Fe,Mn)₃Si₂ impart ductility on the matrix, the increased volume fraction of this intermetallic has improved the resistance to dislocation motion via the Orowan mechanism.
- 3) In the as-cast state, the A356RE-B demonstrated greater creep resistance than the currently used powertrain alloy, T7 A319, at both 250 and 300 °C, suggesting that this alloy system could be a potential replacement for current and next-generation powertrain components.

6.1 Contributions of Research

The research described in this dissertation assisted in the development of a potential replacement alloy for current and next-generation powertrain components (i.e., engine blocks, cylinder heads,

pistons, and connecting rods) as well as any applications which operate at similar stresses (up to ~150 MPa) and temperatures (up to 250-300 °C). These may include certain components in turbines, high temperature radiators, additive manufacturing nozzles, and electric motors and battery cooling systems in electric vehicles. Moreover, the in-depth residual stress analysis of the cast Al engine block provides a thorough understanding of the effects that each stage of the manufacturing process has on the evolution of residual stress in complex castings. Together, the results reported in this dissertation will help the transportation industry improve the performance and efficiencies of their vehicles and lower the production of harmful emissions. Further, the results will support the work of any industry that requires lightweight components with low magnitudes of residual stress and sufficient thermal stability. These include, but are not limited to power generation, aerospace and electric vehicle applications.

The following list summarizes the novel contributions that originate from this research:

1. Characterization of residual stress in I6 engine block
 - a. Comprehensively analyzed the evolution of residual stress, using neutron diffraction, in the cylinder bridge of sand-cast Al engine blocks at each stage of the manufacturing process (i.e., with bore chill, after removal of bore chill, after subjecting to a T4 and T7 heat treatment, and after machining and inserting press-fit cylinder liners). This research provides a better understanding of how the magnitude of residual stress in complex castings can be lowered, thereby increasing the alloy's amount of useable strength. Consequently, this may allow for greater operating stresses (increased performance and/or efficiencies) and efficiencies through mass reduction. These results may be used by all types of manufacturers and industries which develop complex castings.
2. Evaluation of fitness-for-service of the A319 alloy for current and next-generation powertrains
 - a. Validated the effectiveness of cylinder-bore chills for refining and homogenizing the microstructure and tensile properties along the entire depth of the cylinder bridge material in cast Al engine blocks.
 - b. Determined the tensile performance and creep characteristics (i.e., steady-state creep rates, stress exponent and activation energy) of a 200-hour-conditioned T7

A319 alloy at both 250 and 300 °C. The rate-controlling creep mechanisms at each load increment were discussed. These results reveal the alloy's poor thermal stability beyond 250 °C, indicating that the operating conditions of current and next-generation powertrain applications push the A319 alloy beyond its physical limitations.

- c. Identified the steady-state creep rates and rate-controlling creep mechanisms of the 200-hour-conditioned T7 A319 alloy at stresses similar to peak cylinder pressures in internal combustion engines (22 MPa), thermo-mechanical stresses induced during engine heat up (30 MPa), and up to plasticity (35-65 MPa).
3. Next-generation alloy development
- a. Revealed that relatively high additions (8 wt.%) of RE mischmetal to hypereutectic Al-Si alloys (specifically A390, Al-19%Si) with moderate Cu concentrations (2-3 wt.%), may lead to the formation of a large (200-400 μm long) and fibrous, twin-layered AlSiRE precipitate containing large voids and poor intermetallic-matrix and intermetallic-intermetallic bonding.
 - b. Utilized X-ray micro-computed tomography to 3D reconstruct the morphology of an AlSiRE (~Ce(Al_{1.2}Si_{0.8})) intermetallic in the A356RE alloy, revealing the phase's plate-like structure.
 - c. Utilized X-ray micro-computed tomography to 3D reconstruct the morphology of the Al₁₁Ce₃ precipitate in the Al-8%Ce-10%Mg alloy, revealing the morphology transformation caused by the addition of Mg, from blocky or needle-like (as shown in binary Al-Ce alloys) to branched Chinese-script.
 - d. Identified the actual evolution of phases during solidification of the RE-modified Al alloys using *in-situ* neutron diffraction. Further, the fraction solid of phases as a function of temperature were calculated by normalizing the peak intensities from the neutron powder data against the background intensity. A temperature correction factor (Debye-Waller factor) was incorporated to account for the inelastic scattering caused by thermal atomic vibrations.
 - e. A Rietveld refinement of the neutron powder data was performed on the A356RE (A356+3.5 wt.% RE mischmetal) alloy, and the results were combined with the

normalized peak intensities (calculated fraction solid) to establish a relationship between phase mass fraction and temperature.

- f. Utilized *in-situ* neutron diffraction power data to calculate the coefficient of thermal expansion of the $\text{Al}_{11}\text{Ce}_3$ intermetallic. This data was used to explain the observed microcracking of primary $\text{Al}_{11}\text{Ce}_3$ crystals in an Al-16%Ce alloy. To date, literature only contains unsupported claims about the intermetallic cracking.
- g. Determined the fitness-for-service feasibility of the Al-8%Ce-10%Mg, T6 A356, and A356RE alloys at current and next-generation engine temperatures, including tensile and staircase creep at 250 and 300 °C (all alloys conditioned at test temperature for 200 hours).
- h. Identified the rate-controlling creep mechanisms and threshold stresses for the A356RE and A356 alloys.
- i. Characterized the effects that elevated manganese (0.1 to 0.4 wt.%) additions to the A356RE alloy system (which, consequently, almost completely transformed $\text{Al}_9\text{Fe}_2\text{Si}_2$ and $\text{Al}_9\text{FeMg}_3\text{Si}_5$ into $\text{Al}_{15}(\text{Fe},\text{Mn})_3\text{Si}_2$), have on microstructure and elevated-temperature tensile and creep performance.

Chapter 7: Future Recommendations

The research described in the previous chapters provides clear evidence of the high potential that the A356RE system has for replacing the currently used powertrain alloys, specifically A356 and A319. However, to further develop the alloy system and improve FFS performance of the system, several areas of research remain. These includes:

- 1) Study the effects that different quench rates have on the microstructure and FFS performance of the A356RE system
- 2) Optimize the Mg:Mn:Fe ratio to completely transform the Al_5FeSi and $\text{Al}_9\text{FeMg}_3\text{Si}_5$ phases into $\text{Al}_{15}(\text{Fe,Mn})_3\text{Si}_2$
- 3) Investigate methods for reducing the size of the AlSiRE precipitates
- 4) Characterize the effects of nano-level composite additions (i.e., carbon nano tubes, graphene and alumina)
- 5) Determine the thermal conductivity and coefficient of thermal expansion of the Al-RE alloys
- 6) Develop an optimized heat treatment process for the Al-RE system
 - a. Preliminary results indicate that the phases have sluggish kinetics at conventional heat-treating temperatures and times
- 7) Determine the elevated temperature fatigue strength of the A356RE alloy
- 8) Measure the corrosion resistance of the A356RE alloy

References

- [1] Statista Research Department, “Worldwide car sales 1990-2020.” 2020.
- [2] US EPA and OAR, “Inventory of U.S. Greenhouse Gas Emissions and Sinks,” 2018.
- [3] National Highway Traffic Safety Administration, “CAFE Public Information Center Reports: Fleet Fuel Economy Performance Report,” 2019.
- [4] R. K. Lattanzio, L. Tsang, and B. Canis, “Vehicle fuel economy and greenhouse gas standards,” *Congr. Res. Serv.*, pp. 33–90, 2021.
- [5] J. Davis, *Aluminum and aluminum alloys*. ASM International, 1993.
- [6] K. Chang, S. Liu, D. Zhao, Y. Du, L. Zhou, and L. Chen, “Thermodynamic description of the Al-Cu-Mg-Mn-Si quinary system and its application to solidification simulation,” *Thermochim. Acta*, vol. 512, pp. 258–267, 2011.
- [7] J. S. Robinson and D. A. Tanner, “The Magnitude of Heat Treatment Induced Residual Stresses and the Thermal Stress Relief of Aluminium Alloys,” *Mater. Sci. Forum*, vol. 404–407, pp. 355–360, 2009.
- [8] D. Sediako et al., “Analysis of Residual Stress Profiles in the Cylinder Web Region of an As-Cast V6 Al Engine Block with Cast-In Fe Liners Using Neutron Diffraction,” *SAE Int. J. Mater. Manuf.*, vol. 4, no. 1, pp. 138–151, Apr. 2011.
- [9] Z. Sims et al., “High performance aluminum-cerium alloys for high-temperature applications,” *Mater. Horiz.*, vol. 4, no. 6, pp. 1070–1078, 2017.
- [10] S. Shaha, F. Czerwinski, W. Kasprzak, J. Friedman, and D. Chen, “Thermal stability of (AlSi)_x(ZrVTi) intermetallic phases in the Al–Si–Cu–Mg cast alloy with additions of Ti, V, and Zr,” *Thermochim. Acta*, vol. 595, pp. 11–16, Nov. 2014.
- [11] G. Sha, H. Möller, W. E. Stumpf, J. H. Xia, G. Govender, and S. P. Ringer, “Solute nanostructures and their strengthening effects in Al-7Si-0.6Mg alloy F357,” *Acta Mater.*, vol. 60, no. 2, pp. 692–701, Jan. 2012.
- [12] J. Hernandez-Sandoval, G. H. Garza-Elizondo, A. M. Samuel, S. Valtierra, and F. H. Samuel, “The ambient and high temperature deformation behavior of Al-Si-Cu-Mg alloy with minor Ti, Zr, Ni additions,” *Mater. Des.*, vol. 58, pp. 89–101, 2014.
- [13] R. Vogel, “Cerium-Aluminum Alloys,” *J. Franklin Inst.*, vol. 174, no. 3, p. 342, 1912.
- [14] H. W. Gillett and V. H. Schnee, “Cerium in Aluminium Alloys,” *Ind. Eng. Chem.*, pp. 709–711, 1923.
- [15] B. K and V. Vucht J, “The binary systems cerium-aluminum and praseodymium-aluminum,” *Z Met.*, vol. 57, pp. 162–166, 1966.

- [16] K. H. J. Buschow, "Rare Earth-Aluminum Intermetallic Compounds of the Form RAI and R_3Al_2 ," *J. Less-Common Met.*, vol. 8, pp. 209–212, 1965.
- [17] A. S. Cooper, "Precise lattice constants of germanium, aluminum, gallium arsenide, uranium, sulphur, quartz and sapphire," *Acta Crystallogr.*, vol. 15, no. 6, pp. 578–582, Jun. 1962.
- [18] J. Voncken, "The Rare-Earth Elements," *Journal of the American Chemical Society*, vol. 86, no. 21. pp. 1–14, 1964.
- [19] K. Gomes De Mesquita, A. Buschow, "The Crystal Structure of So-Called α - $LaAl_4(La_3Al_{11})$," *Acta Cryst.*, vol. 22, pp. 497–501, 1966.
- [20] D. Weiss, "High Performance Aluminum Casting Alloys for Engine Applications," *SAE Tech. Pap. Ser.*, vol. 1, 2016.
- [21] E. Aghaie, "Effect of cerium addition on improvement of mechanical properties of B319 powertrain aluminum alloy," University of British Columbia Okanagan, 2019.
- [22] W. L. Guesser, P. V. Duran, and W. Krause, "Compacted Graphite Iron for Diesel Engine Cylinder Blocks," *Congrès Le diesel aujourd'hui demain*, pp. 12–13, 2004.
- [23] K. C. Vora, S. S. Ramdasi, N. H. Walke, A. V. Marathe, and N. V. Marathe, "Development Strategy for High Specific Power Low Emission Diesel Engines," *SAE Tech. Pap.*, 2009.
- [24] E. Clapeyron, "Memoire sur la puissance motrice de la chaleur," *J. l'Ecole Polytech.*, pp. 154–190, 1834.
- [25] T. K. Hayes, R. A. White, and J. E. Peters, "Combustion chamber temperature and instantaneous local heat flux measurements in a spark ignition engine," *SAE Tech. Pap.* 930217, no. 930217, 1993.
- [26] Temperature distribution in internal combustion engine. Available: <http://www.software.ricardo.com/support/manuals>.
- [27] A. Farkoosh, "Development of Creep-Resistant Al-Si Cast Alloys Strengthened with Nanoscale Dispersoids," McGill University, 2014.
- [28] J. Stroh and D. Sediako, "Residual Stress Characterization for Marine Gear Cases in As-Cast and T5 Heat Treated Conditions with Application of Neutron Diffraction," *Light Met.* 2019, pp. 395–399, 2019.
- [29] D. R. Gunasegaram, B. R. Finnin, and F. B. Polivka, "Melt flow velocity in high pressure die casting: Its effect on microstructure and mechanical properties in an Al-Si alloy," *Mater. Sci. Technol.*, vol. 23, no. 7, pp. 847–856, 2007.
- [30] P. Poolperm and W. Nakkiew, "Effect of Porosity on Residual Stress of 2024-Aluminum GTAW Specimen," *Trans Tech. Publications*, vol. 872, pp. 28-32.

- [31] Y. Gao, J. Yi, P. Lee, and T. Lindley, "The effect of porosity on the fatigue life of cast aluminium-silicon alloys," *Fatigue Fract. Eng. Mater. Struct.*, vol. 27, no. 7, pp. 559–570, 2004.
- [32] A. J. Martyr and M. A. Plint, "Ch 15: The Combustion Process and Combustion Analysis," in *Engine Testing, Fourth.*, Butterworth-Heinemann, 2012, pp. 375–406.
- [33] D. A. Kouremenos, C. D. Rakopoulos, and C. G. Kotsos, "Phasing cylinder pressure to crank angle in a direct injection diesel engine, by simulation of compression curve and elaboration of measured pressure data," *Forsch. im Ingenieurwes.*, vol. 57, no. 3, pp. 87–95, 1991.
- [34] E. Carrera, A. Rodríguez, J. Talamantes, S. Valtierra, and R. Colás, "Measurement of residual stresses in cast aluminium engine blocks," *J. Mater. Process. Technol.*, vol. 189, no. 1–3, pp. 206–210, 2007.
- [35] A. Lombardi, C. Ravindran, D. Sediako, and R. MacKay, "Determining the Mechanism of In-Service Cylinder Distortion in Aluminum Engine Blocks with Cast-In Gray Iron Liners," *Metall. Mater. Trans. A Phys. Metall. Mater. Sci.*, vol. 45, no. 13, pp. 6291–6303, 2014.
- [36] A. Lombardi, D. Sediako, A. Machin, C. Ravindran, and R. MacKay, "Effect of solution heat treatment on residual stress in Al alloy engine blocks using neutron diffraction," *Mater. Sci. Eng. A*, vol. 697, no. May, pp. 238–247, 2017.
- [37] B. Chen et al., "In situ neutron diffraction measurement of residual stress relaxation in a welded steel pipe during heat treatment," *Mater. Sci. Eng. A*, 2014.
- [38] D. A. Lados, D. Apelian, and L. Wang, "Minimization of residual stress in heat-treated Al-Si-Mg cast alloys using uphill quenching: Mechanisms and effects on static and dynamic properties," *Mater. Sci. Eng. A*, vol. 527, no. 13–14, pp. 3159–3165, 2010.
- [39] J. Rolph, A. Evans, A. Paradowska, M. Hofmann, M. Hardy, and M. Preuss, "Stress relaxation through ageing heat treatment - a comparison between in situ and ex situ neutron diffraction techniques," *Comptes Rendus Phys.*, vol. 13, no. 3, pp. 307–315, 2012.
- [40] A. Lombardi, F. D'Elia, C. Ravindran, D. Sediako, B. S. Murty, and R. MacKay, "Interplay Between Residual Stresses, Microstructure, Process Variables and Engine Block Casting Integrity," *Metall. Mater. Trans. A*, vol. 43, no. 13, pp. 5258–5270, Dec. 2012.
- [41] F. Silva, "Fatigue on engine pistons-A compendium of case studies," *Eng. Fail. Anal.*, vol. 13, no. 2006, pp. 480–492, 2005.
- [42] M. Garat and G. Laslaz, "Improved Aluminium Alloys for Common Rail Diesel Cylinder Heads," *Trans. Am. Foundry Soc.*, vol. 115, no. 07, pp. 1–8, 2007.
- [43] E. H. Wong and Y. W. Mai, "A unified equation for creep-fatigue," *Int. J. Fatigue*, vol. 68, pp. 186–194, 2014.
- [44] M. O. Pekguleryuz and A. A. Kaya, "Creep resistant magnesium alloys for powertrain applications," *Adv. Eng. Mater.*, vol. 5, no. 12, pp. 866–878, 2003.

- [45] G. E. Dieter, D. Bacon, and G. L. of T. heat treatment on thermal stability and wear behaviour of A. 12 5Si 4 5Cu 1 0Mg alloy. pd. Wilkes, METALLURGY SI Metric Edition Adapted by. 2001.
- [46] M. Pekguleryuz and M. Celikin, "Creep resistance in magnesium alloys," *Int. Mater. Rev.*, vol. 55, no. 4, pp. 197–217, 2010.
- [47] A. Rusinko and K. Rusinko, *Plasticity and Creep of Metals*, vol. 14, no. 2. Springer, 2011.
- [48] G. Dieter, *Mechanical metallurgy*, McGraw-Hill Book Company, 1961.
- [49] O. D. Sherby and P. M. Burke, "Mechanical behavior of crystalline solids at elevated temperature," *Prog. Mater. Sci.*, vol. 13, pp. 323–390, 1968.
- [50] J. Weertman, "Creep of Rate Tests As Determined," *J. Mech. Phys. Solids*, vol. 4, pp. 230–234, 1956.
- [51] S. Straub and W. Blum, "Does the 'Natural' Third Power Law of Steady State Creep Hold For Pure Aluminum?," vol. 24, no. 9, pp. 1837–1842, 1990.
- [52] M. E. Kassner, P. Kumar, and W. Blum, "Harper-Dorn creep," *Int. J. Plast.*, vol. 23, no. 6, pp. 980–1000, 2007.
- [53] J. Harper and J. E. Dorn, "Viscous creep of aluminum near its melting temperature," *Acta Metall.*, vol. 5, no. 11, pp. 654–665, 1957.
- [54] M. Kassner, "Chapter 2: Five-Power-Law Creep," in *Fundamentals of Creep in Metals and Alloys: Third Edition*, Elsevier, pp. 7–102, 2015,
- [55] S. P. Deshmukh, R. S. Mishra, and K. L. Kendig, "Creep behavior and threshold stress of an extruded Al-6Mg-2Sc-1Zr alloy," *Mater. Sci. Eng. A*, vol. 381, pp. 381–385, 2004.
- [56] K. E. Knippling and D. C. Dunand, "Creep resistance of cast and aged Al-0.1Zr and Al-0.1Zr-0.1Ti (at.%) alloys at 300-400 °C," *Scr. Mater.*, vol. 59, pp. 387–390, 2008.
- [57] S. Mitra, "Elevated Temperature Deformation Behavior of a Dispersion-Strengthened Al-Fe,V,Si Alloy," *Metall. Mater. Trans. A Phys. Metall. Mater. Sci.*, vol. 27A, pp. 3913–3923, 1996.
- [58] O. Sherby, R. Klundt, and A. Miller, "Flow Stress, Subgrain Size, and Subgrain Stability at Elevated Temperature," *Metall. Trans. A*, vol. 8A, pp. 843–850, 1977.
- [59] E. A. Marquis and D. C. Dunand, "Model for creep threshold stress in precipitation-strengthened alloys with coherent particles," *Scr. Mater.*, vol. 47, pp. 503–508, 2002.
- [60] M. E. Krug and D. C. Dunand, "Modeling the creep threshold stress due to climb of a dislocation in the stress field of a misfitting precipitate," *Acta Mater.*, vol. 59, pp. 5125–5134, 2011.

- [61] ASTM, “E8M Standard Test Methods for Tension Testing Wrought and Cast Aluminum- and Magnesium-Alloy Products,” ASTM B. Stand., pp. 1–16, 2009.
- [62] “ASTM E139-11, Standard Test Methods for Conducting Creep, Creep-Rupture, and Stress-Rupture Tests of Metallic Materials,” ASTM International, 2018.
- [63] A. R. Farkoosh and M. Pekguleryuz, “The effects of manganese on the T-phase and creep resistance in Al-Si-Cu-Mg-Ni alloys,” *Mater. Sci. Eng. A*, vol. 582, pp. 248–256, 2013.
- [64] H. J. Frost and M. F. Ashby, *Deformation Mechanism Maps*. Oxford Pergamon Press, 1982.
- [65] E. Sato, Y. Takayama, T. Shibayanagi, and K. Kitazono, “Re-examination of Deformation Mechanism Map of Pure Aluminum,” *Proc. 12th Int. Conf. Alum. Alloy.*, pp. 1559–1566, 2010.
- [66] D. Sediako, W. Kasprzak, F. Czerwinski, A. Nabawy, and A. Farkoosh, “High Temperature Creep Evolution in Al-Si Alloys Developed for Automotive Powertrain Applications A Neutron In-Situ Study on Hkl-Plane Creep Response,” *Light Met.* 2016, pp. 131–136, 2016.
- [67] G. E. Dieter, *Mechanical Metallurgy*, 3rd ed. McGraw Hill Publishing Co., 1986.
- [68] A. Keyhani, R. Roumina, and S. Mohammadi, “An Efficient Computational Technique for Modeling Dislocation-Precipitate Interactions within Dislocation Dynamics,” *Comput. Mater. Sci.*, vol. 122, pp. 281–287, 2016.
- [69] H. A. Calderon, P. W. Voorhees, J. L. Murray, and G. Kostorz, “Ostwald ripening in concentrated alloys,” *Acta Metall. Mater.*, vol. 42, no. 3, pp. 991–1000, 1994.
- [70] K. E. Knippling, D. C. Dunand, and D. N. Seidman, “Criteria for Developing Castable, Creep-Resistant Aluminum-Based Alloys-A Review,” *Int. J. Mater. Res.*, vol. 97, no. 3, pp. 246–265, 2006.
- [71] H. K. Kanga, D. Larouche, M. Bournane, and A. Rahem, “Mechanical properties of aluminium-copper B206 alloys with iron and silicon additions,” *Int. J. Cast Met. Res.*, vol. 25, no. 1, pp. 15–25.
- [72] ASM Handbook Committee, *Properties and Selection: Nonferrous Alloys and Special-Purpose Materials*. ASM International, 1990.
- [73] M. Tiryakioğlu, J. Campbell, and N. D. Alexopoulos, “Quality indices for aluminum alloy castings: A critical review,” *Metall. Mater. Trans. B Process Metall. Mater. Process. Sci.*, vol. 40, no. 6, pp. 802–811, 2009.
- [74] S. G and M. J, “Factors influencing the mechanical properties of B206 alloy castings,” *Light Meta* 2006, pp. 795–799, 2006,

- [75] R. Donahue and P. A. Fabiyi, “Manufacturing Feasibility of All-Aluminum Automotive Engines Via Application of High Silicon Aluminum Alloy,” SAE Technical Papers, no. 2000-01-0061, 2000.
- [76] H. Choi, W.-H. Cho, H. Konishi, S. Kou, and X. Li, “Nanoparticle-Induced Superior Hot Tearing Resistance of A206 Alloy,” *Metall. Mater. Trans. A*, vol. 44A, pp. 1897–1907, 2013.
- [77] D. Eskin, Suyitno, and L. Katgerman, “Mechanical properties in the semi-solid state and hot tearing of aluminium alloys,” *Progress in Materials Science*, vol. 49, pp. 629–711, 2004.
- [78] M. Zeren, “The effect of heat-treatment on aluminum-based piston alloys,” *Mater. Des.*, vol. 28, pp. 2511–2517, 2006.
- [79] J. Stroh and D. Sediako, “Residual Strain Characterization of an Advanced Aluminum Marine Alloy Using In-Situ Neutron Diffraction,” *Mater. Sci. Tech. (MS&T)* 2018, pp. 974-982, 2018.
- [80] R. Robles-Hernandez, Francisco C, Martin, Ramirez, Mackay, “Al-Si Alloys, Minor, Major, and Impurity Elements,” in *Al-Si Alloys Automotive, Aeronautical, and Aerospace Applications*, Springer Nature, pp. 1–12, 2017.
- [81] “Properties and Selection: Nonferrous Alloys and Special-Purpose Materials,” in *Metals Handbook*, ASM International 10th Ed., 1990.
- [82] A. Edacherian, A. Algahtani, and V. Tirth, “Materials Investigations of the Tribological Performance of A390 Alloy Hybrid Aluminum Matrix Composite,” *Materials*, vol. 11, no. 2524, pp. 1-14, 2018.
- [83] A. Radjai and K. Miwa, “Effects of the intensity and frequency of electromagnetic vibrations on the microstructural refinement of hypoeutectic Al-Si alloys,” *Metall. Mater. Trans. A Phys. Metall. Mater. Sci.*, vol. 31, no. 3, pp. 755–762, 2000.
- [84] L. Hengcheng, S. Yu, and S. Guoxiong, “Restraining effect of strontium on the crystallization of Mg₂Si phase during solidification in Al-Si-Mg casting alloys and mechanisms,” vol. 358, pp. 164–170, 2003.
- [85] J. E. Hatch, Aluminum Association., and American Society for Metals., *Aluminum: properties and physical metallurgy*. American Society for Metals, 1984.
- [86] R. Chen, Q. Xu, H. Guo, Z. Xia, Q. Wu, and B. Liu, “Correlation of solidification microstructure refining scale, Mg composition and heat treatment conditions with mechanical properties in Al-7Si-Mg cast aluminum alloys,” *Mater. Sci. Eng. A*, vol. 685, 2016, pp. 391–402, 2017.
- [87] D. A. Lados, D. Apelian, and L. Wang, “Solution Treatment Effects on Microstructure and Mechanical Properties of Al-(1 to 13 pct)Si-Mg Cast Alloys,” *Metall. Mater. Trans. B*, vol. 42B, pp. 171–180, 2011.

- [88] R. LI et al., "Effect of heat treatment on eutectic silicon morphology and mechanical property of Al-Si-Cu-Mg cast alloys," *Trans. Nonferrous Met. Soc. China*, vol. 14, no. 3, pp. 496–500, 2004.
- [89] E. Aghaie and D. Sediako, "Properties of Various Phases in Al Powertrain Alloys: A Review," *Mater. Sci. Tech. (MS&T)*, pp. 966–973, 2018.
- [90] Y. Li, Y. Yang, Y. Wu, Z. Wei, and X. Liu, "Supportive strengthening role of Cr-rich phase on Al-Si multicomponent piston alloy at elevated temperature," *Mater. Sci. Eng. A*, vol. 528, pp. 4427–4430, 2011.
- [91] A. R. Farkoosh, X. G. Chen, and M. Pekguleryuz, "Dispersoid strengthening of a high temperature Al-Si-Cu-Mg alloy via Mo addition," *Mater. Sci. Eng. A*, vol. 620, pp. 181–189, 2014.
- [92] F. C. Robles Hernández and J. H. Sokolowski, "Thermal analysis and microscopical characterization of Al-Si hypereutectic alloys," *J. Alloys Compd.*, vol. 419, no. 1–2, pp. 180–190, 2006.
- [93] L. Lu, M. O. Lai, and M. L. Hoe, "Formation of nanocrystalline Mg₂Si and Mg₂Si dispersion strengthened Mg-Al alloy by mechanical alloying," *Nanostructured Mater.*, vol. 10, no. 4, pp. 551–563, 1998.
- [94] L. Wang and X. Y. Qin, "The effect of mechanical milling on the formation of nanocrystalline Mg₂Si through solid-state reaction," *Scr. Mater.*, vol. 49, no. 3, pp. 243–248, 2003.
- [95] C. Y. Jeong, "High temperature mechanical properties of AlSiMg(Cu) alloys for automotive cylinder heads," *Mater. Trans.*, vol. 54, no. 4, pp. 588–594, 2013.
- [96] J. A. Taylor, D. H. St John, J. Barresi, and M. J. Couper, "An empirical analysis of trends in mechanical properties of T6 heat treated Al-Si-Mg casting alloys," *Int. J. Cast Met. Res.*, vol. 12, no. 6, pp. 419–430, 2000.
- [97] J. A. Taylor, D. H. St John, J. Barresi, and M. J. Couper, "Influence of Mg content on the microstructure and solid solution chemistry of Al-7%Si-Mg casting alloys during solution treatment," *Mater. Sci. Forum*, vol. 331, pp. 277–282, 2000.
- [98] Q. Wang, C. Caceres, and J. Griffiths, "Damage by Eutectic Particle Cracking in Aluminum Casting Alloys A356/357," *Metall. Mater. Trans. A*, vol. 34A, pp. 2901–2912, 2003.
- [99] Q. Wang and C. Davidson, "Solidification and precipitation behaviour of Al-Si-Mg casting alloys," *J. Mater. Sci.*, vol. 36, pp. 739–750, 2001.
- [100] C. Dinnis, J. Taylor, and A. Dahle, "As-cast Morphology of Iron-Intermetallics in Al-Si Foundry Alloys," *Scr. Mater.*, vol. 53, no. 8, pp. 955–958, 2005.
- [101] J. A. Spittle and S. Sadli, "Effect of alloy variables on grain refinement of binary aluminium alloys with Al-Ti-B," *Mater. Sci. Technol.*, vol. 11, no. 6, pp. 533–537, 1995.

- [102] Y. C. Lee, A. K. Dahle, D. H. StJohn, and J. E. C. Hutt, “The effect of grain refinement and silicon content on grain formation in hypoeutectic Al-Si alloys,” *Mater. Sci. Eng. A*, vol. 259, no. 1, pp. 43–52, 1999.
- [103] L. A. Tarshis, J. L. Walker, and J. W. Rutter, “Experiments on the solidification structure of alloy castings,” *Metall. Trans.*, vol. 2, no. 9, pp. 2589–2597, 1971.
- [104] H. Zahedi, M. Emamy, A. Razaghian, M. Mahta, J. Campbell, and M. Tiryakioğlu, “The effect of Fe-rich intermetallics on the Weibull distribution of tensile properties in a cast Al-5 pct Si-3 pct Cu-1 pct Fe-0.3 pct Mg alloy,” *Metall. Mater. Trans. A*, vol. 38, no. 3, pp. 659–670, 2007.
- [105] G. Timelli, A. Fabrizi, S. Vezzù, and A. De Mori, “Design of Wear-Resistant Diecast AlSi9Cu3 (Fe) Alloys for High-Temperature Components,” *Metals (Basel)*, vol. 10, no. 1, p. 55, 2020.
- [106] L. Jin, K. Liu, and X. G. Chen, “Evolution of dispersoids and their effects on elevated-temperature strength and creep resistance in Al-Si-Cu 319 cast alloys with Mn and Mo additions,” *Mater. Sci. Eng. A*, vol. 770, no. 138554, 2020.
- [107] E. Rincon, H. F. Lopez, M. M. Cisneros, and H. Mancha, “Temperature effects on the tensile properties of cast and heat treated aluminum alloy A319,” *Mater. Sci. Eng. A*, vol. 519, no. 1–2, pp. 128–140, 2009.
- [108] M. T. Di Giovanni, E. Cerri, D. Casari, M. A. T. T. I. A. Merlin, L. A. R. S. Arnberg, and G. L. Garagnani, “The Influence of Ni and V Trace Elements on High-Temperature Tensile Properties and Aging of A356 Aluminum Foundry Alloy,” *Metall. Mater. Trans. A Phys. Metall. Mater. Sci.*, vol. 47, no. 5, pp. 2049–2057, 2016.
- [109] S. L. Pramod, Ravikirana, A. K. P. Rao, B. S. Murty, and S. R. Bakshi, “Effect of Sc addition and T6 aging treatment on the microstructure modification and mechanical properties of A356 alloy,” *Mater. Sci. Eng. A*, vol. 674, pp. 438–450, 2016.
- [110] J. Gambogi, “Rare earths,” U.S. Geological Survey, *Mineral Commodity Summaries*, pp. 132–133, 2019.
- [111] V. Vucht, “Contribution to the knowledge of the system of cerium-aluminum,” *Z. Met.*, vol. 48, pp. 252–258, 1957.
- [112] H. W. Gillett and V. H. Schnee, “Cerium in Aluminium Alloys,” *Ind. Eng. Chem.*, vol. 15, no. 7, pp. 709–711, Jul. 1923.
- [113] S. L. Langenbeck, W. M. Griffith, G. J. Hildeman, and J. W. Simon, “Rapidly Solidified Powder Aluminum Alloys,” *Rapidly Solidified Powder Aluminum Alloys*, pp. 410–422, 1986.
- [114] F. Habashi, “Extractive Metallurgy of Rare Earths,” *Can. J. Metall. Mater. Sci.*, vol. 52, no. 33, pp. 224–233, 2013.

- [115] D. Weiss, "Development and Casting of High Cerium Content Aluminum Alloys," *Mod. Cast.*, vol. 107, no. 12, pp. 35–38, 2017.
- [116] Z. Sims et al., "The Efficacy of Replacing Metallic Cerium in Aluminum–Cerium Alloys with LREE Mischmetal," in *The Minerals, Metals & Materials Society 2020*, 2020, pp. 216–221.
- [117] V. Zolotarevskii, *Casting aluminum alloys*. Elsevier Science, 2007.
- [118] L. F. Mondolfo, "Aluminum–Silicon, Aluminum–Magnesium Silicide Alloys," in *Aluminum Alloys*, Elsevier, pp. 759–805, 1976.
- [119] I. Matveeva, N. Dovzhenko, S. Sidelnikov, L. Trifonenkov, V. Baranov, and E. Lopatina, "Development and Research of New Aluminium Alloys with Transition and Rare-Earth Metals and Equipment for Production of Wire for Electrotechnical Applications by Methods of Combined Processing," in *Light Metals 2013*, Hoboken, NJ, USA: John Wiley & Sons, Inc, pp. 443–447, 2013
- [120] Z. Cao, G. Kong, C. Che, Y. Wang, And H. Peng, "Experimental investigation of eutectic point in Al-rich Al-La, Al-Ce, Al-Pr and Al-Nd systems," *J. Rare Earths*, vol. 35, no. 10, pp. 1022–1028, Oct. 2017.
- [121] M. Gao, N. Ünlü, G. Shiflet, M. Mihalkovic, and M. Widom, "Reassessment of Al-Ce and Al-Nd Binary Systems Supported by Critical Experiments and First-Principles Energy Calculations," *Metall. Mater. Trans. A*, vol. 36, pp. 3269–3279, 2005.
- [122] Z. Sims et al., "Cerium-Based, Intermetallic-Strengthened Aluminum Casting Alloy: High-Volume Co-product Development," *JOM*, vol. 68, no. 7, pp. 1940–1947, 2016.
- [123] Z. Cui and R. Wu, "Phase diagram and properties of ternary Al–Mg–Ce alloys," *Acta Met.*, vol. 20, no. 6, pp. 323–331, 1984.
- [124] J. Gröbner, D. Kevorkov, and R. Schmid-Fetzer, "Thermodynamic modeling of Al-Ce-Mg phase equilibria coupled with key experiments," *Intermetallics*, vol. 10, no. 5, pp. 415–422, May 2002.
- [125] L. Jin, D. Kevorkov, M. Medraj, and P. Chartrand, "Al-Mg-RE (RE = La, Ce, Pr, Nd, Sm) systems: Thermodynamic evaluations and optimizations coupled with key experiments and Miedema's model estimations," *J. Chem. Thermodyn.*, vol. 58, pp. 166–195, 2013.
- [126] Z. Lu, X. Li, and L. Zhang, "Thermodynamic Description of Al-Si-Mg-Ce Quaternary System in Al-Rich Corner and Its Experimental Validation," *J. Phase Equilibria Diffus.*, vol. 39, no. 1, pp. 57–67, Feb. 2018.
- [127] K. Odinaev, I. Ganiev, V. Kinzhibalo, and K. Kurbanov, "Phase equilibria in the Al–Mg–Y and Al–Mg–Ce systems at 673 K," *Izv Vyss. Uchebn Zaved Tsvetn Met.*, vol. 7, pp. 75–77, 1989.
- [128] K. Odinaev, I. Ganiev, and A. Ikromov, "Pseudobinary sections and liquidus surface of the Al–Mg–CeAl₂ system," *Russ Met.*, vol. 3, pp. 122–125, 1996.

- [129] J. Gröbner, D. Mirković, and R. Schmid-Fetzer, “Thermodynamic aspects of the constitution, grain refining, and solidification enthalpies of Al-Ce-Si alloys,” *Metall. Mater. Trans. A Phys. Metall. Mater. Sci.*, vol. 35 A, no. 11, pp. 3349–3362, 2004.
- [130] V. Raghavan, “Al-Ce-Si (Aluminum-Cerium-Silicon),” *J. Phase Equilibria Diffus.*, vol. 28, no. 5, pp. 456–458, Oct. 2007.
- [131] D. Huang, S. Liu, Y. Tang, Y. Du, P. Nash, and B. Sundman, “Experimental investigation and thermodynamic modeling of the Ce-Si system,” *Thermochim. Acta*, vol. 646, pp. 49–58, 2016.
- [132] D. Simonovic and M. H. F. Sluiter, “Impurity diffusion activation energies in Al from first principles,” *Phys. Rev. B*, vol. 79, 2009.
- [133] A. Seman, “the Effect of Cerium Addition on the,” *Solid State Sci Technol*, vol. 16, no. 1, pp. 168–174, 2008.
- [134] X. hui Ao, S. ming Xing, B. shui Yu, and Q. you Han, “Effect of Ce addition on microstructures and mechanical properties of A380 aluminum alloy prepared by squeeze-casting,” *Int. J. Miner. Metall. Mater.*, vol. 25, no. 5, pp. 553–564, May 2018.
- [135] S. A. Alkahtani, E. M. Elgallad, M. M. Tash, A. M. Samuel, and F. H. Samuel, “Effect of rare earth metals on the microstructure of Al-Si based alloys,” *Materials (Basel)*, vol. 9, no. 45, pp. 1–13, 2016.
- [136] H. Yi, D. Zhang, T. Sakata, and H. Mori, “Microstructures and La-rich compounds in a Cu-containing hypereutectic Al-Si alloy,” *J. Alloys Compd.*, vol. 354, no. 1–2, pp. 159–164, May 2003.
- [137] G. Lin, K. Li, D. Feng, Y. Feng, W. Song, and M. Xiao, “Effect of LaCe addition on microstructure and mechanical properties of Al–18Si–4Cu–0.5Mg alloy,” *Trans Nonferr Met Soc China*, 2019.
- [138] E. Elgallad, M. Ibrahim, H. Doty, and F. Samuel, “Microstructural characterisation of Al-Si cast alloys containing rare earth additions Microstructural characterisation of Al-Si cast alloys containing rare earth additions,” *Philos. Mag.*, vol. 98, no. 15, pp. 1337–1359, 2018.
- [139] A. Samuel, F. Samuel, H. Doty, and S. Valtierra, “Porosity formation in Al-Si sand mold castings,” *Int. J. Met.*, vol. 11, no. 4, pp. 812–822, Oct. 2017.
- [140] M. Mahmoud, E. Elgallad, M. Ibrahim, and F. Samuel, “Effect of Rare Earth Metals on Porosity Formation in A356 Alloy,” *Int. J. Met.*, vol. 12, no. 2, pp. 251–265, Apr. 2018.
- [141] S. Kores, M. Voncina, B. Kosec, P. Mrvar, and J. Medved, “Effect of cerium additions on the AlSi17 casting alloy,” *Mater Technol.*, vol. 44, no. 3, pp. 137–140, 2010.
- [142] R. Ahmad and M. B. A. Asmael, “Influence of Cerium on Microstructure and Solidification of Eutectic Al–Si Piston Alloy,” *Mater. Manuf. Process.*, vol. 31, no. 15, pp. 1948–1957, Nov. 2016.

- [143] S. Kores, M. Vončina, B. Kosec, and J. Medved, "Formation of ALFeSi phase in AlSi12 alloy with Ce addition," *Metalurgija*, vol. 51, no. 2, pp. 216–220, 2012.
- [144] Q. Li, T. Xia, Y. Lan, W. Zhao, L. Fan, and P. Li, "Effect of rare earth cerium addition on the microstructure and tensile properties of hypereutectic Al-20%Si alloy," *J. Alloys Compd.*, vol. 562, pp. 25–32, Jun. 2013.
- [145] S. Yii, N. Anas, M. Ramdziah, and A. Anasydia, "Microstructural and mechanical properties of Al–20%Si containing cerium," *Procedia Chem*, vol. 19, pp. 304–310, 2016.
- [146] C. Dinnis, J. Taylor, and A. Dahle, "As-cast Morphology of Iron-Intermetallics in Al-Si Foundry Alloys," *Scr. Mater.*, vol. 53, no. 8, pp. 955–958, 2005.
- [147] Y. Rao, H. Yan, and Z. Hu, "Modification of eutectic silicon and β -Al₅FeSi phases in as-cast ADC12 alloys by using samarium addition," *J. Rare Earths*, vol. 31, no. 9, pp. 916–922, 2013.
- [148] K. Nogita, M. SD, and D. AK, "Eutectic modification of Al–Si alloys with rare earth metals," *Mater. Trans.*, vol. 45, no. 2, pp. 323–326, 2004.
- [149] X. Yu et al., "Improved recrystallization resistance of Al–Cu–Li–Zr alloy through Ce addition," *Metals*, vol. 8, no. 12, Dec. 2018.
- [150] H. C. Liao, Y. Liu, C. L. Lü, and Q. G. Wang, "Effect of Ce addition on castability, mechanical properties and electric conductivity of Al–0.3Si–0.2Mg alloy," *Int. J. Cast Met. Res.*, vol. 28, no. 4, pp. 213–220, Aug. 2015.
- [151] F. Czerwinski, "Cerium in aluminum alloys," *J. Mater. Sci.*, 2019.
- [152] N. A. Belov, A. V. Khvan, and A. N. Alabin, "Microstructure and Phase Composition of Al-Ce-Cu Alloys in the Al-Rich Corner," *Mater. Sci. Forum*, vol. 519–521, pp. 395–400, Jul. 2006.
- [153] N. Belov and A. Khvan, "The ternary Al-Ce-Cu phase diagram in the aluminum-rich corner," *Acta Mater.*, vol. 55, no. 16, pp. 5473–5482, Sep. 2007.
- [154] F. Czerwinski et al., "High-temperature aluminum alloys for automotive powertrains," *Adv Mater Process*, vol. 174, no. 3, pp. 16–20, 2016.
- [155] F. Czerwinski, S. K. Shaha, W. Kasprzak, J. Friedman, and D. L. Chen, "Effect of Transition Metals on Thermal Stability of Al–Si Cast Alloys," in *Frontiers in Materials Processing, Applications, Research and Technology*, Springer Singapore, 2018, pp. 287–296.
- [156] S. K. Shaha, F. Czerwinski, W. Kasprzak, J. Friedman, and D. L. Chen, "Improving High-Temperature Tensile and Low-Cycle Fatigue Behavior of Al-Si-Cu-Mg Alloys Through Micro-additions of Ti, V, and Zr," *Metall. Mater. Trans. A Phys. Metall. Mater. Sci.*, vol. 46, no. 7, pp. 3063–3078, Jul. 2015.
- [157] S. K. Shaha, F. Czerwinski, W. Kasprzak, J. Friedman, and D. L. Chen, "Effect of Cr, Ti, V, and Zr Micro-additions on Microstructure and Mechanical Properties of the Al-Si-Cu-Mg

Cast Alloy,” *Metall. Mater. Trans. A Phys. Metall. Mater. Sci.*, vol. 47, no. 5, pp. 2396–2409, May 2016.

[158] S. K. Shaha, F. Czerwinski, W. Kasprzak, J. Friedman, and D. L. Chen, “Ageing characteristics and high-temperature tensile properties of Al–Si–Cu–Mg alloys with micro-additions of Cr, Ti, V and Zr,” *Mater. Sci. Eng. A*, vol. 652, pp. 353–364, Jan. 2016.

[159] S. K. Shaha, F. Czerwinski, W. Kasprzak, J. Friedman, and D. L. Chen, “Ageing characteristics and high-temperature tensile properties of Al–Si–Cu–Mg alloys with micro-additions of Mo and Mn,” *Mater. Sci. Eng. A*, vol. 684, pp. 726–736, Jan. 2017.

[160] Rogal, J. Dutkiewicz, H. V. Atkinson, L. Lityńska-Dobrzyńska, T. Czeppe, and M. Modigell, “Characterization of semi-solid processing of aluminium alloy 7075 with Sc and Zr additions,” *Mater. Sci. Eng. A*, vol. 580, pp. 362–373, Sep. 2013.

[161] J. Royset and N. Ryum, “Scandium in aluminum alloys,” *Inter Mater Rev*, vol. 50, no. 1, pp. 19–44, 2005.

[162] C. Booth-Morrison, D. C. Dunand, and D. N. Seidman, “Coarsening resistance at 400 °C of precipitation-strengthened Al-Zr-Sc-Er alloys,” *Acta Mater.*, vol. 59, no. 18, pp. 7029–7042, 2011.

[163] Q. Wang, Z. Li, S. Pang, X. Li, C. Dong, and P. K. Liaw, “Coherent precipitation and strengthening in compositionally complex alloys: A review,” *Entropy*, vol. 20, no. 11. MDPI AG, 2018.

[164] W. Wang et al., “Microstructural stability of heat-resistant high-pressure die-cast Mg-4Al-4Ce alloy,” *Int. J. Mater. Res.*, vol. 108, no. 5, pp. 427–430, 2017.

[165] D. Weiss, O. Rios, Z. Sims, S. McCall, and R. Ott, “Casting Characteristics of High Cerium Content Aluminum Alloys,” in *The Minerals Metals & Materials Society (TMS)*, 2017, vol. Light Meta, pp. 205–211.

[166] M. F. Ibrahim, M. H. Abdelaziz, A. M. Samuel, H. W. Doty, and F. H. Samuel, “Effect of Rare Earth Metals on the Mechanical Properties and Fractography of Al–Si-Based Alloys,” *Int. J. Met.*, vol. 14, no. 1, pp. 108–124, 2020.

[167] E. Aghaie, J. Stroh, D. Sediako, A. Rashidi, and A. S. Milani, “Improving the mechanical properties of the B319 aluminum alloy by addition of cerium,” *Mater. Sci. Eng. A*, vol. 793, no. 139899, 2020.

[168] L. Cheah, C. Evans, A. Bandivadekar, and J. Heywood, “Factor of two: Halving the fuel consumption of new U.S. automobiles by 2035,” *Lab. energy Environ.*, no. LFEE 2007-04 RP, pp. 1–51, 2007.

[169] C. Suman, “Creep of Diecast Magnesium Alloys AZ91D and AM60B,” *SAE Tech. Pap. Ser.*, no. 910416, pp. 1–9, 1991.

- [170] H. Yabe and T. Kuji, "Thermal stability and hydrogen absorption / desorption properties of Mg 17 Al 12 produced by bulk mechanical alloying," *J. Alloys Compd.*, vol. 433, pp. 241–245, 2007.
- [171] B. W. Blum, B. Watzinger, and P. Zhang, "Creep of Die-Cast Light-Weight Mg ± Al-base Alloy AZ91hp **," *Adv. Eng. Mater.*, vol. 2, no. 6, pp. 349–355, 2000.
- [172] A. A. Luo, "Recent magnesium alloy development for elevated temperature applications," *Int. Mater. Rev.*, vol. 49, no. 1, pp. 13–30, 2004.
- [173] B. F. Kabirian and R. Mahmudi, "Effects of Zirconium Additions on the Microstructure of As-Cast and Aged AZ91 Magnesium Alloy," *Adv. Eng. Mater.*, vol. 11, no. 3, pp. 189–193, 2009.
- [174] M. Pekguleryuz and E. Baril, "Development of Creep Resistant Mg-Al-Sr Alloys," *Essential Readings in Magnesium Technology*, pp. 282–289, 2001.
- [175] E. Baril, P. Labelle, and M. O. Pekguleryuz, "Elevated Temperature Mg-Al-Sr: Creep Resistance, Mechanical Properties, and Microstructure," *JOM*, vol. 55, no. 11, pp. 34–39, 2003.
- [176] Y. Li, Y. Yang, Y. Wu, L. Wang, and X. Liu, "Quantitative comparison of three Ni-containing phases to the elevated-temperature properties of Al-Si piston alloys," *Mater. Sci. Eng. A*, vol. 527, pp. 7132–7137, 2010.
- [177] C. L. Chen, A. Richter, and R. C. Thomson, "Investigation of Mechanical Properties of Intermetallic Phases in Multi-Component Al-Si Alloys Using Hot-Stage Nanoindentation," *Intermetallics*, vol. 18, no. 4, pp. 499–508, 2010.
- [178] R. M. Robles-Hernandez, Francisco, Jose Martin Herrera Ramírez, *Al-Si Alloys, Automotive, Aeronautical, and Aerospace Applications*. Springer International, 2017.
- [179] A. Lombardi, C. Ravindran, and R. MacKay, "Improvements in Mechanical Properties of 319 Al Alloy Engine Blocks Through Cost-Effective Solution Heat Treatment," *J. Mater. Eng. Perform.*, vol. 23, no. 8, pp. 2766–2771, 2014.
- [180] J. Stroh, A. Piche, D. Sediako, A. Lombardi, and G. Byczynski, "The Effects of Solidification Cooling Rates on the Mechanical Properties of an Aluminum Inline-6 Engine Block," *Light Met.* 2019, pp. 505–512, 2019.
- [181] S. Roy, L. F. Allard, A. Rodriguez, W. D. Porter, and A. Shyam, "Comparative Evaluation of Cast Aluminum Alloys for Automotive Cylinder Heads: Part II — Mechanical and Thermal Properties," *Metall. Mater. Trans. A*, vol. 48, no. 5, pp. 2543–2562, 2017.
- [182] E. Vandersluis, A. Lombardi, C. Ravindran, A. Bois-Brochu, F. Chiesa, and R. Mackay, "Factors influencing thermal conductivity and mechanical properties in 319 Al alloy cylinder heads," *Mater. Sci. Eng. A*, vol. 648, pp. 401–411, 2015.

- [183] G. Byczynski and R. Mackay, "The nemak cosworth casting process latest generation," in *Shape Casting 7th International Symposium*, Springer International Publishing, 2019, pp. 179–185.
- [184] ASTM, "E3-11 Standard Guide for Preparation of Metallographic Specimens 1," ASTM Copyright., vol. i, pp. 1–12, 2011.
- [185] E. Vandersluis, "Influence of Solidification Parameters on Thermal Conductivity of Cast A319 Aluminum Alloy," Ryerson University, 2016.
- [186] E. Vandersluis and C. Ravindran, "Comparison of Measurement Methods for Secondary Dendrite Arm Spacing," *Metallogr. Microstruct. Anal.*, vol. 6, no. 1, pp. 89–94, 2017.
- [187] F. Karlsruhe, "Inorganic Crystals Structures Database," Leibniz Institute for Information Infrastructure, 2018. [Online]. Available: <https://icsd.fiz-karlsruhe.de/search/index.xhtml?jsessionid=BDB6DC046A694F77D5D5C443909832EF>.
- [188] Y. Birol, "Impact of grain size on mechanical properties of AlSi7Mg0.3 alloy," *Mater. Sci. Eng. A*, vol. 559, pp. 394–400, 2013.
- [189] Y. Wu, G. L. Zhu, G. Zhong, and H. Nagaumi, "Effect of cooling rate on modification and grain refinement of 4032 aluminum alloy," *Mater. Sci. Forum*, vol. 877, pp. 20–26, 2017.
- [190] J. Kim, K. Lee, H. Lee, T. Lee, H. Park, and H. Park, "Effects of titanium and boron additions with mechanical stirring on mechanical properties in Al-Si alloys," *Mater. Trans.*, vol. 56, no. 3, pp. 450–453, 2015.
- [191] S. K. Shaha, F. Czerwinski, W. Kasprzak, J. Friedman, and D. L. Chen, "Ageing characteristics and high-temperature tensile properties of Al-Si-Cu-Mg alloys with micro-additions of Cr, Ti, V and Zr," *Mater. Sci. Eng. A*, vol. 652, pp. 353–364, 2016.
- [192] A. Lombardi, "A study of cylinder bore distortion in V6 aluminum alloy engine blocks," Ryerson University, 2014.
- [193] A. Lombardi, "A Study of Cylinder Bore Distortion in V6 Aluminum Alloy Engine Blocks," Ryerson University, 2009.
- [194] H. Kang, M. Kida, H. Miyahara, and K. Ogi, "Age-Hardening Characteristics of Al-Si-Cu-Base Cast Alloys," *AFS Trans*, vol. 107, no. 507, pp. 828–834, 1999.
- [195] W. Callister and D. Rethwisch, *Materials Science and Engineering: An Introduction*, Second edition, John Wiley & Sons, Ltd, 2007.
- [196] G. Schajer, *Practical Residual Stress Measurement Methods*, John Wiley & Sons, Ltd, pp. 195-223, 2013.
- [197] I. 21432:2005, *Non-Destructive Testing - Standard Test Method for Determining Residual Stresses By Neutron Diffraction*. International Organization for Standardization, 2005.

- [198] C. Dong, • Hui-Bin Wu, and X.-T. Wang, “Effect of cooling rate on microstructure, hardness, and residual stress of 0.28C-0.22Ti wear-resistant steel,” *J. Iron Steel Res. Int.*, vol. 26, pp. 866–874, 2019.
- [199] T. Liu et al., “Measurement of residual strain in the cylinder bridge of high-pressure die cast A383 engine blocks using neutron diffraction,” *Miner. Met. Mater. Ser.*, pp. 303–310, 2019.
- [200] K. Satyanarayana, T. V. Hanumantha Rao, I. Niranjana Kumar, P. V. J. Mohan Rao, and V. V. S. Prasad, “Response optimization of four stroke variable compression ratio diesel engine cylinder head with stress analysis,” *Materials Today*, pp. 19497–19506, 2018.
- [201] ASTM, “B557 Tension Testing Wrought and Cast Aluminum- and Magnesium-Alloy Products (Metric),” *ASTM B. Stand.*, pp. 1–16, 2015.
- [202] S. Seifeddine, S. Johansson, and I. Svensson, “The influence of cooling rate and manganese content on the-Al₅FeSi phase formation and mechanical properties of Al-Si-based alloys,” *Mater. Sci. Eng. A*, vol. 490, pp. 385–390, 2008.
- [203] A. Fahad and I. Mohammad, “Effect of Cooling Rates on the 3D Porosity of Permanent Mold Castings Measured by Computed Tomography”, *Society for Nondestructive Testing*, vol. 73, no. 5., 2015.
- [204] R. Michalik, H. Woźnica, and A. Tomaszewska, “Effect of cooling rate on the porosity of the ZnAl₂₂Cu₃ alloy,” *Tran Tech. Publications*, vol. 197, pp. 121-125, 2013.
- [205] J. Ferguson, H. Lopez, K. Cho, and C.-S. Kim, “Temperature Effects on the Tensile Properties of Precipitation-Hardened Al-Mg-Cu-Si Alloys,” *Metals (Basel)*, vol. 6, no. 3, pp. 43, 2016.
- [206] M. Salleh, M. Omar, J. Syarif, K. Alhawari, and M. Mohammed, “Microstructure and mechanical properties of thixoformed A319 aluminium alloy,” *Mater. Design*, vol. 64, pp. 142–152 2014.
- [207] K. Y. Lee, S. L. Lee, C. T. Wu, W. C. Chen, and J. C. Lin, “Effects of T6 heat treatment on thermal stability and wear behaviour of Al-12.5Si-4.5Cu-1.0Mg alloy,” *Mater. Sci. Technol. (United Kingdom)*, vol. 28, no. 6, pp. 639–643, 2013.
- [208] D. Sediako, D. Weiss, and A. Nabawy, “Advanced Aluminum Alloy Development and In-Situ Fitness-for-Service Testing for Automotive Lightweighting,” in *TMS*, 2017, pp. 639–644.
- [209] H. R. Erfanian-Naziftoosi, E. J. Rincón, and H. F. López, “Creep Properties of the As-Cast Al-A319 Alloy: T4 and T7 Heat Treatment Effects,” *Metall. Mater. Trans. A Phys. Metall. Mater. Sci.*, vol. 47, no. 8, pp. 4258–4267, 2016.
- [210] D. Weiss, “Improved High-Temperature Aluminum Alloys Containing Cerium,” vol. 28, no. 4, pp. 1093–1908, 2019.

- [211] J. A. Taylor, “Iron-Containing Intermetallic Phases in Al-Si Based Casting Alloys,” *Procedia Mater. Sci.*, vol. 1, pp. 19–33, 2012.
- [212] J. Stroh, D. Sediako, and D. Weiss, “The Effect of Rare Earth Mischmetal on the High Temperature Tensile Properties of an A356 Aluminum Alloy,” *Light Met.* 2021, pp. 184–191, 2021.
- [213] A. Hawksworth, W. Rainforth, and H. Jones, “Thermal stability of Al/Al₁₁Ce₃ and Al/Al₁₁La₃/Al₃Ni eutectics obtained by Bridgman growth,” *Mater. Sci. Technol.*, vol. 15, no. 6, pp. 616–620, Jun. 1999.
- [214] N. Belov, A. Aksenov, and D. Eskin, *Iron in aluminum alloys: impurity and alloying element*. London: Taylor & Francis, 2002.
- [215] D. Weiss, “Composites and Alloys Based on the Al-Ce System,” in *Aluminum Alloys and Composites*, K. Cooke, 2020.
- [216] E. Vandersluis, D. Sediako, P. Emadi, C. Ravindran, A. Elsayed, and G. Buczynski, “Determination of temperature-dependent crystallographic parameters of Al-Si alloys using in situ neutron diffraction,” *J. Appl. Crystallogr.*, vol. 51, pp. 1141–1150, 2018.
- [217] E. Aghaie, J. Stroh, D. Sediako, and M. Smith, “In-Situ Fitness-for-Service Assessment of Aluminum Alloys Developed for Automotive Powertrain Lightweighting,” *Light Met.* 2018, pp. 397–400, 2018.
- [218] P. Minárik, R. Král, J. Pešička, S. Daniš, and M. Janeček, “Microstructure characterization of LAE442 magnesium alloy processed by extrusion and ECAP,” *Mater. Charact.*, vol. 112, pp. 1–10, 2016.
- [219] M. Starink and A. Zahra, “b' and b Precipitation in an Al±Mg Alloy Studied by DSC and TEM,” *Acta Met.*, vol. 46, no. 10, pp. 3381–3397, 1998.
- [220] Z. Lu and L. Zhang, “Thermal stability and crystal structure of high-temperature compound Al₁₃CeMg₆,” *Intermetallics*, vol. 88, pp. 73–76, 2017.
- [221] M. Qi, B. Bie, F. Zhao, and D. Hu, “A Metallography and X-ray Tomography Study of Spall Damage in Ultrapure Al,” *AIP Adv.*, vol. 4, no. 077118, pp. 1–12, 2014.
- [222] T. Nishiura, “Application of Laboratory Based Cone Beam X-ray CT Techniques to Metallurgical Study” *Nippon Steel & Sumitomo Metal Technical Report*, No. 114, 2017.
- [223] E. Maire and P. Withers, “Quantitative X-ray Tomography,” *Int. Mater. Rev.*, vol. 59, no. 1, pp. 1–43, 2014.
- [224] J. Stroh, D. Sediako, D. Weiss, and V. K. Peterson, “In Situ Neutron Diffraction Solidification Analyses of Rare Earth Reinforced Hypoeutectic and Hypereutectic Aluminum–Silicon Alloys,” in *Light Metals 2020*, pp. 174–178, 2020.

- [225] J. Stroh, D. Sediako, and D. Weiss, "Development of Cerium-Reinforced Specialty Aluminum Alloy With Application of X-ray and Neutron Diffraction," *Int. J. Met. Cast.*, pp. 1–11, 2020.
- [226] C. Xu, W. Xiao, S. Hanada, H. Yamagata, and C. Ma, "The effect of scandium addition on microstructure and mechanical properties of Al-Si-Mg alloy: A multi-refinement modifier," *Mater. Charact.*, vol. 110, pp. 160–169, 2015.
- [227] P. Li, S. Liu, L. Zhang, and X. Liu, "Grain refinement of A356 alloy by Al-Ti-B-C master alloy and its effect on mechanical properties," *Mater. Des.*, vol. 47, pp. 522–528, 2013.
- [228] K. Liss, B. Hunter, M. Hagen, T. Noakes, and S. Kennedy, "Echidna-the new high-resolution powder diffractometer being built at OPAL," *Phys. B Condens. Matter*, vol. 385–386, pp. 1010–1012, Nov. 2006.
- [229] D. Sediako, W. Kasprzak, I. Swainson, and O. Garlea, "Solidification Analysis of Al-Si Alloys Modified With Addition of Cu Using In-Situ Neutron Diffraction," in *The Minerals, Metals & Materials Society (TMS)*, 2011, vol. 2, pp. 279–289.
- [230] B. Fultz and J. Howe, *Transmission Electron Microscopy and Diffractometry of Materials*, Fourth edition. Springer-Verlag, 2013.
- [231] D. B. Sirdeshmukh and L. Sirdeshmukh, "Micro-and Macro-Properties of Solids," *Mater. Sci.*, vol. 80, pp. 77–133, 2006.
- [232] M. Hutchings, P. Withers, T. Holden, and T. Lorentzen, *Introduction to the characterisation of residual stress by neutron diffraction*. Boca Raton, FL: Taylor, 2005.
- [233] A. Elsayed, D. Sediako, and C. Ravindran, "Solidification Analysis of A Magnesium-Zinc Alloy Using in-Situ Neutron Diffraction," in *Shape Casting: 6th International Symposium*, 2016, no. 1, pp. 167–174.
- [234] E. Vandersluis, A. Elsayed, F. D'Elia, P. Emadi, D. Sediako, and C. Ravindran, "Crystalline-Phase Solidification Analysis Using In Situ Neutron Diffraction," *Trans. Indian Inst. Met.*, vol. 71, no. 11, pp. 2777–2781, 2018.
- [235] W. Kasprzak, D. Sediako, M. Walker, M. Sahoo, and I. Swainson, "Solidification analysis of an Al-19 Pct Si alloy using in-situ neutron diffraction," *Metall. Mater. Trans. A*, vol. 42, no. 7, pp. 1854–1862, 2011.
- [236] M. Uichiro, *Hume-Rothery Rules for Structurally Complex Alloy Phases*. Boca Raton, FL: CRC Press, 2011.
- [237] W. Hume-Rothery, "The Freezing Points, Melting Points, and Solid Solubility Limits of the Alloys of Silver and Copper With the Elements of the B Sub-Groups," *R. Soc. London*, vol. 233, pp. 1–97, 1934.
- [238] H. M. Rietveld, "A profile refinement method for nuclear and magnetic structures," *J. Appl. Crystallogr.*, vol. 2, no. 2, pp. 65–71, 1969.

- [239] L. B. McCusker, R. B. Von Dreele, D. E. Cox, D. Loue, and P. Scardi, "Rietveld refinement guidelines," *J. Appl. Crystallogr.*, vol. 32, pp. 36–50, 1999.
- [240] B. H. Toby, "R factors in Rietveld analysis: How good is good enough?," *Powder Diffr.*, vol. 21, no. 1, pp. 67–70, 2006.
- [241] M. Zhu, Z. Jian, G. Yang, and Y. Zhou, "Effects of T6 heat treatment on the microstructure, tensile properties, and fracture behavior of the modified A356 alloys," *Mater. Des.*, vol. 36, pp. 243–249, 2012.
- [242] E. Rincón, H. F. López, M. M. Cisneros, H. Mancha, and M. A. Cisneros, "Effect of temperature on the tensile properties of an as-cast aluminum alloy A319," *Mater. Sci. Eng. A*, vol. 452–453, pp. 682–687, 2007.
- [243] O. D. Sherby, J. L. Lytton, and J. E. Dorn, "Activation energies for creep of high-purity aluminum," *Acta Metall.*, vol. 5, no. 4, pp. 219–227, 1957.
- [244] J. Čadek, M. Pahutová, and V. Šustek, "Creep behaviour of a 2124 Al alloy reinforced by 20 vol.% silicon carbide particulates," *Mater. Sci. Eng. A*, vol. 246, no. 1–2, pp. 431–454, 1998.
- [245] F. A. Mohamed, Kyung-Tae Park, and E. J. Lavernia, "Creep behavior of discontinuous SiC-Al composites," *Mater. Sci. and Eng.*, vol. A150, pp. 21–35, 1992.
- [246] H. R. Erfanian-Naziftoosi, E. J. Rincón, R. Rincón, H. F. López, and L. López, "Creep Properties of the As-Cast Al-A319 Alloy: T4 and T7 Heat Treatment Effects," *Metall. Mater. Trans. A*, vol. 47A, pp. 4258–4267, 2016.
- [247] K. T. Park, E. J. Lavernia, and F. A. Mohamed, "High-temperature deformation of 6061 Al," *Acta Metall. Mater.*, vol. 42, no. 3, pp. 667–678, 1992.
- [248] L. Lu and A. K. Dahle, "Iron-rich intermetallic phases and their role in casting defect formation in hypoeutectic Al-Si alloys," *Metall. Mater. Trans. A*, vol. 36, no. 13, pp. 819–835, 2005.
- [249] T. O. Mbuya, B. O. Odera, and S. P. Ng'ang'a, "Influence of iron on castability and properties of aluminium silicon alloys: Literature review," *Int. J. Cast Met. Res.*, vol. 16, no. 5, pp. 451–465, 2003.
- [250] C. Dinnis and J. Taylor, "Porosity formation and eutectic growth in Al-Si-Cu-Mg alloys containing iron and manganese," *Mater. Sci.*, pp. 1016–1021, 2004.
- [251] E. Arzt, "Creep of Dispersion Strengthened Materials: A Critical Assessment," *Res Mech.*, vol. 31, pp. 399–453, 1991.
- [252] L. Kloc, S. Spigarelli, E. Cerri, E. Evangelista, and T. G. Langdon, "An evaluation of the creep properties of two Al-Si alloys produced by rapid solidification processing," *Metall. Mater. Trans. A*, vol. 27A, pp. 3871–3879, 1996.

[253] L. Kloc, S. Spigarelli, E. Cerri, E. Evangelista, and T. G. Langdon, “Creep behavior of an aluminum 2024 alloy produced by powder metallurgy,” *Acta Mater.*, vol. 45, no. 2, pp. 529–540, 1997.

[254] J. Čadek, H. Oikawa, and V. Šustek, “Threshold creep behaviour of discontinuous aluminium and aluminium alloy matrix composites: An overview,” *Mater. Sci. Eng. A*, vol. 190, no. 1–2, pp. 9–23, 1995.